NIST
National Institute of Standards and Technology
Technology Administration
U.S. Department of Commerce

NIST CENTER FOR NEUTRON RESEARCH

2006 ACCOMPLISHMENTS AND OPPORTUNITIES

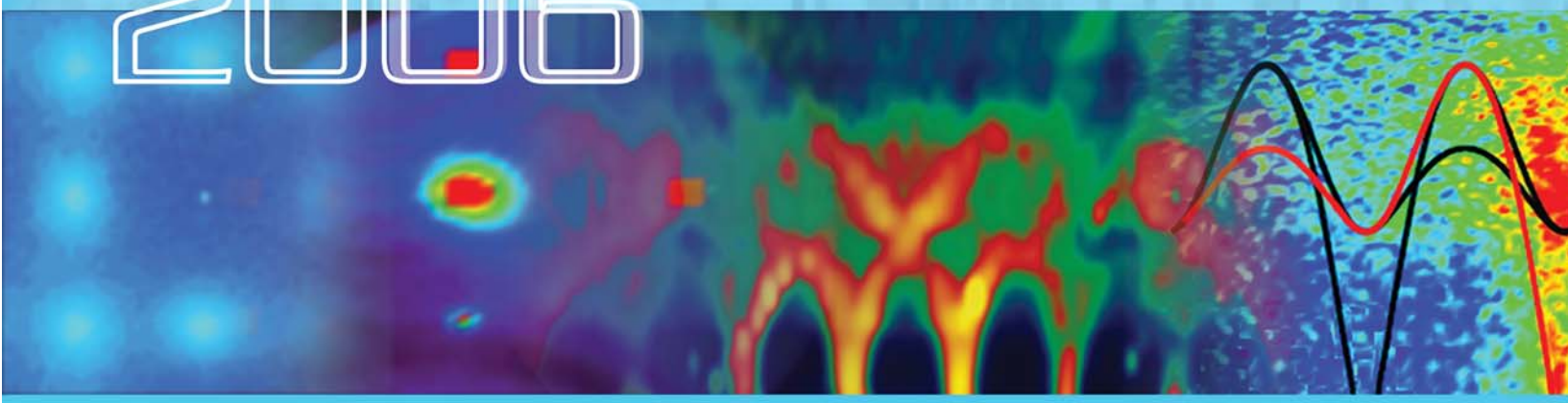

NIST SP 1060

COVER: Some partial images of reduced data from NCNR experiments in 2006. Left to right, material and instrument: "null" matrix ^{62}NiPt alloy Bragg peaks and diffuse scattering (disk chopper spectrometer (DCS)); $Tb_2Ti_2O_7$ magnetic 002 Bragg peak (DCS, see pp. 18,19); $La_{1.5}Sr_{0.5}CoO_4$ magnon and phonon excitations (thermal triple axis spectrometer BT-7); $NaCrO_2$ spin-wave excitations (thermal triple axis spectrometer BT-9, and DCS, see pp. 16,17).

2006 NIST Center for Neutron Research

ACCOMPLISHMENTS AND OPPORTUNITIES

NIST Special Publication 1060

Patrick D. Gallagher, Director

Ronald L. Cappelletti, Editor

December 2006

National Institute of Standards and Technology
William A. Jeffrey, Director

Technology Administration
Robert C. Cresanti
Under Secretary of Commerce for Technology

U.S. Department of Commerce
Carlos M. Gutierrez, Secretary

DISCLAIMER

Certain commercial entities, equipment, or materials may be identified in this document in order to describe an experimental procedure or concept adequately. Such identification is not intended to imply recommendation or endorsement by the National Institute of Standards and Technology, nor is it intended to imply that the entities, materials, or equipment are necessarily the best available for the purpose.

National Institute of Standards
and Technology Special Publication 1060

Natl. Inst. Stand. Technol. Spec. Publ. 1060, 88 pages
(December 2006)

CODEN: NSPUE2

U.S. GOVERNMENT PRINTING OFFICE - WASHINGTON: 2006

For sale by the Superintendent of Documents,
U.S. Government Printing Office

Internet: bookstore.gpo.gov ■ Phone: 202.512.1800
Fax: 202.512.2250 ■ Mail: Stop SSOP, Washington, DC 20402-0001

Table of Contents

Foreword

It is once again my pleasure to present you with our annual summary of activities for the NIST Center for Neutron Research. This has been another very busy and productive year. The NCNR continued its record for safety and reliability by operating 266 days, only missing $3\frac{1}{2}$ days that were scheduled to run. This type of high availability and predictable operation according to an established schedule is at the very heart of our success as a national user facility. It is also the product of a lot of dedication and hard work behind the scenes by our operations staff. We are also making progress on a number of upgrades and enhancements to ensure that this strong record of operation will continue long into the future.

Instrument development at the NCNR has also been very active this year for several reasons. First, a new, upgraded, neutron imaging facility was constructed and commissioned at BT-2 this year. This new, one-of-a-kind facility is optimized for imaging of full-size hydrogen fuel cell systems and is already generating lots of excitement in this research area. There were also continuing efforts on several major on-going projects including the BT-7 triple axis and the Multi-Analyzer Crystal Spectrometer. And finally, we have been very busy planning for some exciting new possibilities for the future! The proposed FY07 budget for NIST that is under consideration by Congress at the time of this writing includes funding for a major expansion of the NCNR beginning next year that would include a second guide hall, new cold source, and additional instruments. To prepare for this important opportunity, we have been actively soliciting input from neutron users to collect ideas on what types of new instrumentation can best serve the future research needs of the U.S. research community. A central part of this effort was a workshop held this July in Bethesda, Maryland to provide a forum for discussion of new neutron instrumentation and the associated scientific opportunities they provide. Now we are hard at work digesting the many ideas we received and analyzing the expected performance of various options so that we can promptly begin the project when it is funded.

The following report contains updates on these and other developments. However, the bulk of this report is centered on the selected highlights from research performed at the NCNR during the past 12 month period. We have tried to select a few examples from each area to represent the large body of exciting research being conducted at the NCNR. It is my hope that these selections will not only demonstrate the tremendous breadth, depth, and quality of the work done at the NCNR this past year, but also capture the excitement and enthusiasm of those performing the research. I also hope that the highlights we selected for this Annual Report will pique your interest enough to visit our website at www.ncnr.nist.gov, where you can get additional information on the many other projects that the limited space did not allow us to include.

I wish to extend my thanks to our users and staff, whose hard work and dedication are celebrated in this report, for another exciting and successful year. I am already looking forward to seeing what next year will bring…

NIST Center for Neutron Research

Neutrons are powerful probes of the structure and dynamics of materials ranging from molecules inserted into membranes that mimic cell walls to protons migrating through fuel cells. The unique properties of neutrons (discussed below) can be exploited using a variety of measurement techniques to provide information not available by other means. They are particularly well suited to investigate all forms of magnetic materials such as those used in computer memory storage and retrieval. Atomic motion, especially that of hydrogen, can be measured and monitored, like that of water during the setting of cement. Residual stresses such as those inside stamped steel automobile parts can be mapped. Neutron-based research covers a broad spectrum of disciplines, including engineering, biology, materials science, polymers, chemistry, and physics.

The NCNR's neutron source provides the intense beams of neutrons required for these types of measurements. In addition to the thermal neutron beams from the heavy water or graphite moderators, the NCNR has a large area liquid hydrogen moderator, or cold source, that provides intense neutron beams for the only cold neutron facility presently operating in the U.S.

There are currently 29 experiment stations: four provide high neutron flux positions for irradiation, and 25 are beam facilities most of which are used for neutron scattering research. The following pages show a schematic layout of the beam facilities. More complete descriptions of instruments can be found at www.ncnr.nist.gov.

The NCNR supports important NIST research needs, but is also operated as a major national user facility with merit-based access made available to the entire U.S. technological community. Each year, approximately 2000 research participants from all areas of the country, from industry, academia, and from government use the facility for measurements. Beam time for research to be published in the open literature is without cost to the user, but full operating costs are recovered for proprietary research. Access is gained mainly through a peer-reviewed, web-based proposal system with beam time allocated by a Program Advisory Committee twice a year. For details see www.ncnr.nist.gov/beamtime.html. The National Science Foundation and NIST co-fund the Center for High Resolution Neutron Scattering (CHRNS) that operates six of the world's most advanced instruments. Time on CHRNS instruments is made available through the proposal system. Some access to beam time for collaborative measurements with the NIST science staff can also be arranged on other instruments.

WHY NEUTRONS?

Neutrons reveal properties not available to other probes. They can behave like microscopic magnets, they can diffract like waves, they can set particles into motion losing or gaining energy and momentum in the process, and they can be absorbed.

WAVELENGTHS–in practice range from < 0.1 Å to < 15 Å (1 Å = 0.1 nm), allowing them to form observable ripple patterns from structures as small as atoms to as large as cells.

ENERGIES–of millielectronvolts, of the same order as those of motions of atoms in solids or liquids, waves in magnetic materials, and vibrations in molecules. Exchanges of energy between neutrons and matter as small as nanoelectronvolts and as large as tenths of electronvolts can be detected.

SELECTIVITY–in scattering power varies from nucleus to nucleus somewhat randomly. Specific isotopes can stand out from other isotopes of the same kind of atom. Specific light atoms, difficult to observe with x-rays, are revealed by neutrons. Hydrogen, especially, can be distinguished from chemically equivalent deuterium.

MAGNETISM–makes the neutron sensitive to the magnetic spins of both nuclei and electrons, allowing the behavior of ordinary and exotic magnets to be detailed precisely.

NEUTRALITY–of the uncharged neutrons allows them to penetrate deeply without destroying samples, and pass through walls controlling a sample's environment allowing measurements under extreme conditions. Properties ranging from the residual stresses in steel girders to the unfolding motions of proteins are amenable to measurement by neutrons.

CAPTURE–characteristic radiation emanating from specific nuclei capturing incident neutrons can be used to identify and quantify minute amounts of material in pollutants or ancient pottery shards.

NIST Center for Neutron Research Layout

1. **BT-5 Perfect Crystal Ultra-Small Angle Neutron Scattering (USANS) Diffractometer** for microstructure up to 10^4 nm, part of CHRNS.

2. **BT-4 Filter Analyzer Neutron Spectrometer** with cooled Be/Graphite filter analyzer for chemical spectroscopy.

3. **BT-2 Neutron Imaging Facility** for imaging hydrogenous matter in large components such as water in fuel cells and lubricants in engines, in partnership with General Motors.

4. **BT-1 Powder Diffractometer** with 32 detectors; incident wavelengths of 0.208 nm, 0.154 nm, and 0.159 nm, with highest resolution of $\delta d/d = 8 \times 10^{-4}$.

5. **BT-9 Thermal Triple Axis Spectrometer** for measurements of excitations and structure in condensed matter.

6. **BT-8 Residual Stress Diffractometer** optimized for depth profiling of residual stresses in large components.

7. **VT-5 Thermal Neutron Capture Prompt Gamma-ray Activation Analysis Instrument** with a neutron fluence rate of 3×10^8 /cm^2/s used for quantitative elemental analysis of bulk materials. Generally used for the analysis of highly hydrogenous materials (≈ 1 % H) such as foods, oils, and biological materials.

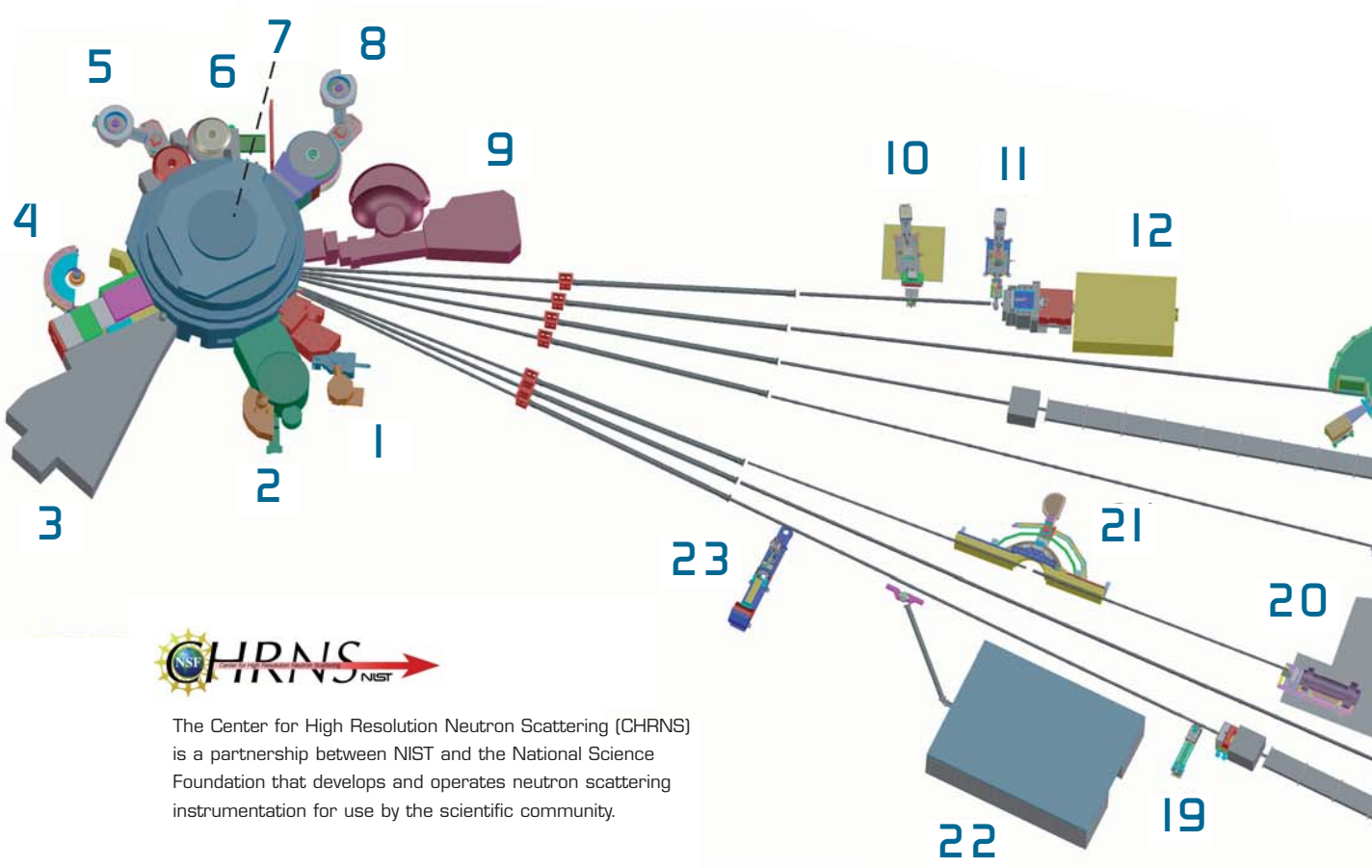

The Center for High Resolution Neutron Scattering (CHRNS) is a partnership between NIST and the National Science Foundation that develops and operates neutron scattering instrumentation for use by the scientific community.

The Cold Neutrons for Biology and Technology (CNBT) program is a partnership between NIST and a consortium led by the University of California at Irvine and funded by the National Institutes of Health. It focuses on the structure of biological membranes.

8. **BT-7 Thermal Triple Axis Spectrometer** with large double focusing monochromator, and interchangable analyzer/detectors systems.

9. **NG-0 MACS a cold neutron triple axis crystal spectrometer** (under construction) with double focusing monochromator and multiple crystal analyzer/detectors that can be flexibly configured for several energies simultaneously or for high throughput at one energy.

10. **NG-1 Advanced Neutron Diffractometer/ Reflectometer (AND/R)** a vertical sample reflectometer with polarization analysis and off-specular reflection capabilities for measuring reflectivities down to 10^{-8}, part of the CNBT.

11. **NG-1 Vertical Sample Reflectometer** instrument with polarization analysis capability for measuring reflectivities down to 10^{-8} to determine subsurface structure.

12. **NG-1 Cold Neutron Depth Profiling** instrument for quantitative profiling of subsurface impurities.

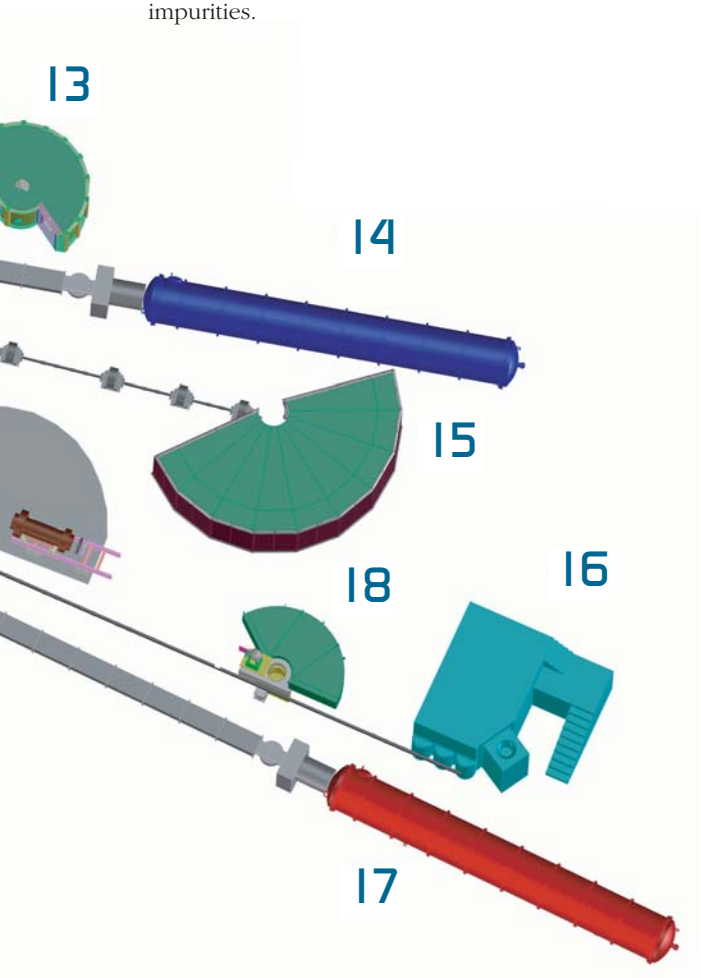

13. **NG-2 Backscattering Spectrometer (HFBS)** high intensity inelastic scattering instrument with energy resolution < 1 μeV, for studies of motion in molecular and biological systems, part of CHRNS.

14. **NG-3 30 m SANS** for microstructure measurements, part of CHRNS.

15. **NG-4 Disk Chopper TOF Spectrometer** for studies of diffusive motions and low energy dynamics of materials. Wavelengths from ≈ 0.18 nm to > 2.0 nm give corresponding energy resolutions from ≈ 2 meV to < 10 μeV, part of CHRNS.

16. **NG-6 Neutron Physics Station** offering three cold neutron beams having wavelengths of 0.5 nm, 0.9 nm, and "white" that are available for fundamental neutron physics experiments.

17. **NG-7 30 SANS** for microstructure measurements, in partnership with NIST, ExxonMobil, and CNBT.

18. **NG-6 Fermi Chopper Hybrid Time-of-Flight (TOF) Spectrometer** for inelastic scattering measurements with selected incident wavelengths between 0.23 nm and 0.61 nm.

19. **NG-7 Prompt Gamma Activation Analysis** cold neutron fluxes allow detection limit for H of 1 μg to 10 μg, depending on the matrix. Focused beams are available for profiling.

20. **NG-5 Spin-Echo Spectrometer** for measuring dynamics from 100 ns to 10 ps, in partnership with ExxonMobil, part of CHRNS.

21. **NG-5 Spin-Polarized Triple Axis Spectrometer (SPINS)** using cold neutrons with position sensitive detector capability for high-resolution studies, part of CHRNS.

22. **NG-7 Neutron Interferometry and Optics Station** with perfect crystal silicon interferometer; vibration isolation system provides exceptional phase stability and fringe visibility.

23. **NG-7 Horizontal Sample Reflectometer** allows reflectivity measurements of free surfaces, liquid/vapor interfaces, as well as polymer coatings.

NCNR Images 2006

"Neutron Research at NIST" (NRAN), a Sept. 2005 symposium to honor NCNR's Mike Rowe and Jack Rush.

Center: NCNR's Jack Rush and Mike Rowe. Some NRAN speakers, from top left: Sam Werner (UMo, ret.), Sunny Sinha (UCSD), Robert Birgeneau (UCB), Karl Michel (U Antwerp), Walter Kohn (UCSD), Pat Dehmer (DOE), John Axe (BNL, ret.), Julia Weertman (NWU, ret.), Lyle Schwartz (AFOSR), Roger Pynn (IUCF).

NCNR researchers Tatiana Guidi and Yiming Qiu involved in a particularly complex experimental arrangement at DCS pause for a photo.

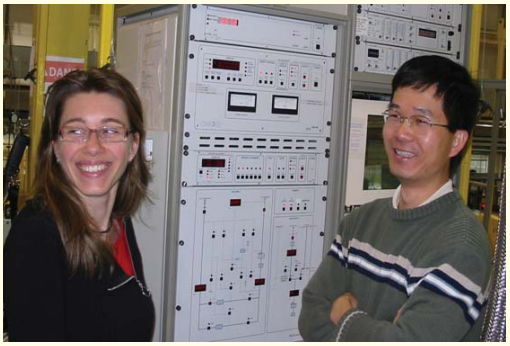

NCNR's Chuck Majkrzak, in signal attire, delivers his Warren Award formal address at the 2006 ACA meeting in Hawaii.

Bob and Toni Carter, seated, chatting with Karl Michel at NRAN. Sadly, Robert S. Carter, a former director of NBSR,passed away in October, 2005.

NCNR's Wangchun Chen holding a ^{3}He neutron polarization cell at the AND/R instrument.

NCNR Director Pat Gallagher describes what neutrons can measure to U.S. Senator Barbara Mikulski (MD) and NIST staff.

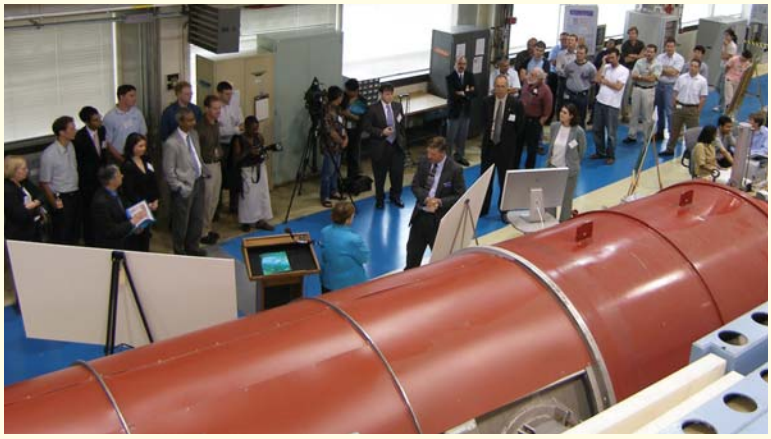

U.S. Senator Barbara Mikulski (MD), gets a lesson in fuel cell technology from GM's Dan O'Connell.

Students and staff of the NCNR 2006 Summer School on Neutron Scattering gather for a photo.

Sushil Satija (front) demonstrates good technique to NCNR Summer School students Andrea Hamill (USC), Peter Bowerman (VT), and Ashish Jha (URI).

Igor Zaliznyak (BNL) comments at the NCNR Expansion Workshop in July.

Mike Fitzsimmons (LANL) leads a discussion on polarized beam methods at the NCNR Expansion Workshop.

Enhanced Hydrogen Storage in a Microporous Metal-Organic Framework

It is a major goal to have a hydrogen fuel system for use in automobiles that can compete with the current gasoline infrastructure and engine efficiency. This effective use of hydrogen as a substitute for fossil fuels relies largely upon the development of a viable on-board storage system. Possible storage methods, such as gas under high pressure, liquefaction, or gas adsorbed in metal hydrides or porous carbons fail to meet at least one of the required criteria of capacity, safety or ability to recharge quickly. Progress is being made in each of these areas, and significant reversible H_2 adsorption has been observed in a class of crystalline hosts known as metal-organic frameworks. Generally, these porous three-dimensional solids are composed of metal ions or metal clusters linked via organic ligands. Evacuation of the solvent molecules entrained in the framework during preparation can lead to high surface area materials capable of adsorbing hydrogen.

M. Dincă[1]
A. Dailly[5,6]
Y. Liu[2,3]
C.M. Brown[2,4]
D.A. Neumann[2]
J.R. Long[1]

[1] University of California at Berkeley Berkeley, CA 94720

[2] NIST Center for Neutron Research National Institute of Standards and Technology Gaithersburg, MD 20899-8562

[3] University of Maryland College Park, MD 20742

[4] Indiana University Cyclotron Facility Bloomington, IN 47408

[5] General Motors Corporation Warren, MI 48090

[6] Purdue University West Lafayette, IN 47907

To maximize the amount of adsorbed H_2 accessible at room temperature and with reasonable applied pressure, it is thought that a binding energy of 15 kJ/mol is necessary [1]. However, in many materials typical binding energies are 4 kJ/mol to 7 kJ/mol between the poorly polarizable H_2 molecules and the pore walls so that cryogenic temperatures are required to obtain significant H_2 uptake. One method used to enhance H_2 binding is to form frameworks with very narrow pores where overlapping potentials from two or more pore walls interact to bind a single H_2 molecule. In this way binding energies of up to 9.5 kJ/mol have been observed [2]. A second mechanism has been proposed to use strong metal-H_2 interactions with coordinatively-unsaturated metal centers [3]. We have recently generated a highly porous framework with exposed Mn^{2+} coordination sites leading to a high total H_2 uptake of 60 g/L (or 6.9 % mass fraction) at 77 K and 90 bar. We have demonstrated direct observation of hydrogen binding to the unsaturated metal center in a metal-organic framework time using neutron powder diffraction. The initial H_2 binding energy is 10.1 kJ/mol. These numbers represent the highest volumetric capacity and largest binding energy obtained thus far for a metal-organic framework.

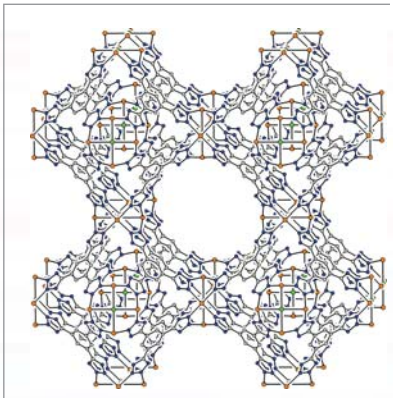

FIGURE 1: Schematic crystal structure showing the arrangements of sodalite cage-like units with hydrogen atoms and solvent molecules omitted for clarity.

Sample preparation is discussed elsewhere [4]. A single crystal of the solvated parent compound was analyzed using x-ray diffraction and the resulting framework structure is illustrated in Fig. 1. Despite numerous attempts, evacuation conditions for removing all of the remaining solvent without degrading the framework have not yet been discovered and residual solvent molecules coordinate 83 % of the framework Mn^{2+} ions, leaving only a small fraction of these metal centers with open coordination sites. From Fig. 1, the high surface area and open pore structure of the desolvated material is clearly evident (N_2 isotherms give an estimated surface area of 2100 m^2/g). The hydrogen storage properties were evaluated using volumetric gas adsorption measurements. The resulting isotherms show fully reversible uptakes of 2.2 % mass fraction at 77 K and 1.2 bar with the highest initial isosteric heat of adsorption reported for a metal-organic framework at 10.1 kJ/mol [5,6].

Neutron powder diffraction experiments, using the BT-1 diffractometer, were performed as a direct check of whether the high binding enthalpy is associated with coordination of H_2 at exposed Mn^{2+} sites. A diffraction pattern was collected for desolvated material prior to adding D_2. Subsequent Rietveld analysis indicated the existence of extra neutron scattering length density close to the Mn^{2+} ions in the framework skeleton, as expected due to the presence of residual methanol molecules. Accordingly, the extra density was modeled using disordered O and C atoms, and this corrected "bare" model was used as a baseline for all subsequent measurements involving D_2.

Figure 2 shows the diffraction pattern observed at 3.5 K upon adsorption of 12 D_2 molecules per formula unit. At this low loading a Fourier difference analysis using the bare material as the initial model clearly identifies the two strongest binding sites as positions I and II in Fig. 3. Significantly, site I is

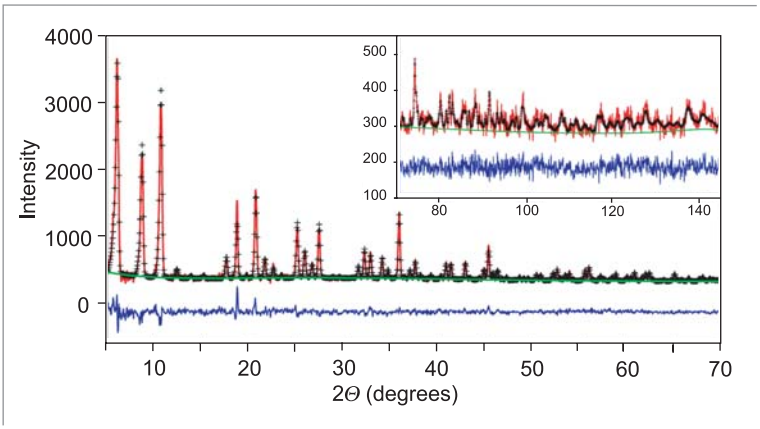

FIGURE 2:
Rietveld refinement of neutron powder diffraction data for a loading of 12 D_2 molecules per formula unit. Green lines, crosses, and red lines represent the background, calculated and experimental diffraction patterns, respectively. The blue line shows the difference between experimental and calculated patterns.

located just 2.2 Å from the Mn^{2+} ions in the framework skeleton, providing the first neutron diffraction evidence for a metal-H_2 interaction within a metal-organic framework. To our knowledge, this is also the first example of H_2 binding to a Mn^{2+} ion. The D_2 molecules at site II are situated inside the sodalite-like cages, and exhibit van der Waals contacts of 3.49 Å and 3.63 Å with a chloride anion and four equidistant ligands, respectively. The sum of the five corresponding attractive interactions is likely responsible for a significant adsorption enthalpy at this site as well. Indeed, this site becomes fully occupied when the total D_2 loading is increased to 24 molecules per formula unit.

Increased D_2 loadings also permitted identification of the next strongest binding site, labeled III, and a possible binding site labeled IV in Fig. 3. The D_2 molecules at site III are situated inside the larger framework cavities, and have van der Waals contacts of 3.33 Å with two equidistant ligands. At site IV, the D_2 molecules are located at the interface between the smaller and larger cavities, and are in closest contact (3.40 Å) with two carbon atoms from neighboring ligands, as well as a site partially-occupied by an extra-framework Mn^{2+} ion (at 3.21 Å). Filling of sites III and IV continues when 48 D_2 molecules are loaded per formula unit. Out of 48 D_2 molecules refined from a model derived from the difference scattering length map, 7.1 reside at site I, 10.7 at site II, 24.0 at site III, and 4.9 at site IV.

A key and challenging aspect of hydrogen storage research is the ability to control the H_2 binding energy that governs the adsorption in materials ranging from microporous solids to metal hydrides. In this regard, a very attractive property of metal-organic frameworks is that their pores can be engineered at the atomic scale, thereby enabling some control over the H_2 binding interaction. The results presented here show that, on a materials characteristic basis, metal-organic frameworks with unsaturated metal centers can exceed the 2010 DOE H_2 storage targets of 6.0 % mass fraction and 45 g/L. Meeting these targets for a complete storage system, however, will require further efforts toward raising the H_2 binding energy, such that storage at closer to ambient conditions can be accomplished. Ultimately, this may be possible in materials related to those reported here through adjustment of the electronic structure of the metal ions and exposure of a higher concentration of coordination sites.

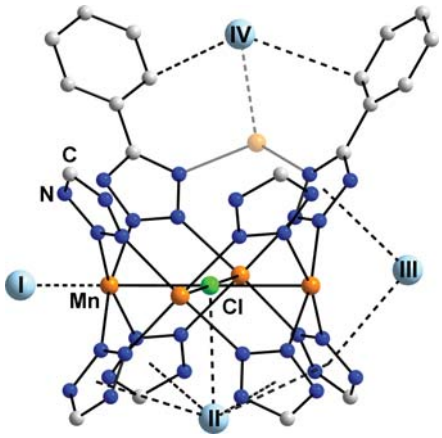

FIGURE 3:
Initial D_2 adsorption sites. Light blue spheres represent D_2 centroids, while the light orange sphere shows the position of a partially-occupied, extra-framework Mn^{2+} ion site. Hydrogen atoms and methanol molecules are omitted for clarity.

REFERENCES

[1] S.K. Bhatia, A.L. Myers, Langmuir **22**, 1688 (2006).
[2] M. Dincă, J.R. Long, J. Am. Chem. Soc. **127**, 9376 (2005).
[3] B. Chen, N.W. Ockwig, A.R. Millward, D.S. Contreras, O.M. Yaghi, Angew. Chem., Int. Ed. **44**, 4745 (2005).
[4] M. Dincă, A. Dailly, Y. Liu, C.M. Brown, D.A. Neumann, J.R. Long, accepted for publication in J. Am. Chem. Soc..
[5] M. Dincă, J.R. Long, J. Am. Chem. Soc. **127**, 9376 (2005).
[6] J.L.C. Rowsell, O.M. Yaghi, J. Am. Chem. Soc. **128**, 1304 (2006).

Structure and Hydrogen Bonding in $CaSiD_{1+x}$: Is There Covalent Character?

H. Wu[1,2]
W. Zhou[1,3]
T.J. Udovic[1]
J.J. Rush[1]
T. Yildirim[1]

[1] NIST Center for Neutron Research National Institute of Standards and Technology Gaithersburg, MD 20899-8562

[2] University of Maryland College Park, MD 20742

[3] University of Pennsylvania Philadelphia, PA 19104

The intermetallic compound, CaSi, has recently been found to reversibly absorb more than one hydrogen per CaSi formula unit, which makes it of interest for storage applications [1]. While both x-ray diffraction and first-principles calculations have shed light on the general structure of $CaSiH_{1+x}$ [1,2], no neutron powder diffraction (NPD) or neutron vibrational spectroscopy (NVS) studies have thus far been reported to elucidate the exact interstitial locations and bonding of the H atoms within the rearranged CaSi lattice, and in so doing, rigorously test the recent theoretical predictions [2]. Here, we report our neutron results for $CaSiD_{1+x}$, which are not consistent with the strongly covalent Si-H bonding predicted for this system.

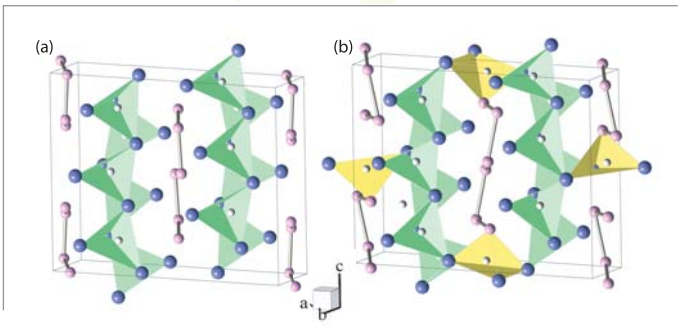

FIGURE 1:
Crystal structure of (a) $CaSiD_{1.2}$ and (b) CaSiD. Blue, pink, and white spheres represent Ca, Si, and D atoms, respectively. Ca_4-site tetrahedra are in green; Ca_3Si-site tetrahedra in yellow.

NPD data were collected for both $CaSiD_{1.2}$ and CaSiD. No significant structural changes or phase transformations were evident from the diffraction patterns at 10 K and 298 K. Rietveld refinements indicated that both compounds possessed *Pnma* symmetry. The refined structures are shown in Fig. 1. Compared to CaSi, the unit cell of $CaSiD_{1.2}$ expands three times along the ***c*** axis (the ***a*** axis of CaSi), and the resultant structure has two kinds of D sites with different nearest neighbors. One kind of D site is defined by four Ca nearest neighbors (Ca_4 sites, 1 per CaSi). Three crystallographically distinct Ca_4 tetrahedra are present and align in a zigzag fashion along the ***c*** direction.

The second kind of D site is located close to the center of a triangle of three Ca atoms as well as one Si atom (Ca_3Si site, 0.33 per CaSi). Since $CaSiD_{1.2}$ is a D-deficient $CaSiD_{1.33}$ phase, the Ca_3Si sites are found to be partially occupied (59 %), presumably in a disordered fashion. The recent theoretical study of $CaSiH_{1.3}$ [2] has concluded that the H atom in the Ca_3Si site is covalently bonded to the Si atom with a Si-H bond length of 1.58 Å, close to the 1.48 Å bond length in SiH_4. Yet, our results indicate that the Si-D distance is 1.82 Å (at 298 K), considerably larger (by ≈ 0.24 Å) than predicted. Figure 2 indicates that fixing this Si-D distance at values either increasingly larger or smaller than 1.82 Å leads to increasing χ^2 and R_{wp} values (*i.e.,* poorer model fits). Similar results are found for calculated deviations in other crystallographic directions. Besides being much larger than the Si-H bond length in SiH_4, 1.82 Å is also larger than that of any Si-H bond reported for various Si-H cluster, defect, and hydrogenated silicon (1.50 Å to 1.56 Å) [3]. These new experimental results clearly call into question the prediction of Si-H covalency by first-principles calculations [2].

The CaSiD structure (Fig. 1b) reveals an empty Ca_3Si site and essentially full occupancies of the other three Ca_4-type sites in the lattice. Compared to $CaSiD_{1.2}$, CaSiD possesses a slight shrinkage along the ***a*** axis and slight expansions along the ***b*** and ***c*** axes.

To further probe the nature of the D bonding in $CaSiD_{1+x}$, we have studied the D vibrations in both phases. Figure 3 shows the NV spectra for both compounds measured at 3.5 K. The vibrational band evi-

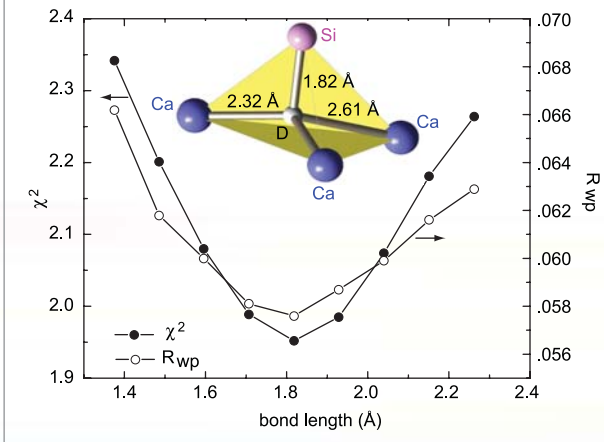

FIGURE 2:
The Rietveld goodness-of-fit parameters χ^2 and R_{wp} vs. the Si-D bond length fixed at various values along the Si-D axis as determined by the refined optimal position of D in the Ca_3Si interstices (shown schematically).

dent in the region of ≈ 50 meV to 70 meV for $CaSiD_{1.2}$ is largely absent for CaSiD. Therefore, this band can be directly associated with the D atoms in the Ca_3Si sites.

The NV spectrum of CaSiD was well-reproduced in Fig. 3 using first-principles phonon calculations, similar to the formalism in Ref. [2], within the plane-wave implementation of the generalized gradient approximation to density functional theory (DFT). DFT phonon calculations were also performed on $CaSiD_{1.33}$ (1 D atom/Ca_3Si site) and $CaSiD_{1.17}$ (0.5 D atoms/Ca_3Si site with ***b***-axis-directed Ca_3Si chains comprised of alternating D atoms and vacancies) using the same procedures and methods. Although the latter ordered configuration results in a different symmetry than observed experimentally for $CaSiD_{1.2}$, it is useful as a basis for calculating the effect of vacancies on the local bonding within $CaSiD_{1+x}$ structures where $x < 0.33$. Starting with the structure model determined from our NPD data, we obtained optimized structures for both stoichiometries very close to the one containing the 1.58 Å Si-H covalent bonds [2]. It is clear in Fig. 3 that the calculated $CaSiD_{1+x}$ vibrational spectra are noticeably dependent on both the occupation and degree of ordering associated with the Ca_3Si sites. For example, the calculated $CaSiD_{1.33}$ spectrum indicates that full occupation of the Ca_3Si sites causes a splitting of the D-associated vibrational modes (parallel to the plane of the Ca_3 triads) at around 57.3 meV and 62.6 meV, presumably due to interactions between nearest-neighbor D atoms occupying these sites. This splitting disappears, yielding a peak near 60.2 meV for the calculated, vacancy-ordered $CaSiD_{1.17}$ spectrum, which possesses no such nearest-neighbor pairs. The orthogonal Si-D stretching mode band (corresponding to the 1.58 Å bond length) is predicted near 142 meV for $CaSiD_{1.33}$ and 147 meV for $CaSiD_{1.17}$.

Compared to calculation, the observed $CaSiD_{1.2}$ spectrum appears to possess a disordered arrangement of occupied Ca_3Si sites as reflected by the significantly broadened, D-related vibrational mode centered near 63.4 meV. Aware that the calculated $CaSiD_{1.33}$ and $CaSiD_{1.17}$ NV spectra are not expected to be exactly comparable to that of disordered $CaSiD_{1.2}$, there are, nonetheless, notable discrepancies in the 50 meV to 70 meV region (*e.g.*, lower predicted peak energies) associated with the Ca_3Si-occupied D atoms as well as in the 70 meV to 100 meV region mainly associated with the Ca_4-occupied D atoms. Of particular note is the higher-than-predicted 63.4 meV feature for $CaSiD_{1.2}$, which is consistent with a Ca_3Si-occupied D atom that is closer to the Ca_3 triad, and therefore, farther from the Si atom than calculated by DFT. Unfortunately, the position of the orthogonal Si-D stretching mode band for $CaSiD_{1.2}$ cannot be definitively determined by the present NVS results due to an overlapping multiphonon band.

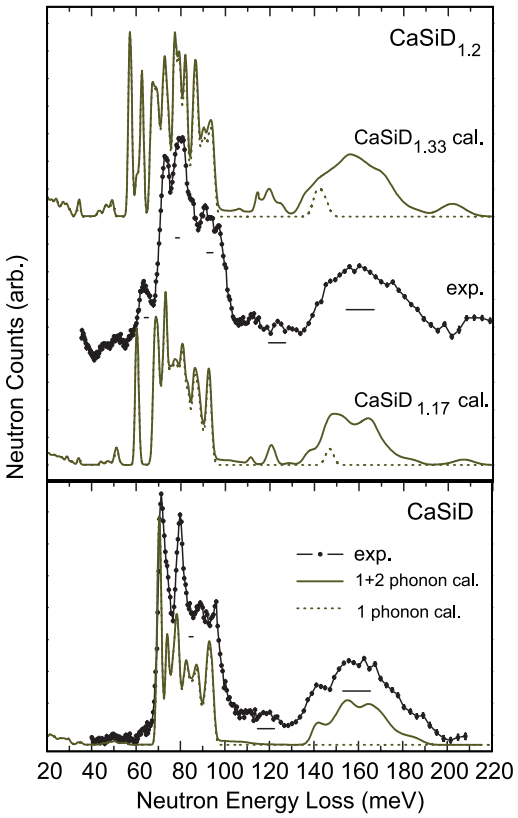

FIGURE 3:
NV spectra of $CaSiD_{1.2}$ and CaSiD. FWHM instrumental resolutions are depicted by the horizontal bars beneath the spectra. Calculated spectra for $CaSiD_{1.33}$, $CaSiD_{1.17}$, and CaSiD delineating both 1 phonon (dotted line) and 1+2 phonon (solid line) contributions are shown for comparison.

In conclusion, the longer Si-D distance and the instability of the Ca_3Si site supported by the NPD and NVS data calls into question the covalent nature of the Si-H bond suggested in Ref. 2. Our neutron results emphasize the importance of validating theoretical predictions by comparison with experimental data. It is clear that further theoretical studies are needed to address the structural and spectroscopic results and establish the nature of the Si-H bonding (and related electronic structure) in this CaSi hydride phase. A fundamental understanding of the Si-H bonding in the various metal-silicide-based hydrides is critical for the successful theory-driven development of improved hydrogen-storage materials containing Si.

REFERENCES

[1] M. Aoki, N. Ohba, T. Noritake, S. Towata, Appl. Phys. Lett. **85**, 387 (2004).
[2] N. Ohba, M. Aoki, T. Noritake, K. Miwa, S. Towata, Phys. Rev. B **72**, 075104 (2005).
[3] R.O. Jones, B.W. Clare, P.J. Jennings, Phys. Rev. B **64**, 125203 (2001), and references therein.

Quantum Rotational Dynamics of Methane in the Metal-Organic Framework MOF5

The dynamics of methane trapped in nano-porous materials is a widely studied problem due to its potential application in energy storage for fuel-cell technologies and also its interesting quantum properties such as rotational tunneling. Metal-organic framework (MOF) compounds, which consist of metal-oxide clusters connected by organic linkers, are a relatively new class of nano-porous material that show promise for storing gases such as H_2 and CH_4 because of their tunable pore size and functionality [1]. Yet despite numerous experimental studies of methane in MOF materials, the nature of the MOF-CH_4 interaction and the manner in which methane molecules are adsorbed onto the structure are still unknown. Answers to these questions hold the key to optimizing these materials for practical energy storage applications.

W. Zhou[1,2]
T. Yildirim[1,2]

[1] University of Pennsylvania Philadelphia, PA 19104

[2] NIST Center for Neutron Research National Institute of Standards and Technology Gaithersburg, MD 20899-8562

Using the difference-Fourier analysis of neutron powder diffraction data along with inelastic neutron scattering (INS) measurements and first-principles total-energy calculations, we first determined the CH_4 adsorption sites in MOF5 (the most widely studied MOF material, which consists of ZnO_4 clusters linked by 1,4-benzenedicarboxylate (BDC)), and then directly visualized the methane orientation distribution with increasing temperature and studied the rotational tunnel splitting [3].

Due to the large incoherent cross section of hydrogen, both the MOF5 and methane used in this experiment are deuterated. The methane loading was achieved by first filling a well-known dosing-volume to a target pressure and then exposing it to the MOF5 sample at 140 K. The sample was then cooled down to 115 K (the boiling point of methane is 111 K) at which point the pressure decreased to a negligible value as the CD_4 was adsorbed. The sample was further cooled down to 4 K before the measurements.

Figure 1 shows the diffraction pattern obtained on the BT-1 powder diffractometer at NIST from a MOF5 sample that was loaded with $4CD_4/4Zn$. In order to locate the methane adsorption sites, we first performed a Rietveld structural refinement using the model for the MOF5 host structure, ignoring the adsorbed CD_4 molecules. The isosurface of the difference-Fourier scattering length density based upon this model (see Fig. 1) clearly indicates that the first adsorption sites for methane are the cup-sites. This is the same as the first adsorption site of H_2 in MOF5 [2]. Interestingly, the orientation of the methane molecule is well resolved, where one of the CD-bonds is along the 3-fold axis. Having determined the location of the first adsorption sites, we then further refined the structural model, explicitly including the CD_4 molecules at the first adsorption site. The final refinement is shown in Fig.1 (solid line). The atomic positions of the CD_4 molecule within the MOF5 unit cell obtained from the structural refinement are also shown.

Diffraction data collected at elevated temperatures (up to 180 K) further indicate that the four hydrogen atoms do not lose their distinct positions as long as the methane molecule remains adsorbed. The isosurfaces of the difference-Fourier scattering length density obtained at sample temperatures of 40 K and 80 K are shown in Fig. 2 as examples. Clearly, the three equivalent hydrogen atoms pointing toward the ZnO_3 faces are much more resistant to thermal fluctuations than the other hydrogen atom, implying significantly different rotation barriers around different CH-bonds.

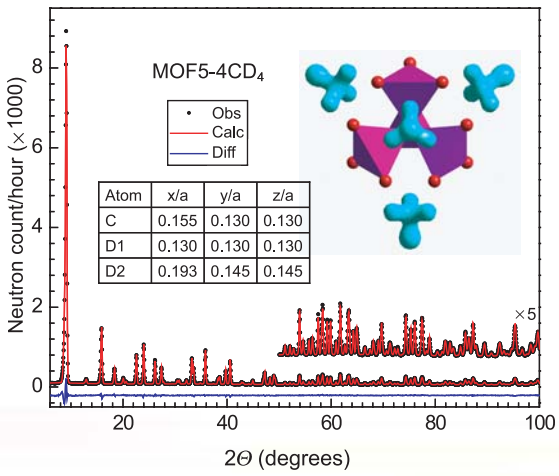

FIGURE 1:
The neutron powder diffraction pattern (λ = 2.08 Å) of the MOF5-$4CD_4$ at 4 K (dots) plus the Rietveld refinement (solid) with space group *Fm3m* and *a* = 25.91 Å, and difference plot (bottom). The inset shows the isosurfaces of the difference-Fourier scattering-length density superimposed with the ZnO_4 clusters of the MOF5 host structure, indicating the location of cup-sites for the first methane adsorption. The well-defined orientation of the adsorbed methane is apparent. The table shows the atomic fractional coordinates of the methane molecule.

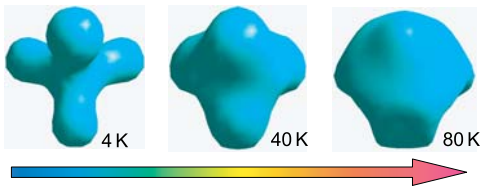

FIGURE 2:
Isosurfaces of the difference-Fourier scattering length density of a methane molecule in MOF5 with increasing temperature.

The fact that a methane molecule in MOF5 has a well defined orientation over a large temperature range implies a strong CH_4-MOF5 interaction and relatively large energy barriers to rotation. This also suggests that one may observe quantum rotational tunneling of a methane molecule between equivalent orientations, since the methane molecule is a quantum rotor. Such quantum tunnel splitting is very sensitive to the gas-host interaction potential and therefore it is an ideal probe to obtain detailed information about the rotational potential barrier, which is not available by other means.

We studied the quantum dynamics of CH_4 in MOF using inelastic neutron scattering (INS). The INS experiment was carried out using the time-of-flight Disk Chopper Spectrometer (DCS) at NIST. The low-energy part of the INS spectrum (after being integrated over the momentum-transfer *Q*) is shown in Fig. 3. The measured two-dimensional intensity contour plot in the momentum (*Q*) and energy (*E*) plane is also shown as an inset to Fig.3. Five-transitions originated from the rotational tunnel splitting were clearly resolved. Despite the rich features of the spectrum, we are able to fully explain the observed data in terms of a simple model where the methane molecule is allowed to tunnel around 3-fold axis and 3'-fold axis (which no longer has 3-fold symmetry due to the crystal field) as shown in the inset to Fig. 3. The calculated spectrum (red curve in Fig. 3) is in excellent agreement with the data in terms of both the energies and intensities of the peaks. The *Q*-dependencies of the peaks are also in good agreement with the measured spectrum. From this simple model, we obtained rotational barriers of 41 meV and 22 meV around the 3-fold and 3'-fold axes, respectively. We expect that our measured tunnel splitting spectrum will be a stringent test for theoretical models and for testing existing intermolecular potentials.

In order to obtain more information about methane host-lattice interactions and energetics, we also performed total energy calculations from density functional theory (DFT). The calculations were performed within the plane-wave implementation of the local-density approximation (LDA) to DFT. The binding energy of the "Cup site" is found to be 0.306 eV.

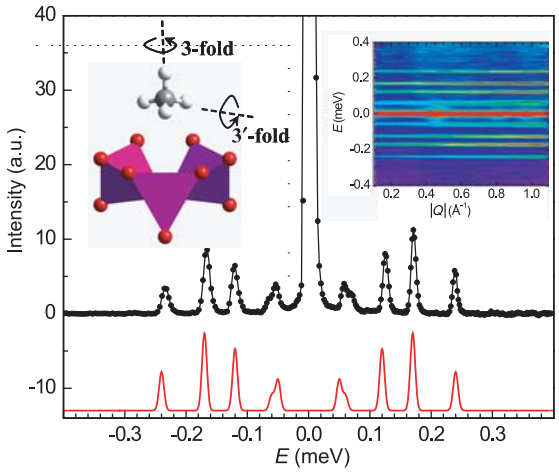

FIGURE 3:
The rotational tunneling spectrum of CH_4 adsorbed at the cup site of MOF5. The inset shows the intensity contour plot in *Q-E* plane. Five transitions were clearly resolved. The red-plot shows the calculated spectrum based on a simple tunneling model around two-axes as shown in the inset.

In contrast, the binding energies of the ZnO_3 site, ZnO_2 site and Hex site (as found for H_2 adsorption in MOF5 [2]) are all negative for CH_4, in agreement with the experimental observation that these sites are not favorable for methane. We also calculated the rotational potentials of CH_4 at the MOF5 cup site. The energy barriers about the 3-fold axis and 3'-fold axis are found to be 46.3 meV and 28.6 meV, respectively, in a reasonable agreement with the experimental values of 41 and 22 meV.

In conclusion, using Rietveld structural refinement of neutron powder diffraction data in conjunction with difference-Fourier (DF) analysis and first-principles calculations, we have determined the methane adsorption sites, binding energies, and tunnel splittings in MOF5 [3]. Initial adsorption occurs at the MOF5 cup site with a well defined CH_4 orientation. The temperature dependent DF-analysis is used to directly visualize the orientational dynamics of the absorbed methane molecule with increasing temperature. Using INS, we studied the quantum tunneling of methane and measured the rotational tunnel splitting. These results not only hold the key to test theoretical models of CH_4-MOF interactions for energy storage applications but also suggest that MOFs can be used as a host lattice to study interesting quantum dynamics of small molecules in a confining potential.

REFERENCES

[1] For more information see http://www.ncnr.nist.gov/staff/taner/h2.
[2] T. Yildirim and M.R. Hartman, Phys. Rev. Lett. **94**, 175501 (2005).
[3] W. Zhou and T. Yildirim, Phys. Rev. Lett. (in prep., 2006).

Counter-ion Dynamics and the Mechanical Properties of Fuel Cell Membranes

A key element of hydrogen fuel cells is the proton exchange membrane which serves both as the separator to prevent direct physical mixing of the hydrogen and the oxygen at the electrodes and as the electrolyte for proton transfer. Improvements that relate to structural changes during use are required in several aspects of these membranes in order to improve durability at higher temperatures, increase resistance to fuel crossover, and reduce water transport rates. Perfluorosulfonate ionomers (PFSI's) are of great importance in polymer electrolyte membrane fuel cell (PEMFC) applications. In order to optimize membrane performance, it is essential to understand the mechanisms of morphological changes that affect properties in these materials. This study aims to expand our fundamental understanding of the influence of electrostatic interactions on chain dynamics and developing morphology in PFSI materials. Quasi-elastic neutron scattering (QENS) was used to investigate the correlations between counter-ion dynamics and bulk mechanical relaxations in alkyl ammonium neutralized membranes, thus advancing the current state of understanding of the properties of materials.

K.A. Page [1]
R.B. Moore [2]
J.K. Park [2]
V. Garcia Sakai [3,4]

[1] Polymers Division National Institute of Standards and Technology Gaithersburg, MD 20899-8542

[2] The University of Southern Mississippi Hattiesburg, MS 39406

[3] NIST Center for Neutron Research National Institute of Standards and Technology Gaithersburg, MD 20899-8562

[4] University of Maryland College Park, MD 20742

FIGURE 1:
Structure of Nafion and the counter-ions tetra-methyl (TMA^+) and tetra-butyl (TBA^+) ammonium.

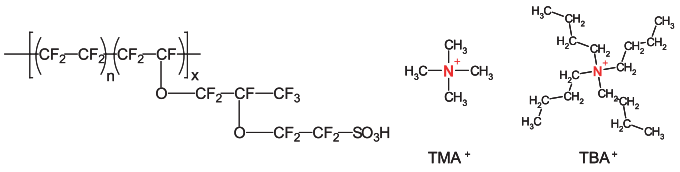

PFSI's are copolymers containing runs of tetrafluoroethylene and generally less than 15 mol % of perfluorovinyl ether units that are terminated with a sulfonic acid exchange site. The most widely studied PFSI and the focus of this study, Nafion, is a product of the E. I. DuPont Chemical Company (Fig. 1). The polar perfluoroether side-chains containing the ionic sulfonate groups aggregate, thus leading to a nanophase-separated morphology where the ionic domains, termed clusters, are distributed throughout the non-polar polytetrafluoroethylene (PTFE) matrix. This morphology gives a characteristic scattering peak in small angle x-ray scattering at $Q \approx 0.2$ Å^{-1}. The membranes used in this study have been neutralized with tetramethyl (TMA^+) and tetrabutyl (TBA^+) ammonium counter-ions (Fig. 1). The size difference between these two counter-ions acts to change the strength of the electrostatic interactions, thus changing the chain dynamics and, in turn, the mechanical properties [1, 2].

Recent studies have shown that the α-relaxation in dynamic mechanical analysis (DMA) of PFSI materials is due to the onset of long-range mobility of both the main and side chains facilitated by a profound weakening of the electrostatic interactions within the ionic aggregates. At temperatures in the vicinity of the α-relaxation, a significant destabilization of the electrostatic network may be observed, which results in the activation of a *dynamic* network facilitated through an ion-hopping process (Fig. 2). In contrast, the β-relaxation is associated with the onset of segmental motions (principally backbone motions) within the framework of a *static* physically cross-linked network of chains [2, 3].

Given the large incoherent scattering length of hydrogen (located only on the counter-ions), the results obtained from QENS can provide specific information about the counter-ion dynamics, thus allowing confirmation and characterization of the ion-hopping process.

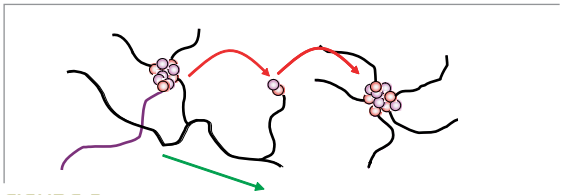

FIGURE 2:
Depiction of the ion-hopping process, in which ions can "hop" from aggregate to aggregate, thus allowing for long-range mobility of the polymer chains.

The temperature dependant elastic scattering at $Q = 0.25$ Å^{-1} for both TMA^+ and TBA^+ Nafion can be seen in Fig. 3. The elastic scattering for each sample is characterized by a distinct drop in intensity, which is attributed to the onset of mobility of the counter-ions that have motions roughly on the size scale of the ionic aggregates. The most striking feature of these data is the excellent correlation between the temperature at which there is a transition in the scattering intensity and the α-relaxation temperature (T_α) obtained by DMA for each material. These data show unequivocally that the α-relaxation is indeed linked to the onset of mobility of the counter-ions, thus lending support to the presence of an ion-hopping process.

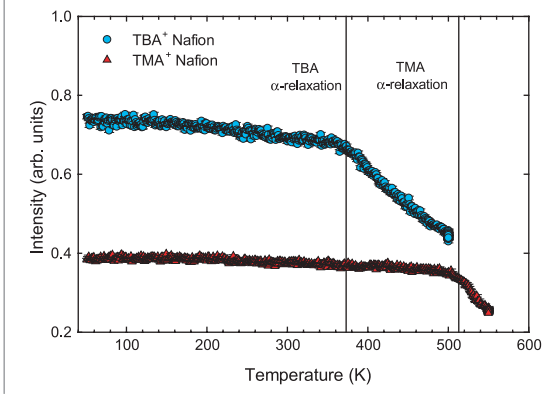

FIGURE 3:
Elastic scattering intensity as a function of temperature (Q = 0.25 Å^{-1}) showing the correlation between the bulk mechanical α-relaxation and the onset of mobility of the counter-ions.

Further information regarding the dynamics of the counter-ions was obtained from quasi-elastic scans in the energy range of ± 17 μeV. By plotting the half-width at half maximum Γ of the quasi-elastic component of the dynamic structure factor $S(Q,\omega)$, the diffusive nature of the counter-ions has been ascertained. The data for both TMA^+ and TBA^+ above their respective T_αs can be seen in Fig. 4. The non-zero intercept of Γ at low Q values is indicative of spatially confined diffusion of the counter-ions, where the rise in Γ at high Q values indicates random jump-diffusion within the confined region. Below the α-relaxation, a drastic decrease in the mobility of the counter-ions results in less quasi-elastic broadening, thus Γ becomes relatively flat and noisy [4, 5].

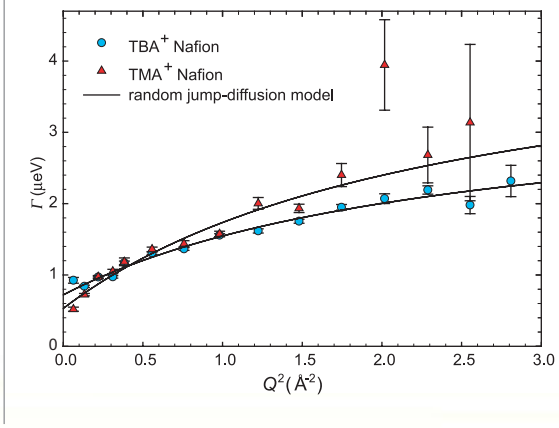

FIGURE 4:
The half-width at half-maximum for TMA^+ and TBA^+ above their respective α-relaxation temperatures. The solid lines represent a fit of a random jump-diffusion model to the data.

Finally, in order to characterize the dynamic length scales of the counter-ion motions, the elastic incoherent structure factor (EISF) was determined for each sample over a range of temperatures. The EISFs for TMA^+ and TBA^+ at temperatures above and below T_α are shown in Fig. 5. Considering the vast difference in counter-ion dynamics above and below T_α, it was necessary to fit the EISF with a model describing diffusion between concentric spheres (*i.e.*, on two different length scales) [6]. The EISF for both counter-ions at low temperatures was dominated by diffusion on a very short length-scale (≈ 1 Å), which means that the dynamics are dominated by local motions of the alkyl "arms" of the counter-ions.

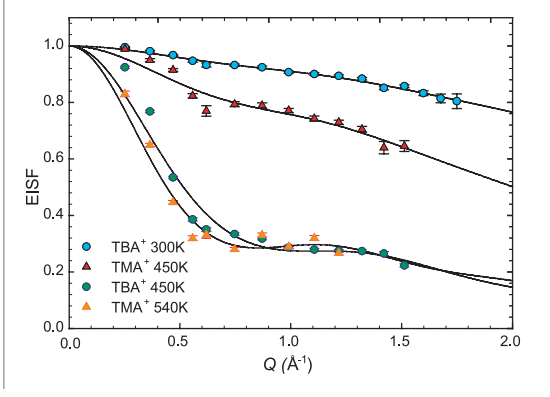

FIGURE 5:
EISF of TMA^+ and TMA^+ above and below $T\alpha$. The solid lines represent the models used to fit the data.

At temperatures above T_α, the EISF showed contributions from diffusion on a larger length-scale. The short-range length-scale was again characteristic of very local diffusive motions, probably facilitated through motions of the alkyl arms of the counter-ion. However, the long-range length-scale was found to be on the order of the size of the counter-ions (6 Å to 7 Å). Therefore, within the time-scales measured by QENS, the counter-ion motions appear to be governed by very local motions at temperatures < T_α. However, at temperatures > T_α the counter-ions are able to move over a much larger length scale on the order of magnitude of the size of the counter-ion itself.

In conclusion, using QENS, we have been able to show explicitly that the α-relaxation in these materials is indeed linked to the onset of mobility of the counter-ions on the length-scale related to the characteristic ionomer morphology, thus lending support to the presence of an ion-hopping process. These data provide further fundamental understanding of the link between electrostatic interactions and dynamics in ionomers.

REFERENCES

[1] K. Mauritz, R.B. Moore, Chem. Rev., **104**, 4535 (2004).
[2] K.A. Page, K. Cable, R.B. Moore, Macro., **38**, 6472 (2005).
[3] K.A. Page, F.A. Landis, A.K. Phillips, R.B. Moore, Macro., **39**, 3939 (2006).
[4] M. Bee, *Quasielastic Neutron Scattering*, Adam Hilger, 1988.
[5] A. Pivovar, B. Pivovar, J. Phys. Chem. B., **109,** 785 (2005).
[6] D. Bicout, Phys. Rev. E, **62**, 261 (2000).

Novel Magnetic Order in $Na_{0.5}CoO_2$

Surprisingly, when you add a bit of water to Na_xCoO_2, where $x \approx 0.3$, it becomes a superconductor—the first known superconducting cobaltate. The parent compound, non-hydrated Na_xCoO_2, is a dopable spin-½ magnet on a frustrated triangular lattice. Doping by sodium changes the average valence for the cobalt ions, formally converting magnetic Co^{4+} to non-magnetic Co^{3+} ions. It has been suggested that the average cobalt valence in the superconducting compound is close to that in the half-doped, non-hydrated phase ($Na_{0.5}CoO_2$), which is *not* superconducting. Understanding the ground state of the half-doped CoO_2 plane may help distinguish how it differs from the superconducting phase, and will help elucidate the important magnetic interactions.

G. Gašparović[1]
R.A. Ott[1]
J.H. Cho[2]
F.C. Chou[1]
Y. Chu[1]
J.W. Lynn[3]
Y.S. Lee[1]

[1] Massachusetts Institute of Technology Cambridge, MA 02139

[2] Pusan National University Busan 609-735, Korea

[3] NIST Center for Neutron Research National Institute of Standards and Technology Gaithersburg, MD 20899-8562

As a function of sodium doping x, non-hydrated Na_xCoO_2 displays a rich electronic phase diagram, consisting of a paramagnetic phase for $x < 1/2$, and an unusual Curie-Weiss metallic phase for $x > 1/2$. In the half-doped compound ($x = 1/2$), a unique state is realized: The Na ions are chemically ordered to form zigzag chains in an orthorhombic superstructure with two-fold symmetry. Based on resistivity, Hall coefficient, thermal transport, and angular magnetoresistance oscillation measurements, the ground state is believed to be a magnetically ordered insulator. In order to further investigate the electronic ground state of the half-doped CoO_2 plane, we have performed neutron scattering, susceptibility, and transport studies on single crystal samples. The combination of polarized and unpolarized neutron scattering data allows us to determine the ordered spin direction and arrangement. We find that the ground state is well described by an ordered array of stripes of antiferromagnetic spins interleaved with stripes of non-ordered Co ions.

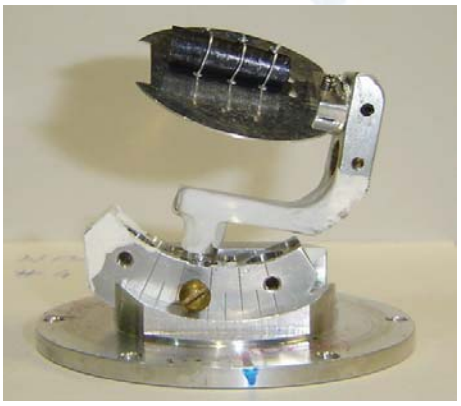

FIGURE 1:
The $Na_{0.5}CoO_2$ sample used in our studies, mounted for neutron scattering measurements in (HHL) reciprocal lattice plane.

The samples used in this study were prepared by electrochemically de-intercalating a floating-zone grown Na_xCoO_2 crystal to yield a final concentration of $x \approx 0.5$. The crystal studied was cylindrically shaped, with mass 2.41 g (Fig.1). Our neutron scattering experiments were conducted at the NCNR using the BT-9 and BT-2 triple-axis spectrometers. Neutrons interact with the magnetic moments of the ions and are an ideal probe for studying magnetism in solids.

Figure 2 shows evidence for magnetic order below $T_N = 88$ K obtained by elastic neutron scattering. At low temperatures, new peaks arise that are distinct from nuclear reflection peaks. In the (HHL) reciprocal lattice plane, we observe such peaks at $\boldsymbol{Q} = (1/2\,1/2$ odd) locations. The temperature dependence of the peak intensities of the $(1/2\,1/2\,1)$ and $(1/2\,1/2\,3)$ peaks are shown in Fig. 2(a). The observed dependence is typical for second-order magnetic phase transitions. Figures 2(b) and 2(c) show reciprocal-space scans through the $(1/2\,1/2\,1)$ peak along the $[HH0]$ and $[00L]$ directions, respectively, at $T = 8$ K and $T = 120$ K. The low temperature peak widths are resolution-limited, indicating a long-range magnetic order (> 50 Å).

In order to confirm that these peaks originate from magnetic order, we performed polarized neutron measurements. This is the clearest way to distinguish magnetic peaks from weak nuclear superlattice peaks. We have measured both the spin-flip and non-spin-flip cross sections with neutron polarizations ($\boldsymbol{P}$) both parallel and perpendicular to the momentum transfer vector ($\boldsymbol{Q}$). Figure 2(d) shows the scattering measured at $T = 8$ K with $\boldsymbol{P} \parallel \boldsymbol{Q}$ at the $(1/2\,1/2\,1)$ peak. In this geometry, all magnetic scattering occurs in the spin-flip channel (•), and nuclear scattering is non-spin-flip (○). The data show that the scattering is entirely spin-flip, *i.e.,* magnetic. The temperature dependence of this scattering, scaled to match the unpolarized data at low T, is denoted by the filled circles in Fig. 1(a). We see that the temperature dependence is identical. Thus, the scattering below 88 K at $(1/2\,1/2\,1)$ is entirely magnetic.

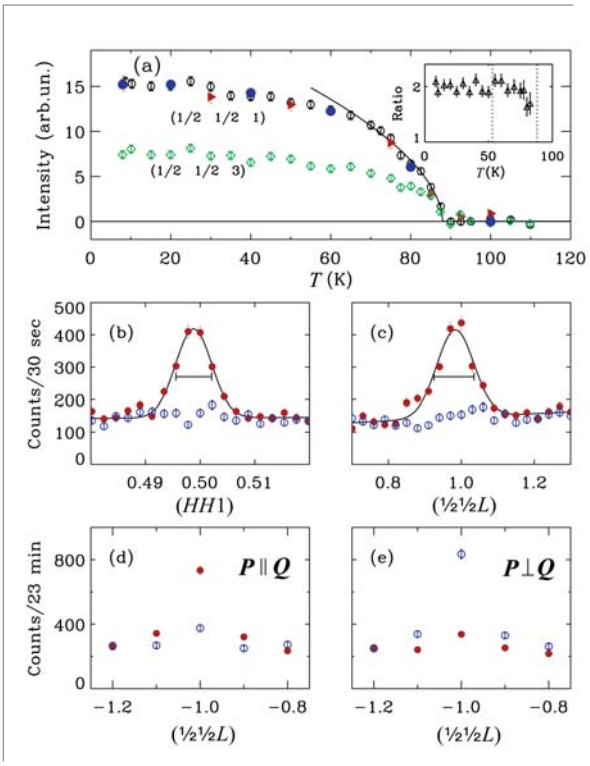

FIGURE 2:
(a) Temperature dependence of the intensities of magnetic Bragg peaks, measured by elastic neutron scattering. The red filled triangles denote the integrated intensities, and the blue filled circles denote the intensities measured using polarized neutrons, both scaled to match the 8 K peak intensity of ($\frac{1}{2}$ $\frac{1}{2}$ 1). (b) (HH1) and (c) ($\frac{1}{2}$ $\frac{1}{2}$ L) scans through ($\frac{1}{2}$ $\frac{1}{2}$ 1) above (○, T = 120 K) and below (•, T = 8 K) the magnetic phase transition. Polarized neutron data with (d) $\boldsymbol{P} \parallel \boldsymbol{Q}$ and (e) $\boldsymbol{P} \perp \boldsymbol{Q}$, for spin-flip (•) and non-spin-flip (○) channels at T = 8 K.

Neutron polarization analysis is also an extremely useful method to deduce the direction of the ordered moment. In Fig. 2(e), we plot the scattering data measured with $\boldsymbol{P} \perp \boldsymbol{Q}$. In this geometry, magnetic scattering can occur in the non-spin-flip channel if the ordered moment has a component parallel to the polarization direction, whereas a moment along the *c*-axis would lead to a large spin-flip component. Here, the signal predominately occurs in the non-spin-flip channel. Therefore, the direction of the ordered moments lies within the *ab* plane, and the ordered moment along the *c* axis must be small. The temperature dependence of the polarized data indicates that the *c*-axis component remains small at all measured temperatures below T_N = 88 K.

The above information can be combined with measurements of intensities of several nuclear and magnetic Bragg peaks to determine the magnetic structure. Our data are well described by the model shown in Fig. 3. Within each CoO_2 layer, the Co ions are arranged in alternating rows (or stripes) of magnetically ordered and "non-ordered" ions. For the magnetic ions, the nearest neighbor spins are coupled antiferromagnetically, both along the row and between rows. Between CoO_2 planes, the rows of magnetic Co ions are stacked directly on top of each other, and the nearest neighbor interplane coupling is also antiferromagnetic. The low temperature (T = 8 K) static magnetic moment is 0.26 μ_B per magnetic Co ion. The size of the observed moment is smaller than that expected for $S = \frac{1}{2}$, which may suggest the presence of quantum fluctuations or deviations from a fully charge-disproportionated local moment picture.

In conclusion, our polarized and unpolarized neutron scattering measurements reveal formation of a novel magnetic order in $Na_{0.5}CoO_2$ below T_N = 88 K. The domains of magnetic order appear to be closely coupled to the domains of Na ion order, consistent with a twofold symmetric spin arrangement. Within each domain, the scattering is consistent with an arrangement of alternating rows of ordered and non-ordered Co ions. Magnetoresistance and anisotropic susceptibility measurements further support this model for the electronic ground state. Understanding the interplay between spin order and charge motion in this correlated electron system remains an important issue for further study.

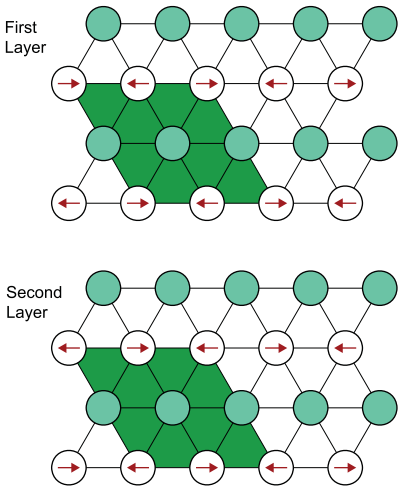

FIGURE 3:
Model of the spin arrangement in $Na_{0.5}CoO_2$. For clarity, only Co ions in the two CoO_2 layers are shown. The solid circles represent non-ordered Co ions, and the hollow circles magnetically ordered Co ions with arrows indicating the directions of the magnetic moments.

REFERENCE

[1] See G. Gašparović, R. Ott, J.H. Cho, F.C. Chou, Y. Chu, J.W. Lynn, and Y.S. Lee, Phys. Rev. Lett. **96**, 046403 (2006).

A Two-Dimensional Magnetically Ordered Phase on a Geometrically Frustrated Lattice

The two-dimensional (2D) triangular lattice antiferromagnet (TLAFM) is an important model in many areas of condensed matter physics including frustrated magnetism and unconventional superconductivity. Theoretically, TLAFMs have been shown to exhibit many exotic magnetic phases including short-range resonating valence bond [1], Kosterlitz-Thouless and Z_2-vortex states [2], which are unique to 2D. However, it is difficult to experimentally access these low temperature phases in bulk crystals because there is usually a cross-over to 3D behavior above the magnetic phase transition. Here we show that inter-plane frustration can impede the cross-over to 3D behavior and thus allow one to see intrinsically 2D low temperature physics.

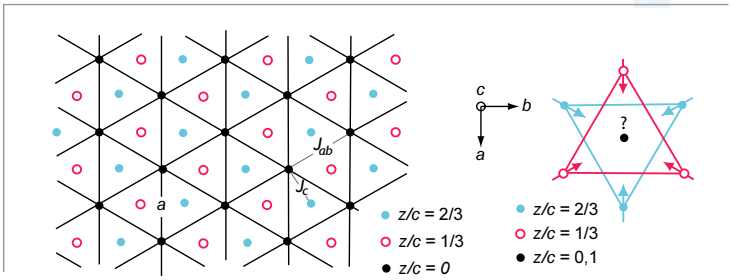

FIGURE 1:
A schematic drawing of the Cr^{3+} sites of $NaCrO_2$ from a (001) projection (left) showing the nearest neighbor in-plane (J_{ab}) and nearest neighbor inter-plane (J_c) exchange interactions. The $q = (\frac{1}{3}\,\frac{1}{3}\,0)$ spin arrangement is shown on the right which illustrates how inter-plane frustration arises.

D. Hsieh [1]
D. Qian [1]
M.Z. Hasan [1]
R.F. Berger [1]
R.J. Cava [1]
B.G. Ueland [2]
P. Schiffer [2]
J.W. Lynn [3]
Q. Huang [3]

[1] Princeton University Princeton, NJ 08544

[2] Pennsylvania State University University Park, PA 16802

[3] NIST Center for Neutron Research National Institute of Standards and Technology Gaithersburg, MD 20899-8562

Of the many materials that are known to possess highly 2D magnetic interactions, those that exhibit a 2D long-range ordered (LRO) phase are extremely rare. This is because even when the inter-plane coupling J_c is much weaker than the in-plane coupling J_{ab}, 3D order is energetically favorable below a temperature T_c at which the in-plane correlation length ξ_{ab} is sufficiently large that

$$k_B T_c = J_c(\xi_{ab}/a)^2 S^2$$

where a is the in-plane inter-spin distance and S is the magnitude of the spin. Therefore a divergence of ξ_{ab} that is driven solely by 2D interactions will simultaneously induce 3D LRO. In a neutron scattering experiment, such behavior is typified by an abrupt conversion from 2D dynamic scattering, due to short-lived in-plane correlations, to 3D Bragg scattering as the system is cooled through the transition temperature. However, if adjacent lattice planes are stacked in such a way that inter-plane interactions cancel out, both the lifetime and spatial extent of in-plane correlations may be allowed to grow without 3D LRO developing.

We investigated such a possibility by performing neutron scattering measurements on the Mott insulator $NaCrO_2$, in which ($S = \frac{3}{2}$) Cr^{3+} sites form a rhombohedrally (ABCABC) stacked TL (Fig. 1). Frustrated inter-plane interactions can arise in this system provided the exchange couplings are highly planar and antiferromagnetic. Since this condition forces the spins in each plane to adopt a $q = (\frac{1}{3}\frac{1}{3}0)$ configuration as shown in Fig. 1, the molecular field that a particular spin feels from its first and second neighboring layers vanishes. A model for the classical ground state of the rhombohedrally stacked TLAFM in the limit $|J_c / J_{ab}| < 3$ was solved by Rastelli and Tassi [3]. They showed that instead of rods through $q = (\frac{1}{3}\frac{1}{3}0)$ in reciprocal space, as would arise from decoupled 120° ordered planes, the ground state is degenerate along helices centered about $q = (\frac{1}{3}\frac{1}{3}0)$. Experimentally however, particular points along the helices would still be selected via further neighbor interactions or quantum order-by-disorder.

Elastic and inelastic neutron scattering measurements were carried out on a powder sample of $NaCrO_2$ using the thermal triple-axis spectrometer (BT-9) and the cold neutron Disk Chopper Spectrometer (DCS) respectively. The magnetic diffraction profile at 40 K (Fig. 2b) is well described by a Warren peak centered around $q = (\frac{1}{3}\frac{1}{3}0)$, arising from rods of low energy scattering. The Warren peak is resolution limited in energy, revealing a correlation time exceeding 0.4 ns. As shown in Fig. 2d, this quasi-elastic 2D scattering survives over an unusually large temperature range (T_l = 35 K < T < T_u = 48 K) over which ξ_{ab} grows from 15a to 28a (Fig. 2e) without the appearance of 3D Bragg peaks. Below T_l, broad peaks emerge along the high q tail of the Warren peak (Fig. 2c) arising from short-range (ξ_c < 1.08c) inter-plane correlations. The positions of these peaks cannot be indexed by $(\frac{1}{3}\frac{1}{3}n)$ where n is integer or half-integer, which means that the stacking arrangement of the triangular planes is not simply ferromagnetic or antiferromagnetic. A concomitant drop in the Warren peak position at T_l (Fig. 2e)

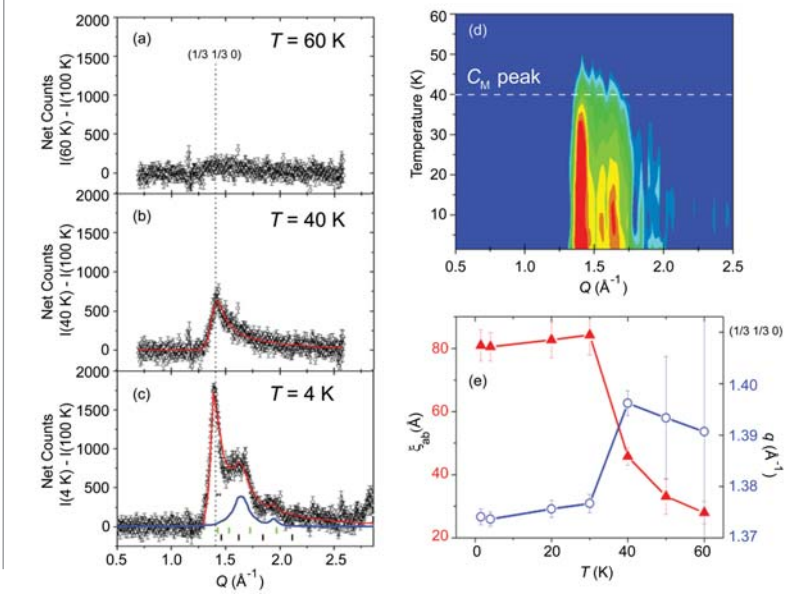

FIGURE 2:
(a-c) The magnetic contribution to the neutron diffraction pattern of $NaCrO_2$ along with fits to a combination of Warren and Lorentzian lineshapes (red). Peaks arising from inter-plane correlations are shown in blue (c) and should be compared to the green and black bars which mark the ($\frac{1}{3}$ $\frac{1}{3}$ n); n integer and half-integer positions respectively. (d) shows the temperature dependence of the magnetic diffraction signal and the peak position of the measured magnetic specific heat (C_M) peak. (e) displays the temperature dependence of ξ_{ab} and q extracted from the fits.

suggests that coupling between planes is instead established by an in-plane modulation of the 120° order which relieves the inter-plane frustration. A departure from purely 120° in-plane order is consistent with a degenerate helix ground state, but the mechanism that lifts the degeneracy is still unclear.

The dynamic structure factor of the spin correlations is shown in Fig. 3a-c. Despite a long in-plane correlation length (ξ_{ab} = 15a) at 40 K, there is strong incoherent inelastic scattering and no finite energy spin wave modes, indicating that spin correlations are slowly fluctuating but not truly static. This 2D fluctuation regime is also extended between T_u and T_l (Fig. 3d). Below T_l, dispersive modes that are both gapped and gapless at the Brillouin zone center (q = 1.4 Å^{-1}) begin to appear and are well described by the spin wave spectrum of a 2D Heisenberg TLAFM with a single-ion easy-plane anisotropy D = 1.2 meV (Fig. 3e). Such a large value of D is inconsistent with electron paramagnetic resonance measurements on $NaCrO_2$ which support a Heisenberg ($D \approx 0$) character. The origin of the large effective "D" term can be understood in analogy with square-lattice $Sr_2Cu_3O_4Cl_2$ [4]. Since $NaCrO_2$ can be separated into multiple Heisenberg AFM sublattices that can be rotated relative to each other without costs in energy, strong fluctuations can then lift one of the zero-energy modes to a finite energy. This provides support for inter-plane correlations developing from an order-by-disorder mechanism.

Our measurements on $NaCrO_2$ demonstrate that inter-plane frustration provides a new avenue to stabilize 2D magnetic phases in strongly correlated electron systems. Such a phase can be a host for exotic superconductors where pairing could be mediated by spin fluctuations or the lifted zero-modes upon doping.

REFERENCES

[1] R. Moessner *et al.*, Phys. Rev. Lett. **86**, 1881 (2001).
[2] H. Kawamura *et al.*, J. Phys.: Condens. Matter **10**, 4707 (1998).
[3] Rastelli *et al.*, J. Appl. Phys. **63**, 3823 (1988).
[4] Y. J. Kim *et al.*, Phys. Rev. Lett. **83**, 852 (1999).

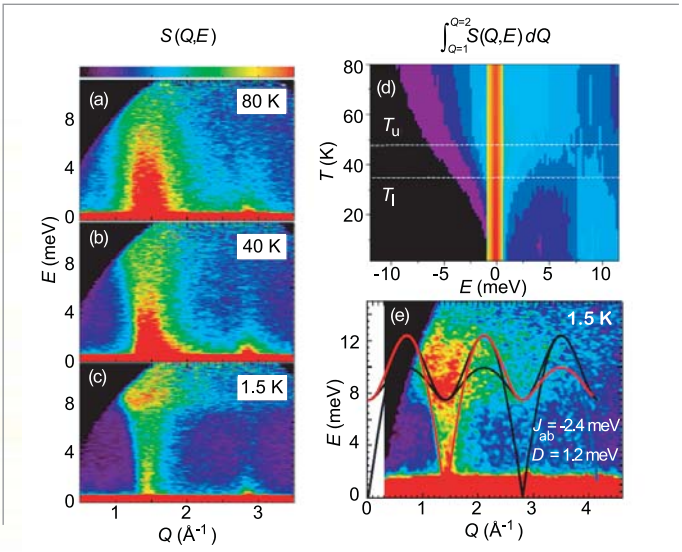

FIGURE 3:
(a-c) The dynamic structure factor $S(Q,E)$ of $NaCrO_2$ where Q and E are the neutron momentum and energy transfers respectively. (d) shows the temperature dependence of the Q integrated dynamic structure factor and the dashed lines enclose the extended fluctuation regime. (e) shows the same data as (c) over a larger dynamic range. The solid lines are the spin wave spectrum calculated using the Hamiltonian $H = -J_{ab} \Sigma \boldsymbol{S}_i \cdot \boldsymbol{S}_j + D \Sigma (S_i^z)^2$.

Field-Induced Order and Spin Waves in the Pyrochlore Antiferromagnet $Tb_2Ti_2O_7$

Geometric lattices consisting of triangular building blocks are well known venues for phenomena known as magnetic frustration. When combined with antiferromagnetism, such materials often cannot reach a minimum classical ground state energy for the interacting spins, which leads to exotic magnetic ground state behavior. The Disk Chopper Spectrometer (DCS) at the NCNR has allowed us to investigate the influence of an applied magnetic field on the frustrated, pyrochlore antiferromagnet, $Tb_2Ti_2O_7$. These measurements reveal a complex magnetic field versus temperature phase diagram which includes the zero field cooperative paramagnetic phase, a polarized paramagnetic phase and a high-field long-range ordered magnetic phase with spin wave excitations.

K.C. Rule[1]
J.P.C. Ruff[1]
B.D. Gaulin[1]
S.R. Dunsiger[1]
J.P. Clancy[1]
M.J. Lewis[1]
H.A. Dabkowska[1]
I. Mirebeau[2]
P. Manuel[3]
J.S. Gardner[4]
Y. Qiu[4]
J.R.D. Copley[4]

[1] McMaster University Hamilton, ONT, L8S 4M1, Canada

[2] Laboratoire Leon Brillouin CEA-CNRS, CE-Saclay 91191 Gif-sur-Yvette, France

[3] ISIS Facility Rutherford Appleton Laboratory Didcot, Oxon, OX11 0QX, UK

[4] NIST Center for Neutron Research National Institute of Standards and Technology Gaithersburg, MD 20899-8562

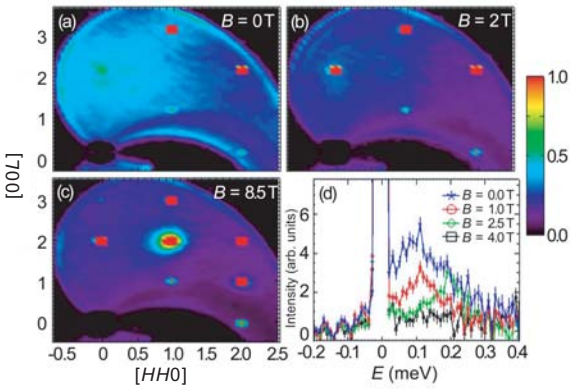

FIGURE 1:
Neutron scattering for -0.5 meV < $\hbar\omega$ < 0.5 meV, and within the (*HHL*) plane of $Tb_2Ti_2O_7$ at T = 1 K is shown for (a) B = 0 T, (b) B = 2 T and (c) B = 8.5 T. Fields were applied along the crystallographic [110] direction. Panel (d) shows high energy resolution scattering at T = 0.1 K, integrated in Q and including the (002) position.

$Tb_2Ti_2O_7$ is a geometrically frustrated cubic pyrochlore in which magnetic Tb^{3+} ions are located at the vertices of a network of corner-sharing tetrahedra. At ambient pressure and zero applied magnetic field, $Tb_2Ti_2O_7$ is known to remain a cooperative paramagnet down to temperatures as low as 20 mK [1-3]. Calculations of the crystal field levels appropriate to the Tb^{3+} site predict local [111] Ising anisotropy such that the spins are oriented either into or out from the center of each tetrahedron [4]. Both the ground state and first excited state crystal field levels form doublets which are separated by $\hbar\omega \approx 1.5$ meV, while the next highest levels are at $\hbar\omega \approx 10.5$ meV and 14.5 meV [1].

Previous studies show that applied pressure and magnetic fields may relieve the geometric frustration and induce long-range order in $Tb_2Ti_2O_7$. Neutron studies have shown an increase in the nuclear Bragg intensity when a magnetic field is applied along the Ising [111] axis [5]. Also, combinations of unidirectional and hydrostatic pressure along with magnetic fields have induced magnetic long-range order at low temperatures and applied fields [6, 7]. More recently, in relatively high applied fields and temperatures of 10 K to 20 K, a very slow relaxation rate to an equilibrium state was observed [8].

Time-of-flight neutron scattering measurements were performed with 5 Å and 9 Å incident neutrons using NCNR's disk chopper spectrometer (DCS). Figures 1(a–c) show reciprocal space maps in the (*HHL*) plane, integrating over -0.5 meV < $\hbar\omega$ < 0.5 meV in energy, and taken at T = 1 K. In zero field (Fig. 1a), extensive diffuse magnetic scattering was observed around (002) indicating short-ranged spin correlations restricted to distances of about the dimension of a single tetrahedron. This diffuse scattering appears to be quasi-elastic or very weakly inelastic, with a characteristic extent in energy of ≈ 0.3 meV (Fig. 1d). In a 2 T applied field, oriented along the [110] direction (Fig. 1b), sharp Bragg intensity was observed not only at the allowed nuclear positions, but also at 002 which is forbidden within the $Fd\bar{3}m$ space group. Finally, by 8.5 T (Fig. 1c) a new set of magnetic Bragg peaks was observed signaling a new ordered state. The strongest of these new field-induced peaks is the 112, as can be seen in Fig. 1c.

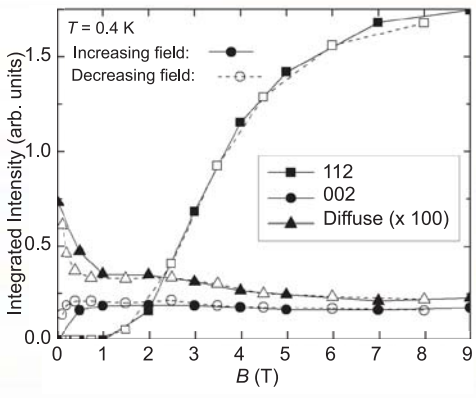

FIGURE 2:
The integrated intensity of the 112 and 002 Bragg peaks as a function of B at T = 0.4 K are shown, along with the integrated quasi-elastic scattering making up the diffuse scattering.

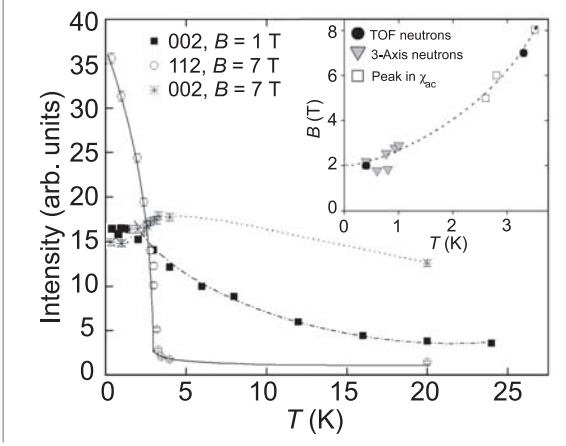

FIGURE 3:
The temperature dependence of the 112 Bragg peak in B = 7 T, and the 002 Bragg peak in both B = 1 T and 7 T is shown. The inset shows the phase diagram for the magnetically long-range ordered state in $Tb_2Ti_2O_7$, as determined by time-of-flight and triple axis neutron scattering and by ac-susceptibility measurements. All lines shown are guides-to-the-eye.

The intensity of the 002 and 112 Bragg peaks were followed as a function of applied field and temperature. In Fig. 2, the intensity of the 002 peak rises to a maximum by ≈ 0.5 T while the 112 follows an "S-shaped" increase to saturation at around 8 T. Figure 3 shows the temperature dependence of both peaks in applied magnetic fields. At 7 T, the 112 peak falls off sharply with temperature displaying downward curvature with a phase transition near T_N ≈ 3 K. In contrast, the 002 at 7 T shows an anomaly at T_N but remains finite and large up to at least 20 K.

Figure 4 shows the inelastic magnetic scattering spectrum taken around the (002) position as a function of applied field. In zero field (Fig. 4a), quasi-elastic scattering (responsible for the diffuse scattering in Fig. 2a) can be seen at energies less than ≈ 0.3 meV. As the field was increased, this quasi-elastic scattering appeared to weaken and finally split from the elastic scattering by 3 T (Fig. 4d) leaving a clearly resolved inelastic mode at ≈ 0.3 meV. A broad distribution of inelastic scattering was also observed in zero field between 0.8 meV to 1.8 meV. This inelastic magnetic scattering is also resolved into narrow energy bands as the magnetic field was increased (Fig. 4b-c). At 2 T and 3 T, sharp dispersive spin wave excitations could be seen which appear to have minima in their dispersion near (001) and (003).

These results suggest the 002 Bragg peak which appears on application of a very weak [110] magnetic field, is the signature of a polarized paramagnetic phase. This is supported by the absence of a well defined phase transition associated with the 002

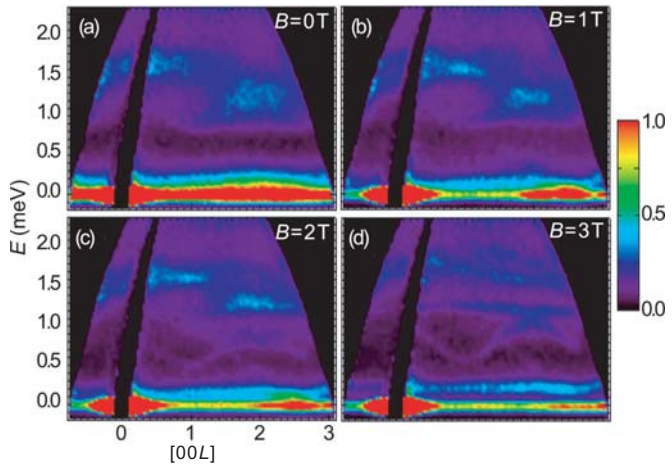

FIGURE 4:
Neutron scattering data within the (00L) – energy plane at T = 0.4 K and (a) B = 0, (b) B = 1 T, (c) B = 2 T, and (d) B = 3 T are shown.

Bragg intensity with temperature up to 24 K at a field of 1 T (Fig. 3), as well as with the absence of collective spin wave excitations in the magnetic inelastic scattering. In this state, the magnetic Bragg peaks arise from a single-ion polarization of much of the paramagnetic moment along the applied field direction. In contrast, the high field magnetically ordered state shows both well defined spin wave excitations and a clear phase transition at T_N ≈ 3 K. It is evident, however, that purely [111] Ising spins, as implied by the crystal field calculations, cannot describe the high field state as the dispersive spin wave excitations require continuous spin degrees of freedom. Instead, a model similar to that reported for the pressure induced magnetic order [6, 7] is more likely, suggesting that magnetoelastic effects may play a significant role in the eventual ordering of $Tb_2Ti_2O_7$.

Our DCS results clearly show how the frustrated pyrochlore antiferromagnet $Tb_2Ti_2O_7$ is brought to order at low temperatures by the application of relatively weak magnetic fields applied along [110]. This complex phase behavior and the spin wave dispersion it displays in its high field ordered phase are expected to motivate theoretical study aimed at a complete understanding of $Tb_2Ti_2O_7$ and its enigmatic low temperature behavior.

REFERENCES

[1] J.S. Gardner, *et al.*, Phys. Rev. B **64**, 224416 (2001).
[2] J.S. Gardner, *et al.*, Phys. Rev. Lett. **82**, 1012 (1999).
[3] J.S. Gardner, *et al.*, Phys. Rev. B **68**, 180401 (2003).
[4] M.J.P. Gingras, *et al.*, J. Phys. Chem. Sol. **62**, 343 (2001).
[5] Y. Yasui, *et al.*, Phys. Chem. Sol. **62**, 343 (2001).
[6] I. Mirebeau, *et al.*, Phys. Rev. Lett. **93**, 187204/1 (2004).
[7] I. Mirebeau and I. N. Goncharenko, J. Phys.: Cond. Matt. **17**, S771 (2005).
[8] B.G. Ueland, *et al.*, Phys. Rev. Lett. **96**, 27216 (2006).

Resonance Mode in the Electron-Doped Superconducting Cuprate $Pr_{.88}LaCe_{.12}CuO_4$

The nature of the mechanism of high temperature superconductivity (high-T_c) in the cuprates, despite nearly two decades of study, remains one of the major unresolved problems in condensed matter physics. Instead of phonons mediating the electron pairing for superconductivity as in conventional BCS superconductors, it is thought that magnetism plays a fundamental role in the superconductivity of these high-T_c materials, largely because all parent compounds of high-T_c superconductors are long-range ordered antiferromagnets. Studies of universal features in the spin dynamics of the cuprates, via inelastic neutron scattering probing the wave vector and energy dependence of spin fluctuations, provide valuable insight into the precise nature of the interplay between magnetism and superconductivity. We have used the triple-axis spectrometers BT-9 and SPINS at the NCNR to establish a magnetic excitation mode, known as the "resonance", as the unifying feature in the spin dynamics between hole and electron-doped cuprates. This resonance is therefore an essential component of superconductivity in the cuprates [1].

S.D. Wilson[1]
P. Dai[1,2]
S. Li[1]
S. Chi[1]
H.J. Kang[3,4]
J.W. Lynn[3]

[1] The University of Tennessee Knoxville, Tennessee 37996-1200

[2] Center for Neutron Scattering Oak Ridge National Laboratory, Oak Ridge, Tennessee 37831

[3] NIST Center for Neutron Research National Institute of Standards and Technology Gaithersburg, MD 20899-8562

[4] University of Maryland College Park, MD 20742

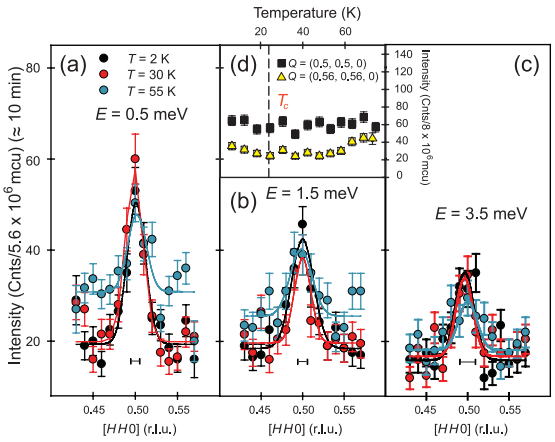

FIGURE 1:
Low energy neutron scattering results from SPINS, (mcu stands for monitor counts units and r.l.u. stands for reciprocal lattice units). a) – c) Constant-*E* scans through the $\boldsymbol{Q}$ = (½, ½, 0) point at *E* = 0.5 meV, 1.5 meV, and 3.5 meV, respectively. Scans were taken along the [*HH* 0] direction and show no change from 2 K (black symbols) to 30 K (red symbols). The magnetic scattering centered at (π, π) is much broader than resolution (horizontal bars) and remains gapless down to 0.5 meV. d) *T*-dependence of 1.5 meV channel at $\boldsymbol{Q}$ = (½, ½, 0) (black squares) and nonmagnetic background (yellow triangles).

The novel phase of high-T_c superconductivity occurs when charge carriers, either holes or electrons, are doped into the CuO_2 planes of their antiferromagnetically (AF) ordered insulating parent compounds. This AF order consists of a simple doubling of the chemical unit cell in the CuO_2 planes, with an in-plane ordering wave vector $\boldsymbol{Q}$ = (½, ½). Upon doping, long-range AF order is dramatically suppressed but strong spin fluctuations persist in all superconducting concentrations. Experiments probing these spin fluctuations in hole-doped cuprates have uncovered a seemingly universal structure of dispersion amongst different families of cuprates. In these hole-doped systems, including the bilayer system $YBa_2Cu_3O_{7-\delta}$ and monolayer cuprates $La_{2-x}(Sr, Ba)_xCuO_4$, low energy magnetic fluctuations are split away from the commensurate $\boldsymbol{Q}$ = (½, ½) wave vector and instead are observed along incommensurate positions $\boldsymbol{Q}$ = (0.5 ± δ, 0.5 ± δ). With increasing energy transfer these low energy fluctuations disperse inward until they reach the commensurate wave vector $\boldsymbol{Q}$ = (½, ½), where upon further increase in energy transfer they then disperse back outward but rotated from their original orientation. In $YBa_2Cu_3O_{7-\delta}$, at energies where these incommensurate fluctuations disperse into a commensurate position, a significant enhancement in the spectral weight occurs below T_c and a localized magnetic mode is observed. This mode, known as the resonance excitation, is strongly coupled to superconductivity and appears only below T_c in optimally-doped systems. The resonance mode has also been discovered in a variety of hole-doped systems, and the characteristic energy for this mode, E_R, is intrinsically tied to the superconducting phase of the system through the universal relation $E_R = 5.8\ k_B T_c$ thus suggesting that the resonance is linked to the electron-electron pairing mechanism in high-T_c materials.

While the resonance mode and incommensurability are seemingly common in the magnetic spectrum of hole-doped cuprates, the question then arises: are these features also present in the spin excitations of the electron-doped cuprates? In order to address this question, we probed the spin dynamics of the optimally electron-doped cuprate $Pr_{.88}LaCe_{.12}CuO_{4-\delta}$ (PLCCO) with a T_c = 24 K. Using the SPINS cold-

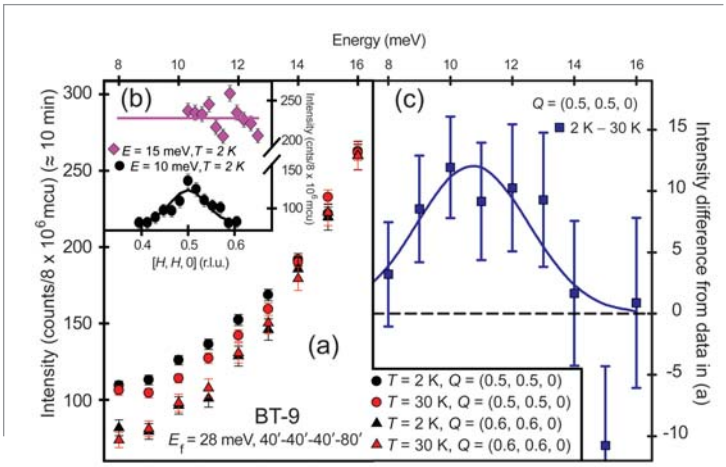

FIGURE 2:
Thermal neutron scattering results from BT-9. a) Constant-Q scans at (½, ½, 0) (circles) and nonmagnetic background (triangles) taken both below and above T_c. b) Constant-E scans at 10 meV (black circles) and 15 meV (purple diamonds) taken through (½, ½, 0) along the [*HH*0] direction. A clear peak appears at 10 meV centered at (½, ½) while no peak is discernable at 15 meV. c) Subtraction of 30 K from 2 K *E*-scans at (½, ½, 0) in panel (a). A clear localized mode appears centered at ≈ 11 meV when the system is cooled below T_c.

neutron triple-axis spectrometer, our investigations of the low energy excitations of this system reveal that the spin fluctuations are gapless down to 0.5 meV and remain commensurate. This contrasts with the gapped, incommensurate response observed in optimally hole-doped cuprates (Fig. 1). Additionally, these low energy dynamics are independent of the superconductivity in the system as shown by an identical response both below T_c (2 K) and above T_c (30 K). While the commensurate nature of the low energy spin excitations in the electron-doped cuprates seemingly precludes the incommensurability seen in hole-type cuprates as universal to all high-T_c, the question remains as to the existence of the resonance mode in the electron-doped cuprates.

In order to investigate the possible presence of the resonance in PLCCO, we utilized the BT-9 thermal triple-axis spectrometer, allowing higher energy spin excitations to be probed. In the range 8 meV ≤ $\hbar\omega$ ≤ 15 meV the spin dynamics are no longer decoupled from the onset of superconductivity in the system, and instead, a localized magnetic mode appears as the system is cooled below T_c (Fig. 2). This mode appears centered at ≈ 11 meV and exactly at the commensurate wave vector (½, ½). Temperature scans from another spectrometer, HB-1 at Oak Ridge National Laboratory, also confirm that this mode appears only below T_c, and therefore is the identical resonance mode feature observed in hole-doped cuprates.

The resonance energy for this electron-doped system can then be compared to equivalent resonances observed in hole-doped cuprates, as shown in Fig. 3. Surprisingly, E_R for PLCCO falls exactly onto the universal curve for all systems, thus establishing this excitation as fundamental to all high-T_c copper oxides regardless of carrier type. Additionally, the discovery of the resonance mode in a system with known commensurate low energy excitations dispersing into it (Fig. 3) implies that there exists no fundamental connection between the resonance energy and the inward dispersion of incommensurate excitations observed in the hole-doped classes of cuprates. To fully understand the microscopic origin of the resonance mode requires the use of complementary probes in addition to neutron scattering, such as angle resolved photoemission or scanning tunneling electron-microscopy, for which PLCCO is suitable. Thus, a systematic investigation in a single material is now possible for the first time using several complementary probes, with inelastic neutron scattering providing a foundation for finally deciphering the microscopic origin of the resonance.

REFERENCE

[1] S.D. Wilson, P. Dai, S. Li, S. Chi, H.J. Kang, and J.W. Lynn, Nature 442, **59** (2006).

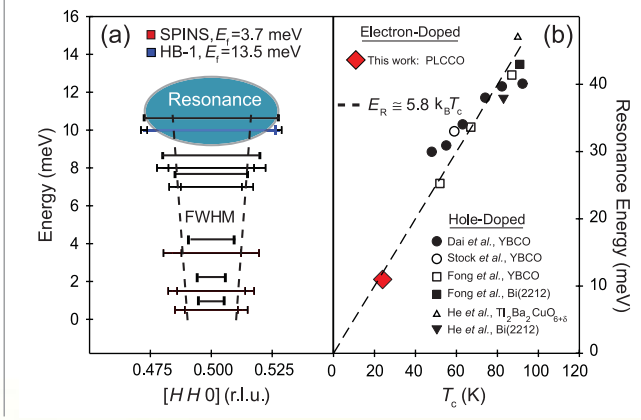

FIGURE 3:
Dispersion relation for PLCCO and universal plot of E_R vs. T_c. a) Dispersion of the commensurate excitations in PLCCO with increasing E. Colored bars represent the FWHM of the measured peak along [*HH*0] while the black bars display the respective instrument's resolution. b) Universal plot showing discovered resonance modes in various classes of cuprates versus their respective system's T_c. The new E_R for PLCCO falls exactly onto the universal curve for all systems, thus signifying a common origin for all resonances in the high-T_c cuprates regardless of carrier type. The citations in the figure can be found in Ref. 1.

Quasiparticle Breakdown in a Quantum Spin Liquid

In the standard microscopic description of condensed matter, elementary excitations, or quasiparticles, are fundamental quanta of energy and momentum. Scattering neutrons from a two dimensional quantum-magnet, we have identified a region of energy-momenta where this description fails [1]. Experiments probed magnons in piperazinium hexachlorodicuprate (PHCC) [2], wherein spin-1/2 copper atoms form a non-magnetic quantum spin liquid ground state. Elementary magnetic excitations in this system are magnon quasiparticles existing above an energy gap. Beyond a threshold where energy and momentum conservation allow one magnon to decay into two, single-particle excitations become unstable and the magnon spectrum ends. In PHCC we have observed a rapid transfer of magnetic intensity to the 2-particle continuum and an abrupt development of damping when a threshold momentum is exceeded.

M.B. Stone[1]
I.A. Zaliznyak[2]
T. Hong[3]
C.L. Broholm[3]
D.H. Reich[3]

[1] Oak Ridge National Laboratory Oak Ridge, TN 37831

[2] Brookhaven National Laboratory Upton, NY 11973-5000

[3] The Johns Hopkins University Baltimore, Maryland 21218

The quasiparticle concept has proven remarkably successful in describing collective phenomena in condensed matter, in particular quantum fluids which are among the most interesting and fundamental condensed matter systems. The study of quasiparticles which govern the properties of quantum liquids was pioneered by physicist Lev Landau. Landau explained a variety of properties of superfluid ^{4}He in terms of a system of Bose quasiparticles with a spectrum that has a finite energy minimum (an energy gap) at a particular wave vector [3]. He also realized that the presence of such a quantum gap in the excitation spectrum has dramatic consequences for a quantum Bose liquid and results in an unusual feature – a singular point where the single-quasiparticle spectrum terminates [4]. Like unstable elementary particles in the universe, quasiparticles may not survive beyond an energy-momentum threshold where certain decays become allowed by conservation laws, so the quasiparticle spectrum ends at this threshold. Neutron scattering experiments in ^{4}He indeed indicate that the spectrum of quasiparticles there (longitudinal acoustic waves, or phonons) ends at about twice the quantum gap energy, where phonon quasiparticles start decaying into pairs of near-gap excitations [1,6].

While only two elemental liquids, the helium isotopes ^{4}He and ^{3}He, fail to crystallize at $T = 0$ K, electrons in metals and superconductors and trapped ultracold atoms also form quantum liquids, and some remarkable new examples were recently identified among quantum spins in magnetic crystals [1,2,5]. The organo-metallic material PHCC provides an excellent physical realization of a two-dimensional (2D) quantum spin liquid (QSL). It has Cu^{2+} spins coupled through a complex network of interactions with high degree of frustration, forming a pseudo-square lattice of $S = 1/2$ dimer pairs in the crystalline $\boldsymbol{a}$-$\boldsymbol{c}$ plane [2]. Spin excitations have spectral gap $\Delta_s \approx 1$ meV and a nearly isotropic 2D dispersion relation in PHCC's ($h0l$) plane, with a bandwidth slightly larger than Δ_s, above the gap. In the absence of an external magnetic field, magnetic order in PHCC does not occur down to $T = 0$ K. We explored magnetic excitations in the 2D QSL in PHCC by inelastic neutron scattering and found remarkable similarities with ^{4}He, particularly where the quasi-particle dispersion reaches the threshold for two-particle decay and interferes destructively with the continuum. There are also distinctions which can be ascribed to the different nature of decay interactions in the 2D QSL.

The generality of the physics underlying termination of the quasiparticle spectrum in ^{4}He suggests that similar effects may occur in gapped QSLs. The spin-pair dominated structure factor of PHCC is favorable for probing the interaction of magnon quasiparticles with their two particle continuum. In Fig. 1 (a) we present a series of constant wave vector measurements for energies $\hbar\omega \leq 7$ meV along the [$1/2 0 l$] and [h0-1-h] directions chosen to elucidate both single-particle and multiparticle excitations and the possibility of spectrum termination in a 2D QSL. There is a clear change in the character of the excitation spectrum at $\boldsymbol{Q}_c = (h_c, 0, -1-h_c)$ with $h_c \approx 0.15$ near the magnetic Brillouin zone (BZ) boundary, where the one-magnon dispersion reaches the lower boundary of the two-magnon continuum, $\hbar\omega_{2m}(\boldsymbol{Q}) = \min_q \{\hbar\omega(\boldsymbol{q}) + \hbar\omega(\boldsymbol{Q}\text{-}\boldsymbol{q})\}$. For $h \leq 0.2$ there are two distinct contributions to magnetic scattering, the resolution-limited quasiparticle peak at lower energy and a broad feature with a sharp onset at higher energy, which we associate with the two-particle continuum. For $h \leq 0.15$ the quasiparticle

peak joins the continuum to form a complex spectral feature that extends from 2.5 meV to 4.5 meV. The first frequency moment integrated over different ranges of energy transfer shown in Fig. 1b illustrates how the oscillator strength is transferred from the quasiparticle excitation to the multiparticle continuum upon approaching the wavevector $\boldsymbol{Q}_c$ where they intersect. This differs markedly from the picture of excitations in [$^1/_2 0 l$] direction shown in Fig. 1a on the left. There, the magnon dispersion is weaker, and single-particle excitation never reaches the boundary of the 2-magnon continuum and therefore does not decay.

Quasiparticles are ubiquitous in nature and quasiparticle spectrum termination as seen in superfluid ^{4}He can also occur in other condensed matter systems, in quantum magnets in particular. While this has been generally expected, the extent of the phenomenon and how it reveals itself in real materials has not been clear. Our experiments offer a detailed view of quasiparticle decays in the 2D quantum spin liquid of the metallo-organic magnet PHCC. The termination point predicted from the measured quasiparticle dispersion is marked by dramatic changes in the spectrum of magnetic excitations: a rapid transfer of intensity from the magnon peak to the continuum at higher energies and by an abrupt appearance of damping. Our findings have important implications for other quantum magnets such as lamellar copper oxide superconductors where spin excitations above a gap are considered as possible mediators of electron pairing and high-temperature superconductivity.

REFERENCES

[1] M. B. Stone, I. A. Zaliznyak, , T. Hong, C. L. Broholm, D. H. Reich, Nature **440**, 187 (2006).

[2] M. B. Stone, I. Zaliznyak, D. H. Reich and C. Broholm, Phys. Rev. B **64**, 144405 (2001).

[3] L.D. Landau and E. M. Lifshitz, *Course of Theoretical Physics: Statistical Physics, Part 2*, by E. M. Lifshitz, and L. P. Pitaevskii, Vol. 9, 125-139, Pergamon Press, Oxford (1981).

[4] L. P. Pitaevskii, Sov. Phys. JETP **9**, 830 (1959).

[5] M. B. Stone, J. Rittner, Y. Chen, H. Yardimci, D. H. Reich, C. Broholm, T. Ferraris, and D. V. Lectka, Phys. Rev. B **65**, 064423 (2002).

[6] B. Fåk, and J. Bossy, J. Low Temp. Phys. **112**, 1 (1998), and W. Montfrooij, and E. C. Svensson, J. Low Temp. Phys. **121**, 293 (2000).

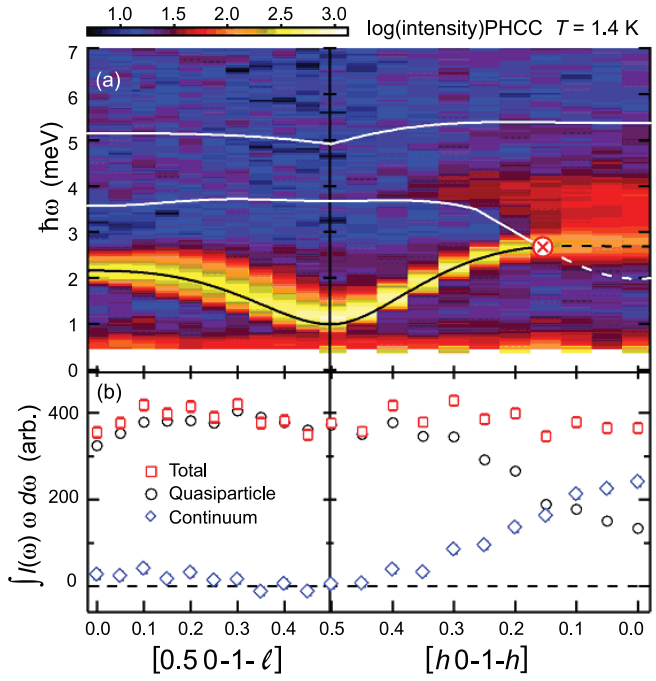

FIGURE 1:
Magnetic excitation spectrum in PHCC at T = 1.4 K. (a) Background corrected intensity along [$^1/_2$0 -1-l] and [h0-1-h] directions smoothed by a $\delta\hbar\omega$ = 0.25 meV running average applied to each constant wave-vector scan. Black line is the single-magnon dispersion [2], white lines are bounds of the two-magnon continuum calculated from this dispersion. (b) First frequency moment of measured scattering intensity integrated over different energy ranges, 0.8 $\hbar\omega \leq$ 5.5 meV (red squares, total), 0.8 $\leq \hbar\omega \leq$ 3 meV (black circles, quasiparticle) and 3 $\leq \hbar\omega \leq$ 5.5 meV (blue diamonds, continuum).

Radiative Decay Mode of the Free Neutron

Beta decay of the neutron into a proton, electron, and antineutrino is accompanied by the emission of an inner-bremsstrahlung photon. Despite decades of precision measurements of neutron beta decay, this rare branch of a fundamental weak decay has never been observed in the free neutron. We present an experiment to observe the radiative decay mode by detecting photons with energies between 15 keV and 340 keV in coincidence with both the electron and proton emitted in neutron decay.

J.S. Nico[1]
M.S. Dewey[1]
T.R. Gentile[1]
H.P. Mumm[1]
A.K. Thompson[1]
B.M. Fisher[2]
I. Kremsky[2]
F.E. Wietfeldt[2]
T.E. Chupp[3]
R.L. Cooper[3]
E.J. Beise[4]
K.G. Kiriluk[4]
J. Byrne[5]
K.J. Coakley[6]

[1] Ionizing Radiation Division
National Institute of Standards and Technology
Gaithersburg, MD 20899-8460

[2] Tulane University
New Orleans, LA 70118

[3] University of Michigan
Ann Arbor, MI 48109

[4] University of Maryland, College Park, MD 20742

[5] University of Sussex
BN1 9QH, U.K.

[6] Statistical Engineering Division
National Institute of Standards and Technology
Boulder, CO 80305

The neutron is composed of two down quarks and an up quark, and it is stable under the strong and electromagnetic interactions. The weak interaction, however, can convert a down quark into an up quark through the emission of the *W* gauge boson that subsequently decays into an electron and an antineutrino. This decay is also accompanied by an inner-bremsstrahlung (IB) photon in the rare process $n \rightarrow p + e^- + \bar{\nu}_e + \gamma$, which is an order-$\alpha$ radiative correction to the main branch. While IB has been measured in nuclear beta decay and electron capture decays, the mode has never been observed for the neutron, the fundamental beta decay. A previous experiment resulted in an upper limit of 6×10^{-3} (at the 90 % confidence level) for the branching ratio of photons between 35 keV and 100 keV [1].

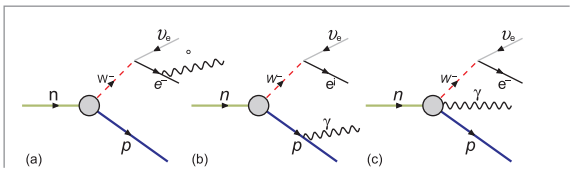

FIGURE 1:
Contributions to radiative neutron decay, showing (a) electron bremsstrahlung, (b) proton bremsstrahlung, and (c) radiation directly from the weak vertex.

The photon energy spectrum and branching ratio for neutron radiative decay has been calculated within a quantum electrodynamics (QED) framework [2] and recently using heavy baryon chiral perturbation ($HB_\chi PT$) theory [3]. The QED calculation takes into account the IB produced from the electron and proton (Figs. 1a and 1b) while the $HB_\chi PT$ approach includes the photon emission from the weak interaction vertex (Fig. 1c). The latter diagram contributes less than one percent and creates only a very slight change in the final photon spectrum and branching ratio calculations; both the photon energy spectrum and the photon polarization observables are dominated by electron IB.

The experimental challenge is to distinguish definitively the low rate of radiative decay events in the large photon background of a neutron beam. The branching ratio above 15 keV is only about 3×10^{-3}, which coupled with the long neutron lifetime (about 15 minutes) makes the rate of detectable photons quite small. An apparatus was mounted at the NG-6 fundamental physics end-station at the Center for Neutron Research at the National Institute of Standards and Technology to search for the decay mode. The experiment registers electron-photon coincidences for electrons followed by a delayed proton, thereby reducing the probability of uncorrelated background events. A strong magnetic field transports charged particles away from the photon detector, which increases the solid angle for detection and minimizes correlated backgrounds. An electrostatic mirror permits one to change the rate of electron-proton coincidences with no change in the photon background rate, thus providing an important systematic check on possible backgrounds.

A cold neutron beam enters parallel to the 4.6 T magnetic field produced by a superconducting solenoid, as illustrated in Fig. 2. When a neutron decays inside the high field region, the charged decay products are confined to move in tight cyclotron orbits typically less than 1 mm in diameter, whose guiding centers are locked to the local magnetic field lines. The solenoid has a slight bend in the magnetic field direction at one end, allowing the decay proton and electron to be guided out of the beam and into a thick silicon surface barrier detector (SBD). The SBD is held at a high negative potential (-25 kV) to accelerate the low energy protons to detectable energies. The apparatus was previously employed on NG-6 to measure the neutron lifetime using a proton trap; its mode of operation has been described in detail elsewhere [4].

Nearly all of the decay electrons have much higher energy (several hundred keV) and reach the detector first, whereas the much slower proton (maximum energy of 751 eV) drifts to the detector a few microseconds later. The electrostatic mirror was constructed in an annular form to permit free passage of the neutron beam, and it was used to reverse the direction of protons with initial momenta away from the detector. Thus, the magnetic field and electrostatic mirror allow for nearly 2 π solid angle coverage for the electron detection and up to 4 π coverage of the proton detection.

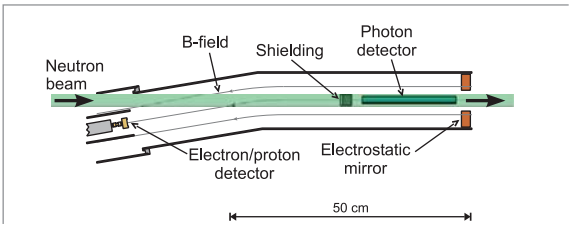

FIGURE 2:
A top-view illustration of the detection scheme for measuring the radiative decay of the neutron. The shielding and photon detector lie below the neutron beam.

To satisfy the need for a large solid-angle photon detector that can operate in a strong magnetic field and at low temperatures, a photon detector consisting of scintillating crystals coupled to avalanche photodiodes was employed. The photon was detected by a single bismuth germanate (BGO) crystal viewed by a silicon avalanche photodiode (APD) [5]. The gain of the APD increases and its noise decreases as the temperature decreases [6]. In addition, BGO exhibits increased light output at low temperatures [7], which reduces the low-energy detection threshold. The BGO crystal was mounted in an aluminum holder and placed below the neutron beam in the downstream end of the bore of the solenoid. The placement of the photon detector well away from the SBD significantly reduces correlated background from external bremsstrahlung photons in the SBD. The photon singles rate, and hence the uncorrelated background rate, was kept low by using a well-collimated neutron beam and gamma-ray shielding.

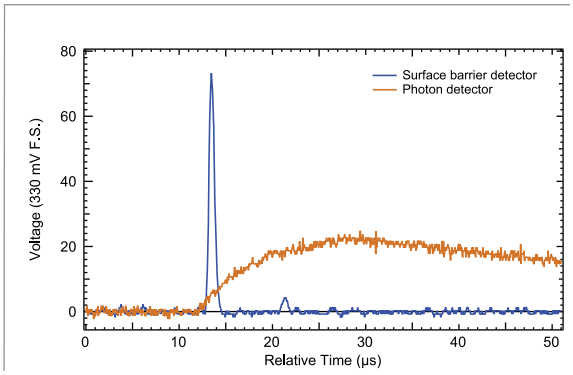

FIGURE 3:
Traces of the digitized waveforms for the two detectors. The blue line shows the SBD signal for an electron event followed by a delayed proton; the orange line shows the much slower preamplified output of the APD for a photon event occurring coincident with the electron.

If a proton was detected within a 20 μs timing window after an electron, a conversion signal triggered a computer-based digital oscilloscope board that recorded the amplified electron-proton coincidence signal and the preamplifier output of the APD. Figure 3 shows an example of the two waveforms. Protons are distinguished from electrons based on their pulse heights. Events attributable to radiative decay photons will occur as prompt events in the timing spectrum, as shown in Fig. 4, and appear at -1.25 μs due to electronic delays. The approximately 1 μs width of the peak arises primarily from noise on the APD signal. The flat background rate observed is consistent with a calculation of the random coincidence rate determined from the measured singles rates.
The apparatus permits a check of correlated backgrounds by varying the electrostatic mirror potential, which changes the electron-proton coincidence rate. The available phase space of the neutron's 4-body decay does not change linearly with the electron-proton rate, in contrast with some sources of correlated backgrounds. Monte Carlo techniques were used to calculate the expected rates as a function of mirror potential. For true radiative decay events, it yields a specific dependence on the neutron decay kinematics and the detector acceptance, thus providing a strong systematic check.

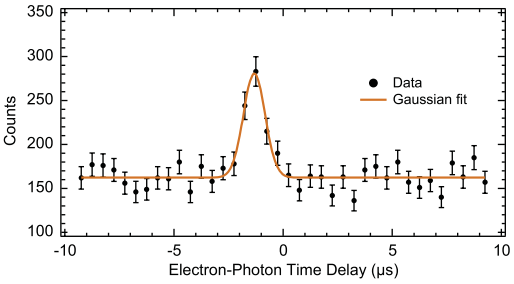

FIGURE 4:
The electron-photon timing spectrum for a three-day run with the mirror reflecting all protons. The spectrum shows all photons in a 20 μs window for which the electron start pulse was accompanied by a delayed proton event.

The analysis of the data is in progress; a precise measurement of the photon spectrum should be possible with a straightforward upgrade of the detector by covering more of the available solid angle. A measurement of the spectrum below the 1 % level would reveal the contributions from the weak vertex and provide an alternative determination of the weak coupling constants g_V and g_A. Similarly, if the photon's circular polarization could be measured, it would reveal information about the Dirac structure of the weak current [2,3].

REFERENCES

[1] M. Beck, *et al.*, JETP Lett **76**, 392 (2002).
[2] Y. V. Gaponov, R. U. Khafizov, Phys. Atom. Nucl. **59**, 1213 (1996); Phys. Lett. B **379**, 7 (1996); Nucl. Instrum. Meth. A **440**, 557 (2000).
[3] V. Bernard, S. Gardner, U.-G. Meißner, C. Zhang, Phys. Lett. B **593**, 105 (2004); Phys. Lett. B **599**, 348 (2004).
[4] J.S. Nico, *et al.*, Phys. Rev. C **71**, 055502 (2005); M.S. Dewey, *et al.*, Phys. Rev. Lett. **91**, 152302 (2003).
[5] B.M. Fisher, *et al.*, J. Res. Natl. Inst. Stand. Technol. **110**, 421 (2005).
[6] L. Yang, *et al.*, Nucl. Instrum. Meth. A **508**, 388 (2003).
[7] H.V.J. Piltingsrud, J. Nucl. Med. **20**, 1279 (1979).

Shear-rate Dependent Structure of Polymer-stabilized TiO_2 Dispersions

How are house-paints designed to spread easily and not lump up or discolor when they are brushed on or applied with other devices? The interactions between polymer chains and colloidal particles are a key to controlling the dispersion of the pigment particles. While studies of polymer-colloid structure and interactions have been performed under quiescent conditions, little is known about the influence of shear (as occurs during brushing) on these properties, where the rheology of such mixtures is strongly shear-rate dependent.

A.I. Nakatani[1]
A. VanDyk[1]
L. Porcar[2]
J.G. Barker[2]

[1] Rohm and Haas Company Spring House, PA 19477

[2] NIST Center for Neutron Research National Institute of Standards and Technology Gaithersburg, MD 20899-8562

Most paints are typically mixtures of inorganic pigments and latex emulsions, where all particle dimensions are in the range of scattering vectors attainable by light scattering measurements. However, light scattering studies on coatings formulations are not possible due to the opacity/turbidity of these samples. While typical small angle neutron scattering (SANS) measurements are capable of overcoming the opacity issues associated with coatings formulations, the maximum size scale which can be measured by SANS measurements (typical d_{max} = 300 nm) is smaller than the particles encountered in coatings. The perfect crystal diffractometer for ultra-high resolution small-angle neutron scattering (USANS) measurements at the NCNR is capable of measuring size features as large as 10^4 nm, providing the potential for obtaining structural information on coatings formulations which was previously unachievable by other methods.

We measured the shear-rate dependent structure of TiO_2 dispersions (37 % volume fraction) stabilized with commercial polymer dispersants in water. The TiO_2 is a commercial grade product with a nominal particle diameter of approximately 400 nm. The solvent compositions were adjusted to the contrast match point of each dispersant to isolate the behavior of the TiO_2. Two different molecular weight (MW) poly acid dispersants (referred to as "low MW acrylate polymer salt" and "high MW acrylate polymer salt") and two different molecular weight alkali soluble acrylate copolymers (referred to as "low MW hydrophobic acrylate copolymer salt" and "high MW hydrophobic acrylate copolymer salt") were used in this study. The shear cell that was used is a couette geometry consisting of double quartz cylinders with a 0.5 mm gap. The shear cell was equipped with a vapor trap which was filled with D_2O to prevent sample drying during the course of the experiment. All experiments were performed at ambient temperature. Data were collected with the incident radiation parallel to the shear gradient and the collected scattering pattern is in the flow — vorticity plane. The shear-rate dependence of the scattering from each sample was measured at 0.1 s^{-1}, 1 s^{-1}, 10 s^{-1}, 100 s^{-1}, and 1000 s^{-1}. After the measurement at 1000 s^{-1}, the scattering was measured at rest. For each shear-rate a counting time of 3.4 h was employed to obtain good counting statistics. All data were corrected for the empty cell scattering and slit smearing effects.

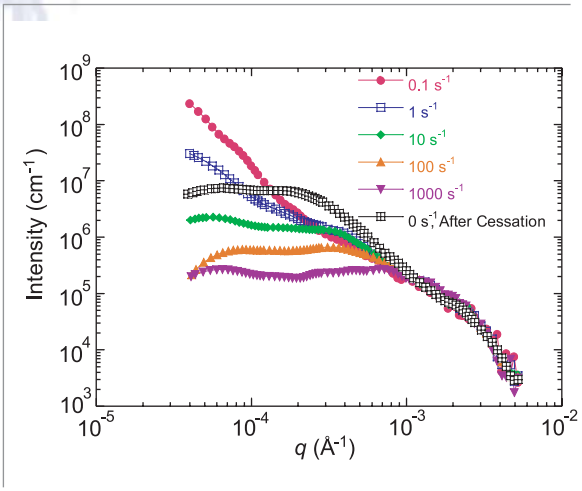

FIGURE 1:
Smearing-corrected shear-rate dependent scattering from a TiO_2 dispersion stabilized with a high MW acrylate polymer salt.

The shear-rate dependent scattering for each of the TiO_2 dispersions with a different polymer dispersant contrast matched are shown in Figs. 1-4. The TiO_2 dispersed with the high MW acrylate polymer salt shows a decrease in low angle scattering with increasing shear-rate (Fig. 1), indicating a shear induced breakup of aggregates of TiO_2. After cessation of shear, the low angle scattering intensity increases, indicating reaggregation of the TiO_2 with the high MW acrylate polymer salt. Conversely, the TiO_2 dispersed with the low MW acrylate polymer salt shows a slight increase in scattering with increasing shear-rate (Fig. 2). This indicates a shear induced aggregation of TiO_2 particles. This aggregation appears to be irreversible, since the scattering after cessation of shear has the highest intensity.

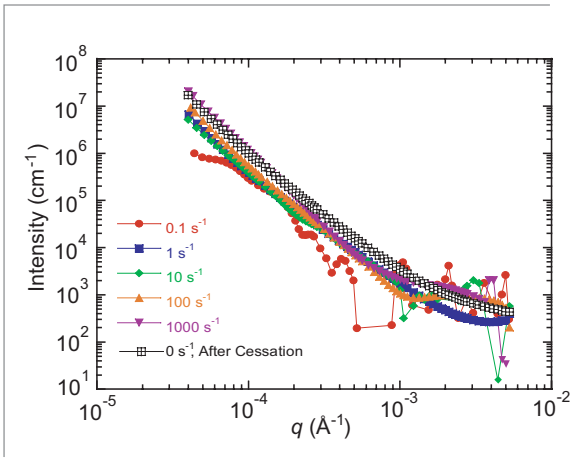

FIGURE 2:
Smearing-corrected shear-rate dependent scattering from a TiO_2 dispersion stabilized with a low MW acrylate polymer salt.

The TiO_2 dispersed with the high MW hydrophobic acrylate copolymer salt shows a decrease in low angle scattering intensity with increasing shear-rate (Fig. 3). After cessation of shear, the low angle scattering appears to increase, but not to the level observed at the start of the shear history. These results indicate the TiO_2 dispersed with the high MW hydrophobic acrylate copolymer salt exhibits a shear induced break up of aggregates and after cessation of shear, reaggregation of the TiO_2 occurs. Finally, the TiO_2 dispersion stabilized with the low MW hydrophobic acrylate copolymer salt also shows an increase in low angle scattering intensity with increasing shear-rate (Fig. 4). Therefore, the low MW hydrophobic acrylate copolymer salt also appears to produce a dispersion which undergoes shear induced aggregation. However, on cessation of shear the scattering intensity decreases, indicating the aggregates formed during shear slowly redisperse.

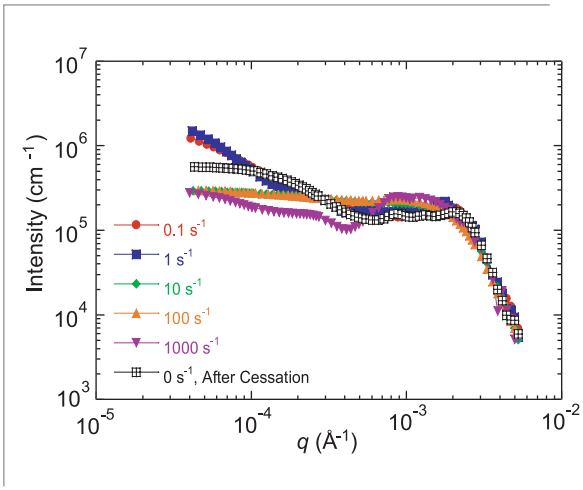

FIGURE 3:
Smearing-corrected shear-rate dependent scattering from a TiO_2 dispersion stabilized with a high MW hydrophobic acrylate copolymer salt.

We believe these are the first results which demonstrate the sensitivity of dispersions to the molecular weight and chemistry of the dispersant molecules, along with the shear-rate dependent behavior of the dispersions. The unique capabilities of the USANS instrumentation were a key in obtaining these results. The complimentary study of these dispersions, in which the TiO_2 has been contrast matched, so the scattering from the dispersant molecules as a function of shear-rate will be reported separately.

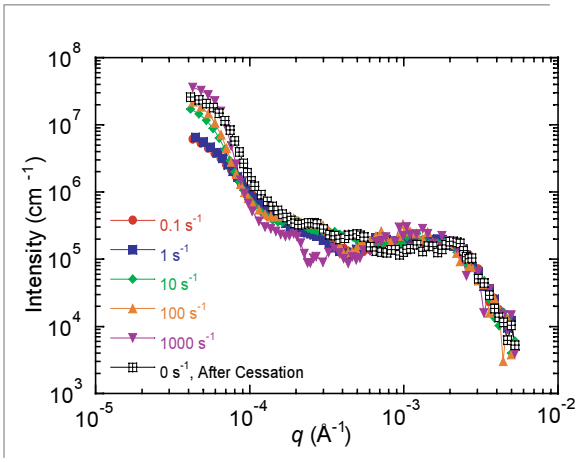

FIGURE 4:
Smearing-corrected shear-rate dependent scattering from a TiO_2 dispersion stabilized with a low MW hydrophobic acrylate copolymer salt.

Changes in Blood Protein Structure under Static and Hydrodynamic Shear Conditions

The binding of multimeric blood plasma protein von Willebrand factor (VWF) to platelet receptor GpIbα under high shear stress is an important step regulating atherothrombosis [2,3] (Fig. 1). The function of this protein is also altered under pathological fluid flow conditions in abnormally constricted (stenosed) arteries. In the current study we measured the structure in solution of VWF that was isolated from various human blood-type samples. In order to understand how the individual domains of VWF are organized in the multimeric protein, a dimeric form of the protein called protomer VWF was produced recombinantly and its solution structure was also measured. Finally, in order to determine if large scale or local protein structural changes are sufficient to affect function, we measured VWF conformation under two distinct conditions: upon addition of denaturant (Guanidine·HCl) and under fluid shear.

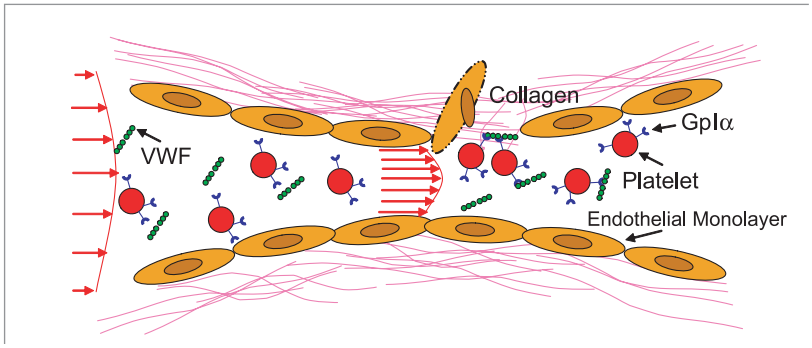

FIGURE 1:
Immobilized von Willebrand Factor (VWF) binding to platelets promotes platelet deposition at sites of vascular injury where the endothelial monolayer is disrupted. High fluid shear stress as may occur in constricted (stenosed) regions of the arterial circulation may also promote VWF binding to specific receptors on blood platelet surface.

S. Neelamegham[1]
I. Singh[1]
P. Alexandridis[1]
L. Porcar[2,3]

[1] State University of New York at Buffalo
Buffalo, NY 14260

[2] NIST Center for Neutron Research
National Institute of Standards and Technology
Gaithersburg, MD 20899-8562

[3] University of Maryland
College Park, MD 20742

Light scattering and small-angle neutron scattering (SANS) were applied under static (no fluid flow) conditions to study the solution structure of human VWF multimers and protomer. Our observations suggest that these proteins resemble prolate ellipsoids in solution with radii of gyration (R_g) of ≈ 75 nm and ≈ 30 nm for the multimer and protomer forms, respectively. The ellipsoid major and minor axes radii were of length ≈ 175 nm and ≈ 28 nm for multimers, and ≈ 70 nm and 9.1 nm for protomers. The multimer is organized into substructural domains at length scales indicative of the entire protein itself (≈ 75 nm), elements of the protomer quarternary structure (≈ 16 nm), and individual functional domains (≈ 4.5 nm) (Fig. 2a). Individual domains of ≈ 4.5 nm were also observed in the protomer. Amino acids occupied a small (≈ 2 %) volume in both multimeric and protomer VWF ellipsoids, compared to other proteins like bovine serum albumin (98 %) and fibrinogen (35 %). ADAMTS-13, a metalloprotease that cleaves VWF, is found in blood, and the absence of this protease leads to severe bleeding complications. In our studies, we observed that treatment of VWF with 1.25M denaturant Guanidine·HCl, which increases the susceptibility of VWF to proteolysis by ADAMTS-13, caused local structural changes at length scales below 10 nm without altering the protein R_g (Fig. 2b). Measurements by other methods reveal a pattern of dimer and trimer units that indicate stable non-covalent interactions within the multimer.

Since the function of von Willebrand Factor is altered upon application of fluid forces, VWF isolated from blood plasma cryoprecipitate was placed in a quartz couette cell [4] (Fig. 3a) and laminar fluid shear was applied in the range from 300/s to 3000/s. SANS measurements were simultaneously performed to assay *in situ* protein solution structural changes in response to hydrodynamic forces. In five out of six different experiments performed with different pools of human VWF, we observed changes at length scales < 10 nm (Fig. 3b) which were reminiscent of the above-mentioned changes in protein structure upon addition of denaturant Guanidine·HCl. These structural changes were irreversible on the time scales studied. Further, even though careful studies were performed to test the hypothesis that changes in protein conformation on a larger scale take place in response to fluid shear, no unequivocal evidence in support of this view was obtained. Control runs were performed to confirm that the observed protein conformation change can indeed be attributed to VWF in solution and not to VWF bound to the Couette-wall. Our studies also show that changes in neutron scattering patterns were specific to VWF, since a smaller protein bovine serum albumin did not undergo similar changes in scattering intensity upon application of fluid shear.

Overall, the small angle scattering and biochemical investigations performed under no flow conditions demonstrate for the first time that the VWF solution structure is stabilized by non-covalent interactions between different monomer units. Studies performed with Guanidine·HCl suggest that local, and not large-scale, changes in protein conformation are sufficient for ADAMTS-13 mediated proteolysis. Studies performed under fluid shear conditions also support the proposition that local changes at length scales < 10 nm may have significant functional consequences during human vascular pathologies. These functional alterations may be due to changes in the nature of interaction between neighboring domains of VWF or due to release of non-covalent interactions that stabilize VWF solution structure under static conditions. Finally, the results motivate further biochemical and small angle scattering investigations of VWF structure at smaller time scales and under different shear protocols.

SANS data were obtained using the 30m NG-3 instrument. The study was supported by NIH grants HL76211 and HL77258.

REFERENCES

[1] G. Beaucage, G., J. Appl. Crystallog. **29**, 134 (1996).
[2] Z.M. Ruggeri, Nat. Med., **8** (11) 1227 (2002).
[3] H. Shankaran, P. Alexandridis, and S. Neelamegham, Blood **101,** 2637 (2003).
[4] L. Porcar, W.A. Hamilton, P.D. Butler, and G.G. Warr, Rev. Sci. Inst. **73**, 2345 (2002).

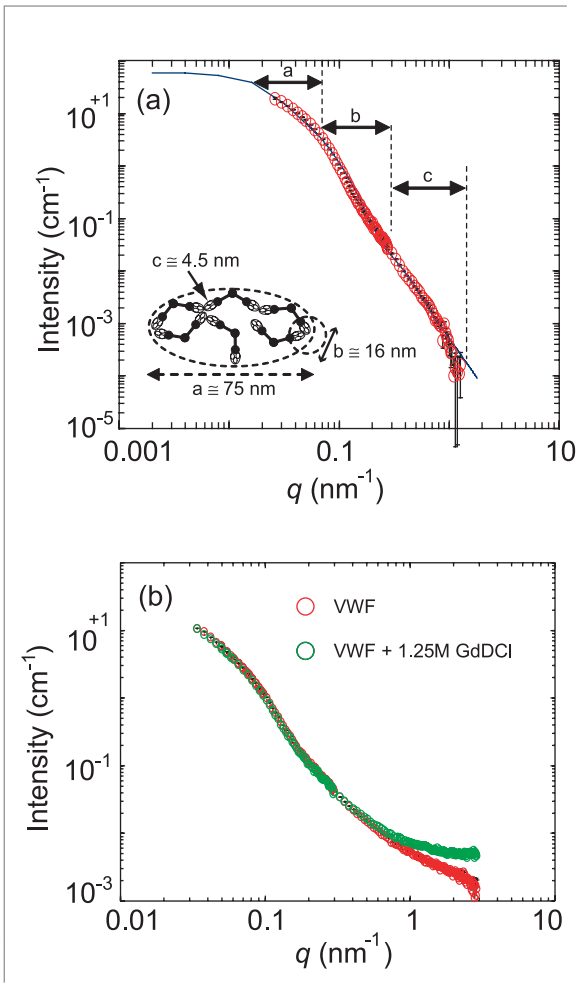

FIGURE 2:
(a) Small angle scattering data were fit to the unified equation in Ref. 1. This analysis revealed that human VWF has three distinct structural levels *a*,*b*,*c* within multimeric protein. Level *a* is the multimeric molecule, *b* is an intermediate structure that likely represents the globular domain at the N-terminus of VWF, and *c* represents individual protein domains. Discrete points represent experimental data while smooth lines are model fits. (b) SANS data for multimeric VWF before and after treatment with 1.25M Gd·DCl shows that Gd·DCl does not affect the R_g of the protein, though it alters structural features at length scales < 10 nm.

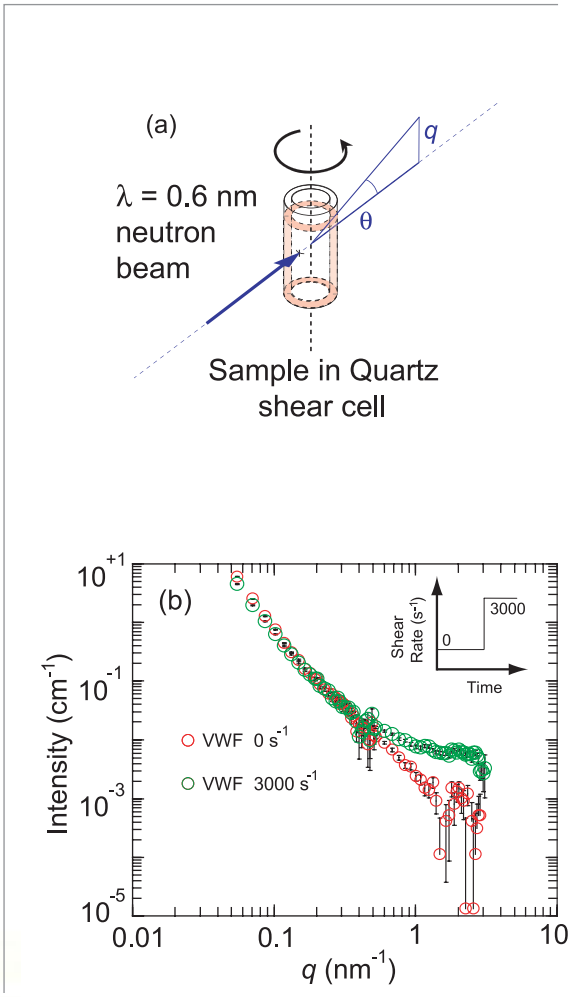

FIGURE 3:
(a) Schematic drawing of a couette shear cell in which VWF was sheared and protein solution structure was evaluated in real-time. (b) A representative shear run where the fluid shear rate was increased from 0/s to 3000/s at a fixed time point. Increase in scattering intensity is observed in the high q range and a small decrease is observed at low q.

Why Are Double-Network Hydrogels So Tough?

Recent advances in preparing double-network hydrogels (DN-gels) from crosslinked polyelectrolyte and linear polymer have resulted in materials with fracture toughness comparable to that of joint cartilage while containing more than a 90 % volume fraction of water (Fig. 1) [1]. DN-gels are prepared by polymerizing a high molecular weight linear polymer within a swollen polyelectrolyte network. In general, the polyelectrolyte network is rigid but extremely fragile (like jelly) while the neutral linear polymer is highly viscous but readily deformable (like putty).

Since neither of the components is individually tough, the unique double-network morphology should be expected to account for this intriguing mechanical behavior. Here we highlight the use of neutron scattering in determining, for the first time, the structure of DN-gels as well as the structure of the individual components. To cover a broad range over four orders-of-magnitude in wavevector q, data from both ultra-small angle neutron scattering (USANS) and SANS were collected and compiled from each sample. The measurements were made using USANS instrument at BT-5 and the SANS diffractometers at NG-3 and NG-7 at the NCNR.

The DN-gels studied in this work were prepared *in situ* by polymerizing linear polyacrylamide (PAAm) at several concentrations within a crosslinked poly(2-acrylamide,2-methyl,1-propanesulfonicacid) (PAMPS) network. The total network structure was rendered observable using neutron scattering contrast by immersing the hydrogenated double-networks in deuterated water. To determine the structure of PAAm chains within the DN, samples were prepared by polymerizing deuterium-labeled acrylamide monomer (d_3-PAAm) within the PAMPS network swollen in regular water. Matching the neutron contrast of the d_3-PAAm chains with that of a mixture of light and heavy water then allows us to characterize the PAMPS network structure within the DN-gels. Figure 2 shows the total structure of DN-gels measured over four orders-of-magnitude in wavevector, q. The scattering intensity at ultra-small angles (I(q), $q \rightarrow 0.00001$ Å^{-1}), which is related to the extent of heterogeneity in DN-gels, surprisingly, decreases with the addition of PAAm to the PAMPS single-network. This suggests that the PAAm chains are preferentially situated within the low crosslink density regions of the PAMPS gel, thus resulting in a gradually homogenized double-network structure with increasing PAAm concentration [2]. But the heterogeneity reoccurred to some extent for the DN-gel with more than 1.5M polyacrylamide. While the initial homogenization of the PAMPS network slightly improved the toughness of DN-gels prepared at low PAAm concentration, the toughest of the DN-gels, containing more than 1.5M PAAm, is almost as heterogeneous as the primary PAMPS network. However, the individual component structure of PAMPS and PAAm within the DN-gels gets homogenized at high PAAm loadings, as determined from the USANS results.

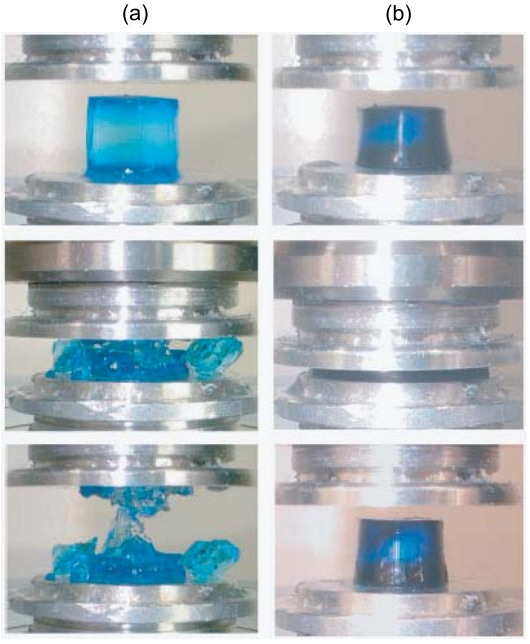

FIGURE 1:
Pure PAMPS gel breaks down under compression at 40 % by volume (a), but the toughest DN-gel regains its size and shape after 90 % compression by volume (b). (Reproduced with permission from Ref. 1.)

T. Tominaga[1,2]
V.R. Tirumala[1]
P. Butler[3]
E.K. Lin[1]
H. Furukawa[2]
J.P. Gong[2]
Y. Osada[2]
W-L. Wu[1]

[1] Polymers Division
National Institute of Standards and Technology
Gaithersburg, MD 20899-8541

[2] Hokkaido University
Sapporo, Japan

[3] NIST Center for Neutron Research
National Institute of Standards and Technology
Gaithersburg, MD 20899-8562

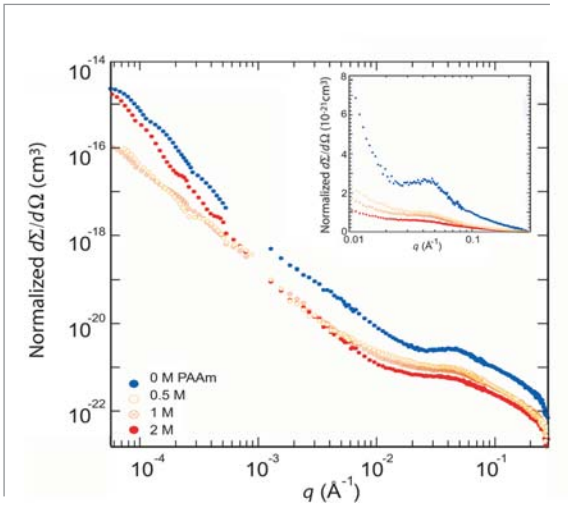

FIGURE 2:
SANS and USANS data from DN-gels prepared at different PAAm concentrations as shown in the legend. The inset shows the change in the polyelectrolyte scattering peak with the addition of PAAm. The data are normalized to the contrast factor.

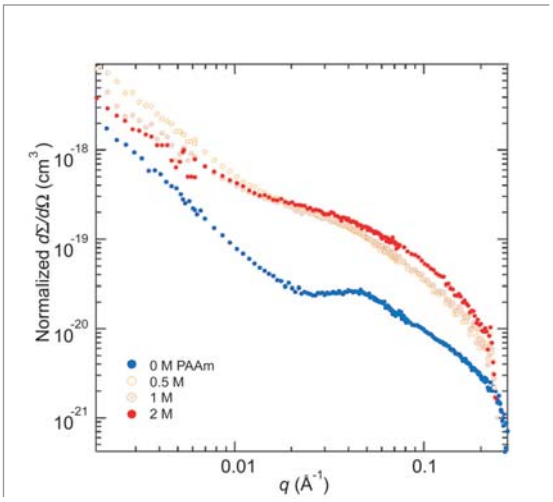

FIGURE 3:
SANS data from the PAMPS network alone measured from DN-gels prepared at different PAAm concentrations shown in the legend. The data are normalized to the contrast factor. The PAAm network has been rendered invisible by contrast-matching it to the aqueous matrix.

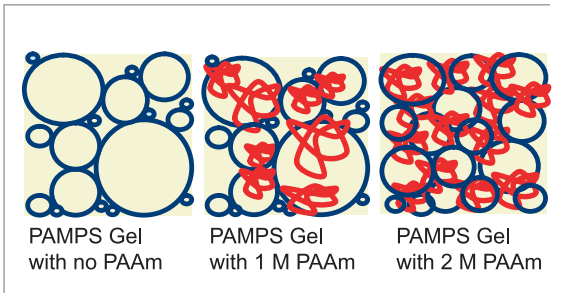

FIGURE 4:
Schematic diagram showing the evolution of double-network structure from the primary PAMPS gel with increase in PAAm concentration from 0 M to 1 M and 2 M. PAMPS and PAAm are represented by blue and red colors respectively.

The scattering data at high-q offers insight into the interactions between the linear PAAm and the PAMPS network. A well-defined scattering peak resulting from intrachain correlations is characteristic of a swollen polyelectrolyte in a polarizable medium [3]. For the present case of the PAMPS primary network used in DN-gels, this scattering maximum occurs at $q \approx 0.045$ Å^{-1}. By making the PAAm network invisible using contrast matching to the aqueous matrix, the behavior of the PAMPS network alone can be measured. Figure 3 shows the result of varying the (invisible) PAAm concentration on the PAMPS peak. The peak position remains constant for DN-gels at all PAAm concentrations but the peak amplitude diminishes with PAAm loading since the electrostatic repulsion is screened by PAAm. This is noteworthy since PAAm is not expected to be sufficiently ionized to screen out the electrostatic repulsions among the PAMPS, even though water soluble. Regardless of their origin, the SANS results at high q suggest strong interactions between PAMPS and PAAm in aqueous solution. From these results, the structural changes in the PAMPS gel with the addition of PAAm to form the toughest DN-gel can be conceptualized as shown in Fig. 4. We are currently investigating the origin of these interactions to further determine their effect on the fracture toughness of DN-gels.

REFERENCES

[1] J.P. Gong, Y. Katsuyama, T. Kurokawa, Y. Osada, Adv. Mater. **15** 1155 (2003).
[2] Y.-H. Na, T. Kurokawa, Y. Katsuyama, H. Tsukeshiba, J.P. Gong, Y. Osada, S. Okabe, T. Karino, M. Shibhayama, Macromolecules **37**, 5370 (2004).
[3] V.M. Prabhu, E.J. Amis, D.P. Bossev, N. Rosov, J. Chem. Phys. **121**, 4424 (2004).

A Mechanism for the Onset of Bioactivity in Biomolecules

At low temperatures biomolecules (proteins and DNA) exist in a glassy state, a state which has no conformational flexibility and shows no biological functions. In a hydrated biomolecule, at and above 220 K, this flexibility is restored and the protein or DNA is able to sample more conformational sub-states, thus becoming biologically functional. This 'dynamical' transition of biomolecules is believed to be triggered by its strong coupling with the hydration water, which also shows a similar dynamic transition. Our experiments described below demonstrate that the origin of the characteristic temperature controlling both the activity of the biomolecules and the transition in the behavior of $\langle x^2 \rangle$ is the Fragile-to-Strong dynamic crossover (FSC) phenomenon in the hydration water, which shares the same crossover temperature at 222 ± 2 K with the biomolecules. At the FSC, the structure of hydration water makes a transition from predominantly high-density (more fluid state) to low-density (less fluid state) forms derived from existence of the second critical point at an elevated pressure.

S-H. Chen[1]
L. Liu[1]
X. Chu[1]
Y. Zhang[1]
E. Fratini[2]
P. Baglioni[2]
A. Faraone[3,4]
E. Mamontov[3,4]
V. Garcia Sakai[3,4]

[1] Massachusetts Institute of Technology Cambridge MA 02139

[2] University of Florence 50019 Florence, Italy

[3] University of Maryland College Park, MD 20742

[4] NIST Center for Neutron Research National Institute of Standards and Technology Gaithersburg, MD 20899-8562

Using the high-resolution quasielastic neutron scattering (QENS) method at the High Flux Backscattering Spectrometer (HFBS) at the NCNR and the Relaxing-Cage Model (RCM) [1] for the analysis, we determine the temperature dependence of the average translational relaxation time, $\langle \tau_T \rangle$, for the hydration water. The dynamic crossover temperature of hydration water is defined as follows. At high temperatures, $\langle \tau_T \rangle$ follows a super-Arrhenius behavior (called a 'fragile' behavior [2]) describable approximately by a Vogel-Fulcher-Tammann (VFT) law: $\langle \tau_T \rangle = \tau_1 \exp[DT_0/(T - T_0)]$, where D is a constant providing the measure of fragility and T_0, the ideal glass transition temperature at which the relaxation time appears to diverge. In reality, however, this divergence is avoided by the system. Instead, an Arrhenius behavior (called a 'strong' behavior [2]) sets in below the crossover temperature T_L where the functional dependence of the relaxation time switches to a law: $\langle \tau_T \rangle = \tau_1 \exp[E_A/k_B T]$. In this equation, E_A is the activation energy for the relaxation process and k_B, the Boltzmann constant. The crossover temperature T_L is defined by the intersection of these two laws, which gives $1/T_L = 1/T_0 - (Dk_B)/E_A$. In the case of hydration water in both lysozyme protein and DNA, we found $T_L = 222 \pm 2$ K, which agrees well with the characteristic transition temperature in protein observed before [3]. Since the average relaxation time $\langle \tau_T \rangle$ is a measure of the mobility of a typical hydration water molecule, this result implies that the sudden change in the trend of mobility of water molecules at the crossover temperature triggers the so-called glass transition of biomolecules [4-7].

Figure 1 shows the mean-squared hydrogen atom displacements $\langle x^2 \rangle$ (calculated from the translational Debye-Waller factor, $S_H(Q,\omega=0) = \exp[-Q^2 \langle x^2 \rangle]$)

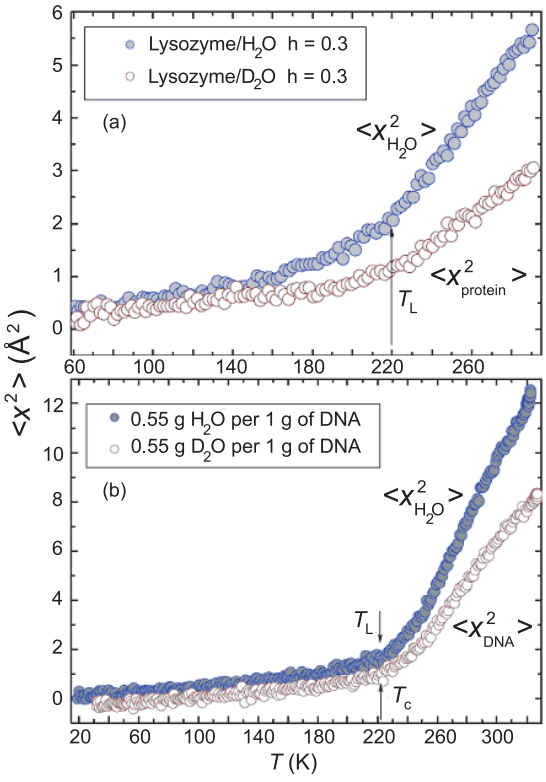

FIGURE 1:
Mean-squared atomic displacement $\langle x^2 \rangle$ of all the hydrogen atoms at 2 ns time scale measured by an elastic scan with resolution of 0.8 μeV (HFBS at NIST), as a function of temperature for H_2O hydrated and D_2O hydrated protein (Panel a) and DNA (Panel b). The solid circles represent $\langle x^2 \rangle$ dominated by contributions from H atoms in hydration water, while the empty circles, that dominated by H atoms contained in protein or DNA molecules.

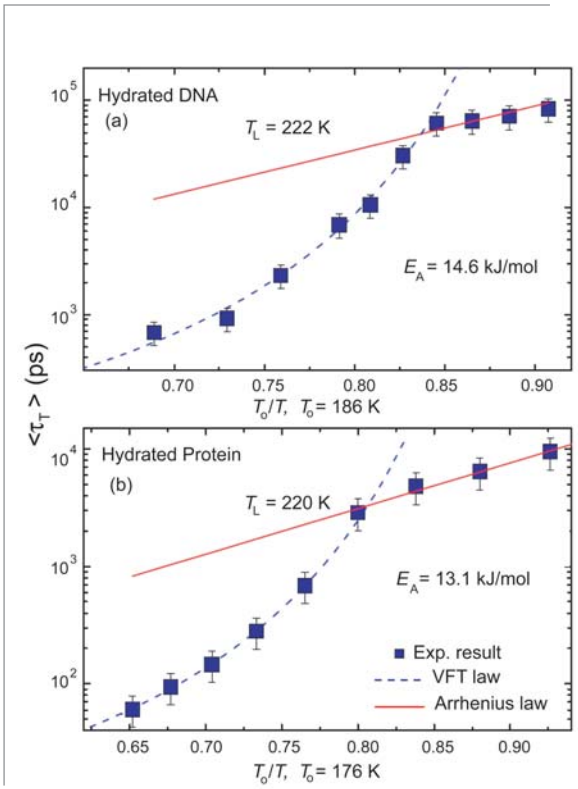

FIGURE 2:
The extracted Q-independent average translational relaxation time <τ_T> vs. T_O/T from fittings of the quasielastic spectra plotted on a log scale. Panel (a) is a result from hydrated DNA [8], whereas Panel (b) is the same quantity measured in hydrated lysozyme protein [9]. There is clear evidence in both cases that a well-defined cusp-like dynamic crossover behavior occurs at T_L indicated in the respective figures. The dashed lines represent fitted curves using the VFT law, while for the solid lines the fitting is according to the Arrhenius law. T_L in both cases occurs at 222 ± 2 K.

obtained by a method of elastic scan in hydrated lysozyme protein (Panel a) and hydrated DNA (Panel b), respectively. In both panels, one sees that at low temperatures up to their respective crossover temperatures, all curves have a gentle linear temperature dependence. However, at above the crossover temperatures, they rise sharply with different slopes. We call the crossover temperature of H_2O T_L, and that of protein or DNA T_C, with both values at approximately 222 ± 2 K. This is to say that the dynamic crossover phenomenon of both protein and DNA and that of their hydration water are highly correlated, and occur at a similar temperature. It is more striking to note that the T_L of H_2O hydrated in protein and that in DNA are close to each other. These results signal our later conjecture that the dynamic crossover temperature is independent of the biomolecules. To define precisely the T_L, we performed dynamic measurements at HFBS. In Fig. 2, we present the temperature dependence of the average translational relaxation time, <τ_T>, for the hydrogen atom in a water molecule, calculated by RCM, for both protein and DNA cases [8-9]. Both H_2O and D_2O hydrated samples were measured. The contribution of scattering from biomolecules is subtracted out during the signal processing by taking the difference of the signals between the two samples. It is seen that, in the temperature range from 270 K to 230 K, <τ_T> obeys VFT law, a signature of fragile liquid, quite closely. But at T_L = 222 ± 2 K it suddenly switches to an Arrhenius law, a signature of a strong liquid. So we have a clear evidence of FSC in a cusp form. It is to be noted that the crossover temperature of protein hydration water is sharply defined at T_L = 220 K, the T_0 for the fragile liquid turns out to be 176 K, and the activation energy for the strong liquid, E_A = 13.1 kJ/mol, which are slightly lower than in the DNA case, T_L = 222 K, T_0 = 186 K, and E_A = 14.6 kJ/mol.

In summary, an investigation of the average translational relaxation time, of protein and DNA hydration water as a function of temperature reveals a hitherto unnoticed Fragile-to-Strong dynamic crossover at T_L = 222 ± 2 K, close to the universal dynamic transition temperature T_C documented for biomolecules in the literature. The coincidence of the dynamic transition temperature T_C of biomolecules, signaling the onset of anharmonic molecular motion, and the FSC temperature T_L of the hydration water suggests that the change of mobility of the hydration water molecules across T_L drives the dynamic transition in biomolecules.

REFERENCES

[1] S.-H. Chen, C. Liao, F. Sciortino, P. Gallo, P. Tartaglia, Phys. Rev. E **59**, 6708 (1999).
[2] C.A. Angell, J. Non-Crys. Sol. **131-133**, 13 (1991).
[3] B.F. Rasmussen, A.M. Stock, D. Ringe, G.A. Petsko, Nature **357**, 423 (1992).
[4] W. Doster, S. Cusack, W. Petry, Nature **337**, 754 (1989).
[5] W. Doster, S. Cusack, W. Petry, Phys. Rev. Lett. **65**, 1080 (1990).
[6] M. Tarek, D.J. Tobias, Phys. Rev. Lett. **88**, 138101 (2002).
[7] D. Vitkup, D. Ringe, G.A. Petsko, M. Karplus, Nat. Struct. Biol. **7**, 34 (2000).
[8] S.-H. Chen, L. Liu, X. Chu, Y. Zhang, E. Fratini, P. Baglioni, A. Faraone, E. Mamontov, submitted to Phys. Rev. Lett. (2006).
[9] S.-H. Chen, L. Liu, E. Fratini, P. Baglioni, A. Faraone, E. Mamontov, to appear in Proc. Nat. Acad. Sci. USA (2006).

The Dynamic Transition in RNA is Solvent-Induced

Much as glasses 'melt' when heated through a glass transition, all hydrated proteins undergo an analogous 'dynamic transition' in the temperature range of $T_D \approx 200$ K to 230 K, in which there is a distinct onset of increased motion within these large molecules. An intriguing aspect of this transition is that it correlates well with the appearance of measurable biochemical activity in proteins [1-2]. Much evidence exists, both experimental and computational, that supports the idea that solvent dynamics controls the observed dynamic transition [3-4]. A contrasting view is that the transition is an inherent property of proteins themselves, and arises from components such as the methyl groups on the side chains [5]. To assess if a universal mechanism drives the dynamical transition in biomolecules we studied the dynamics of tRNA using neutron scattering spectroscopy. Despite vast differences in the architecture and backbone structure of proteins and RNA, hydrated tRNA undergoes the dynamic transition at the same temperature as hydrated lysozyme, a common protein found in egg-white. This similarity supports the idea that the dynamic transition is solvent induced. Our results also suggest that methyl groups are not the main contributor to the dynamic transition in biological macromolecules; however, they may explain strong differences in the dynamics of tRNA and lysozyme observed at low temperatures.

G. Caliskan[1,2]
R.M. Briber[3]
D. Thirumalai[3]
V. García Sakai[2,3]
S.A. Woodson[1]
A.P. Sokolov[4]

[1] Johns Hopkins University Baltimore, MD 21218

[2] NIST Center for Neutron Research National Institute of Standards and Technology Gaithersburg, MD 20899-8562

[3] University of Maryland College Park, MD 20472

[4] University of Akron Akron, OH 44325

Neutron scattering probes molecular dynamics directly and the observable time scales cover the range of internal motions occurring in proteins. Incoherent neutron scattering probes the dynamics of H atoms because their scattering cross-section is significantly larger than that of any other atom. H atoms are distributed throughout tRNA and lysozyme, providing information on their overall motions. Measurements were performed on the High Flux Backscattering Spectrometer (HFBS) at the NCNR. Elastic scans were measured at a heating/cooling rate of 0.7 K/min and quasielastic scattering measurements were taken using an energy window of ± 17 μeV (with a resolution of 0.85 μeV).

Figure 1 shows the mean square hydrogen displacement $\langle u^2 \rangle$ of tRNA and lyzosyme in dry and hydrated states, obtained from analyzing the elastic scattering intensity as a function of the scattering wavevector. In both hydrated samples, $\langle u^2 \rangle$ increases sharply above $T \approx 200$ K to 220 K, characteristic of the dynamic transition. Dry tRNA exhibits a linear increase in $\langle u^2 \rangle$ over the entire temperature range, a signature of harmonic behavior. In contrast, dry lyzosyme shows an onset of anharmonicity with a stronger temperature dependence at $T \approx 100$ K. In Fig. 2 the resulting quasielastic spectra shows significant broadening relative to the instrumental resolution at 300 K for both hydrated tRNA and lyzosyme. This indicates a relaxation process occurring in the 300 ps to 5 ns timescale. Hydrated tRNA at 200 K and dry tRNA at 300 K show no broadening, consistent with the harmonic behavior observed in $\langle u^2 \rangle$. In contrast, the spectra of dry lyzosyme at 320 K and wet lyzosyme at 200 K show quasielastic broadening, indicating a relaxation process occurring at temperatures below the dynamic transition, in agreement with the anharmonicity observed in $\langle u^2 \rangle$, and which is absent in tRNA.

FIGURE 1:
Mean-squared hydrogen displacement as a function of temperature for lysozyme (solid symbols) and tRNA (open symbols) in hydrated (black) and dry (red) forms. Error-bars are smaller than ±0.02 Å².

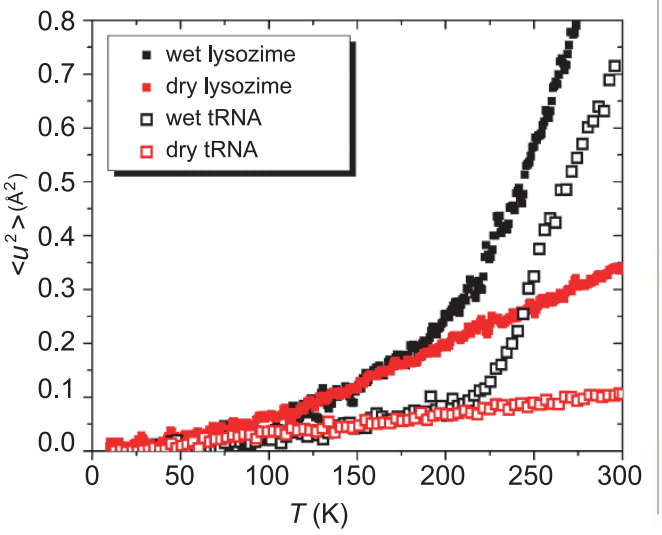

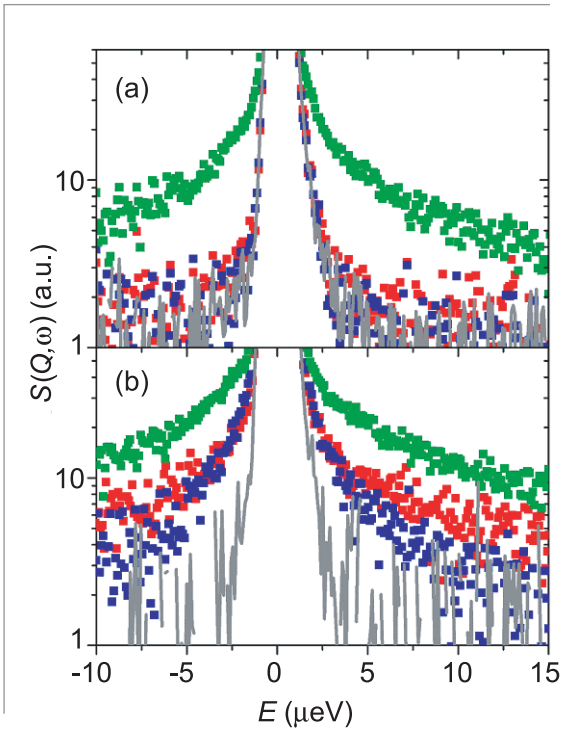

FIGURE 2:
Quasi-elastic scattering spectra of wet tRNA at 300 K (green) and 200 K (blue) and dry tRNA at 300 K (red) (a). Similar data for wet lysozyme at 295 K (green) and 200 K (blue) and dry lysozyme at 320 K (red) (b). The solid gray lines represent the resolution.

The similarity in T_D of hydrated tRNA and lyzosyme indicates that the dynamic transition is not an intrinsic property of the macromolecule. Extensive measurements on various hydrated proteins, DNA and now tRNA, reveal the dynamic transition in the same temperature range, despite differences in backbone chemistry and 3D structure. It has been argued that the dynamic transition of hydrated biomolecules is primarily a result of the transition from liquid-like to solid-like dynamics that occurs in water on molecular time and length scales. The dynamic crossover for water occurs at $T_C \approx 220$ K to 230 K.

Further evidence for a solvent induced transition is the observation that the dynamic transition of lyzosyme in glycerol [3] occurs at the same temperature as the dynamic crossover of pure glycerol. Furthermore, simulations have shown that when the translational motion of water is artificially restricted, the protein behaves as if it were below the dynamic transition even at 300 K [6]. This suggests that arrest of the translational motion of the solvent molecules blocks the motion of the biomolecule.

Based on the similarity of the temperature dependence of $<u^2>$ and NMR-determined orientational order parameter for methyl-bearing side chains, it has been proposed [5] that the freezing of rotational relaxation is the cause of the dynamic transition in proteins. However, the paucity of methyl groups in tRNA suggests that the freezing of their rotational motion is unlikely to be the cause of the dynamic transition. Instead, the dynamic transition is related to another relaxation process that enters the energy window of the backscattering spectrometer at temperatures above T_D and appears as a significant broadening of the scattering spectra in the hydrated biomolecules [Fig. 2]. The microscopic nature of this process is unknown for proteins or for DNA. One suggestion based on MD-simulations is that the α-helices in myoglobin become dynamically active above T_D. If this is correct, this type of motion would require translational motion of water molecules.

The most significant difference between the dynamics of tRNA and lyzosyme is the absence of anharmonicity in tRNA at low temperatures. An additional relaxation process occurs in lyzosyme. It has been ascribed to methyl group dynamics that contribute significantly to the scattering spectra. This is consistent with our results for tRNA which lacks this relaxation component at low temperatures. However, these differences could also be due to the different flexibility of the polypeptide and polynucleotide backbones.

The present analysis clearly demonstrates that neither the 3D structure of biological macromolecules nor their chemical backbone affect the dynamic transition. This conclusion supports the idea [6] that unfreezing the translation of solvent molecules is the main cause of the dynamic transition in biomolecules. Our results also suggest that the rotation of methyl groups is not the main cause of the dynamic transition, although they may cause the low-temperature anharmonicity observed in proteins. Understanding the microscopic nature of the motions that activate in the nanosecond-picosecond time range in biological macromolecules above T_D remains an important challenge as these motions are intrinsically linked to biochemical interactions.

REFERENCES

[1] B.F. Rasmussen, A.M. Stock, D. Ringe, G.A. Petsko, Nature **357**, 423 (1992).
[2] H. Lichtenegger, W. Doster, T. Kleinert, A. Birk, B. Sepiol, G. Vogl, Biophys. J. **76**, 414 (1999).
[3] A.M. Tsai, D.A. Neumann, L.N. Bell, Biophys. J. **79**, 2728 (2000).
[4] A.L. Tournier, J. Xu, J.C. Smith, Biophys. J. **85**, 1871 (2003).
[5] A.L. Lee, J. Wand, Nature **411**, 501 (2001).
[6] M. Tarek, D.J. Tobias, Phys. Rev. Lett. **88**, 138101 (2002).
[7] L. Cordone, M. Ferrand, E. Vitrano, G. Zaccai, Biophys. J. **76**, 1043 (1999).

Studying Intrinsically Disordered Proteins by Small-Angle Neutron Scattering

A suite of computational methods is being developed with the double aim of aiding the analysis of small angle (neutron: SANS, x-ray: SAXS) scattering data from measurements on macromolecular systems and aiding in the design of subsequent experiments. Specifically, we are merging methods developed to search conformational space of small molecular pharmaceuticals with the conformational search problem posed by intrinsically disordered proteins and nucleic acids. This is achieved by generating an ensemble of macromolecular structures that have small angle scattering patterns that are consistent with experiment by varying sets of backbone dihedral angles and using importance sampling and linear algebraic methods. These algorithms have been incorporated into a graphical user interface called SASSIE intended for the NCNR user community.

FIGURE 1:

Analysis of an ensemble of protein structures of the full-length HIV-1 Gag protein by comparison of calculated patterns with experimentally determined small-angle neutron scattering data. Histogram of Rg values (left panel) and a comparison of experimental and theoretical SANS patterns of HIV-1 Gag protein (right panel). The experimental data are shown as points with error bars, while the best (black) and worst fit (grey) are shown as lines. The generation and evaluation of millions of Gag-1 structures indicates that monomeric HIV-1 Gag protein is folded over and not extended under physiological conditions. This implies that the protein undergoes a major conformational change when assembled into the intact virus particle.

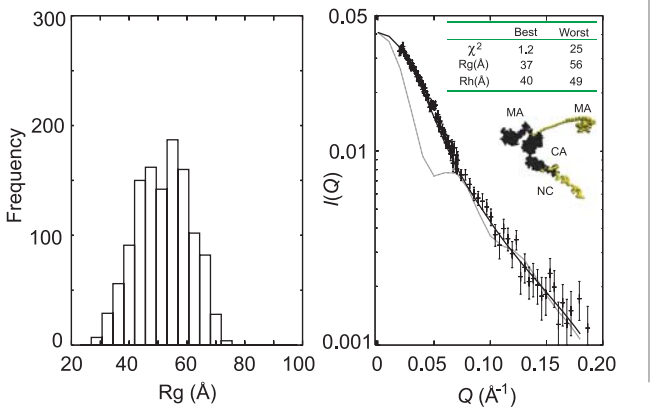

J.E. Curtis[1]
N.F. Berk[1]
S. Krueger[1]
P. Coleman[2]
S.J. Moeller[2]
R.B. Ross[2]
S. Datta[3]
A. Rein[3]

[1] NIST Center for Neutron Research National Institute of Standards and Technology Gaithersburg, MD 20899-8562

[2] 3M Corporate Research Laboratory, USA 3M Center St. Paul, MN 55144-1000

[3] National Cancer Institute, NCI-Frederick Frederick, MD 21702-1201

We have used these tools to predict the first full-length structures of the HIV-1 Gag protein [1]. This macromolecule is the major structural protein element in the virus that causes AIDS. The knowledge of the structure of this protein may allow for the development of drugs that prevent the assembly of virus particles *in vivo*. Additionally, we have determined structures of full-length Protein A, which is the major reagent used to purify antibodies by the pharmaceutical industry. Knowledge of the structures that Protein A adopts at thermal equilibrium may help to improve product yields. These tools, once mature, may be useful in the study of many intrinsically disordered proteins and the elucidation of macromolecular interactions in solution.

Proteins are vital components of biological systems that have a variety of structural and catalytic functional roles. Historically, atomic level structural knowledge of proteins has relied upon x-ray diffraction and nuclear magnetic resonance (NMR) spectroscopy. These methods have had an immeasurable impact on the elucidation of many biological problems. Recently, however, it has been estimated that ≈ 20 % to 30 % of the proteins encoded by the eukaryotic genome have regions that are structurally ill-defined and thus many proteins are intrinsically disordered [2]. These disordered proteins have biological function and control mechanisms that are largely unclassified. Thus, a less realized role of proteins in many biological processes has emerged. Many disordered proteins have functionality that is directly related to their flexibility. Due to their inherent disorder, atomic descriptions are not generally available for the entire molecule since the molecules occupy an ensemble of interchanging conformations in solution.

Structural data for several regions of the HIV-1 Gag protein have been determined by x-ray and NMR methods. However, the determination of a full-length structure from either protein crystals or solution has not been achieved. The five major regions of the HIV-1 Gag protein are connected by amino acid residues that have been determined by experiment to

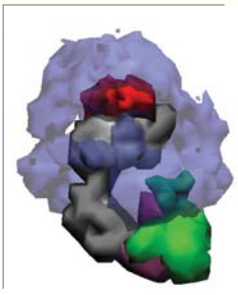

FIGURE 2:

Probability density plot depicting allowed structural arrangements of the individual sub-domains of the HIV-1 Gag protein. The regions are colored as follows: matrix, transparent blue; amino-terminal linker, red; capsid, grey; p2-linker; mauve; nucleocapsid, green.

FIGURE 3:

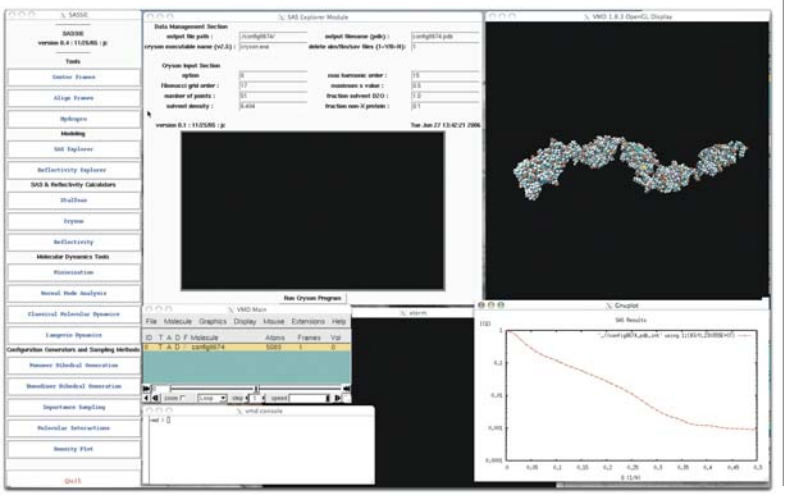

An example of the SASSIE software environment applied to the calculation of the SANS patterns from the atomic coordinates of a single configuration of protein-A. The interface allows for real-time calculation of SAS and reflectivity profiles of molecular objects as well has methods to generate and analyze ensembles of intrinsically disordered proteins and nucleic acids.

be highly flexible. Despite a large experimental effort to find a single structure, this flexibility suggests that given the disordered nature of the HIV-1 Gag protein, its non-aggregated state is characterized by an ensemble of structures. We have used the 30 m SANS instrument on the NG-3 beamline at the NCNR to determine the structural characteristics of the HIV-1 Gag protein in the monomeric state under physiological conditions. Using atomic positions available from experiment as a starting point, we have developed molecular models of the full-length HIV-1 Gag protein to create large ensembles of structures for analysis. While not rigorously exhaustive, the generation of millions of structures by varying the protein backbone dihedral angles is reasonably tractable using modest computational resources.

In Fig. 1 we compare the experimentally determined SANS patterns of monomeric HIV-1 Gag protein to a few theoretically determined curves from full-length atomistic models of the protein. Clearly, in all cases, extended structures have SANS patterns that deviate significantly from the experimentally determined data. Thus, in the case of the search for a single representative structure of the protein, extended structures do not have SANS patterns consistent with experiment.

In Fig. 2 we show a probability density plot of various regions of the HIV-1 Gag protein. The density plot was created using a Metropolis importance sampling method to determine representative linear combinations of structures that are consistent with the experimental data. As before, the most likely conformations are those that are folded over and not extended. Thus, one advantage of these methods is that they are useful in ruling out candidate structures that do not significantly contribute to the observed patterns.

In the native assembled HIV-1 virus particle the Gag protein is oligomerized to form the outer shell of the virus. The individual Gag protein molecules have been shown to align in extended conformation that is ordered with other Gag protein molecules to form the concentric shell of the virus. Thus the HIV-1 Gag protein must undergo a major conformational change upon virus assembly. A detailed analysis of the microscopic interactions that are involved in this oligomerization process from the disordered/folded-over state may potentially lead to the development of therapeutic molecules to disrupt this process that may have value in the treatment of AIDS.

We have condensed the modeling, structure generation, and analysis algorithms into a graphical user interface called SASSIE. In addition to the analysis of structurally disordered proteins, the analysis package allows for the calculation of SAS (SAXS/SANS) and reflectivity profiles in real-time as the user manipulates the molecule(s) on the display. For example, in Fig. 3, we show the calculation of the SANS patterns of a single conformation of the Protein A described above.

In summary, we have developed methods and user-friendly graphical software to aid in the design and analysis of SANS experiments of disordered molecules. We have applied these methods to study the conformation of several proteins [1,3]. While the individual structural or ensemble solutions may not be unique, we have found that there is utility in knowing both what types of structures do and do not significantly contribute to a particular patterns. This knowledge allows for a more systematic analysis of both single and ensemble conformation structures that can exist in solution. Therefore, these methods will have important applications in the use of SANS to study the structure and function of disordered proteins.

REFERENCES

[1] S.A.K. Datta, J.E. Curtis, W. Ratcliff, P.K. Clark, R.M. Crist, J. Lebowitz, S. Krueger, and A. Rein, J. Mol Biol. (submitted).

[2] C.J. Oldfield, Y. Cheng, M.S. Cortese, C.J. Brown, V.N. Uversky, and A.K. Dunker, Biochemistry **44**, 1989-2000 (2005).

[3] D. Lee, *et al.*, Mol. Cell **22**, 423-430 (2006), D. Lee, *et al.*, Mol. Cell (in preparation).

Managing Disorder In Lipid Membranes

Micro-organization of lipids and cholesterol in cellular lipid membranes is thought to be an essential regulatory mechanism important for cell survival [1]. Improper distribution and organization of the various lipids and cholesterol in mammalian cell membranes can profoundly affect the initiation and progression of disease [2]. The organization of the hydrocarbon core of lipid bilayers, such as the chain ordering and orientation, is still rather unclear due to the lack of experimental quantitative data. The time and ensemble average of lipid terminal methyl groups in lipid bilayers is a key to answering many questions regarding the organization and motion of the acyl chains.

M. Mihailescu[1]
F. Castro-Roman[1]
R. Chamberlin[1]
D.L. Worcester[2]
D.J. Tobias[1]
S.H.White[1]

[1] University of California at Irvine Irvine, CA 92697

[2] University of Missouri at Columbia Columbia, MO 65211

Recent molecular dynamics simulation results [3], as well as nuclear magnetic resonance studies [4-6], suggest that some acyl chains undergo extreme bending motions, which bring the methyls close to the bilayer polar interface. The simulations were aimed at reproducing the complete structure of the DOPC (dioleoylphosphatidylcholine) bilayer reported by Wiener and White [7]. Excellent agreement was found between the simulated and experimental results for the transbilayer positions and widths of the carbonyl, glycerol, phosphate, and choline groups, but the results for the water and the double-bonds showed significant discrepancies with respect to the experiment. These differences, however, were not as dramatic as those observed between the simulated and experimental terminal methyl group width. A much wider terminal methyl distribution was predicted by the simulation (Fig. 1).

Neutron diffraction and specific molecular deuteration were therefore employed in this work to determine the methyl group distribution directly. All the neutron diffraction experiments were performed at the Advanced Neutron Diffractometer/Reflectometer (AND/R) [8] located at the NCNR. High-purity terminal-methyl deuterated oleic acid was synthesized and in turn was used to synthesize DOPC with deuterated terminal methyl groups (d6-DOPC).

Because of the much higher coherent scattering length of deuterium (^{2}H) compared with hydrogen, the d6-DOPC allowed direct determination of the mean transbilayer position and distribution of the label. This was accomplished through a direct comparison of the profiles obtained for d6-DOPC bilayers with those obtained for the hydrogenous form. A similar approach was used to determine the transbilayer distribution of the waters of hydration, except H_2O and ^2H_2O were used. The water distribution shows the extent of water penetration into the polar regions of the bilayer. As shown in Fig. 2, while the water distribution can be described by a Gaussian, the methyl distribution is characterized by a central Gaussian-shaped part accompanied by long tails that extend into the polar interface. The area under these tails accounts for ≈ 20 % of the total area under the total methyl profile.

These experimental results are broadly consistent with the prediction of the MD simulation [3]. An analysis of the simulation trajectories of the terminal methyl groups shows that about 30 % of the methyl groups eventually visit the polar membrane interface. Most visit the interface for 5 ns or so, but a small percentage stay much longer, 20 ns to 50 ns. We conclude that, though the hydrocarbon core of a lipid bilayer is organized into distinct domains, the acyl

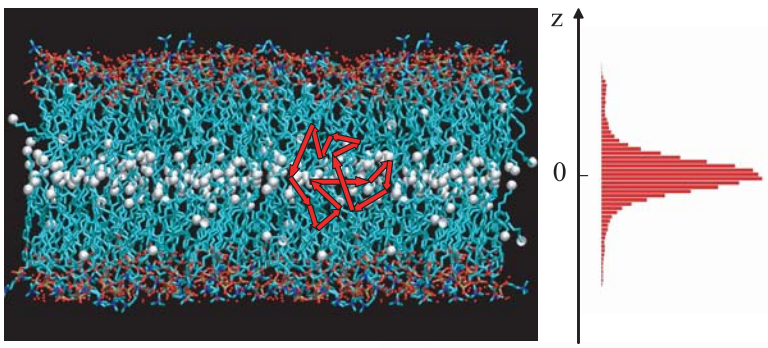

FIGURE 1:
Molecular dynamics simulation of a DOPC bilayer. CHARMM [11] force fields were used to simulate a bilayer constituted of dioleoylphosphatidylcholine (DOPC) lipids hydrated with 5.4 waters/lipid (66 % relative humidity). The terminal methyl groups are shown as white beads. The density distribution of the terminal methyl groups resulting from the simulation is shown in the bar graph on the right.

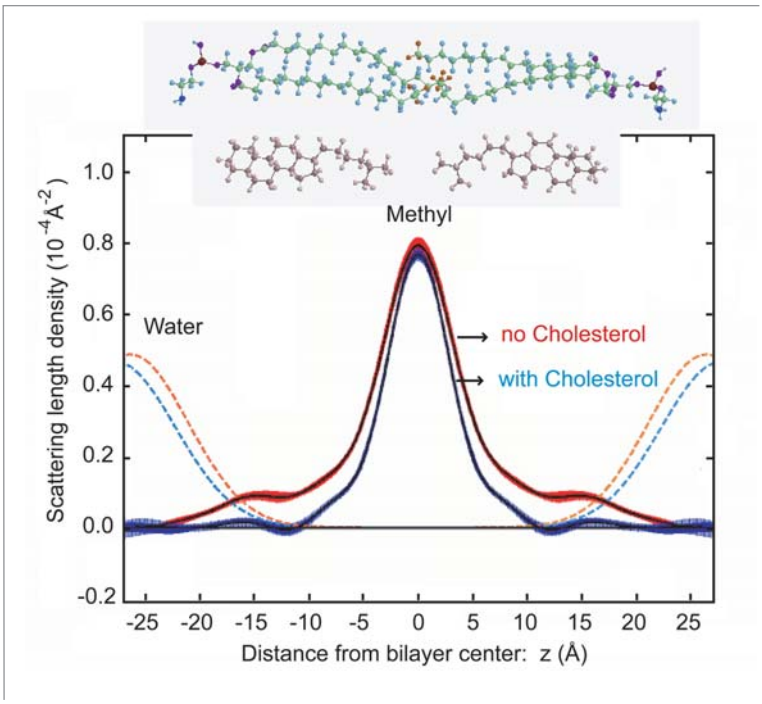

FIGURE 2:
Cholesterol effect on the chain order. The terminal methyl distribution in a pure DOPC bilayer (red) and a DOPC bilayer containing 33 % Cholesterol (blue), respectively, measured at 86 % relative humidity. The blue and orange dotted curves represent the water distributions with and without cholesterol, respectively. The top inset illustrates the general arrangement of two opposing DOPC lipids in a bilayer with the terminal methyls shown as orange beads. Cholesterol molecules (lower images) insert into each leaflet of the bilayer with their steroid ring part toward the water interface.

chain ends visit the water interface surprisingly often due to molecular disorder. One can speculate that this extreme form of disorder could be detrimental to membrane protein function. Many proteins involved in signaling, for example, apparently prefer to associate with ordered cholesterol-rich domains [9]. Cholesterol, acting as an important regulator of lipid bilayer organization may create optimal conditions for fast dynamical interactions of membrane receptors with their ligands during signaling.

How does cholesterol affect the terminal-methyl distribution? To answer this question, the experiment of Fig. 1 was repeated with cholesterol in the DOPC bilayer. Figure 2 reveals that cholesterol causes a general retraction of the chain ends, because cholesterol restricts the motion of the chains due to the rigidity of its steroid moiety. The retraction of the chain ends to the center of the bilayer in the presence of cholesterol is a dramatic demonstration of the ordering and stabilizing role of cholesterol in lipid bilayers. The results demonstrate unambiguously that, without the ordering effect of cholesterol, the terminal methyl groups can explore the space over the entire hydrocarbon region, and parts of the headgroup region. These are unprecedented direct experimental observations, which were stimulated by recent progress in neutron diffraction instrumentation for biological systems [8], molecular dynamics simulation procedures [3], and methods for molecular deuterium labelling [10].

ACKNOWLEDGMENTS

This study was carried out as part of the *Cold Neutrons for Biology and Technology* project supported by the NIH National Center for Research Resources (RR14812) and The Regents of the University of California. Additional support was provided by a grant from the National Institute of General Medical Sciences (GM68002).

REFERENCES

[1] K. Simons, and E. Ikonen, Nature **387**, 569 (1997).
[2] F.R. Maxfield, and I. Tabas, Nature **438**, 612 (2005).
[3] R.W. Benz, F. Castro-Roman, D.J. Tobias, and S.H. White, Biophys. J. **88**, 805 (2005).
[4] Z.-C. Xu, and S. Cafiso, Biophys. J. **49**, 779 (1986).
[5] P.E. Godici, and F.R. Landsberger, Biochemistry **13**, 362 (1974).
[6] D. Huster, and K.J. Gawrisch, J. Am. Chem. Soc. **121**,1992 (1999).
[7] M.C. Wiener, and S.H. White, Biophys. J. **61**, 434 (1992).
[8] *http://www.ncnr.nist.gov/programs/reflect/ANDR*
[9] L. Finegold, Ed., *Cholesterol in Membrane Models*, CRC Press, Boca Raton, FL (1993).
[10] R. Chamberlin, *et al.*, unpublished.
[11] S.E. Feller, *et al.*, Biophys. J. **73**, 2269 (1997).

Changes of Diphtheria Toxin Bound to Lipid Membranes

M.S. Kent[1]
H. Yim[1]
J.K. Murton[1]
S. Satija[2]
C.F. Majkrzak[2]
D.J. McGillivray[2,3]
M. Lösche[2,3]

[1] Sandia National Laboratories Albuquerque, NM 87185

[2] NIST Center for Neutron Research National Institute of Standards and Technology Gaithersburg, MD 20899-8562

[3] Carnegie Mellon University Pittsburgh, PA 15213

In order to control bacterial toxins, it is important to understand how they invade cells. The bacterial toxins diphtheria, tetanus, and botulinum invade cells through a process of high affinity binding, internalization via formation of a membrane-bound compartment within a cell (an endosome), and subsequent membrane penetration of the catalytic domain activated by a pH drop in the endosome [1,2]. Each of these toxins is composed of three domains: a binding domain, a translocation domain, and an enzyme or catalytic domain. The process of enzyme translocation across the membrane is not well understood with regard to the detailed conformational changes that occur at each step and whether the proteins act alone or as oligomers. A detailed understanding of the mechanism of enzyme translocation may enable means of inhibiting the harmful effects of these toxins. A particularly important long-term goal is to mitigate the lethality of botulinum neurotoxin, which is a potential terrorist or biowarfare agent. While botulinum, tetanus, and diphtheria are extremely potent toxins, they also have tremendous potential utility in medicine [1, 3]. Further development of new therapies and cancer treatments based on the re-engineering of the toxins will benefit greatly from a full understanding of the enzyme translocation mechanisms.

To begin to address these questions, we performed neutron reflectivity measurements for diphtheria toxin (DT) bound to Langmuir monolayers and to tethered lipid bilayers. We followed pH-dependent conformational changes of the toxin for several bulk DT concentrations. First we examined the structure of DT (CRM197, a nontoxic mutant) adsorbed to Langmuir monolayers of dipalmitoylphosphatidylglycerol (DPPG) at different bulk concentrations. Reflectivity data are shown in Fig. 1 for a DT concentration of 0.93 μM. In these measurements the lipids and the proteins were protonated and the subphase was a phosphate buffer solution in H_2O.

The measurements revealed pH ranges over which large conformational changes occurred as well as pH ranges over which little or no observable change occurred. The main stages of conformational change are shown in Fig. 1. The detailed structure of the adsorbed layer at each state will be unambiguously determined only when data for another contrast is obtained (d-lipids), and so the profiles in Fig. 1b should not be considered unique. However the qualitative trends are clearly evident in the data. While no adsorption could be detected at pH 7.6, strong adsorption occurred at pH 6.5, where the data are consistent with one principle layer of ≈ 80 Å. Adsorption continued to increase to pH 6.3, but with little change in the profile shape (not shown). Below pH 6.3, the adsorbed amount is nearly constant, and the changes in the reflectivity data indicate changes in conformation of the adsorbed protein. At pH 5.81 two layers are resolved. Some segments have penetrated into the lipid tails at this point. With a decrease in pH to 5.26 the layer adjacent to the lipid film became thinner and more concentrated in amino acids whereas the outer layer extended still further

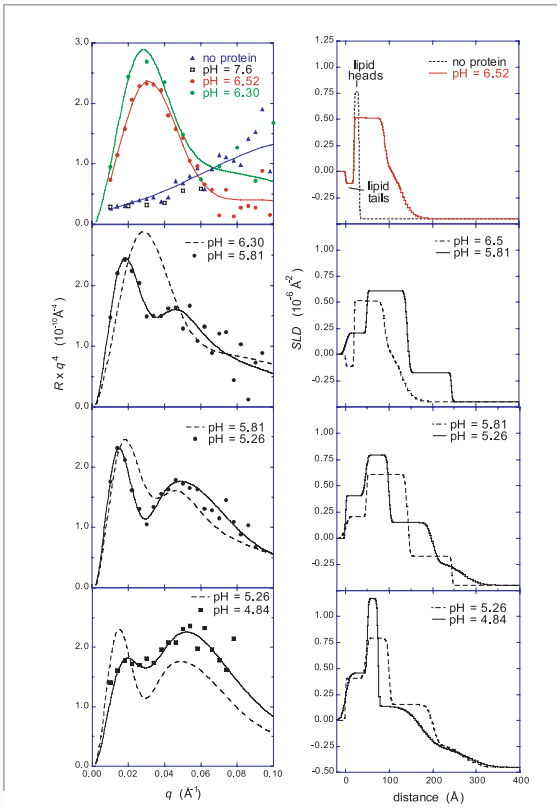

FIGURE 1:
Reflectivity and fitted scattering length density (SLD) profiles for DT binding to Langmuir monolayers of DPPG at 0.93 μM.

into the subphase. Upon further decrease in pH to 4.84, the inner layer became even thinner and more concentrated. The outer layer appeared to contract somewhat, but this cannot be determined unambiguously from the present data alone. Overall, with decreasing pH it appears that one domain, presumably the translocation domain, collapses and inserts into the membrane, whereas a second domain, pre-

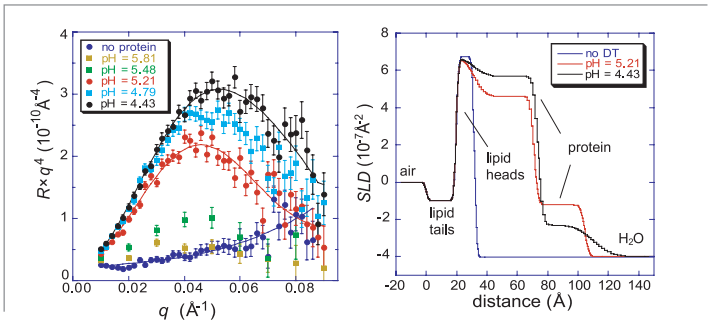

FIGURE 2:
Reflectivity and fitted SLD profiles for DT binding to Langmuir monolayers of DPPG at 0.31 μM.

sumably the catalytic domain, extends or unfolds. Analogous data at a bulk DT concentration of 0.31 μM are shown in Fig. 2. These data show several important differences relative to the data at 0.93 μM. First, no significant adsorption occurs until pH 5.5. Second, upon initial adsorption the layer is much thinner (≈ 50 Å) than that at 0.93 μM. This may indicate adsorption of monomers at 0.31 μM and adsorption of dimers at 0.93 μM. The data fitting suggests two layers for the protein structure and little penetration of amino acids into the lipid film, but these details must be confirmed by acquiring data for a second contrast. Third, with decreasing pH the peak simply moves to slightly higher q. A second peak never appeared at lower q as was the case for 0.93 μM. At 0.31 μM the layer remains thin and simply becomes more concentrated, in contrast to the results for 0.93 mM.

A series of measurements was performed for DT binding to tethered bilayers of dimyristoylphosphatidylglycerol (DMPG) from a 0.31 μM solution in D_2O phosphate buffer. The bilayers were tethered onto gold-coated wafers using the solvent exchange method [4]. The tethering molecule and tethering protocol were supplied by the Cold Neutrons for Biology and Technology group [4]. Some data for this series are shown in Fig. 3. Data were obtained to q_z = 0.3 Å^{-1}, but only the lower q_z range where the effect of the protein is most prominent is shown in Fig. 3. No adsorption occurred until pH = 5.6, at which point two layers are required to fit the data. With decreasing pH the layer expanded substantially, and three layers are required to fit the data at pH 5.2 and below. The strong expansion with decreasing pH is similar to the results observed for binding to Langmuir monolayers of DPPG at 0.93 μM and in contrast to the results for binding to DPPG at 0.31 μM. Strong insertion into the bilayer did not occur, as indicated by the low SLD of the lipid tail region throughout the series. However, the fitting suggests a small perturbation of the inner leaflet, which could indicate helices lying parallel to the headgroups in that layer. Such a result would be consistent with a structure proposed previously [5].

In conclusion, this initial work has revealed a rich variety of structures for DT bound to monolayers and tethered bilayers as a function of bulk concentration and pH. Much more work is needed to sort out this complex behavior. However, the present data reveal several important features and suggest a number of interesting hypotheses to be tested in future work. First, distinctly different interfacial structures of DT resulted at different bulk protein concentrations. This suggests that oligomerization of DT may impact the translocation process. Second, at 0.93 μM several distinct layers could be resolved within the adsorbed protein structure, with a large expansion of the outer layer and strong insertion of the inner layer occurring with decreasing pH. The large expansion may indicate unfolding of one of the domains, presumably the catalytic domain. Finally, at the lipid monolayer and bilayer membranes under the same conditions of concentration and pH, different adsorbed layer structures resulted. This could be due to the use of gel versus fluid phase lipids, the constraint of constant area in the bilayer case versus constant pressure in the monolayer work, or the obvious structural difference in one versus two leaflets.

Sandia is a multiprogram laboratory operated by Sandia Corporation, a Lockheed Martin Company, for the United States Department of Energy under contract DE-AC04-94AL85000.

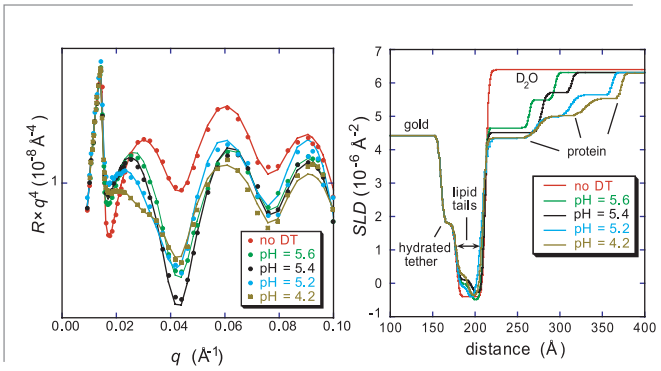

FIGURE 3:
Reflectivity and fitted SLD profiles for DT binding to tethered bilayers of DMPG at 0.31 μM.

REFERENCES

[1] A. Chenal, P. Nizard, and D. Gillet, J. Toxicology Toxin Reviews **21** 321 (2002).
[2] G. Lalli, S. Bohnert, K. Deinhardt, C. Verastegui, and G. Schiavo, Trends in Microbiology **11** 431 (2003).
[3] G. Schiavo, M. Matteoli, and C. Montecucco, Physiological Reviews **80**, 717 (2000).
[4] G. Valincius, D.J. McGillivray, W. Febo-Ayala, D.J. Vanderah, J.J. Kasianowicz, M. Lösche, J. Phys. Chem. B. **110** 10213 (2006).
[5] L. Senzel, M. Gordon, R.O. Blaustein, K.J. Oh, R.J. Collier, and A. Finkelstein, J. Gen. Physiol. **115** 421 (2000).

Functional Toxin Pores in Tethered Bilayers: Membrane Association of α-hemolysin

Several toxins form pores on the surface of susceptible cells that penetrate the membrane barrier. The pores allow unregulated ion diffusion across the membrane, leading to cell death (lysis). The protein α-hemolysin (αHL) is a toxin produced by the bacteria *Staphylococcus aureus* which is the subject of recent study, in particular because it shows promise for development as a stochastic biosensor for small ions [1], proteins [2], and large molecules, including DNA [3, 4]. Using a system that we previously designed and optimized, we have incorporated the protein into a robust biomimetic solid-tethered bilayer membrane (tBLM). Monitoring the incorporated pore's ion transport properties with electrical impedance spectroscopy, we verified that the toxin retains its natural functionality. This enabled the characterization of the interaction between the membrane and protein using neutron reflectometry (NR) at the Cold Neutrons for Biology and Technology's Advanced Neutron Reflectometer/Diffractometer (AND/R) [5].

D.J. McGillivray[1,2]
F. Heinrich[1,2]
M. Lösche[1,2]
I. Ignatjev[3]
G. Valincius[3]
D.J. Vanderah[4]
J.J. Kasianowicz[5]

[1] Carnegie Mellon University Pittsburgh, PA 15213

[2] NIST Center for Neutron Research National Institute of Standards and Technology Gaithersburg, MD 20899-8562

[3] Institute of Biochemistry and Vilnius Gedimino Technical University, LT-2600, Vilnius Lithuania

[4] Biochemical Sciences Laboratory National Institute of Standards and Technology Gaithersburg, MD 20899-8312

[5] Electrical and Electronic Engineering Laboratory National Institute of Standards and Technology Gaithersburg, MD 20899-8110

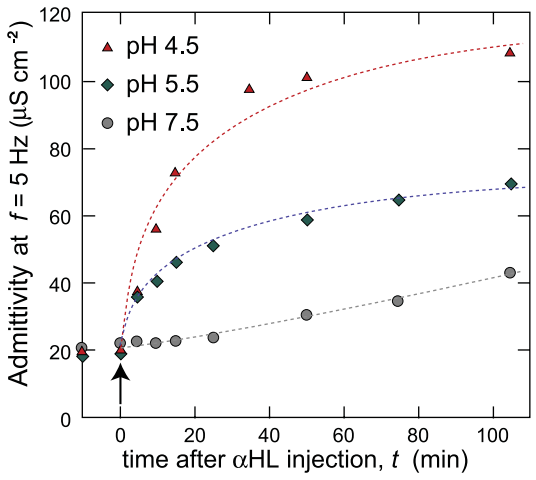

FIGURE 1:
Change in tBLM-covered electrode admittivity at f = 5 Hz, indicative of αHL incorporation, as a function of buffer pH.

The development of practical biosensors based on natural membrane proteins, such as αHL, is a subject of considerable effort. However, many problems must be overcome in the design of a system suitable for technical manipulation and measurement while preserving the biological activity of the protein. Natural cell membranes are intrinsically complex and disordered, a specific molecular architecture of lipids, sterols, proteins, glycolipids, etc., which drives the development of simpler model systems that are more amenable to preparation and characterization. Biosensors must also be robust, preferably reusable, and allow the behavior of the membrane-associated protein to be readily probed.

Using a common approach [6] we have addressed these issues in developing a solid-supported, tethered bilayer membrane (tBLM), which can be formed in a simple fashion on gold-covered surfaces, and which is surface-decoupled through a controllable hydrated polymer spacer [7]. The tBLMs were optimized for αHL incorporation using electroimpedance spectroscopy (EIS), a technique that is capable of rapidly probing the ion transport properties of the membrane pore. The increase in the tBLM admittivity is a function of the number of active pores incorporated (Fig. 1).

The electrical parameters of the toxin in the tBLM can compared with αHL in unsupported black lipid membranes, where they have been comprehensively studied [8]. Unfortunately, unsupported lipid membranes are limited for structural studies of the protein because of their limited size (≈ 10^2 mm^2), and unsuitable for biosensor development as they are fragile, being sensitive to shock and vibration. However, the comparison of the effects of polymers on pore conductivity [8] and response to pH [9], confirms that the toxin has retained its functionality in the tBLM, with the implication that the protein has also retained its native structure.

Using the optimized conditions, incorporation of αHL into the biomimetic tBLM occurs at a surface coverage large enough that its effect is readily observable in the raw neutron reflectivity (Fig. 2). These effects can be fitted using a simple layer model, which accounts for the most prominent feature of the protein, its large cap domain exterior to the membrane. In order to obtain more information about the interactions between the protein and the tBLM it was assumed that the in the tBLM the αHL channel x-ray crystal structure is valid.

The modeling of the NR shows that the protein spans the tBLM, with the stem penetrating ≈ 5 Å into the headgroup region on the inner leaflet (Fig. 3). The protein rim appears to interact strongly with the lipid headgroups, and even perturbs the hydrophobic tails, of the outer leaflet. This confirms the predictions of Song *et al.,* from analysis of the crystal structure that the cap region would be "probably in close proximity, if not in direct contact, with the membrane bilayer" [10]. The overhang between the membrane-penetrating stem domain and the rim domains is lined with basic and acidic residues, forming a suitable enclosure for the zwitterionic phospholipid headgroups, while the very edge of the rim contains a number of aromatic residues that can interact with the tail region of the lipid bilayer. The extension of the stem into the polar headgroup region on the far side of the membrane also stabilizes the band of charged residues that rings the bottom of the stem domain.

The NR modeling shows that the protein is incorporated into the bilayer at ≈ 36 % of the estimated maximum possible packing density of the protein. This packing density, ≈ 1 channel per 310 nm^2, is qualitatively similar to that observed in lysed cells [11]. The incorporation of such a large amount of the protein in the bilayer, without bilayer collapse, emphasizes the robustness of the solid-supported system.

The authors acknowledge useful discussions with Dr Hirsh Nanda. This work was supported by the NSF (grant nos. 0555201 and 0457148). ML and AND/R are supported, through the CNBT, by the NIH under grant no. 1 R01 RR14812 and by The Regents of the University of California. JJK is supported in part by the NIST Office of Law Enforcement Standards and a NIST Single Molecule Manipulation and Measurement Competence Award.

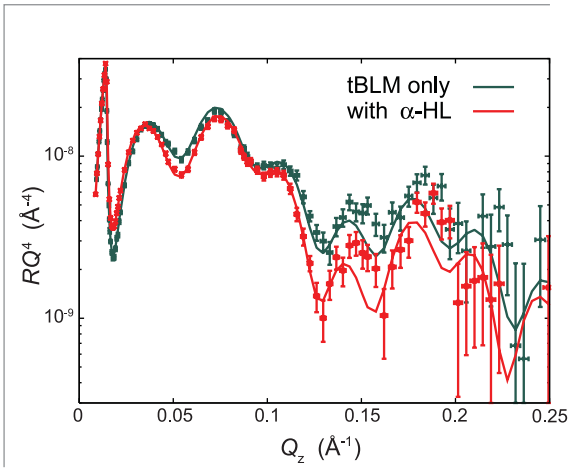

FIGURE 2:
NR and fitted models of the tBLM before and after αHL exposure, measured in D_2O. Fits were also constrained to other water contrasts (not shown).

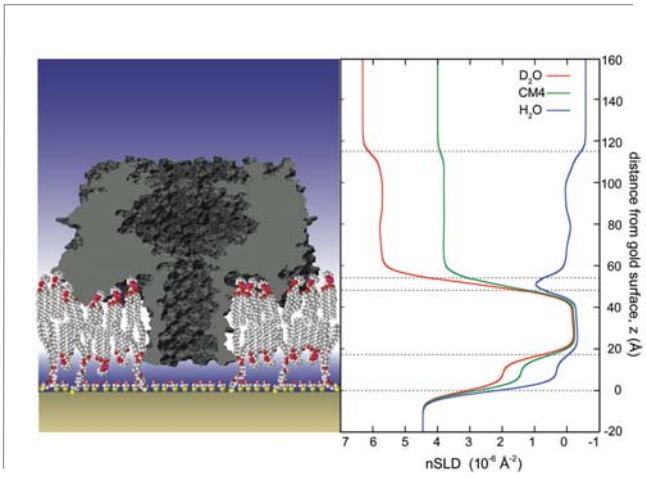

FIGURE 3:
(Left) A scaled cartoon of the functional αHL pore incorporated into a tBLM on gold, derived from the neutron scattering length density (nSLD) profile depicted on the right. (Right) The nSLD profile derived from simultaneous fitting of data measured in D_2O, H_2O and a D_2O:H_2O mixture (CM4) using the x-ray crystal structure of the protein. The combination of EIS and neutron reflectometry on a robust tethered membrane system has enabled the combined study of the structure and the functionality of a toxin with potential biotechnology applications. The functionality of the membrane is preserved in the biomimetic environment, and the neutron reflectometry reveals that the x-ray crystal structure is well-preserved in the membrane-bound form of the protein. The scattering also reveals details of the intimate binding between the protein and the membrane, confirming predictions based on the toxin structure.

REFERENCES

[1] S.M. Bezrukov, J.J. Kasianowicz, Phys. Rev. Lett. **70**, 2352 (1993).
[2] J.J. Kasianowicz, S.E. Henrickson, H.H.Weetall, B. Robertson, Anal. Chem. **73**, 2268 (2001).
[3] J.J. Kasianowicz, E. Brandin, D. Branton, D.W. Deamer, Proc. Natl. Acad. Sci. U.S.A. **93**, 13770 (1996).
[4] J.J. Kasianowicz, Nat. Mater. **3**, 355 (2004).
[5] J.A. Dura, D. Pierce, C.F. Majkrzak, N. Maliszewskyj, D.J. McGillivray, M. Lösche, K.V. O'Donovan, M. Mihailescu, U.A. Perez-Salas, D.L. Worcester, S. White, Rev. Sci. Instr. (2006), in press.
[6] B.A. Cornell, V.L.B. Braach-Maksvytis, L.G. King, P.D.J. Osman, B. Raguse, L. Wieczorek, R.J. Pace, Nature **387**, 580 (1997).
[7] G. Valincius, D.J. McGillivray, W. Febo-Ayala, D.J. Vanderah, J.J. Kasianowicz, M. Lösche, J. Phys. Chem. B **110**, 10213 (2006).
[8] S.M. Bezrukov, I. Vodyanoy, R.A. Brutyan, J.J. Kasianowicz, Macromolecules, **29**, 8517 (1996).
[9] J.J. Kasianowicz, S.M. Bezrukov, Biophys. J. **69**, 94 (1995).
[10] L.Z. Song, M.R. Hobaugh, C. Shustak, S. Cheley, H. Bayley, J.E. Gouaux, Science **274**, 1859 (1996).
[11] S. Bhakdi, J. Tranumjensen, Microbiol. Rev. **55**, 733 (1991).

Modeling Neutron Measurements on Friction Stir Welded Steel

The accurate prediction of the macroscopic deformation response of a material, especially in complex loading conditions, requires the consideration of the underlying microstructural changes. Simulation of polycrystal material deformation based on deformation of the constituent crystallites holds the promise to do just that — and to predict a wide range of properties both on the continuum and crystal levels. For the latter, neutron diffraction has the ability to probe crystallite deformation selectively, and to track certain changes in the crystallite orientation distribution during deformation, thus making it an ideal tool for in-situ experiments. The results of such a simulation-experiment comparison, based on elastoviscoplastic polycrystal plasticity implemented in a finite element framework, and applied to the deformation of a friction stir welded stainless steel show good agreement with both macroscopic and neutron diffraction data.

D.E. Boyce[1]
P.R. Dawson[1]
B. Sidle[1]
T. Gnäupel-Herold[2]
H.J. Prask[2]

[1] Cornell University
Ithaca, NY 14853

[2] NIST Center for Neutron Research
National Institute of Standards and Technology
Gaithersburg, MD 20899-8562

Design of modern high performance engineering components requires increased understanding of material response to a variety of loading conditions. However deformation processing of polycrystalline materials alters their microstructure and thus leads to changes in their macroscopic properties. Therefore, to adequately predict the response of the material to any loading condition, the ability to represent the microstructure of the modeled material is key. Multiscale models, such as polycrystal plasticity based models, possess the ability to do just that by modeling the response of the individual crystals and their interactions to accurately predict the macroscopic response. Moreover, they offer the rare possibility of direct comparison of simulated crystal deformation-derived quantities with those obtained by diffraction. The importance of this approach cannot be overstated because it offers the rare possibility of direct comparison of simulated crystal deformation-derived quantities with those obtained by diffraction.

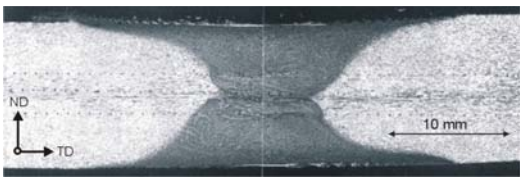

FIGURE 1:
Weld zone of an actual specimen [1]. The grain size in the weld zone (dark) is approximately 5 times smaller than in the base material (light). The heat affected zone is not visible but it extends about 1 mm away from the weld zone.

Such an approach is especially suitable for configurations in which nonuniform initial microstructures cause strength gradients and nonuniform deformations under applied load. The stainless steel friction stir weld samples studied here are prime examples with relatively large-grained base material where the size distribution peaks at 20 μm, followed by a narrow heat affected zone (HAZ) and a fine-grained weld zone (grain size peak at 4 μm) (Fig. 1). Also, the crystallite orientation distribution (ODF) in the base and weld material are different, with the base material having a weak rolling texture and the weld exhibiting a weak cube texture component.

The simulation methodology used here [1,2] accounts for the specimen heterogeneity in two ways: first, by assigning each finite element the orientation dependent elastic/plastic properties of a single crystal, and second, by a similar finite element formulation for the continuum scale, for which the element properties are derived from the first formulation. This is done using a polycrystal average based on a Taylor-like linking assumption. Furthermore, the polycrystal average is not uniform but depends on the location in the specimen to account for macroscopic property gradients. Model initialization parameters include the initial local ODFs and location-dependent slip system hardness. The latter is chosen such that it accounts for grain size differences using a Hall-Petch relationship. By tracking certain finite elements with single crystal properties throughout the deformation, it is possible to derive certain quantities such as orientation dependent strain and change in orientation due to rotations. With respect to the neutron experiments, the first is compared to (hkl)-dependent lattice strains, the second to changes in peak intensities. The peak width — which is very sensitive to dislocation density and therefore plastic strain — was not used for comparison because it was strongly affected by instrumental parameters. The deconvolution of instrumental effects on peak broadening will be the subject of future work.

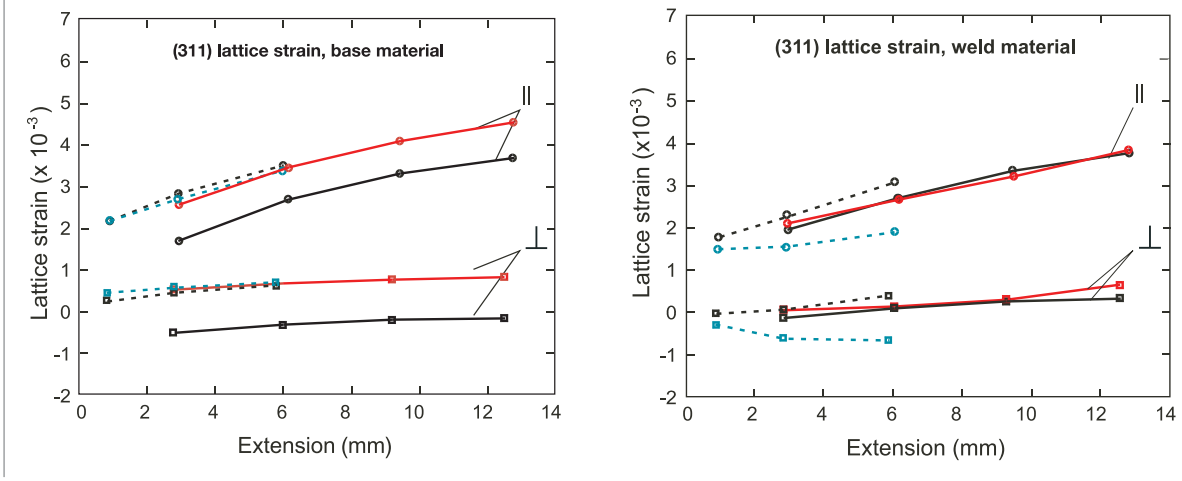

FIGURE 2:
Lattice strain comparisons for base and weld material. Solid lines are Specimen A. Dashed lines are Specimen B. Black lines are experiment. Colored lines are simulation. The uncertainties are 1 × 10^{-4}. The symbols || and ⊥ denote the scattering vector parallel and perpendicular to the applied stress direction.

The diffraction experiments were conducted at the BT8 Residual Stress Diffractometer. Several specimen geometries with different gage section shapes were used. The specimens were deformed in the TD-direction using a screw-driven load frame with 3-4 unloading episodes up to the final extensions > 12 mm, equivalent to more than 20 % strain. Diffraction peaks were collected for the weld and the base separately using appropriate sampling volumes depending on the specimen dimensions. Results are presented for two geometries: specimen A with 6.70 mm (ND) × 1.98 mm (RD) and specimen B with 3.94 mm (ND) × 3.34 mm (RD).

The elastic strains for grains in certain orientations can be inferred directly from the change in the peak positions in the neutron data. The results of both measurement and simulation for weld and base material are shown in Fig. 2.

The overall agreement between simulation and experiment is very good; if there is a difference then it is by a constant offset, which is most likely due to the reference d-spacing chosen to calculate the experimental lattice strains from the d-spacings. The results shown here along with results for other reflections [3] indicate that the change in slip system hardness is predicted correctly. Further evidence for the performance of the simulation is found in the good estimate of the overall hardening as seen in Fig. 3. This graph compares the experimental and predicted extension for a given applied force (at the start of an unloading episode), showing very good agreement overall.

The multiscale methodology used here for simulation performed well on the microscopic and on the macroscopic scale. It represents one of the rare attempts to reconcile microscopic and macroscale behavior in deformation and, as such, illustrates very well the complexity necessary for the success of such a model. As a payoff, the model is able to predict many parameters that were equally well matched by experimental results, such as specimen shape after deformation, crystallite orientation distribution function, and slip system strength. (For a full account, see Ref. 3.)

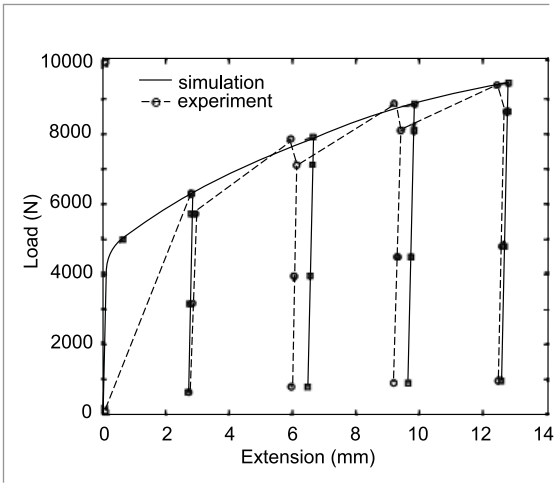

FIGURE 3:
Load-extension curve for specimen B for a series of loading-unloading cycles.

REFERENCES

[1] E. Marin, P. Dawson, Comput. Method Appl. Mech. Eng. **165**, 1 (1998).
[2] E. Marin, P. Dawson, Comput. Method Appl. Mech. Eng. **165**, 23 (1998).
[3] D.E. Boyce, P.R. Dawson, B. Sidle, T. Gnäupel-Herold, accepted for publication in Computational Materials Science.

High Resolution Depth Profiling in a Plane Strain Channel Section

The emergence of new materials has created additional challenges in the simulation of sheet metal forming with one problem being the accurate prediction of springback. The residual stresses responsible for springback can be measured non-destructively by two methods: synchrotron x-ray and neutron diffraction. Through improvements in methodology, neutron diffraction has made much progress in improving the spatial resolution down to 0.1 mm, thus enabling through-thickness stress measurements on sheets as thin as 0.8 mm.

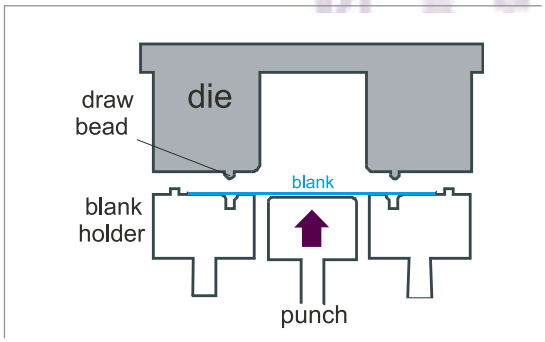

FIGURE 1:
Sketch of the channel draw (first stage).

Advances in steel production have brought about new kinds of steel, typically with substantial increases in strength without sacrificing formability. A significant fraction of steels is used in the form of sheet metal which is usually further processed through forming operations such as stamping and deep drawing. In order to ensure quality and cost effectiveness in the application of these processes for production parts, the simulation of various aspects of forming has become a key stage in the application of these materials. In order to characterize forming-related properties and to compare finite element codes used for the simulation, standardized tests are used in which specimens are deformed by large bi-axial strains using complex strain paths. For a number of years now there has been a good tradition of a strong collaboration between industrial concerns such as car companies and government/academia which entails participation in sheet metal forming benchmark tests.

One of the most recent tests is the "Numisheet 2005 Benchmark #3: Channel Draw/Cylindrical Cup" which is a two stage forming test consisting of a channel draw (Fig. 1), followed by a cup test on the channel side walls [1,2]. The concept was to verify not only the strain fields achieved during the two stage forming process, but also to test the ability of numerical models to predict both strain and stress fields during multi-stage forming processes. Accurate numerical results for the first stage forming and springback are essential to guarantee proper initial state variables for the subsequent stage simulation.

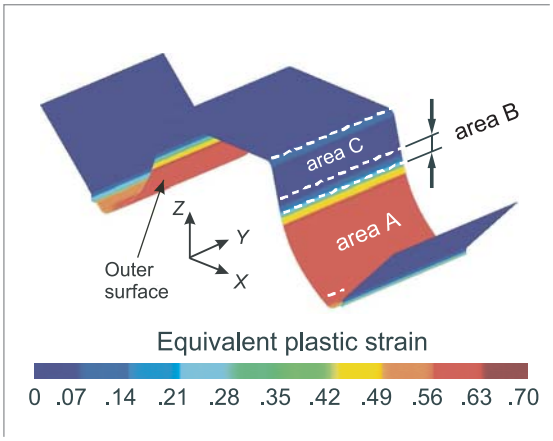

FIGURE 2:
Equivalent plastic strain distribution for a channel after springback with predicted strains. Neutron measurements were performed in area A.

The main parameter varied in this test was the draw bead penetration which essentially varies the magnitude of a bending/unbending cycle and acts as a pre-strain. The characteristic shape of a specimen with draw bead pre-strain is shown in Fig. 2. The curvatures of areas A, B and C (opening of the "U") represent the springback and it is caused by through-thickness stresses.

T. Gnäupel-Herold[1]
D.E. Green[2]
T.B. Stoughton[3]
M.A. Iadicola[4]
T. Foecke[4]

[1] National Institute of Standards and Technology NIST Center for Neutron Research Gaithersburg, MD 20899-8562

[2] University of Windsor Windsor, ONT, Canada N9B 3P4

[3] General Motors R&D Center Warren, MI 48090-9055

[4] National Institute of Standards and Technology Metallurgy Division Materials Science and Engineering Laboratory Gaithersburg, MD 20899-8553

The task of measuring stresses with a minimum of seven locations through walls of curved panels with thicknesses ≤ 1 mm poses a considerable challenge because it essentially requires neutron beams to be no more than 0.1 mm wide in the thickness direction. In order to keep the data acquisition time within ≈ 1 h, aperture configurations were chosen such that the total illuminated gage volume was > 1 mm^3. An example is shown in Fig. 3. It also illustrates the new concept of "shaped apertures" where for certain directions the incident beam aperture takes on the shape of the specimen, *e.g.,* by giving it a curvature. Depending on the aperture-to-specimen distance resolutions down to 0.1 mm can be achieved. It can be argued that, at the current state of beam optics for neutron diffraction, higher spatial resolutions < 0.1 mm become unfeasible due to beam divergence. Using this technique, a series of through-thickness measurements in area A of the channel sidewall was performed, the results of which are shown in Fig. 4.

The results of the neutron stress measurements highlight the long-known fact that springback decreases with higher draw bead penetration due to increased plastic deformation. In this forming experiment springback is characterized as the curvature of area A which generally decreases with increasing draw bead penetration. A similar tendency is visible in the stress distributions where the magnitude of compressive stresses at and near the outer surface (Fig. 2) increases with the draw bead penetration. However, the mechanical equilibrium of both stresses and bending moments appears to be severely affected, most likely by intergranular stresses as suggested by the stresses becoming overall compressive at higher draw bead penetrations and therefore higher levels of accumulated plastic deformation. Intergranular stresses arise because when stress is applied grains with a certain orientation yield at different stresses than neighboring grains (having different orientations). Upon release of the applied stress, grains with different orientations relative to each other are typically at different states of residual stress. This issue cannot be resolved from the data present; it requires either the averaging over different (hkl) or the tracking of the change in *d*-spacing on a specimen with a similar deformation path but without long-range residual stresses (such as through thickness stresses).

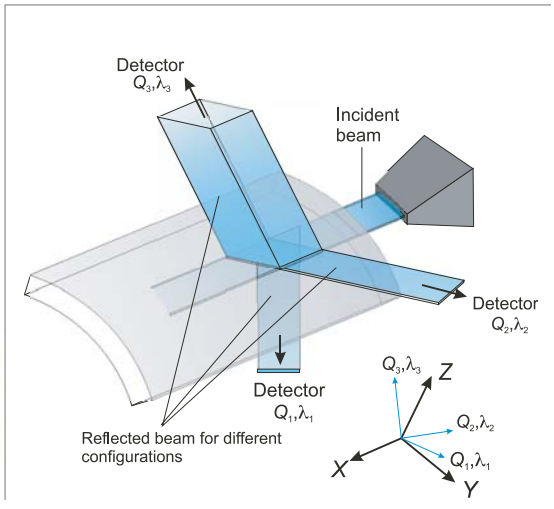

FIGURE 3:
High spatial resolution strain measurement on sheet metal specimens. The three reflected beams Q_1, Q_2, Q_3 represent three different orientations of the specimen.

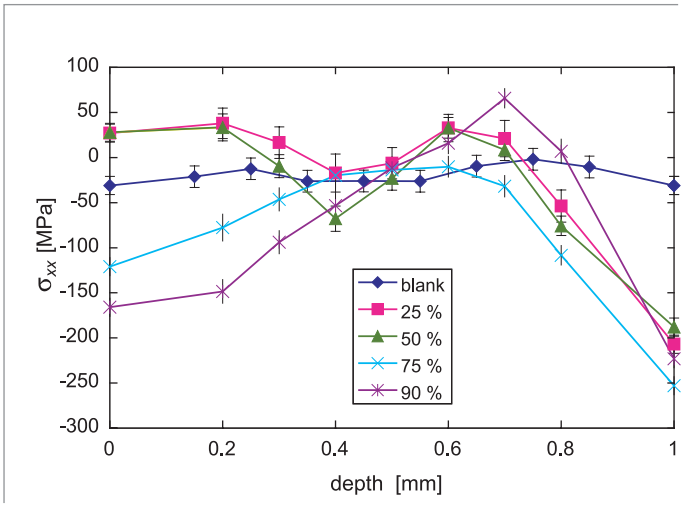

FIGURE 4:
Through-thickness residual stresses (*x*-direction), measured in area A.

The neutron diffraction results presented here, although incomplete, represent a step forward in the methodology of making strain measurements at the highest possible spatial resolution at moderate durations for data acquisition. The demand for such measurements arises where two requirements have to be met at the same time: that for spatial resolution ≈ 0.1 mm and that for good averages, *i.e.,* that the strains measured are representative for larger areas > 10 mm^2. The latter is problematic for synchrotron radiation diffraction but becomes a necessity in neutron diffraction due to the need for large gage volumes.

REFERENCES

[1] M.C. Oliveira, A.J. Baptista, J.L. Alves, L.F. Menezes, D.E. Green, T. Gnaeupel-Herold, M.A. Iadicola, T. Foecke, T.B. Stoughton, *Two Stage Forming: Experimental and FE Analysis*, Proceedings of International Deep Drawing Research Group (IDDRG), June 2006, Porto, Portugal.

[2] D.E. Green, T.B. Stoughton, T.Gnaeupel-Herold, M.A. Iadicola, T. Foecke, *Influence of Drawbeads in Deep Drawing of Plane-Strain Channel Sections*, Proceedings of IDDRG, June 2006, Porto, Portugal.

Neutron Imaging Facility at BT-2 and Tomography of Fuel Cells

Understanding and modeling the polymer electrolyte membrane (PEM) fuel cell is critical to optimally engineering these systems for consumer vehicles. Until recently, experimental data on the water distribution inside an operating fuel cell has been unavailable to researchers modeling these devices. However, the application of neutron radiography to image PEM fuel cells is now providing valuable insight into the details of where liquid water is formed during fuel cell during operation [1-4]. This is due to the unique ability of neutrons to penetrate the components of the fuel cell and yet still scatter strongly from hydrogen bound mainly in water molecules. Neutron radiography is sensitive to water at the level of 500 μg/cm^2 (depending on the conditions of the experiment). In order to make this capability widely available to the scientific and engineering communities in the United States, the NCNR in collaboration with the NIST Physics Laboratory Ionizing Radiation Division and General Motors Fuel Cell Activities has built a new facility for neutron radiography that incorporates extensive infrastructure support for fuel cell experiments.

D.L. Jacobson[1]
D.S. Hussey[1]
M. Arif[1]
J. Gagliardo[2]
J. Owejan[2]
T. Trabold[2]

[1] Ionizing Radiation Division
National Institute of Standards and Technology
Gaithersburg, MD 20899-8461

[2] General Motors Fuel Cell Activities
Honeoye Falls, NY 14472

The Neutron Imaging Facility is a thermal neutron radiography facility located at BT-2 at the NCNR. It is depicted in Figs. 1 and 2. It was built and commissioned in early 2006 after the previous Neutron Imaging Facility located at BT-6 was decommissioned. This new facility provides ample room to set up fuel cell experiments and provides fuel cell testing equipment, hydrogen, nitrogen, air, deionized water and chilled water inside the C100 confinement room. To do this, an extensive safety review was required to understand the hazards associated with the use of hydrogen gas, which is a potential hazard. After extensive computational fluid dynamics modeling using the NIST Fire Dynamics Simulator (FDS) [5] available through the Building and Fire Research Laboratory, it was determined that hydrogen accidentally or purposefully released in the room would turbulently mix with surrounding air lowering the concentration below the flammability limit (4 % in air by volume) at 1.2 m above the release point at the maximum release rate of 22.4 L/min. Throughout the room the concentrations were found to be 40 times lower than the flammability limit. This maximum release rate is assured because hydrogen used in the facility is produced by an electrolysis unit at a maximum rate of 18.8 L/min. No stored inventories of hydrogen are used, so the possibility of an accidental release of a large amount of hydrogen does not exist.

FIGURE 1:
Photo of the Neutron Imaging Facility at BT-2

Running fuel cells requires accurate control over the mass flow rate of hydrogen, air and nitrogen that are supplied to the fuel cell. In addition to controlling the mass flow, the humidity of the gases must also be controlled from 0 % to 100 % for a range of tempera-

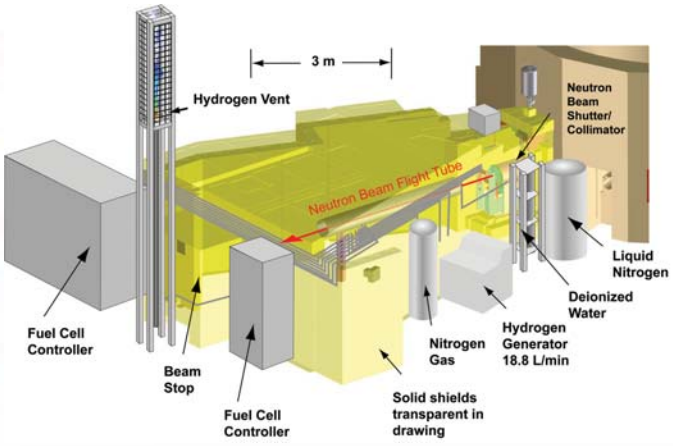

FIGURE 2:
Schematic drawing of the Neutron Imaging Facility at BT-2.

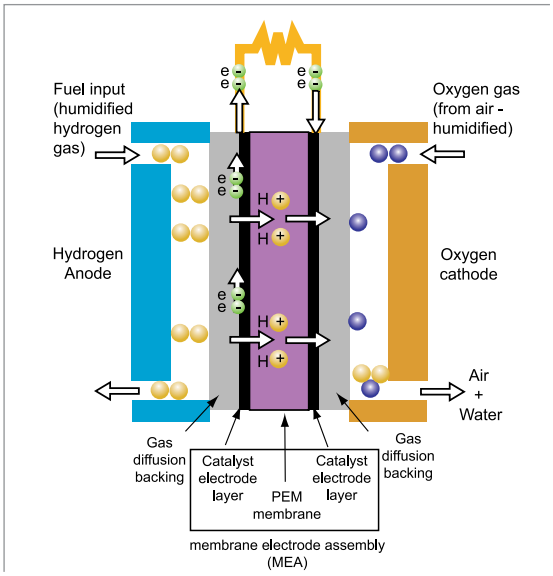

FIGURE 3:
Schematic diagram of the operation of a fuel cell.

tures. These functions are performed using a fuel cell test stand that incorporates accurate mass flow control for all gases used by the cell. In addition to mass flow control, an electronically controlled electrical load can also be applied. All of these features are automated to allow users to step through an extensive series of testing protocols.

Researchers using the facility are only required to bring fuel cells of their own design to the facility. A diagram of how a fuel cell works is shown in Fig. 3, and an example of a fuel cell designed for the purpose of demonstrating tomography is shown in Fig. 4. Fig. 4 also shows the reconstructed 3-D distribution of water in the fuel cell as measured at the facility. Both the anode and the cathode are distinguished, and the water distribution is shown in slices going from the anode to the cathode. Although water is produced on the cathode side during cell operation, these data demonstrate that in the steady state, unexpectedly, the anode side also remains wet. Water formed on the cathode may be transferred back to the anode through various mechanisms such as chemical back-diffusion and hydraulic pumping associated with the material properties of both the membrane electrode assembly and the gas diffusion media. In addition to these source mechanisms, gas flow (of hydrogen) is much less effective at removing water on the anode side compared to the cathode side where the much higher flow rate of air aids in water removal.

Although this new facility is optimized to provide state-of-the-art fuel cell systems control infrastructure for fuel cell developers, it is by no means limited to the study of fuel cells alone. This facility is open to a diverse user community through formal peer reviewed research proposals. Applications of neutron imaging to a variety of non-destructive and *in situ* investigations, from the dynamics of two phase fluid flows to geology and beyond are expected. Future developments for the facility will produce an order of magnitude increase in image resolution as well as a further expansion of fuel cell testing infrastructure to allow freeze-thaw testing of fuel cells.

REFERENCES

[1] R.J. Bellows, M.Y. Lin, M. Arif, A.K. Thompson, D. Jacobson, J. Electrochem. Soc. **146**, 1099 (1999).

[2] M.A. Hickner, N.P. Siegel, K.S. Chen, D.N. McBrayer, D.S. Hussey, D.L. Jacobson, and M. Arif, J. Electrochem. Soc. **153**, A902 (2006).

[3] P.A. Chuang, A. Turhan, A.K. Heller, J.S. Brenizer, T.A. Trabold, and M.M. Mench, in *FUEL CELL 2005, 3rd International Conference on Fuel Cell Science, Engineering and Technology*, pp. 31–37, ASME Proceedings, New York (2005).

[4] D. Kramer, J. Zhang, R. Shimoi, E. Lehmann, A. Wokaun, K. Shinohara, and G. G. Scherer, Electrochim. Acta **50**, 2603 (2005).

[5] NIST Fire Dynamics Simulator and Smokeview http://fire.nist.gov/fds/.

FIGURE 4:
Results from neutron tomography of a fuel cell running in the steady state. The upper part shows a 3-D drawing of the cell studied and the lower part displays the tomography data showing water in slice planes scanned from anode to cathode on either side of the membrane electrode assembly (MEA). A significant finding shown here is that water is observed distributed on both the anode and the cathode.

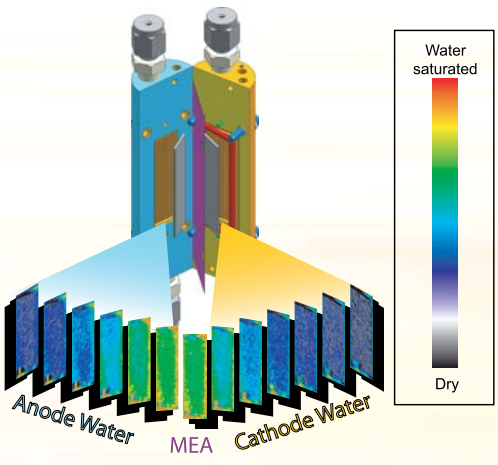

Development of New Cold Neutron Sources at the NCNR

P. Kopetka
R.E. Williams
J.M. Rowe

NIST Center for Neutron Research
National Institute of Standards and Technology
Gaithersburg, MD 20899-8560

The NCNR is planning an upgrade of the existing cold neutron source in addition to the proposed new cold source that is central to the expansion initiative announced in February, 2006. A large volume, liquid deuterium (LD_2) source is being developed as a replacement for the advanced liquid hydrogen source, Unit 2, installed in 2002. It will reduce the effective temperature of the source spectrum from 38 K to 28 K, providing gains of at least 50 % for wavelengths greater than 4 Å, and more than a factor of two for wavelengths greater than 9 Å. The second source, for the proposed west guide hall, is necessarily a small volume of liquid hydrogen (LH_2) installed in BT-7 that will have the same spectral shape as Unit 2, but about twice its brightness.

As in the past, the neutron performance and energy deposition in these sources is simulated using the Monte Carlo transport code, MCNP. Figure 1, a geometry plot of the MCNP model, shows locations of the proposed sources. During spring and early summer, design of the LH_2 source has taken priority in preparation for the NCNR Expansion Initiative Workshop, and the Facility Developments section of this report contains some information about it. The cryostat assembly of this source, including the source, insulating vacuum, helium containment and D_2O cooling jacket, must have a diameter of less than 150 mm, so the moderator vessel has an OD of 110 mm with an exit cavity of 80 mm ID, and an optimum LH_2 thickness of about 4 mm. A 300 W to 400 W nuclear heat load is expected, not including refrigerator load-line and condenser losses.

Unlike BT-7, the cryogenic beam port, CT, has a 560 mm ID thimble, offering space for a large volume of LD_2. A wide range of sizes and shapes have been analyzed, from a "small", 20 L LD_2 vessel (with several percent hydrogen) to the maximum size, 460 mm OD, 60 L, vessel that could be installed in CT with the required vacuum, He and D_2O jackets. The design will be optimized by varying the vessel diameter and length, the LH_2 content, if any, and the reentrant-hole width and depth, subject to the constraint of full illumination of the CTE (East) and CTW beam ports. Although the addition of H_2 can increase the brightness of an undersized LD_2 source, a large volume of LD_2 will produce the lowest effective temperature. This distribution will double the brightness of the longest wavelengths ($\lambda > 9$ Å), but will decrease the intensity at short wavelengths ($\lambda < 4$ Å). It is possible to adjust the shape of the LD_2 source spectrum, somewhat, by adding a small amount of hydrogen, and using a deeper reentrant hole.

A 35 L, 38 cm x 38 cm vessel was chosen as a compromise to mitigate the losses below 4 Å, and present a 2000 W to 2500 W heat load that could potentially be cooled by the existing refrigerator. Many choices concerning the LD_2 source were made last year, however, prior to the announcement of the expansion initiative. A new refrigerator may now be required because tests have shown that the capacity of our refrigerator is likely insufficient for the addition of the BT-7 source to the Unit 2 load. The new refrigerator would have the capability of cooling both the LD_2 and BT-7 sources. Full-scale mockups of both will be tested to ensure that each can be cooled with a naturally circulating thermosiphon; Unit 2 has operated very reliably in this mode.

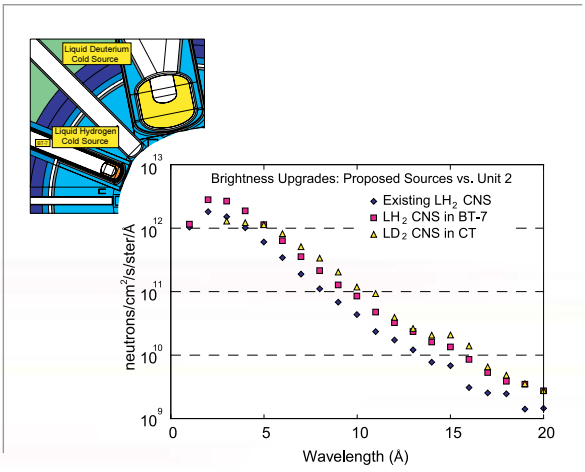

FIGURE 1: Left: northwest region of the NBSR core, showing the proposed cold neutron sources (CNS) upgrades. The existing LH_2 source in the CT port will be replaced by a large-volume, 35 L liquid deuterium source, and a new LH_2 source, just 0.75 L, will be installed in BT-7 for the West Guide Hall. Right: brightness comparison of the proposed CNS to Unit 2.

Improved Analysis of Short-lived Neutron Activation Products in Foods

TABLE 1:

LOD ranges and LOD/LOQ improvement factors for 16 elements in 40 TDS foods with Compton suppression INAA. NaCl content from < 0.005 % to 3.6 % mass fraction

Element Nuclide	keV	half-life	LOD range[a] mg/kg	average improvement factor vs. singles	number of foods[a] > LOD	> LOQ
^{128}I	443	25.0 min	0.029-1.35	1.38	17	9
^{24}Na	1368, 2754	15.0 h	0.68-26	1.28	40	40
^{38}Cl	1642, 2168	37.2 min	0.58-29	1.49	40	40
^{42}K	1524	12.36 h	9.6-636	1.76	39	34
^{56}Mn	847	2.58 h	0.0041-0.22	1.74	38	35
^{49}Ca	3084	8.72 min	1.13-169	1.74	40	37
^{27}Mg	844	9.46 min	1.5-99	1.71	40	38
^{66}Cu	1039	5.10 min	0.22-11.9	2.04	13	1
^{139}Ba	166	1.40 h	0.72-34	1.13	0	0
^{69m}Zn	439	13.76 h	19-880	1.36	1	0
^{80m}Br	616	4.42 h	0.056-2.8	1.57	38	23
^{28}Al	1779	2.25 min	0.60-18	1.12	15	7
^{51}Ti	320	5.76 min	0.83-32	1.28	3	3
^{52}V	1434	3.75 min	0.010-0.22	1.42	10	4
^{87m}Sr	388	2.81 h	1.0-53	1.36	2	0
^{76}As	559	26.32 h	0.28-15	1.50	0	0

[a] *e.g.*, for I, 9 of the 17 values > LOD were also > LOQ

The Total Diet Study (TDS), sometimes called the market basket study, is an ongoing FDA program that determines levels of various contaminants and nutrients in foods. FDA's Laboratory at the NCNR provides quality assurance instrumental neutron activation analysis (INAA) for this FDA's this program [1]. To improve element limits of detection [2] (LODs), especially for iodine (recently added to the TDS Program), a Compton suppression system that discriminates eliminates against strayscattered background photons by using a coincident signal from a scintillator surrounding the Ge detector, previously used for prompt gamma-ray activation analysis, was converted to an INAA instrument. Combined with new irradiation and counting procedures, LODs improved by up to a factor of 4 for 16 elements with short-lived neutron capture products (half-lives of about 2 min to 1.5 d). Iodine mass fractions (0.075 to 2.03) mg/kg) were measured in 17 of 40 TDS foods, with LODs ranging from (0.03 to 1.4) mg I/kg.

Irradiation facilities at the NCNR, accessed through "rabbit tubes" (RTs), are highly thermalized. To determine the best irradiation site for iodine measurements (*i.e.*, which location had the greater epithermal and fast neutron component), NaCl/KI standards were irradiated in central and peripheral positions in RT1 and RT4. The central RT1 location was chosen for irradiations because it showed a 16 % enhancement of iodine activity over Na and Cl activity vs. the RT4 peripheral location. Forty foods from the TDS Program, multielement standards, NaCl fluence/geometry monitors, blanks, and control portions (NIST SRMs 1572 Citrus Leaves, 1566a Oyster Tissue, 1549 Milk Powder, and 1846 Infant Formula) were analyzed. Irradiations were performed for 10 s with counts beginning 2 to 3 min later. Count times were 30 min, with spectral data also saved after an initial 10 min count time for analysis of the short-lived species.

Compton suppression INAA results for TDS foods were compared to previous INAA procedures that used RT4 with singles counting and a 9 % relative efficiency Ge detector. ("Singles" are data collected at the Ge detector without any reference to coincidence background reductions.) Figure 1 shows the effect of Compton suppression for iodine analysis compared to a simultaneous singles count for the same system and to the previous procedure. For all foods, an LOD improvement of about a factor of 4 was observed. Compton suppression results yielded LODs (and therefore limits of quantitation: LOQs) an average of 40 % lower than for singles data collected on the same system. A summary of the results for 16 elements in 40 TDS foods is given in Table 1. Greatest improvement is shown for Cu, K, Mn, and Ca. For control SRMs, agreement with certified values was found for all elements (All z-scores are < 1.7, where scores < 2 indicate agreement. A z-score of +1.7 corresponds to a measurement being 1.7 standard deviations above the mean [3].)

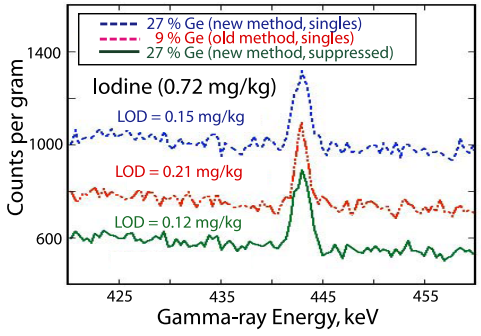

FIGURE 1.

Comparison of spectral data (30 min count times) for the iodine region for TDS food # 177 vanilla ice cream, light. Top and bottom spectra are from the present study (portion mass: 2.0 g). Middle spectrum is from previous work (portion mass 1.6 g).

REFERENCES

[1] Total Diet Study website: http://www.cfsan.fda.gov/~comm/tds-toc.html
[2] L.A. Currie, Anal. Chem. **40** (1), 586 (1968).
[3] M. Thompson, R. Wood, J. AOAC Int. **76**, 926 (1993).

D.L. Anderson
W.C. Cunningham

Elemental Research Branch (HFS-338)
U.S. Food and Drug Administration
College Park, MD 20740-3835

The New SRM 695 for Trace Elements in Multi-Nutrient Fertilizer

E.A. Mackey[1]
C.N. Fales[1]
R.R. Greenberg[1]
M.P. Kronise[1]
S. Leigh[1]
S.E. Long[1]
K.E. Murphy[1]
R. Oflaz[1]
J.R. Sieber[1]
M.S. Rearick[1]
L.J. Wood[1]
L.L.Yu[1]
P.F. Kane[2]
W. Hall[3]

[1] National Institute of Standards and Technology Analytical Chemistry Division Gaithersburg, MD 20899-8390

[2] Office of Indiana State Chemist Purdue University West Lafayette, IN 47907-2063

[3] The Mosaic Company Mulberry, FL 33860

During the past seven years, several states within the U.S. have enacted new regulations that limit the amounts of selected non-nutritive elements in fertilizers. Internationally, several countries including Japan, China, and Australia, and the European Union also limit the amount of selected elements in fertilizers. Fertilizer manufacturers and state regulatory authorities, faced with meeting and verifying these limits, need to develop analytical methods for determination of the elements of concern and to validate results obtained using these methods. A new Standard Reference Material, SRM 695 Trace Elements in Multi-Nutrient Fertilizer, was developed to help meet these new requirements. SRM 695 has recently been issued with certified mass fraction values for 17 elements, reference values for five elements, and information values for two elements.

Until 1998, U.S. fertilizer manufacturers generally were required to guarantee only the nutrient content of their products. However, the recent discovery of high levels of As in some iron-based fertilizer materials and high levels of Cd in some zinc-sulfate based fertilizer materials prompted some states to enact regulations limiting the amount of selected non-nutritive (potentially toxic) elements in fertilizer materials. To date, ten states have enacted or proposed regulations, and other states are expected follow suit. When the non-nutritive metals As, Cd Co, Hg, Mo, Ni, Pb, Se and Zn were first limited by regulation in the U.S., there were few certified reference materials (CRMs) available to assist manufacturing and regulatory laboratories in method development and measurement validation and none with matrices similar to typical agricultural or homeowner fertilizer blends. NIST worked with the members of the manufacturing and regulatory community to develop the new SRM 695 Trace Elements in Multi-Nutrient Fertilizer.

The experimental design for certification of SRM 695 was based on the use of two or more independent analytical techniques performed at NIST to provide values for all regulated elements and for the nutrient elements (B, Ca, Cu, Fe, K, Mg, Mn, N, and P) and other elements if possible. The approach relied on non-destructive analytical techniques, instrumental neutron activation analysis (INAA), prompt gamma ray activation analysis (PGAA) and x-ray fluorescence spectrometry (XRF) for most elements. A combination of inductively coupled plasma optical emission spectrometry (ICP-OES), ICP-mass spectrometry (MS) and cold vapor isotope dilution (CV-ID) ICP-MS was used for six elements.

The certified values for 17 elements and reference values for five elements are shown in Table 1, together with the analytical techniques used. Certified values for all elements except As and Hg are the unweighted means of results from two or three analytical methods. The uncertainty listed with each value is an expanded uncertainty about the mean, with coverage factor 2, calculated by combining a between-method variance with a pooled, within-method variance [1] following the ISO Guide to the Expression of Uncertainty in Measurement/NIST Special Publication 1297 [2,3]. Reference values were provided when only one analytical technique was used or in cases for which there was not a complete evaluation of all sources of uncertainty. (See Ref. 4 for a complete description of certified, reference and information values for SRMs.)

TABLE 2. CERTIFIED AND REFERENCE MASS FRACTION VALUES FOR SRM 695

Element	Methods Used	Certified Values
As	INAA	(200 ± 5) mg/kg
Ca	INAA, XRF	2.26 % ± 0.04 %
Cd	INAA, ID-ICP-MS	(16.9 ± 0.2) mg/kg
Co	INAA, XRF	(65.3 ± 2.4) mg/kg
Cr	INAA, XRF	(244 ± 6.2) mg/kg
Cu	ID-MS, ICP-OES, XRF	(1225 ± 9) mg/kg
Fe	INAA, PGAA, XRF	3.99 % ± 0.08 %
Hg	ID-MS	(1.955 ± 0.036) mg/kg
K	PGAA, XRF	11.65 % ± 0.13 %
Mg	INAA, XRF	1.79 % ± 0.05 %
Mn	INAA, PGAA, XRF	0.305 % ± 0.005 %
Mo	ICP, XRF	(20.0 ± 0.03) mg/kg
Ni	ICP, XRF	(135 ± 2) mg/kg
Pb	ICP-OES, XRF	(273 ± 17) mg/kg
Na	INAA, XRF	0.405 % ± 0.07 %
V	INAA, XRF	(122 ± 3) mg/kg
Zn	INAA, XRF	0.325 % ± 0.005 %

Element	Method	Reference Values
Al	INAA, XRF	0.61 % ± 0.03 %
B	PGAA	0.111 % ± 0.002 %
N	PGAA	13.9 % ± 0.04 %
P	XRF	7.2 % ± 0.1 %
Se	INAA	(2.1 ± 0.1) mg/kg

REFERENCES

[1] M.S. Levenson, D.L. Banks, K.R. Eberhardt, L.M. Gill, W.F. Guthrie, H.K. Liu, M.G. Vangel, J.H. Yen, N.F. Zhang, J. Res. NIST **105**, 571 (2000).
[2] Guide to the Expression of Uncertainty in Measurement, ISBN 92-67-10188-9, 1st Ed. ISO, Geneva, Switzerland, (1993).
[3] B.N. Taylor, C.E. Kuyatt, NIST Special Publication 1297, Guidelines for Evaluating and Expressing the Uncertainty of NIST Measurements Results 1994 Edition.
[4] W.E. May, T.E. Gills, R.Parris, C.M. Beck II, J.D. Fassett, R.J. Gettings, R.R. Greenberg, F.R. Guenther, G. Kramer, B.S. MacDonald, S.A. Wise, Definitions of Terms and Modes Used at NIST for Value-Assignment of Reference Materials for Chemical Measurements NIST Special Publication 260-136 (1999).

Residual Stress Determination as a Benchmark for a New Strain Measurement Technique

A friction stir welded (FSW) butt joint of 25.4 mm thick plates of aluminum alloys 7050-T7451 and 2024-T351 was used to measure cross-sectional maps of residual stresses using neutron diffraction and the recently developed contour method. Such thicknesses represent the state-of-the-art in FSW, and both measurement techniques validated that ability of FSW to produce low-magnitude stresses.

Friction Stir Welding (FSW) is a joining process which has seen remarkable growth in research, development and application in recent years. This is due to the ability of FSW to join a variety of alloys that can be dissimilar, difficult to weld in fusion welding, and to produce defect free welds with favorable strength properties without going through a melting process. FSW is heavily utilized in the aircraft industry where it offers the possibility of unitized structures made up of parts of different alloys and joined by FSW, thus reducing the cost associated with alignment and assembly.

A significant potential contributor to the durability behavior of FSW joints and surrounding material, however, will be the magnitude and distribution of residual stresses as an important influence on crack growth rates. Therefore, knowledge of residual stresses is crucial if accurate property measurements are required. Neutron diffraction is among the best-established methods for measuring sub-surface, tri-axial residual stresses which makes it useful as a comparative benchmark for other techniques such as the contour method [1]. The basic idea of this technique is as follows: One starts with an undisturbed part containing the stresses to be determined. Then, the part is cut in two which releases stresses and causes distortion on the cut surfaces of the two halves. The distortions can be measured very precisely by, for example, confocal laser ranging probes (used here).

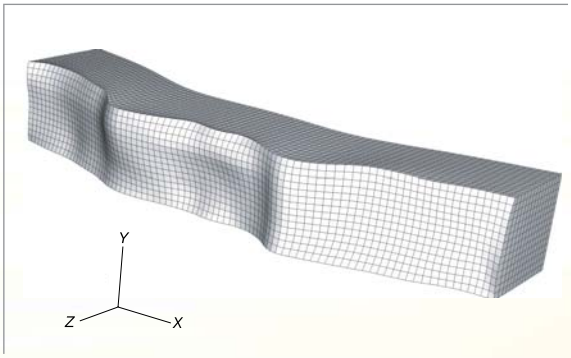

FIGURE 1:
Elastic finite element of half of test specimen with cut surface deformed into opposite of measured surface contour. Displacements magnified by factor of 1000. Part dimensions before the cut were 162(x) × 54(z) × 25.4(y) (in mm).

Using this numerical representation of the cut surface virtual stresses are applied to force the surface back into its original shape. The stresses applied in the last step are equal but opposite in sign to residual stresses before the cut.

Neutron measurements were performed along the x-direction (Fig. 1) close to the surfaces and in the mid-plane with 19 locations each (see Fig. 2 for spacing). After completing the neutron measurements the specimen was then cut by EDM and the contour analysis was performed (Fig. 1) using a mesh with approximately 30 locations per mm^2. The stresses obtained by the two methods are shown in Fig. 2.

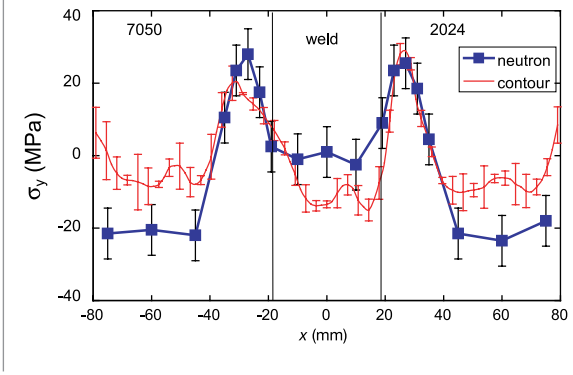

FIGURE 2:
Stresses normal to the mid-plane (Fig.1) at 12.7 mm depth.

There is a general agreement between the two methods, and the findings show the ability of FSW to produce welds with low stress magnitudes (6 % of the yield strength) even in structures as thick as 25 mm. The subtle differences can be attributed to variations of the unstressed d-spacing and to the presence of intergranular stresses. The first is caused by inhomogenous mixing of the two parent materials [2], creating mm-sized regions with differing d_0, the second is due to the fact that both parent plates were stretched by 1.5 % prior to welding, thus creating grain-orientation dependent stresses between grains. The contour method, while being destructive, demonstrates superior area resolution and it is independent of the two factors affecting the neutron measurements.

REFERENCES

[1] M.B. Prime, Journal of Engineering Materials and Technology **123**, 162 (2001).
[2] M.B. Prime, T. Gnäupel-Herold, J.A. Baumann, R.J. Lederich, D.M. Bowden, R.J. Sebring, accepted for publication in Acta Mat.

M.B. Prime[1]
T. Gnäupel-Herold[2]
H.J. Prask[2]
J.A. Baumann[3]
R.J. Lederich[3]
D.M. Bowden[3]
R.J. Sebring[3]

[1] Los Alamos National Laboratory
Los Alamos, NM 87545

[2] NIST Center for Neutron Research
National Institute of Standards and Technology
Gaithersburg, MD 20899-8562

[3] The Boeing Company
St. Louis, MO 63166-0516

DEDICATED BEAM LINE FOR COLD NEUTRON ANALYTICAL CHEMISTRY INSTRUMENTATION

Cold neutrons are used for analytical chemistry at the NCNR via the techniques of Neutron Depth Profiling (NDP) and Prompt Gamma Ray Activation Analysis (PGAA). In NDP, measurement of the energies of charged particles produced by sub-surface neutron capture by certain elements (B, Li, Cl, N, for example) provides a powerful, non-destructive method for determining concentration as a function of depth below a surface with sub-nanometer resolution. In PGAA, the enhanced probability of neutron capture that cold neutrons provide, translates into increased sensitivity to elements, such as hydrogen, that give off a characteristic gamma ray essentially instantaneously after absorbing a neutron. Specialized instruments for both techniques have been in operation at the NCNR for over fifteen years, often at locations with higher than ideal ambient background radiation. A dedicated beam line is now under development to alleviate this situation and provide a more accessible and flexible sample area for both instruments.

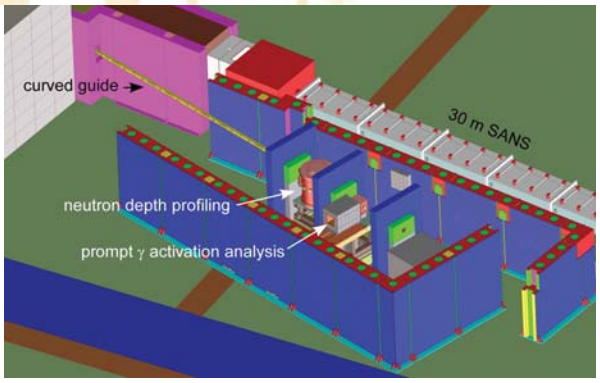

FIGURE 1:
Computer model of the analytical chemistry NDP and PGAA instruments as they will be configured on the new neutron bender to be installed on the NG-7 neutron guide.

The beam for the NDP and PGAA instruments will come for a curved supermirror-coated neutron guide (critical angle = 3x natural nickel) that will direct a 5 cm wide x 4 cm high portion of the NG-7 neutron guide away from the main beam line to provide a dedicated beam in a lower background environment for these instruments. The curved guide is preceded by a tapered section to increase the flux by compressing the beam size to 3 cm x 3 cm. The compressed beam will then pass through a segmental arc of 50 cm long guide sections to deflect the beam by 9°. Following the bend is 5 m of straight guide to homogenize the beam and increase the lateral separation from the main guide (see Fig. 1).

Figure 1 is a computer model of a typical configuration for the NDP and PGAA instruments at their future location on the supermirror bender. The bender provides sufficient space for the instruments to be well-shielded, particularly from stray radiation from the neighboring 30-m SANS instrument. In this design, the two instruments can operate in tandem, and are fitted with kinematic mounts that enable either instrument to be easily moved to the higher flux forward position. The enclosed space also provides an additional test station for future development.

The development of new stations for the NDP and PGAA instruments is part of a larger project to rebuild the NG-7 guide to incorporate an optical filter similar to that installed in the NG-3 guide in 2004 serving the CHRNS 30-m SANS instrument [1]. Installation of the optical filter, neutron bender, and the redesigned space and shielding for the NDP and PGAA instruments is scheduled for early 2007.

INSTALLATION OF THE HIGH INTENSITY MULTI-AXIS COLD NEUTRON SPECTROMETER (MACS) CONTINUES

The highly innovative multi-axis crystal spectrometer, MACS, is being installed in thermal neutron beam hall on the one beam line, NG-0, that views the present cold neutron source through a nearly 20 cm diameter beam port. This prime location, along with the instrument's 1400 cm^2 doubly focusing monochromator, promises to make MACS perhaps the highest flux cold neutron spectrometer in the world.

Nearly all of the beam conditioning components for MACS have been installed. These include a variable beam aperture to minimize background and to control wave vector resolution, a four-position radial collimation system to control energy resolution, and the translating, doubly focusing graphite monochromator. All of these components are housed in a helium-filled cask to further reduce background from air scattering.

FIGURE 2:
Collin Broholm, Johns Hopkins University, inspects the installation of the doubly focusing monochromator and other components that comprise the beam conditioning optics for the high intensity cold neutron multi-axis spectrometer, MACS.

Proceeding in parallel with the beam line installation has been the detailed engineering of the multi-axis analyzer/detector section of MACS. This section of the instrument, shown in the model in Fig. 3, comprises 20 identical detection channels, each with a vertically-focused, double graphite crystal analyzer and individual detector tubes, in a common shielded housing. Fronting the radial array of detection channels will be automatically interchangeable soller collimators and cryogenically cooled beryllium, beryllium oxide and graphite filters.

The first beam characterization measurements on MACS will take place before the end of 2006, while the multi-axis detection system is being assembled and tested offline. The first actual experiments with this system in place are planned for mid-2007.

PLANNING FOR EXPANSION OF THE NCNR

In support of the NCNR Expansion Initiative (see page 58) working groups have been formed to develop conceptual designs and implementation plans for all aspects of this initiative. One group, made up primarily of staff scientists and engineers, has been studying the feasibility and projected performance of the new cold source and neutron guide configuration that is at the heart of the expansion. Neutron transport calculations have been carried out in conjunction with structural and hydrodynamic calculations to arrive at a design that achieves high source brightness and optimal guide illumination. The source calculations indicate that a liquid hydrogen source located in a beam tube would have a higher brightness than the existing large volume source; perhaps by as much as a factor of two for 15 Å neutrons. The engineering calculations indicate that this performance can be achieved with the same type of passive thermo-siphon technology used with the present cold source, which has proven to be highly reliable and safe to operate. Figure 4 shows a computer model of one possible configuration of the new source in relation to the geometry of a beam tube.

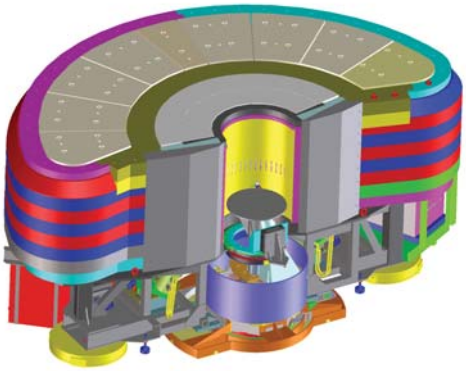

FIGURE 3:
Model of the assembly of components comprising the 6-axis sample positioning stage and the 20-channel crystal analyzer/detector section of the MACS spectrometer.

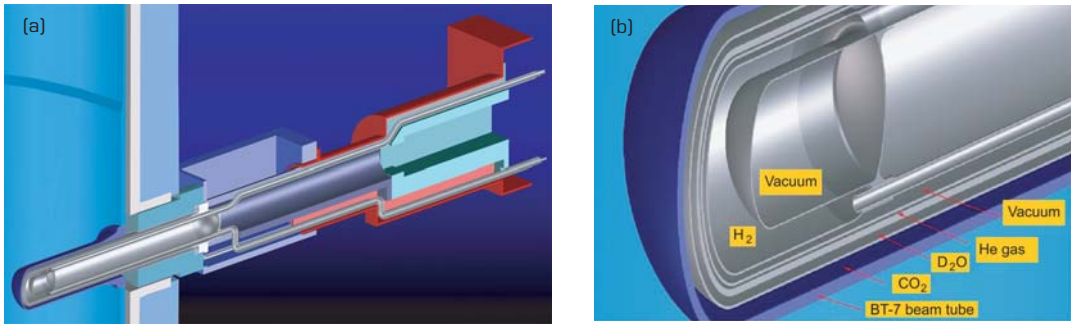

FIGURE 4:

a) A cross sectional view of one possible configuration of the new liquid hydrogen cold source within the BT-7 beam tube. b) Expanded view of the innermost section of the cold source showing the reentrant cylindrical geometry of the liquid hydrogen chamber.

A second working group has been gathering requirements for upgrades to utilities and other facility infrastructure that would be needed for a second neutron guide hall and associated office and laboratory space. Finally, a third group has been exploring and soliciting ideas for new neutron instrumentation and scientific opportunities that would be enabled given the expected performance characteristics of the new cold source.

IMPROVEMENTS IN SAMPLE ENVIRONMENT EQUIPMENT

A small but dedicated group of scientists and technicians at the NCNR develops and maintains an ever expanding variety of sample environment equipment for neutron scattering experiments. Recent additions to the inventory of available equipment include: Top Loading Closed Cycle Refrigerators (TLCCRs) capable of reaching temperatures from 5 K to 800 K; upgraded bottom-loading CCRs capable of reaching temperatures from 5 K to 325 K; an 11 T superconducting magnet; and a variety of "sample sticks" for use with the TLCCRs including ones customized for gas-loading, high pressure, and high voltage experiments.

Considerable information on the nanoscale structure of complex fluids can be derived from SANS measurements with the fluid subjected to controlled steady or oscillatory shear stresses. For some years the NCNR has had a couette shear cell which has been used extensively to explore shear-induced structural changes in colloids and microemulsions. More recently, a commercial research rheometer has been adapted for use on the SANS instruments to enable rheological data to be collected during scattering measurements. The rheometer cell also has cou-

FIGURE 5:

Research scientist Lionel Porcar (left) and mechanical engineer Jim Moyer (right) install the new alignment fixtures they designed to improve the accuracy and reproducibly of the coaxial alignment of the cup and bob on a commercial fluids rheometer for use on the NCNR's SANS instruments.

FIGURE 6:
A still from the recently produced "how-to" video on "How to Refill Liquid Helium" featuring sample environment technician Sarah McKenney in the starring role.

ette geometry and may be cooled or heated over a wide range (– 20 °C to 150 °C) by flowing nitrogen gas. The cell is also equipped with a vapor seal to inhibit sample evaporation without interfering with accurate rheological measurements, and an outer layer of trapped dry cover gas to prevent condensation when measurements are made at temperatures below the ambient dew point. The latest improvement in this apparatus is a reengineered alignment system (seen in Fig. 5) that allows the cell to be readily removed for cleaning and quickly realigned, thus saving considerable time when changing samples. Included in the cell support is a holder for precisely positioning beam-defining masks for measurements in both radial (beam intersects cylindrical rotation axis of cell) and tangential geometries (beam passes through gap between coaxial cylinders).

With the improved shear apparatus, measurements in both the velocity-vorticity (1-3) and the velocity gradient-vorticity (2-3) planes are possible. However, it is often desirable to make measurements in any direction between the velocity and velocity-gradient directions (1-2 plane). For this purpose a new type of couette shear cell has been designed, in collaboration with Prof. Norm Wagner at the University of Delaware, which allows the beam to be incident along the vorticity direction. The increased path length in this cell, 5 mm, for use with deuterated solvents, typically produces enough scattered intensity to allow a narrow slit (0.2 mm) to be scanned across the 1.5 mm gap between the coaxial cylinders to provide gap-resolved data — another new capability to distinguish wall effects on the observed scattering patterns. The prototype cell tested thus far is now being refined to be easier to use and more robust and will then be available for user experiments.

INSTRUCTIONAL VIDEOS FOR USERS

To further aid users in preparing for and running an experiment, the sample environment group has begun producing freely accessible instructional videos. The latest video, Fig. 6, takes the mystery out of refilling cryostats with liquid cryogens. This 6.58 minute movie is a comprehensive supplement to the short manual found in the equipment booklets. It can be used as either an introduction to or review of the art of refilling cryostats. The visual cues and directives are intended to help users avoid common pitfalls and make the refilling process generally less cumbersome. Available in multiple formats, the movie as well as other videos on loading and unloading sample cans can be found under the "How-to Videos" subsection of the NCNR's sample environment website: http://www.ncnr.nist.gov/equipment/ancequip.html.

REFERENCE

[1] Cook, J.C., Glinka, C.J., Schroder, I.G., Rev. Sci. Instrum. 76, 025108 (2005).

The NCNR Expansion Initiative

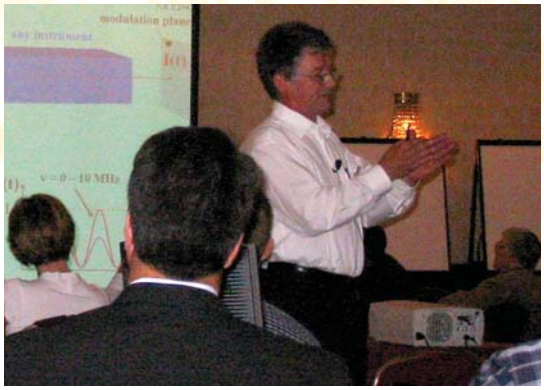

FIGURE 1:
Roland Gähler (ILL) presents his vision for next generation instrumentation and methods in a plenary session at the NCNR Expansion Workshop.

The proposed FY07 federal budget includes funding to begin a major, five-year project to expand the NIST Center for Neutron Research. Specifically, the project includes a second guide hall, new cold source, and five additional instruments. When completed, this project would result in a substantial expansion in cold neutron measurement capability at NIST and will allow us to exploit the latest neutron methods and open up new capabilities to the U.S. research community. The proposal is making its way through the congressional budget process as this report is being prepared.

To prepare for this exciting opportunity, we have been actively soliciting input from the neutron user community to collect ideas on what types of new instrumentation can best serve the future research needs of the U.S. research community. This effort began with an evening presentation during the March Meeting of the American Physical Society in Baltimore, shortly after the announcement of the FY07 budget, at which the NCNR Expansion Initiative was presented and followed by an informal discussion of potential instrumentation for the new facility.

A more substantial effort was a workshop held July 17-19, 2006 in Bethesda, Maryland attended by 125 neutron researchers from academia, industry and government. Participants at the workshop represented a broad research community, including experts in: neutron instrumentation, neutron detectors and optics, polymer science, complex fluids, biology, magnetic systems, small molecule systems, and nuclear physics. In order to stimulate an active forum for discussion of new neutron instrumentation and the associated scientific opportunities they provide, participants were asked to provide written contributions on research opportunities within their area of expertise in advance of the workshop. The meeting began with a general overview of the expansion project, a discussion of how the NCNR expansion fit into the larger U.S. neutron scattering picture, and a presentation of the expected performance of the new cold source. Later, members divided into working groups covering specific topical areas. These groups were charged with producing a summary document with suggestions in their respective areas, and the chairs of each group convened on the second day to summarizing these suggestions and discuss any cross-cutting issues. A final report, based on these documents gathered by a NIST team, is being used to guide planning for the enhanced facility so that it will best meet the needs of the community. The executive summary of this report is posted on the NCNR website.

FIGURE 2:
The Instrumentation Concepts breakout group at work at the NCNR Expansion Workshop. Around the table from left heading back: David Mildner (NCNR), Roland Gähler (ILL), Mike Rowe (NCNR), Lee Robertson (ORNL), Georg Ehlers (ORNL), Igor Zaliznyak (BNL), John Copley (NCNR), Larry Passell (BNL), and Don Pierce (NCNR).

Operations

FIGURE 3:
Engineer Tony Norbedo places a test module designed to monitor thermal shield performance.

This year, the NIST reactor operated for 266 full power (20 MW) days or 99 % of the scheduled time. A typical operating year consists of seven cycles. A cycle consists of 38 days of continuous, full-power operation followed by 11 days for maintenance, refueling, and startup preparations. The facility is operated under a license from the U.S. Nuclear Regulatory Commission (NRC). Currently, an application for renewal of the license is under consideration by the NRC, and regulations allow for continued operation under the original license until there is a final decision on the application.

FIGURE 4:
Operator Ricky Sprow testing a portion of a newly installed condensate removal system.

A variety of important projects were completed this year despite the limited time available for maintenance due to the full operating schedule. The RT2 in-core pneumatic sample assembly was replaced and sample testing is underway to determine the exact conditions existing in the assembly tip for sample irradiations prior to initiating routine use of this facility. A detailed engineering study was completed for the replacement of the thermal column tank. Current efforts focus on developing detailed plans and equipment for the installation of the new tank. The thermal shield cooling system was fit up with new diagnostic equipment to gauge the effectiveness of changes to the system, including pump modifications and the recent addition of a helium gas blanket for the storage tank water. Major upgrades to the building ventilation system were completed with the replacement of filters, fans, and controllers using the newest technology to maintain flows and pressures. All electrical switchboards in the facility were thermographically inspected and characterized. These tests are necessary for the future upgrades to the building's electrical equipment.

Our engineering team added both an experienced electrical engineer and mechanical engineer to its staff. For the first time, reactor operator biennial requalification was conducted over four separate training periods instead of one. This eliminated the need to shutdown the facility to retrain the operations staff. The two operator candidates hired last year are expected to be licensed by the NRC soon and recruiting efforts continue to fill expected vacancies. The NCNR continues to work closely with NIST, local, county, and federal officials in a variety of areas including environmental management, emergency response, and security.

Awards 2006

NIST GRANTS THE 2006 STRATTON AWARD TO JEFFREY LYNN

Jeff Lynn of the NCNR is being awarded the 2006 Samuel Wesley Stratton Award by NIST for his neutron scattering work on materials that display colossal magneto-resistance. The Stratton Award, established in 1962, recognizes an unusually significant research contribution to science or engineering that merits the acclaim of the scientific world and supports NIST's objectives. This award consists of an engraved plaque and a $5,000 honorarium.

TANER YILDIRIM RECEIVES THE 2006 NSSA SCIENCE PRIZE

Taner Yildirim of the NCNR is the recipient of the 2006 Science Prize of the Neutron Scattering Society of America with the citation: *"For his innovative coupling of first principles theory with neutron scattering to solve critical problems in materials science"*. The Neutron Scattering Society of America (NSSA) established the Science Prize to recognize a major scientific accomplishment or important scientific contribution within the last five years using neutron scattering techniques. The prize and a $2,500 honorarium were awarded at the June 2006 ACNS meeting in St. Charles, IL.

JOHN BARKER RECOGNIZED WITH NIST SAFETY AWARD

John Barker of the NCNR was awarded the NIST Safety Award as part of a group award for superior accomplishments in implementing NIST-wide safety activities as articulated in the NIST Safety Plan, and for demonstrating outstanding leadership by successfully coordinating these activities among various NIST organizational units. The Award consists of a framed certificate and an honorarium.

SIGMA XI HONORS YAMALI HERNANDEZ

Yamali Hernandez, chemist at the NCNR, has been selected to receive this year's NIST Chapter of Sigma Xi Award for *Outstanding Service Support of Research Scientists*. This award recognizes her sustained excellence of service to the users of the NIST Center for Neutron Research. She received the award at the annual NIST Chapter Sigma Xi Banquet in May.

DEPARTMENT OF COMMERCE BRONZE MEDAL AWARDED TO ROBERT DIMEO

Rob Dimeo of the NCNR, who is currently serving at U.S. Office of Science and Technology Policy, was awarded the Department of Commerce's Bronze Medal "*For his leadership in the development of the DAVE suite of neutron scattering data reduction, analysis, and visualization software tools that are widely used at NIST and at neutron research centers around the country*" in December, 2005. The Bronze Medal recognizes superior performance characterized by outstanding or significant contributions which have increased the efficiency and effectiveness of NIST. It is the highest honorary award granted by the NIST Director.

BRIAN TOBY GRANTED DEPARTMENT OF COMMERCE BRONZE MEDAL

Brian Toby, who recently moved from the NCNR to the Advanced Photon Source, Argonne National Laboratory, was awarded the Department of Commerce's Bronze Medal "*For the development of a suite of software programs for powder diffraction crystallography*" in December, 2005. The Bronze Medal recognizes superior performance characterized by outstanding or significant contributions which have increased the efficiency and effectiveness of NIST. It is the highest honorary award granted by the NIST Director.

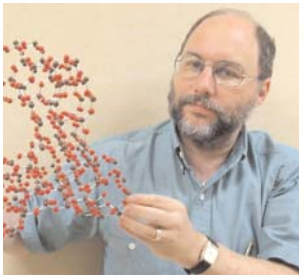

CHRISTOPHER SOLES OF THE NIST POLYMERS DIVISION AWARDED A PECASE

Chris Soles of NIST Polymers Division who is a frequent user of the NCNR facility, has received a Presidential Early Career Awards for Scientists and Engineers, the nation's highest honor for professionals at the outset of their independent research careers. The honor was presented at the White House in July in a ceremony presided over by John H. Marburger III, Science Advisor to the President and Director of the White House Office of Science and Technology Policy.

DIVYA SINGH WINS NSSA THESIS RESEARCH PRIZE

Divya Singh, a graduate student at Johns Hopkins with Robert Leheny and a guest researcher at the NCNR, has been awarded the NSSA Prize for Outstanding Student Research by the Neutron Scattering Society of America at the June 2006 meeting of the ACNS in St. Charles, IL. The prize recognizes neutron scattering research that has been performed as part of a thesis or degree. The award consists of a certificate, plaque, and $500. The presented work, based on collaboration with NCNR and ORNL scientists, is entitled "*Self-assembly models for binary phospholipid mixtures: Understanding bicelle formation*".

HUI WU AWARDED THE S. J. STEIN PRIZE AT THE UNIVERSITY OF PENNSYLVANIA

Hui Wu, a guest researcher at the NCNR, has been selected to be the co-recipient of the 2006 S. J. Stein prize awarded to a Ph.D. degree recipient *"for superior achievement in the field of new or unique materials or applications for materials in electronics"* by the Department of Materials Science and Engineering at the University of Pennsylvania. The recognition includes $500 and a certificate. Hui worked with Peter Davies at Penn.

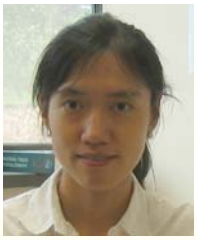

XUE HAN WINS STUDENT RESEARCH AWARD FROM THE BIOPHYSICAL SOCIETY

Xue Han, a graduate student with Kalina Hristova of the Department of Materials Science and Engineering at Johns Hopkins University, won the Student Research Achievement Award in "Membrane structure and assembly" at the meeting of the Biophysical Society in February. The title of his poster, based on measurements using AND/R at the NCNR, was "*Determining FGFR3 Transmembrane Domain Topology Using Neutron Diffraction*".

MATTHEW PAOLETTI RECEIVES THE APS 2005 APKER AWARD

Matthew Paoletti, physics graduate of Bucknell University and currently a physics graduate fellow at the University of Maryland at College Park in nonlinear dynamics, was the recipient of the 2005 LaRoy Apker Award for *"Experimental Studies of the Effects of Chaotic Mixing on an Advection-Reaction-Diffusion System"* presented at the March meeting of the American Physical Society. Matt spent two summers at the NCNR as a SURF student characterizing and developing bioencapsulated enzymatic proteins.

Serving the Science and Technology Community

The mission of the NIST Center for Neutron Research is to assure the availability of neutron measurement capabilities to meet the needs of U.S. researchers from industry, university and other Government agencies. To carry out this mission, the NCNR uses several different mechanisms to work with participants from outside NIST, including a competitive proposal process, instrument partnerships, and collaborative research with NIST.

THE CURRENT PAC MEMBERS ARE:

- Kenneth Herwig (Oak Ridge National Laboratory, chair)
- Andrew Allen (NIST Ceramics Division)
- Collin Broholm (Johns Hopkins University)
- Ken Chen (Sandia National Laboratories)
- Mark Foster (University of Akron)
- Michael Kent (Sandia National Laboratories)
- Ramanan Krishnamoorti (University of Houston)
- Joanna Krueger (University of North Carolina at Charlotte)
- Young Lee (Massachusetts Institute of Technology)
- Robert Leheny (Johns Hopkins University)
- Lee Magid (University of Tennesssee, Knoxville)
- Janna Maranas (The Pennsylvania State University)
- Dawn Sumner (University of California, Davis)
- Michael Toney (Stanford Synchrotron Radiation Laboratory)
- John Tranquada (Brookhaven National Laboratory)

PROPOSAL SYSTEM

A significant fraction of the time on NCNR instruments is made available through a competitive, peer-review proposal process. The NCNR calls for proposals approximately twice a year. Proposals are reviewed at several different levels. First, expert external referees evaluate each proposal on merit and provide us with written comments and ratings. This is a very thorough process where several different referees review each proposal. Second, the proposals are evaluated on technical feasibility and safety by NCNR staff. Third, we convene our Program Advisory Committee (PAC) to allocate the available instrument time. Finally, using the results of the external peer review and their own judgment, the PAC makes recommendations to the NCNR Director on the amount of beam time to allocate to each approved experiment. Approved experiments are scheduled by NCNR staff members in consultation with the experimenters.

PARTNERSHIPS

The NCNR may form partnerships with other institutions to fund the development and operation of selected instruments. These partnerships, or "Participating Research Teams", may have access to as much as 75 % of the available beam time on the instrument depending on the share of total costs born by the team. A minimum of 25 % of the available beam time is always made available through the NCNR proposal program to all users. Partnerships are negotiated for a fixed period (usually three years) and may be renewed if there is mutual interest and a continued need. These partnerships have proven to be an important and effective way to expand the research community's access to NCNR capabilities and have been very successful in developing new instruments.

COLLABORATION WITH NIST

Some time on all instruments is available to NIST staff in support of our mission. This time is used to work on NIST research needs, instrument development, and promoting the widespread use of neutron measurements in important research areas, particularly by new users. As a result of these objectives, a significant fraction of the time available to NIST staff is used collaboratively by external users, who often take the lead in the research. Access through such collaborations is managed through written beam time requests. In contrast to proposals, beam time requests are reviewed and approved internally by NCNR staff. We encourage users interested in exploring collaborative research opportunities to contact an appropriate NCNR staff member.

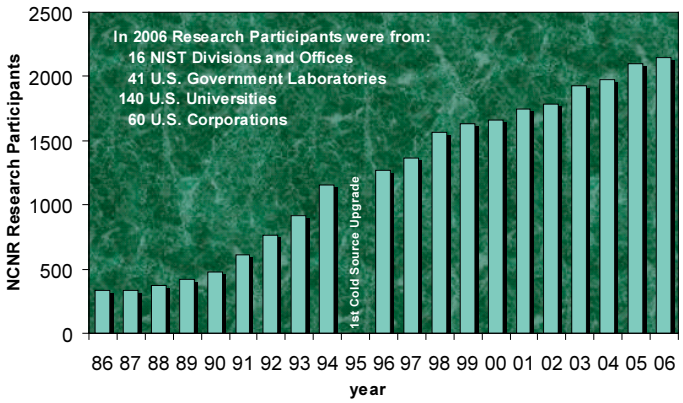

FIGURE 1:
Research Participants at the NCNR 1986-2006

RESEARCH PARTICIPATION AT THE NCNR

The NCNR continued its strong record of serving the U.S. research community this year. Over the 2006 fiscal year, 2,143 research participants benefited from use of the NCNR. (Research participants include users who come to the NCNR to use the facility as well as active collaborators, including co-proposers of approved experiments, and co-authors of publications resulting from work performed at the NCNR.) Research participants represented 241 external institutions, including 140 U.S. universities, 41 national laboratories, and 60 U.S. industries. The NCNR is a national facility, with participants from 40 states, DC, and Puerto Rico.

2006 NCNR PROPOSAL PROGRAM

Two calls in the past year resulted in the submission of 600 proposals, a record number, of which 376 were approved and received beam time. The oversubscription, *i.e.*, the ratio of days requested on all proposals to the days available, was 1.9 on the average, but as high as 2.9 for specific instruments in one call. Proposal demand has grown constantly since the NCNR first began accepting proposals in 1991, and has doubled in the past six years. The following table shows the data for several instrument classes:

IMAGING FACILITY JOINS USER PROGRAM

In the latest call for proposals, 25 % of the time available on the new Neutron Imaging Facility was offered to the general user community. Twelve proposals were submitted, yielding an oversubscription of about a factor of two in terms of instrument days. These proposals covered a wide range of topics from archeology to mechanical engineering, and we foresee that the demand for, and the diverse applications of, neutron imaging will continue to grow in coming years.

USER GROUP HOLDS FIRST ELECTION

The NCNR User Group (NUG) provides an independent forum for all NCNR users to raise issues or concerns to the NCNR. The NUG works through its executive officers to carry out this function. In December 2005, it held its first online election of officers. The winning candidates are Kalina Hristova (Johns Hopkins University), Stephan Rosenkranz (Argonne National Laboratory), Roger Pynn (Indiana University), and Goran Gašparović (formerly at MIT, now at NIST). Other current members of the NUG executive are Tonya Kuhl (University of California, Davis), Robert Leheny (Johns Hopkins University), and Nitash Balsara (University of California,

TABLE 1

Instrument class	Proposals	Days requested	Days allocated
SANS and USANS	288	979	487
Reflectometers	66	490	399
Spectrometers	234	1607	741
Imaging	12	65	35
TOTAL	600	3141	1662

FIGURE 2:
NCNR guest researcher Saibal Basu (B.A.R.C., Mumbai) checks as summer school participants analyze results.

Berkeley, chair). The NUG executive meets monthly via a conference call and occasionally meets in person when the opportunity presents itself at national meetings. In addition, as part of the NCNR Expansion Workshop held in Bethesda, MD, in July, we held the first meeting of the NUG including an open forum for discussion at the workshop banquet. Robert Leheny represented the executive officers at the meeting.

NEW PARTNERSHIP WITH GM

NIST and General Motors have joined forces to exploit the capabilities of neutron imaging for research on fuel cells for automotive applications. In 2006 a new imaging facility developed under a NIST-GM Participating Research Team was commissioned at BT-2. Because it allows researchers to see the distribution of water directly and in real time, neutron imaging offers a unique means of evaluating the performance of operating fuel cells. This capability has recently received independent credit in a report from the National Academy of Sciences, which states that: "The NIST effort ... is a considerable achievement and one of the most significant analytical advances in the membrane fuel cell realm in decades. The NIST facility offers the entire fuel cell community unique research opportunities that previously eluded them."

THE CENTER FOR HIGH RESOLUTION NEUTRON SCATTERING (CHRNS)

The Center for High Resolution Neutron Scattering (CHRNS) is a national user facility that is jointly funded by the National Science Foundation and the NCNR. The primary aim of this partnership is to maximize access to state-of-the-art neutron scattering instrumentation for the academic research community through the NCNR's proposal system. Proposals for use of the CHRNS facilities are considered solely on the basis of scientific merit or technological importance.

The collection of six instruments currently operated through CHRNS provides structural information on length scales from 1 nm to ~ 10 μm and dynamical information on energy scales from ~ 30 neV to ~ 100 meV. This wide-range of accessible length and time scales supports a very diverse scientific program, allowing researchers in materials science, chemistry, biology, and condensed matter physics to investigate materials such as polymers, metals, ceramics, magnetic materials, porous media, fluids and gels, and biological molecules. About half the users of scattering instruments at the NCNR employ instruments that are part of CHRNS and nearly 40 % of the publications that report scattering results from the NCNR contain research performed on these six instruments.

A particularly important aspect of CHRNS is the enhanced service it provides to users. Examples of this include staff to maintain and operate an expanded range of sample environment equipment, staff to assist users in well-stocked wet laboratories, and the development of data reduction, visualization, and analysis software through the DAVE package. CHRNS also supports education and outreach programs that are aimed at strengthening the neutron community in the U.S. In particular, CHRNS sponsors a variety of activities designed to help train the next generation of neutron scientists including the annual CHRNS summer school (see next section). The success of these education and outreach efforts is perhaps best exemplified by the more than 20 Ph.D.'s that are awarded by U.S. universities each year for work done at least in part on CHRNS instruments.

TWELFTH ANNUAL CHRNS SUMMER SCHOOL

Training young scientists in the theory and practice of neutron scattering is an ongoing activity at the NCNR. The week-long school that the NCNR hosts every summer is a very effective way of introducing graduate students and postdoctoral researchers to neutron scattering. The 2006 summer school attracted 80 applicants for the 36 available places. The school, sponsored by CHRNS, alternates its emphasis in successive years between dynamical and structural methods. This year the school focused on the latter. Following introductory lectures and a facility tour, "hands-on" groups of six were formed and guided though experiments using SANS and USANS methods to study clay dispersions in water, bicelles and micelles in solution, and void formation in fatigued copper metal, as well as neutron reflectometry tech-

niques to investigate magnetic multilayers, tethered polymer brushes, and phospholipid membranes. On the final day, the student groups gave some impressive presentations on the results of their experiments. In written comments about the school, the students frequently mentioned close interaction with NCNR staff as the most valuable aspect of their learning experience.

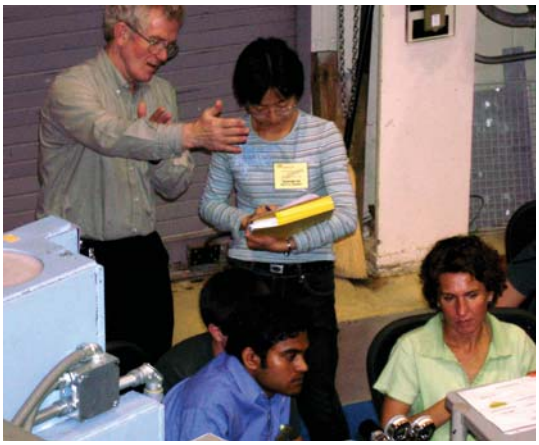

Figure 3:
NCNR guest researcher David Worcester (U. Mo., left) provides summer school participants some advice on reflectometry.

COLD NEUTRONS FOR BIOLOGY AND TECHNOLOGY (CNBT)

Another major partnership, the CNBT, is dedicated to studies of biological membrane systems and is funded by the National Institutes of Health (NIH-NCRR) along with contributions from NIST, the University of California, Irvine, the University of Pennsylvania, and Carnegie Mellon University. The CNBT collaboration maintains the Advanced Neutron Diffractometer/Reflectometer (AND/R) for structural biology, shares 10 % of the time on the NG-7 30 m SANS diffractometer, and operates a fully equipped biology laboratory as well as two state-of-the-art computer clusters – one at the NCNR and one at UC Irvine – for molecular dynamics simulations. This combination provides a unique and powerful suite of capabilities to assist U.S. researchers interested in structural biology problems involving membranes.

NG-7 SANS CONSORTIUM

A consortium that includes NIST, the University of Minnesota, the ExxonMobil Research and Engineering Company, and CNBT operates, maintains, and conducts research at the NG-7 30 m SANS instrument. The consortium uses 75 % of the beam time on this instrument, with the remaining 25 % allocated to the general scientific community through the NCNR's proposal system. Consortium members conduct independent research programs primarily in the area of large-scale structure in soft matter. For example, ExxonMobil has used this instrument to deepen their understanding of the underlying nature of ExxonMobil's products and processes, especially in the fields of polymers, complex fluids, and petroleum mixtures. CNBT, which joined in 2001, adds a focus on biological research, mostly through solution scattering studies that complement the membrane-related research carried out on the CNBT reflectometer/diffractometer at NG-1.

INTERAGENCY COLLABORATIONS

The Smithsonian Institution's Nuclear Laboratory for Archeological Research is part of the Anthropology Department at the National Museum of Natural History. It has had a productive 29-year partnership with the NCNR, during which time it has chemically analyzed over 32,500 archaeological artifacts by Instrumental Neutron Activation Analysis (INAA), drawing extensively on the collections of the Smithsonian, as well as on those of many other institutions in this country and abroad. Such chemical analyses provide a means of linking these diverse collections together in order to study continuity and change involved in the production of ceramic and other artifacts.

The Center for Food Safety and Applied Nutrition, U.S. Food and Drug Administration (FDA), directs and maintains a facility at the NCNR that provides agency-wide analytical support for food safety and food defense programs. Neutron activation (instrumental, neutron-capture prompt-gamma, and radiochemical), x-ray fluorescence spectrometry, and low-level gamma-ray detection techniques provide diverse multi-element and radiological information about foods and related materials. Recent studies include homogeneity determinations following cryogenic preparation of foods, improved detection capabilities for iodine and other toxic and nutritional elements in foods, and rapid screening of food products for dangerous levels of cadmium, lead, mercury, and other toxic elements.

Publications

Abdurashitov, J.N., Barsanov, V.I., Bowles, T.J., Cleveland, B.T., Elliott, S.R., Gavrin, V.N., Girin, S.V., Gorbachev, V.V., Gurkina, P.P., Haxton, W.C., Ibragimova, T.V., Janelidze, A.A., Kalikhov, A.V., Karpenko, A.I., Khairnasov, N.G., Khomyakov, Yu.S., Knodel, T.V., Korenkova, A.V., Kotelnikov, N.A., Lande, K., Maltsev, V.V., Markov, Yu.S., Maltveev, V.A., Mormov, I.N., Mishin, O.V., Nico, J.S., Oshkanov, N.N., Poplavsky, V.M., Petrov, A.N., Popov, V.V., Selin, V.V., Shakirov, Z.N., Shikhin, A.A., Suzuki, A., Teasdale, W.A., Tuchkov, A.M., Vasiliev, B.A., Veretenkin, E.P., Vermul, V.M., Voronov, S.A., Wilkerson, J.F., Yants, V.E., Zamyatina, A.A., Zatsepin, G.T., Zlokazov, S.B., "Measurement of the Response of a Ga Solar Neutrino Experiment to Neutrinos From an ^{37}Ar Source," J. Phys.: Conf. Ser. **39**, 284 (2006).

Abdurashitov, J.N., Gavrin, V.N., Girin, S.V., Gorbachev, V.V., Gurkina, P.P., Ibragimova, T.V., Kalikhov, A.V., Khairnasov, N.G., Knodel, T.V., Matveev, V.A., Mirmov, I.N., Shikhin, A.A., Veretenkin, E.P., Vermul, V.M., Yants, V.E., Zatsepin, G.T., Bowles, T.J., Elliot, S.R., Teasdale, W.A., Cleveland, B.T., Haxton, W.C., Wilkerson, J.F., Nico, J.S., Suzuki, A., Lande, K., Khomyakov, Yu. S., Poplavsky, V.M., Popov, V.V., Mishin, O.V., Petrov, A.N., Vasiliev, B.A., Voronov, S.A., Karpenko, A.I., Maltsev, V.V., Oshkanov, N.N.,Tuchkov, A.M., Barsanov, V.I., Janelidze, A.A., Korenkova, A.V., Kotelnikov, N.A., Markov, S. Yu., Selin, V.V., Shakirov, Z.N., Zamyatina, A.A., Zlokazov, S.B., "Measurement of the Response of a Ga Solar Neutrino Experiment to Neutrinos from a ^{37}Ar Source," Phys. Rev. C **73**, 045805 (2006).

Ahmad, F., Constabel, F., Geckeler, K.E., Seeck, O.H., Seo, Y.S., Satija, S.K., Kubik, S., Shin, K., "X-Ray Reflectivity Study of Cyclic Peptide Monolayers at the Air-Water Interface," Israel J. Chem. **45** (3), 345 (2005).

Alessi, M.L., Norman, A.I., Knowlton, S.E., Ho, D.L., Greer, S.C., "Helical and Coil Conformations of Poly(ethylene Glycol) in Isobutyric Acid and Water," Macromol. **38** (2), 9333 (2005).

Alexandridis, P., Tsianou, M., Antoniou, E., Katori, Y., Singh, I., Neelamegham, S., "Interactions Between Fibrinogen and PEG Polymers: A Neutron Scattering Investigation," Polym. Prepr. **46** (2), 1250 (2005).

Allen, A.J., Thomas, J.J., "Analysis of Cement Paste and C-S-H Gel by Small-Angle Neutron Scattering," Cem. Concr. Res., in press.

Anderson, I.S., Cook, J., Felcher, G., Gentile, T.R., Greene, G., Klose, F., Koetzle, T., Lelievre-Berna, E., Parizzi, A., Pynn, R., Zhao, J., "Polarized Neutrons for Pulsed Neutron Sources," J. Neutron Res. **13**, 193 (2005).

Babcock, E., Chann, B., Walker, T.G., Chen, W.C., Gentile, T.R., "Limits to the Polarization for Spin-Exchange Optical Pumping of ^{3}He," Phys. Rev. Lett. **96**, 083003 (2006).

Bailey, M.S., Shen, D.Y., McGuire, M.A., Frederickson, D.C., Toby, B.H., DiSalvo, F.J., Yamane, H., Sasaki, S., Shimada, M., "The Indium Subnitrides $Ae_6In_4(In_xLi_y)N_{3-z}$ (Ae = Sr and Ba)," Inorg. Chem. **44**, 6680 (2005).

Balogh, M.P., Jones, C.Y., Herbst, J.F., Hector Jr., L.G., Kundrat, M., "Crystal Structures and Phase Transformation of Deuterated Lithium Imide, Li_2ND," J. Alloys Compd., in press.

Barker, J.G., Glinka, C.J., Moyer, J.J., Kim, M.-H., Drews, A.R., Agamalian, M., "Design and Performance of a Thermal-Neutron Double-Crystal Diffractometer for USANS at NIST," J. Appl. Cryst. **38** (6), 1004 (2005).

Barnes, P.W., Lufaso, M.W., Woodward, P.M., "Structure Determination of $A_2M^{3+}TaO_6$ and $A_2M^{3+}NbO_6$ Ordered Perovskites: Octahedral Tilting and Pseudosymmetry," Acta Crystallogr., Sect. B: Struc. Sci. **B62**, 384 (2006).

Bauer, B.J., Bajpai, V., Fagan, J.A., Becker, M.L., Hobbie, E.K., "Chromatographic Separation of Single Wall Carbon Nanotubes," Mater. Res. Soc. Symp. Proc. **922**, U09-01 (2006).

Bauer, B.J., Hobbie, E.K., Becker, M.L., "Small-Angle Neutron Scattering from Labeled Single-Wall Carbon Nanotubes," Macromol. **39** (7), 2637 (2006).

Besancon, B.M., Soles, C.L., Green, P.F., "Glass Transition of Miscible Binary Polymer-Polymer Thin Films," Phys. Rev. Lett. **97**, 057801 (2006).

Bhat, H., Peral, I., Copley, J.R.D., Angell, C.A., "The Boson Peak in Melt-Formed and Damage-Formed Glasses: A Defect Signature?," J. Non-Cryst. Solids, in press.

Bishop, R.L., Sears, E.L., Blackman, M.J., "A Través del Rio del Cambio," Estudios de Cultura Maya **XXVI**, 17 (2005).

Bitton, R., Schmidt, J., Biesalski, M., Tu, R., Tirrell, M., Bianco-Peled, H., "Self-Assembly of Model DNA-Binding Peptide Amphiphiles," Langmuir **21** (25), 11888 (2005).

Bordallo, H.N., Aldridge, L.P., Desmedt, A., "Water Dynamics in Hardened Ordinary Portland Cement Paste or Concrete: From Quasielastic Neutron Scattering," J. Phys. Chem. B, in press.

Boyce, D.E., Dawson, P.R., Sidle, B., Gnäupel-Herold, T., "A Multiscale Methodology for Deformation Modeling Applied to Friction Stir Welded Steel," Comp. Mater. Sci., in press.

Brown, C.M., Jacques, T.L., Hess, N.J., Daemen, L.L., Mamontov, E., Linehan, J.C., Stowe, A.C., Autrey, T., "Dynamics of Ammonia Borane Using Neutron Scattering," Physica B, in press.

Caciuffo, R., Guidi, T., Amoretti, G., Carretta, S., Magnani, N., Santini, P., Mondelli, C., "Spin Dynamics of Molecular Nanomagnets," Physica B, in press.

Caliskan, G., Briber, R.M., Thirumalai, D., García Sakai, V., Woodson, S.A., Sokolov, A.P., "Dynamic Transition in tRNA is Solvent Induced," J. Am. Chem. Soc. **128** (1), 32 (2006).

Caliskan, G., Hyeon, C., Perez-Salas, U., Briber, R.M., Woodson, S.A., Thirumalai, D., "Persistence Length Changes Dramatically as RNA Folds," Phys. Rev. Lett. **95**, 268303 (2005).

Cappelletti, R.L., "NCNR 2005 NIST Center for Neutron Research Accomplishments and Oppurtunities," NIST SP 1045 (2005).

Cappelletti, R.L., Chowdhuri, Z., Udovic, T.J., Dimeo, R.M., Hauback, B.C., Maeland, A.J., "Quasielastic Neutron Scattering Study of Diffusive Hydrogen Motion in $ZrBe_2H_{0.56}$," Phys. Rev. B **73**, 224109 (2006).

Cappelletti, R.L., Udovic, T.J., Chowdhuri, Z., Hauback, B.C., Maeland, A.J., Dimeo, R.M., "Diffusive Hydrogen Motion in $ZrBe_2H_{0.56}$: A Quasielastic Neutron Scattering Study," Physica B, in press.

Carretta, S., Santini, P., Amoretti, G., Guidi, T., Dyson, J., Caciuffo, R., Stride, J.A., Caneschi, A., Copley, J.R.D., "Inelastic-Neutron-Scattering Study of Excited Spin Multiplets and Low-Energy Phonons in the Fe_8 Nanomagnet: Implications for Relaxation," Phys. Rev. B **73**, 144425 (2006).

Castro-Roman, F., Porcar, L., Porte, G., Ligoure, C., "Quantitative Analysis of Lyotropic Lamellar Phases SANS Patterns in Powder Oriented Samples," Euro. Phys. J. E **18** (3), 259 (2005).

Chauhan, S., Caliskan, G., Briber, R.M., Perez-Salas, U., Rangan, P., Thirumalai, D., Woodson, S.A., "RNA Tertiary Interactions Mediate Native Collapse of a Bacterial Group I Ribozyme," J. Mol. Biol. **353**, 1199 (2005).

Chen, C., Depa, P., García Sakai, V., Maranas, J.K., Lynn, J.W., Peral, I., Copley, J.R.D., "A Comparison of United Atom, Explicit Atom, and Coarse-Grained Simulation Models for Poly(ethylene Oxide)," J. Chem. Phys. **124**, 234901 (2006).

Chen, S.-H., Liu, L., Fratini, E., Baglioni, P., Faraone, A., Mamontov, E., "Observation of Fragile-to-Strong Dynamics Crossover in Protein Hydration Water," Proc. National Academy of Sciences **103** (24), 9012 (2006).

Chen, S.-H., Loong, C.-K., "Neutron Scattering Investigations of Proton Dynamics of Water and Hydroxyl Species in Confined Geometries," Nucl. Eng. Technol. **38** (3), 201 (2006).

Chen, W.-R., Butler, P.D., Magid, L.J., "Incorporating Intermicellar Interactions in the Fitting of SANS Data From Cationic Wormlike Micelles," Langmuir **22** (15), 6539 (2006).

Chen, Y., Bao, W., Qiu, Y., Lorenzo, J.E., Sarrao, J.L., Ho, D.L., Lin, M.Y., "Slow Spin-Glass and Fast Spin-Liquid Components in Quasi-Two-Dimensional La_2 (Cu, Li)O_4," Phys. Rev. B **72** (18), 184401 (2005).

Chen, Y., Lynn, J.W., Huang, Q., Woodward, F.M., Yildirim, T., Lawes, G., Ramirez, A.P., Rogado, N., Cava, R.J., Aharony, A., Entin-Wohlman, O., Harris, A.B., "Complex Magnetic Order in the Kagomé Staircase Compound $Co_3V_2O_8$," Phys. Rev. B **74**, 014430 (2006).

Christianson, A.D., Llobet, A., Bao, W., Gardner, J.S., Swainson, I.P., Lynn, J.W., Mignot, J.-M., Prokes, K., Pagliuso, P.G., Moreno, N.O., Sarrao, J.L., Thompson, J.D., Lacerda, A.H., "Novel Coexistence of Superconductivity With Two Distinct Magnetic Orders," Phys. Rev. Lett. **95**, 217002 (2005).

Chung, J.-H., Matsuda, M., Lee, S.-H., Kakurai, K., Ueda, H., Sato, T.J., Takagi, H., Hong, K.-P., Park, S., "Statics and Dynamics of Incommensurate Spin Order in a Geometrically Frustrated Antiferromagnet $CdCr_2O_4$," Phys. Rev. Lett. **95**, 247204 (2005).

Chung, M.K., Huang, P.J., Li, W.-H., Yang, C.C., Chan, T.S., Liu, R.S., Wu, S.Y., Lynn, J.W., "Crystalline and Magnetic Structures of Sr_2FeMoO_6 Double Perovskites," Physica B, in press.

Cicerone, M.T., Soles, C.T., Chowdhuri, Z., Pikal, M.J., Chang, J., "Fast Dynamics as a Diagnostic for Excipients in Preservation of Dried Proteins," Am. Pharm. Rev. **8** (6), 22 (2005).

Ciezak, J.A., Leão, J.B., "Structural and Vibrational Characterization of Tetracyanoethylene-Hexamethylbenzene as a Function of Pressure," J. Phys. Chem. A **110** (10), 3759 (2006).

Ciezak, J.A., Trevino, S.F., "Inelastic Neutron Scattering Spectrum of Cyclotrimethylenetrinitramine: A Comparison With Solid-State Electronic Structure Calculations," J. Phys. Chem. A **110** (15), 5149 (2006).

Ciezak, J.A., Trevino, S.F., "The Inelastic Neutron Scattering Spectrum of 1,4-Dinitroimidazole and the Reproduction of Its Solid-State Features by Periodic DFT Methods," Mater. Res. Soc. Symp. Proc. **896**, H05-02 (2006).

Ciezak, J.A., Trevino, S.F., "Theoretical and Experimental Study of the Inelastic Neutron Scattering Spectra of β-5-Nitro-2,4-Dihydro-3H-1,2,4-Triazol-3-One," J. Mol. Struct.: THEOCHEM **732** (1-3), 211 (2005).

Cipriano, B.H., Raghavan, S.R., McGuiggan, P.M., "Surface Tension and Contact Angle Measurements of a Hexadecyl Imidazolium Surfactant Absorbed on a Clay Surface," Colloids Surf. A **262** (1-3), 8 (2005).

Coakley, K.J., Doyle, J.M., Dzhosyuk, S.N., Yang, L., Huffman, P.R., "Chaotic Scattering and Escape Times of Marginally Trapped Ultracold Neutrons," J. Res. Natl. Inst. Stand. Technol. **110** (4), 367 (2005).

Collett, B., Anderman, R., Balashov, S., Bateman, F.B., Byrne, J., Dewey, M.S., Fisher, B.M., Goldin, L., Jones, G., Komives, A., Konopka, T., Leuschner, M., Mostovoy, Yu., Nico, J.S., Thompson, A.K., Trull, C., Wietfeldt, F.E., Wilson, R., Yerozolimsky, B.G., "Proposed Measurement of the Beta-Neutrino Correlation in Neutron Decay," J. Res. Natl. Inst. Stand. Technol. **110** (4), 401 (2005).

Connolly, J., Bertram, W., Barker, J., Buckley, C., Edwards, T., Knott, R., "Comparison of the Structure on the Nanoscale of Natural Oil-Bearing and Synthetic Rock," J. Petrol. Sci. Eng., in press.

Cook, L.P., Klein, R., Wong-Ng, W., Huang, Q., Ribeiro, R.A., Canfield, P.C., "Thermodynamics of MgB_2 - by Calorimetry and Knudsen Thermogravimetry," IEEE Trans. Appl. Superconduct. **15** (2), 3227 (2005).

Copley, J.R.D., "The NIST Center for Neutron Research Honors Mike Rowe and Jack Rush," Neutron News **17** (1), 10 (2006).

Copley, J.R.D., "The Disk Chopper Spectrometer at NIST: the Good, the Bad, and the Ugly," in *Proceedings of the 17th Meeting of the International Collaboration on Advanced Neutron Sources* (Santa Fe, New Mexico) Vol. 3, p. 974 (2006).

Cremer, J.T., Piestrup, M.A., Park, H., Gary, C.K., Pantell, R.H., Glinka, C.J., Barker, J.G., "Imaging Hydrogenous Materials With a Neutron Microscope," Appl. Phys. Lett. **87** (16), 161913 (2005).

Crichton, M.A., Bhatia, S.R., "Large-Scale Structure in Gels of Attractive Block Copolymer Micelles," Langmuir **21** (22), 10028 (2005).

Crichton, M.A., Forbes, N.S., Bhatia, S.R., "USANS as a Probe of Large-Scale Structure in Attractive Colloidal Glasses of Block Copolymer Micelles," Mater. Res. Soc. Symp. Proc. **840**, Q07-11 (2005).

Cui, J., Huang, Q., Toby, B.H., "Magnetic Structure Refinement with Neutron Powder Diffraction Data Using GSAS: A Tutorial," Powder Diff. **21** (1), 71 (2006).

Dag, S., Ozturk, Y., Ciraci, S., Yildirim, T., "Adsorption and Dissociation of Hydrogen Molecules on Bare and Functionalized Carbon Nanotubes," Phys. Rev. B **72**, 155404 (2005).

Dag, S., Tongay, S., Yildirim, T., Durgun, E., Senger, R.T., Fong, C.Y., Ciraci, S., "Half-Metallic Properties of Atomic Chains of Carbon-Transition-Metal Compounds," Phys. Rev. B **72**, 155444 (2005).

Das, S.K., Heinrich, F., Butz, T., "The Nuclear Quadrupole Interaction at Inequivalent Lattice Sites in Ammonium Paramolybdate: A TDPAC Study," Chem. Phys., in press.

Davidock, D.A., Hillmyer, M.A., Lodge, T.P., "Mapping Large Regions of Diblock Copolymer Phase Space by Selective Chemical Modification," Macromol. **37**, 397 (2004).

Davies, T.S., Ketner, A.M., Raghavan, S.R., "Self-Assembly of Surfactant Vesicles That Transform Into Viscoelastic Wormlike Micelles Upon Heating," J. Am. Chem. Soc. **128**, 6669 (2006).

Davis, T.M., Drews, T.O., Ramanan, H., He, C., Dong, J., Schnablegger, H., Katsoulakis, M.A., Kokkoli, E., McCormick, A.V., Penn, R.L., Tsapatsis, M., "Mechanistic Principles of Nanoparticle Evolution to Zeolite Crystals," Nature Mater. **5** (4), 400 (2006).

dela Cruz, C.R., Yen, F., Lorenz, B., Gospodinov, M.M., Chu, C.W., Ratcliff II, W., Lynn, J.W., Park, S., Cheong, S.-W., "Structural Anomalies at the Magnetic and Ferroelectric Transitions in RMn$_2$O$_5$ (R = Tb, Dy, Ho)," Phys. Rev. B **73**, 100406(R) (2006).

dela Cruz, C.R., Yen, F., Lorenz, B., Park, S., Cheong, S.-W., Gospodinov, M.M., Ratcliff II, W., Lynn, J.W., Chu, C.W., "Evidence for Strong Spin-Lattice Coupling in Multiferroic RMn$_2$O$_5$ (R = Tb, Dy, Ho) via Thermal Expansion Anomalies," J. Appl. Phys. **99**, 08R103 (2006).

Dewey, M.S., Arif, M., Gentile, T.R., Gilliam, D.M., Jacobson, D.L., Nico, J.S., Thompson, A.K., "The Fundamental Neutron Physics Facilities at NIST," Nucl. Instrum. Meth. Phys. Res. B **241**, 213 (2005).

Dewey, M.S., Kessler Jr., E.G., Deslattes, R.D., Börner, H.G., Jentschel, M., Doll, C., Mutti, P., "Precision Measurement of the ^{29}Si, ^{33}S, and ^{36}Cl Binding Energies," Phys. Rev. C **73**, 044303 (2006).

Diallo, M.S., Glinka, C.J., Goddard III, W.A., Johnson Jr., J.H., "Characterization of Nanoparticles and Colloids in Aquatic Systems 1. Small Angle Neutron Scattering Investigations of Suwannee River Fulvic Acid Aggregates in Aqueous Solutions," J. Nanopart. Res. **7**, 435 (2005).

DiNoia, T.P., Park, I.-H., McHugh, M.A., van Zanten, J.H., "Observation of Polymer Chain Contraction Near the Overlap Concentration," Macromol. **38** (22), 9393 (2005).

Dirama, T.E., Curtis, J.E., Carri, G.A., Sokolov, A.P., "Coupling Between Lysozyme and Trehalose Dynamics: Microscopic Insights From Molecular-Dynamics Simulations," J. Chem. Phys. **124**, 034901 (2006).

Doucet, M., Maliszewskyj, N., Pheiffer, S., "New Instrumentation Control Software at the NCNR," in *Proceedings of the 17th Meeting of the International Collaboration on Advanced Neutron Sources* (Santa Fe, New Mexico) Vol. 3, p.1124 (2006).

Downing, R.G., Centiner, S.M., Ünlü, K., "Development and Application of Time-of-Flight Neutron Depth Profiling (TOF-NDP)," J. Radioanal. Nucl. Chem., in press.

Duggan, J.L., Naab, F., Hossain, K., Holland, O.W., McDaniel, F.D., Xu, J.J., Zhao, Z.Y., Guo, B.N., Liu, J., Shim, K.H., Jeong, U., "Analysis of the Accuracy of Several Methods for Determining the Concentration of ^{11}B$^+$ Implanted Silicon," Nucl. Instrum. Meth. Phys. Res. B **243**, 205 (2006).

Dura, J.A., Pierce, D.J., Majkrzak, C.F., Maliszewskyj, N.C., McGillivray, D.J., Loesche, M., O'Donovan, K.V., Mihailescu, M., Perez-Salas, U., Worcester, D.L., White, S.H., "AND/R: Advanced Neutron Diffractometer/ Reflectometer for Investigation of Thin Films and Multilayers for the Life Sciences," Rev. Sci. Instrum. **77**, 074301 (2006).

Dyck, M., Lösche, M., "Interaction of the Neurotransmitter, Neuropeptide Y, With Phospholipid Membranes: Film Balance and Fluorescence Microscopy Studies," J. Phys. Chem. B, in press.

Dzhosyuk, S.N., Copete, A., Doyle, J.M., Yang, L., Coakley, K.J., Golub, R., Korobkina, E., Kreft, T., Lamoreaux, S.K., Thompson, A.K., Yang, G.L., Huffman, P.R., "Determination of the Neutron Lifetime Using Magnetically Trapped Neutrons," J. Res. Natl. Inst. Stand. Technol. **110** (4), 339 (2005).

Ehlers, G., Gardner, J.S., Booth, C.H., Daniel, M., Kam, K.C., Cheetham, A.K., Antonio, D., Brooks, H.E., Cornelius, A.L., Bramwell, S.T., Lago, J., Häussler, W., Rosov, N., "Dynamics of Diluted Ho Spin Ice $Ho_{2-x}Y_xTi_2O_7$ Studied by Neutron Spin Echo Spectroscopy and ac Susceptibility," Phys. Rev. B **73**, 174429 (2006).

El-Khatib, S., Llobet, A., Purwanto, A., Robinson, R.A., Lee, S.-H., Lynn, J.W., Chang, S., Nakotte, H., "Magnetic Structures in UCuSn," J. Appl. Phys. **99**, 08P704 (2006).

Estermann, M., Dubois, J., "Investigation of the Properties of Amorphous Silicon Flat-Panel Detectors Suitable for Real-Time Neutron Imaging," IEEE Trans. Nucl. Sci. **52** (1), 356 (2005).

Farrell, D.F., Ijiri, Y., Kelly, C.V., Borchers, J.A., Rhyne, J.J., Ding, Y., Majetich, S.A., "Small Angle Neutron Scattering Study of Disordered and Crystalline Iron Nanoparticle Assemblies," J. Magn. Magn. Mater., in press.

Fedeyko, J.M., Vlachos, D.G., Lobo, R.F., "Understanding the Differences Between Microporous and Mesoporous Synthesis Through the Phase Behavior of Silica," Micro. Meso. Mater. **90** (1-3), 102 (2006).

Feng, X.-M., Liu, G.-Y., Huang, Q.-Z., Rao, G.-H., "Influence of Annealing Treatment on Structural and Magnetic Properties of Double Perovskite Sr_2FeMoO_6," Trans. Nonfer. Met. Soc. China **16**, 122 (2006).

Fennell, T., Petrenko, O.A., Fåk, B., Gardner, J.S., Bramwell, S.T., Ouladdiaf, B., "Neutron Scattering Studies of the Spin Ices $Ho_2Ti_2O_7$ and $Dy_2Ti_2O_7$ in Applied Magnetic Field," Phys. Rev. B **72**, 224411 (2005).

Fisher, B.M., Wietfeldt, F.E., Dewey, M.S., Gentile, T.R., Nico, J.S., Thompson, A.K., Coakley, K.J., Beise, E.J., Kiriluk, K.G., Byrne, J., "Detecting the Radiative Decay Mode of the Neutron," J. Res. Natl. Inst. Stand. Tech. **110** (4), 421 (2005).

Fitzsimmons, M.R., Park, S., Dumesnil, K., Dufour, C., Pynn, R., Borchers, J.A., Rhyne, J.J., Mangin, Ph., "Vector Magnetization Depth Profile of a Laves-Phase Exchange-Coupled Superlattice Obtained Using a Combined Approach of Micromagnetic Simulation and Neutron Reflectometry," Phys. Rev. B **73**, 134413 (2006).

Foecke, T., Gnäupel-Herold, T., "Robustness of the Sheet Metal Springback Cup Test," Met. Mat. Trans. A, in press.

Foias, A.E., Bishop, R.L., "Fine Paste Wares and the Terminal Classic in the Petexbatun and Pasion Regions, Peten, Guatemala," in *Geographies of Power: Understanding the Nature of Terminal Classic Pottery in the Maya Lowlands*, edited by S.L. López Varela, A.E. Foias, British Archaeological Reports **S1447**, p. 124 (2005).

Foo, M.L., Huang, Q., Lynn, J.W., Lee, W.-L., Klimczuk, T., Hagemann, I.S., Ong, N.P., Cava, R.J., "Synthesis, Structure, and Physical Properties of Ru Ferrites: $BaMRu_5O_{11}$ (M = Li and Cu) and $BaM'_2Ru_4O_{11}$ (M' = Mn, Fe, and Co)," J. Solid State Chem. **179** (2), 563 (2006).

Foo, M.L., Klimczuk, T., Li, L., Ong, N.P., Cava, R.J., Huang, Q., Lynn, J.W., "Synthesis of Three Layer Na_xCoO_2 (x = 0.3, 0.5, 0.6, 0.75, 1.0) and Superconductivity in Three Layer $Na_{0.3}CoO_2 \bullet 1.3H_2O$," Mater. Res. Soc. Symp. Proc. **848**, FF06-11 (2005).

Foster, M.D., Akgun, B., Brittain, W.J., Li, X., Wang, J., Majkrzak, C.F., "Internal and Interface Structure in Diblock Copolymer Brushes Synthesized by ATRP," Polymer Prepr. **46** (2), 33 (2005).

Fry, D., Langhorst, B., Kim, H., Grulke, E., Wang, H., Hobbie, E.K., "Anisotropy of Sheared Carbon-Nanotube Suspensions," Phys. Rev. Lett. **95**, 038304 (2005).

García Sakai, V., Higgins, J.S., Trusler, J.P.M., "Cloud Curves of Polystyrene of Poly(Methyl Methacrylate) or Poly(Styrene-*co*-Methyl Methacrylate) in Cyclohexanol Determined With a Thermo-Optical Apparatus," J. Chem. Eng. Data **51** (2), 743 (2006).

García Sakai, V., Maranas, J.K., Chowdhuri, Z., Peral, I., Copley, J.R.D., "Miscible Blend Dynamics and the Length of Local Compositions," J. Polym. Sci., Part B: Polym. Phys. **43**, 2914 (2005).

Gardner, J.S., Cornelius, A.L., Chang, L.J., Prager, M., Brückel, Th., Ehlers, G., "Spin Dynamics in $Ho_2Ru_2O_7$," J. Phys.: Condens. Matter **17**, 7089 (2005).

Garlea, V.O., Nagler, S.E., Zaretsky, J.L., Stassis, C., Vaknin, D., Kögerler, P., McMorrow, D.F., Niedermayer, C., Tennant, D.A., Lake, B., Qiu, Y., Exler, M., Schnack, J., Luban, M., "Probing Spin Frustration in High-Symmetry Magnetic Nanomolecules by Inelastic Neutron Scattering," Phys. Rev. B **73**, 024414 (2006).

Garlea, V.O., Zaretsky, J.L., Jones, C.Y., Lin, L.-L., Schlagel, D.L., Lograsso, T.A., Tsokol, A.O., Pecharsky, V.K., Gschneider Jr., K.A., Stassis, C., "Neutron Diffraction Studies of the Magnetoelastic Compounds $Tb_5Si_xGe_{4-x}$ (x = 2.2 and 2.5)," Phys. Rev. B **72**, 104431 (2005).

Garvey, C.J., Knott, R.B., Searson, M., Conroy, J.P., "USANS Study of Wood Structure," Physica B, in press.

Gašparović, G., Ott, R.A., Cho, J.-H., Chou, F.C., Lynn, J.W., Lee, Y.S., "Neutron Scattering Study of Novel Magnetic Order in $Na_{0.5}CoO_2$," Phys. Rev. Lett. **96**, 046403 (2006).

Gauzzi, A., Gilioli, E., Prodi, A., Bolzoni, F., Licci, F., Marezio, M., Calestani, G.L., Affronte, M., Huang, Q., Santoro, A., Lynn, J.W., "Unusual e_g $3d$ x^2-y^2 Orbital Ordering and Low-Energy Excitations in the CE Structure of $NaMn_7O_{12}$," J. Supercond. **18** (5-6), 675 (2005).

Gawrys, K.L., Blankenship, G.A., Kilpatrick, P.K., "On the Distribution of Chemical Properties and Aggregation of Solubility Fractions in Asphaltenes," Energy and Fuels **20** (2), 705 (2006).

Gehring, P.M., Copley, J.R.D., "NCNR Holds Eleventh Annual Summer School on Neutron Scattering," Neutron News **16** (4), 11 (2005).

Geissler, E., Hecht, A.M., Horkay, F., "Nanoscale Inhomogeneities and Thermodynamics of Unfilled Polymer Gels," J. Macromol. Sci. Part B: Physics **44**, 873 (2005).

George, M., Funkhouser, G.P., Terech, P., Weiss, R.G., "Organogels With Fe(III) Complexes of Phosphorus-Containing Amphiphiles as Two-Component Isothermal Gelators," Langmuir, in press.

George, M., Snyder, S.L., Terech, P., Weiss, R.G., "Gelation of Perfluorinated Liquids by *N*-Alkyl Perfluoroalkanamides," Langmuir **21** (22), 9970 (2005).

Gerber, M.J., Walker, L.M., "Controlling Dimensions of Polymerized Micelles: Micelle Template Versus Reaction Conditions," Langmuir **22** (3), 941 (2006).

Gericke, M.T., Blessinger, C., Bowman, J.D., Carlini, R.D., Chupp, T.E., Coulter, K.P., Dawkins, M., Dabaghyan, M., Desai, D., Freedman, S.J., Gentile, T.R., Gillis, R.C., Greene, G.L., Hartfield, J., Hersman, F.W., Ino, T., Jones, G.L., Lauss, B., Leuschner, M., Losowski, B., Mahurin, R., Masuda, Y., Mitchell, G.S., Muto, S., Nann, H., Page, S.A., Penttilä, S.I., Ramsay, W.D., Santra, S., Seo, P.-N., Sharapov, E.T., Smith, T.B., Snow, W.M., Tasson, J., Wilburn, W.S., Zhu, H., "A Low-Noise CsI Detector Array for the Precision Measurement of Parity Nonconservation in $n + p \rightarrow d + \gamma$," AIP Conf. Proc. **769**, 696 (2005).

Gilliam, S.B., Gidcumb, S.M., Forsythe, D., Parikh, N.R., Hunn, J.D., Snead, L.L., Lamaze, G.P., "Helium Retention and Surface Blistering Characteristics of Tungsten With Regard to First Wall Conditions in an Inertial Fusion Energy Reactor," Nucl. Instrum. Meth. Phys. Res. B **241**, 491 (2005).

Gilliam, S.B., Gidcumb, S.M., Parikh, N.R., Forsythe, D.G., Patnaik, B.K., Hunn, J.D., Snead, L.L., Lamaze, G.P., "Retention and Surface Blistering of Helium Irradiated Tungsten as a First Wall Material," J. Nucl. Mater. **347**, 289 (2005).

Glade, S.C., Wirth, B.D., Odette, G.R., Asoka-Kumar, P., "Positron Annihilation Spectroscopy and Small Angle Neutron Scattering Characterization of Nanostructural Features in High-Nickel Model Reactor Pressure Vessel Steels," J. Nucl. Mater. **351**, 197 (2006).

Gnäupel-Herold, T., Foecke, T., Iadicola, M.A., "Through-Thickness Residual Stress Measurements on Springback Test Specimens," AIP Conf. Proc. **778**, 221 (2005).

Gnäupel-Herold, T., Foecke, T.J., Prask, H.J., Fields, R.J., Levine, L.E., Xia, C.Z., Lienert, U., "An Investigation of Springback Stresses in Deep-Drawn Cups Using Diffraction Techniques," SAE Trans. J. Mater. Man., 175 (2005).

Gnäupel-Herold, T., Prask, H.J., Barker, J., Biancaniello, F.S., Jiggetts, R.D., Matejicek, J., "Microstructure, Mechanical Properties, and Adhesion in IN625 Air Plasma Sprayed Coatings," Mater. Sci. Eng. A **421** (1-2), 77 (2006).

Gogotsi, Y., Dash, R.K., Yushin, G., Yildirim, T., Laudisio, G., Fischer, J.E., "Tailoring of Nanoscale Porosity in Carbide-Derived Carbons for Hydrogen Storage," J. Am. Chem. Soc. **127** (46), 16006 (2005).

Granado, E., Urbano, R.R., Pérez, C.A., Azimonte, C., Lynn, J.W., Souza, R.A., Souza-Neto, N.M., Ramos, A.Y., Bychkov, G.L., Shiryaev, S.V., Barilo, S.N., "Strong Orbital Correlations in a Fe-Substituted Spin-Glass-Manganite," Phys. Rev. B **72**, 052406 (2005).

Grandjean, J., Mourchid, A., "Entropic Attraction and Fluid-Glass Transition in Micellar Solutions of Associative Diblock Copolymers," Phys. Rev. E **72**, 041503 (2005).

Green, D.E., Stoughton, T.B., Gnäupel-Herold, T., Iadicola, M.A., Foecke, T., "Influence of Drawbeads in Deep Drawing of Plane-Strain Channel Sections," in *Proceedings of the International Deep Drawing Research Group Conference* (Porto, Portugal), p. 559 (2006).

Greenberg, R.R., "CCQM-K13.1 Subsequent Key Comparison: Cadmium and Lead in Sediment," Metrologia **43**, 08004 (2005).

Greenberg, R.R., Mackey, E.A., "CCQM-K31 Key Comparison: Arsenic in Shellfish," Metrologia **43**, 08003 (2005).

Gutberlet, T., Lösche, M., "Complex Biomimetic Structures at Fluid Surfaces and Solid/Liquid Interfaces," in *Neutron Scattering in Biology - Techniques and Applications*, edited by Fitter, J., Gutberlet, T., Katsaras, J., (Springer, Berlin), p. 283 (2006).

Hamill, A.C., Wang, S.-C., Lee Jr., C.T., "Probing Lysozyme Conformation With Light Reveals a New Folding Intermediate," Biochem. **44** (46), 15139 (2005).

Hamilton, W.A., Smith, G.S., Taylor, G.B., Larkins, B.M., Porcar, L., "Current and Future Capabilities of the Neutron Reflectometer MIRROR at Oak Ridge National Laboratory's High Flux Isotope Reactor," Physica B, in press.

Hammouda, B., Worcester, D., "The Denaturation Transition of DNA in Mixed Solvents," Biophys. J., in press.

Harris, A.B., Yildirim, T., Aharony, A., Entin-Wohlman, O., "Towards a Microscopic Model of Magnetoelectric Interactions in $Ni_3V_2O_8$," Phys. Rev. B **73**, 184433 (2006).

Hartman, M.R., Peterson, V.K., Liu, Y., Kaye, S.S., Long, J.R., "Neutron Diffraction and Neutron Vibrational Spectroscopy Studies of Hydrogen Adsorption in the Prussian Blue Analogue $Cu_3[Co(CN)_6]_2$," Chem. Mater. **18** (14), 3221 (2006).

Hauet, T., Borchers, J.A., Mangin, Ph., Henry, Y., Mangin, S., "Training Effect in an Exchange Bias System: The Role of Interfacial Domain Walls," Phys. Rev. Lett. **96**, 067207 (2006).

Healy, J., Edward, G.H., Knott, R.B., "Residual Orientation in Injection Micro-Molded Samples," Physica B, in press.

Hedden, R.C., Bauer, B.J., Lee, H.-J., "Characterization of Nanoporous Low-*k* Thin Films by Contrast Match SANS," Mater. Res. Soc. Symp. Proc. **766**, E09-07 (2003).

Hickner, M.A., Siegel, N.P., Chen, K.S., McBrayer, D.N., Hussey, D.S., Jacobson, D.L., Arif, M., "Real-Time Imaging of Liquid Water in an Operating Proton Exchange Membrane Fuel Cell," J. Electrochem. Soc. **153** (5), A902 (2006).

Ho, D.L., Hammouda, B., Kline, S.R., Chen, W.-R., "Unusual Phase Behavior in Mixtures of Poly(ethylene Oxide) and Ethyl Alcohol," J. Polym. Sci., Part B: Polym. Phys. **44**, 557 (2006).

Hobbie, E.K., Bauer, B.J., Stephens, J., Becker, M.L., McGuiggan, P., Hudson, S.D., Wang, H., "Colloidal Particles Coated and Stabilized by DNA-Wrapped Carbon Nanotubes," Langmuir **21** (23), 10284 (2005).

Horkay, F., "Osmotic and Structural Properties of Biopolymer Solutions and Gels," Polym. Prepr. **47** (2), 274 (2006).

Horkay, F., Basser, P.J., Hecht, A.M., Geissler, E., "Calcium Induced Volume Transition in Polyelectrolyte Gels," Macromol. Symp. **200**, 21 (2003).

Horkay, F., Basser, P.J., Hecht, A.M., Geissler, E., "Comparison Between the Effect of Calcium Ions on the Osmotic Properties of Synthetic and Biopolymer Gels," Polym. Prepr. **46** (1), 127 (2005).

Horkay, F., Basser, P.J., Hecht, A.M., Geissler, E., "Cross-Linked Polyacrylate Hydrogels: Osmotic and Neutron Scattering Properties," Polym. Prepr. **44** (1), 3 (2003).

Horkay, F., Basser, P.J., Hecht, A.M., Geissler, E., "Effect of Calcium Ions on the Structure of Synthetic and Biopolymer Gels," Polym. Mater.: Sci. Eng. Prepr. **93**, 105 (2005).

Horkay, F., Basser, P.J., Hecht, A.M., Geissler, E., "Osmotic and Small-Angle Neutron Scattering Properties of DNA Gels," Polym. Prepr. **45** (2), 459 (2004).

Horkay, F., Basser, P.J., Hecht, A.M., Geissler, E., "Osmotic Behavior of DNA Gels Swollen in Physiological Salt Solutions," Polym. Mater.: Sci. Eng. Prepr. **90**, 319 (2004).

Horkay, F., Basser, P.J., Hecht, A.M., Geissler, E., "SANS and Osmotic Observations on Polyacrylate Networks Swollen in Physiological Salt Solutions," Polym. Prepr. **44** (2), 721 (2003).

Horkay, F., Basser, P.J., Hecht, A.M., Geissler, E., "Similarities Between the Osmotic and Scattering Properties of Synthetic and Biopolymer Gels," Polym. Mater.: Sci. Eng. Prepr. **94**, 668 (2006).

Hough, L.A., Islam, M.F., Hammouda, B., Yodh, A.G., Heiney, P.A., "Structure of Semidilute Single-Wall Carbon Nanotube Suspensions and Gels," Nano Lett. **6** (2), 313 (2006).

Huffman, P.R., Arif, M., Black, T.C., Jacobson, D.L., Schoen, K., Snow, W.M., Werner, S.A., "Precision Neutron Interferometric Measurements of the n-p, n-d, and n-^{3}He Zero-Energy Coherent Neutron Scattering Amplitudes," Physica B, in press.

Ireson, R.G., Easter, M .D., Lakin, M.L., Ondov, J.M., Clark, N.N., Wright, D.B., "Estimation of Diesel Particulate Matter Concentrations in a School Bus Using a Fuel-Based Tracer — A Sensitive and Specific Method for Qualifying Vehicle Contributions," Trans. Res. Rec. **1880**, 24 (2004).

Ishiwata, S., Bos, J.W.G., Huang, Q., Cava, R.J., "Structure and Magnetic Properties of Hollandite $Ba_{1.2}Mn_8O_{16}$," J. Phys.: Condens. Matter **18**, 3745 (2006).

Jackson, A., White, J., "Small Angle Scattering From Protein/Sugar Conjugates," Physica B, in press.

Jeng, U.-S., Lin, T.-L., Lin, J.M., Ho, D.L., "Contrast Variation SANS for the Solution Structure of the β-Amyloid Peptide 1-40 Influenced by SDS Surfactants," Physica B, in press.

Jennings, H.M., Thomas, J.J., Gevrenov, J.S., Constantinides, G., Ulm, F.-J., "Relating the Nanostructure of Concrete to Engineering Properties," in *Proceedings of the 2nd International Symposium on Nanotechnology in Construction* (Bilbao, Spain), in press.

Jentschel, M., Börner, H.G., Mutti, P., Kessler Jr., E.G., Dewey, M.S., Henins, A., "Accurate Determination of Neutron Binding Energies," AIP Conf. Proc. **769**, 617 (2005).

Jomaa, H.W., Schlenoff, J.B., "Salt-Induced Polyelectrolyte Interdiffusion in Multilayered Films: A Neutron Reflectivity Study," Macromol. **38** (20), 8473 (2005).

Jones, C.Y., Luecke, W.E., Copland, E., "Neutron Diffraction Study of Oxygen Dissolution in α_2-Ti_3Al," Intermetallics **14** (1), 54 (2006).

Jones, G.L., Dias, F., Collett, B., Chen, W.C., Gentile, T.R., Piccoli, P.M.B., Miller, M.E., Schultz, A.J., Yan, H., Tong, X., Snow, W.M., Lee, W.T., Hoffmann, C., Thomison, J., "Test of a Continuously Polarized ^{3}He Neutron Spin Filter With NMR-Based Polarization Inversion on a Single-Crystal Diffractometer," Physica B, in press.

Jones, R.L., Indrakanti, A., Briber, R.M., Müller, M., Kumar, S.K., "Phase Behavior of Ultrathin Polymer Mixtures," Macromol. **37**, 6676 (2004).

Kalur, G.C., Frounfelker, B.D., Cipriano, B.H., Norman, A.I., Raghavan, S.R., "Viscosity Increase With Temperature in Cationic Surfactant Solutions Due to the Growth of Wormlike Micelles," Langmuir **21** (24), 10998 (2005).

Kang, S., Jia, Z., Zoto, I., Reed, D., Nikles, D.E., Harrell, J.W., Thompson, G., Mankey, G., Krishnamurthy, V.V., Porcar, L., "Sintering Behavior of Spin-Coated FePt and FePtAu Nanoparticles," J. Appl. Phys. **99**, 08N704 (2006).

Katsaras, J., Harroun, T.A., Nieh, M.P., Chakrapani, M., Watson, M.J., Raghunathan, V.A., "Neutron Scattering From Biomaterials in Complex Sample Environments," in *Neutron Scattering in Biology - Techniques and Applications*, edited by Fitter, J., Gutberlet, T., Katsaras, J., (Springer, Berlin), p. 107 (2006).

Kenzelmann, M., Harris, A.B., Aharony, A., Entin-Wohlman, O., Yildirim, T., Huang, Q., Park, S., Lawes, G., Broholm, C., Rogado, N., Cava, R.J., Kim, K.H., Jorge, G., Ramirez, A.P., "Field Dependence of Magnetic Ordering in Kagomé- Staricase Compound $Ni_3V_2O_8$," Phys. Rev. B **74**, 014429 (2006).

Kenzelmann, M., Harris, A.B., Jonas, S., Broholm, C., Schefer, J., Kim, S.B., Zhang, C.L., Cheong, S.-W., Vajk, O.P., Lynn, J.W., "Magnetic Inversion Symmetry Breaking and Ferroelectricity in $TbMnO_3$," Phys. Rev. Lett. **95**, 087206 (2005).

Kepa, H., Kolesnik, S., Wiren, Z., Leao, J., Brown, C.M., Dabrowski, B., Furdyna, J.K., Giebultowicz, T.M., "Inelastic Neutron Scattering From Antiferromagnetically Coupled Nearest-Neighbor Spin Pairs in Zn(Mn)O and Zn(Mn)Te," Physica B, in press.

Kepa, H., Majkrzak, C.F., Sankowski, P., Kacman, P., Giebultowicz, T.M., "Neutron Diffraction and Reflectivity Studies of Eu Chalcogenide Based Superlattices," J. Alloys Compd. **401**, 238 (2005).

Kim, M.-H., Glinka, C.J., "Application of *In Situ* Vapor Sorption Small-Angle Neutron Scattering (SANS) to Semicrystalline Polymers: Vapor Pathway and Structure Evolution in Semicrystalline Linear Polyethylene," J. Appl. Cryst. **38** (5), 734 (2005).

Kim, M.-H., Glinka, C.J., "Ultra Small Angle Neutron Scattering Study of the Nanometer to Micrometer Structure of Porous Vycor," Micro. Meso. Mater. **91** (1-3), 305 (2006).

Kim, M.-H., Glinka, C.J., Carter, R.N., "*In Situ* Vapor Sorption Apparatus for Small-Angle Neutron Scattering and its Application," Rev. Sci. Instrum. **76** (11), 113904 (2005).

Kim, M.-H., Glinka, C.J., Grot, S.A., Grot, W.G., "SANS Study of the Effects of Water Vapor Sorption on the Nanoscale Structure of Perfluorinated Sulfonic Acid (NAFION) Membranes," Macromol. **39** (14), 4775 (2006).

Kim, T.-H., Choi, S.-M., Kline, S.R., "Polymerized Rodlike Nanoparticles with Controlled Surface Charge Density," Langmuir **22** (6), 2844 (2006).

Kim, T.-H., Choi, S.-M., Kline, S.R., "SANS Studies of Polymerized Nano-Particles Using Nonionic/Cationic Surfactant Mixture," Physica B, in press.

Kim, T.-H., Choi, S.-M., Kline, S.R., "Surface Charge Variation of Nano Particles With High Aspect Ratio: A SANS Study," in *Proceedings of the International Symposium on Research Reactor and Neutron Science*, (Daejeon, Korea), p. 853 (2005).

Kline, S.R., "Reduction and Analysis of SANS and USANS Data Using IGOR Pro," J. Appl. Cryst., in press.

Klupp, G., Kamarás, K., Nemes, N.M., Brown, C.M., Leão, J., "Static and Dynamic Jahn-Teller Effect in the Alkali Metal Fulleride Salts A_4C_{60} (A = K, Rb, Cs)," Phys. Rev. B **73**, 085415 (2006).

Koga, T., Jerome, J.L., Seo, Y.-S., Rafailovich, M.H., Sokolov, J.C., Satija, S.K., "Effect of Density Fluctuating Supercritical Carbon Dioxide on Polymer Interfaces," Langmuir **21** (14), 6157 (2005).

Kolesnik, S., Dabrowski, B., Wiren, Z.Q., Kepa, H., Giebultowicz, T.M., Brown, C.M., Leão, J., Furdyna, J.K., "Determination of Antiferromagnetic Interactions in Zn(Mn)O, Zn(Co)O, and Zn(Mn)Te by Inelastic Neutron Scattering," J. Appl. Phys. **99**, 08M122 (2006).

Komives, A., Sint, A.K., Bowers, M., Snow, M., "A Gamma Polarimeter for Neutron Polarization Measurement in a Liquid Deuterium Target for Parity Violation in Polarized Neutron Capture on Deuterium," J. Res. Natl. Inst. Stand. Tech. **110** (3), 221 (2005).

Kopetka, P.A., Rowe, J.M., Williams, R.E., "Cold Neutrons at NIST," Nucl. Eng. Technol. **38** (5), 427 (2005).

Kostko, A.F., Cipriano, B.H., Pinchuk, O.A., Ziserman, L., Anisimov, M.A., Danino, D., Raghavan, S.R., "Salt Effects on the Phase Behavior, Structure, and Rheology of Chromonic Liquid Crystals," J. Phys. Chem. B **109** (41), 19126 (2005).

Krueger, S., Ho, D., Tsai, A., "Small Angle Neutron Scattering as a Probe for Protein Aggregation at Many Length Scales," in *Misbehaving Proteins: Protein (Mis)Folding, Aggregation, and Stability*, edited by Murphy, R.M., Tsai, A.M., (Springer, New York), p. 125 (2006).

Krueger, S., Perez-Salas, U.A., Gregurick, S.K., Kuzmanovic, D., "Small Angle Neutron Scattering From Proteins, Nucleic Acids, and Viruses," in *Neutron Scattering in Biology - Techniques and Applications*, edited by Fitter, J., Gutberlet, T., Katsaras, J., (Springer, Berlin), p. 161 (2006).

Kulkarni, A., Goland, A., Herman, H., Allen, A.J., Dobbins, T., DeCarlo, F., Ilavsky, J., Long, G.G., Fang, S., Lawton, P., "Advanced Neutron and X-Ray Techniques for Insights Into the Microstucture of EB-PVD Thermal Barrier Coatings," Mater. Sci. Eng. A **426** (1-2), 43 (2006).

Kumar, R.S., Cornelius, A.L., Nicol, M.F., Kam, K.C., Cheetham, A.K., Gardner, J.S., "Pressure-Induced Structural Transitions in Tb-Pyrochlore Oxides," Appl. Phys. Lett. **88**, 031903 (2006).

Kuzmanovic, D.A., Elashvili, I., Wick, C., O'Connell, C., Krueger, S., "Quantification of RNA in Bacteriophage MS2-Like Viruses in Solution by Small-Angle X-Ray Scattering," Rad. Phys. Chem. **75** (3), 359 (2006).

Kuzmanovic, D.A., Elashvili, I., Wick, C., O'Connell, C., Krueger, S., "The MS2 Coat Protein Shell is Likely Assembled Under Tension: A Novel Role for the MS2 Bacteriophage A Protein as Revealed by Small-Angle Neutron Scattering," J. Mol. Biol. **355** (5), 1095 (2006).

Lavery, K.A., Choi, K-W., Vogt, B.D., Prabhu, V.M., Lin, E.K., Wu, W.-L., Satija, S.K., Leeson, M.J., Cao, H.B., Thompson, G., Deng, H., Fryer, D.S., "Fundamentals of the Reaction-Diffusion Process in Model EUV Photoresists," in *Advances in Resist Technology and Processing XXIII*, edited by Lin, Q., Proc. of SPIE **6153**, 615313 (2006).

Law, M., Gnäupel-Herold, T., Bowie, G., "Residual Stresses in Gas Pipelines," J. Pipeline Integ. **4** (3), 173 (2005).

Law, M., Prask, H., Luzin, V., Gnäupel-Herold, T., "Residual Stress Measurements in Coil, Linepipe and Girth Welded Pipe," Mater. Sci. Eng. A, in press.

Lawes, G., Harris, A.B., Kimura, T., Rogado, N., Cava, R.J., Aharony, A., Entin-Wohlman, O., Yildirim, T., Kenzelmann, M., Broholm, C., Ramirez, A.P., "Magnetically Driven Ferroelectric Order in $Ni_3V_2O_8$," Phys. Rev. Lett. **95**, 087205 (2005).

Lee, D., Walsh, J.D., Mikhailenko, I., Yu, P., Migliorini, M., Wu, Y., Krueger, S., Curtis, J.E., Harris, B., Lockett, S., Blacklow, S.C., Strickland, D.K., Wang, Y.-X., "RAP Uses a Histidine Switch to Regulate its Interaction With LRP in the ER and Golgi," Mol. Cell **22** (3), 423 (2006).

Lee, J.-H., Agarwal, V., Bose, A., Payne, G.F., Raghavan, S.R., "Transition From Unilamellar to Bilamellar Vesicles Induced by an Amphiphillic Biopolymer," Phys. Rev. Lett. **96**, 048102 (2006).

Lee, J.-H., Choi, S.-M., Pate, B.D., Chisholm, M.H., Han, Y.-S., "Magnetic Uniaxial Alignment of the Columnar Superstructure of Discotic Metallomesogens Over the Centimetre Length Scale," J. Mater. Chem. **16**, 2785 (2006).

Lee, J.S., Foster, M.D., Wu, D.T., "Effects of Branch Points and Chain Ends on the Thermodynamic Interaction Parameter in Binary Blends of Regularly Branched and Linear Polymers," Macromol. **39** (15), 5113 (2006).

Lee, Y.S., Wagner, N.J., "Rheological Properties and Small-Angle Neutron Scattering of a Shear Thickening, Nanoparticle Dispersion at High Shear Rates," Ind. Eng. Chem. Res., in press.

Liang, K., Li, G., Toghiani, H., Koo, J.H., Pittman Jr., C.U., "Cyanate Ester/Polyhedral Oligomeric Silsesquioxane (POSS) Nanocomposites: Synthesis and Characterization," Chem. Mater. **18** (2), 301 (2006).

Liberatore, M.W., Nettesheim, F., Wagner, N.J., Porcar, L., "Spatially Resolved Small-Angle Neutron Scattering in the 1-2 Plane: A Study of Shear-Induced Phase-Separating Wormlike Micelles," Phys. Rev. E **73** (2), 020504(R) (2006).

Lin, Q., Greenblatt, M., Caspi, E.N., Avdeev, M., "Crystallographic and Magnetic Properties of $CaLaMnMoO_6$ Double Perovskite," J. Solid State Chem. **179** (7), 2086 (2006).

Lindstrom, R.M., "Toolkits for Nuclear Science: Data and Spreadsheets," J. Radioanal. Nucl. Chem., in press.

Lindstrom, R.M., Brocker, C., Mackey, E.A., Paul, R.L., Downing, R.G., "Design of the New Analytical Cold-Neutron Beam Line at NCNR," Trans. Am. Nucl. Soc. **93**, 868 (2005).

Lindstrom, R.M., Zeisler, R., Greenberg, R.R., "Accuracy and Uncertainty in Radioactivity Measurement for NAA," J. Radioanal. Nucl. Chem., in press.

Lin-Gibson, S., Bencherif, S., Antonucci, J.M., Jones, R.L., Horkay, F., "Synthesis and Characterization of Poly(ethylene Glycol) Dimethacrylate Hydrogels," Macromol. Symp. **227**, 243 (2005).

Lin-Gibson, S., Jones, R.L., Bencherif, S., Washburn, N.R., Horkay, F., "Structure-Properties Relationships of PEGDM Hydrogels," Polym. Prepr. **45** (2), 374 (2004).

Liu, J., García Sakai, V., Maranas, J.K., "Composition Dependence of Segmental Dynamics of Poly(methyl Methacrylate) in Miscible Blends With Poly(ethylene Oxide)," Macromol. **39** (8), 2866 (2006).

Liu, L., Chen, S.-H., Faraone, A., Yen, C.-W., Mou, C.-Y., "Pressure Dependence of Fragile-to-Strong Transition and a Possible Second Critical Point in Supercooled Confined Water," Phys. Rev. Lett. **95**, 117802 (2005).

Liu, L., Chen, S.-H., Faraone, A., Yen, C.-W., Mou, C.-Y., Kolesnikov, A.I., Mamontov, E., Leao, J., "Quasielastic and Inelastic Neutron Scattering Investigation of Fragile-to-Strong Crossover in Deeply Supercooled Water Confined in Nanoporous Silica Matrices," J. Phys.: Condens. Matter, in press.

Liu, L., Tan, G., Agarwal, V., Bose, A., He, J., McPherson, G.L., John, V.T., "A Simple Extrusion Method for the Synthesis of Aligned Silica Nanowires Using the Template of a Rigid Surfactant Mesophase," Chem. Commun. **36**, 4517 (2005).

Liu, Y., Fratini, E., Baglioni, P., Chen, W.-R., Chen, S.-H., "Effective Long-Range Attraction Between Protein Molecules in Solutions Studied by Small Angle Neutron Scattering," Phys. Rev. Lett. **95**, 118102 (2005).

Liu, Y., Fratini, E., Baglioni, P., Chen, W.-R., Porcar, L., Chen, S.-H., "Reply to: Effective Long-Range Attraction Between Protein Molecules in Solutions Studied by Small Angle Neutron Scattering," Phys. Rev. Lett. **96**, 219802 (2006).

Lodge, T.P., Bang, J., Li, Z., Hillmyer, M.A., Talmon, Y., "Strategies for Controlling Intra-and Intermicellar Packing in Block Copolymer Solutions: Illustrating the Flexibility of the Self-Assembly Toolbox," Faraday Discuss. **128**, 1 (2005).

Loizou, E., Butler, P., Porcar, L., Schmidt, G., "Dynamic Responses in Nanocomposite Hydrogels," Macromol. **39** (4), 1614 (2006).

Loizou, E., Porcar, L., Butler, P., Malwitz, M., Schmidt, G., "Dynamic Responses in Polymer- Clay Gels," Mater. Res. Soc. Symp. Proc. **840**, Q02-07 (2005).

Long, T.M., Simmons., B.A., McElhanon, J.R., Kline, S.R., Wheeler, D.R., Loy, D.A., Rahimian, K., Zifer, T., Jamison, G.M., "Metathesis Depolymerization for Removable Surfactant Templates," Langmuir **21** (20), 9365 (2005).

Lu, L., Chabot-Couture, G., Zhao, X., Hancock, J.N., Kaneko, N., Vajk, O.P., Yu, G., Grenier, S., Kim, Y.J., Casa, D., Gog, T., Greven, M., "Charge-Transfer Excitations in the Model Superconductor $HgBa_2CuO_{4+\delta}$," Phys. Rev. Lett. **95**, 217003 (2005).

Ludlow, D.J., Calebrese, C.M., Yu, S.H., Dannehy, C.S., Jacobson, D.L., Hussey, D.S., Arif, M., Jensen, M.K., Eisman, G.A., "PEM Fuel Cell Membrane Hydration Measurement by Neutron Imaging," J. Power Sources, in press.

Lynn, J.W., Huang, Q., Cava, R.J., Lee, Y.S., "Structure and Dynamics of Na_xCoO_2 and the Hydrated Superconductor," Mater. Res. Symp. Proc. **840**, Q04-04 (2005).

Ma, M., Chernova, N.A., Zavalij, P.Y., Whittingham, M.S., "Structural and Electrochemical Properties of $LiMn_{0.4}Ni_{0.4}Co_{0.2}O_2$," Mater. Res. Soc. Symp. Proc. **835**, K11-03 (2005).

Maciejczyk, P.B., Zeisler, R.L., Hwang, J.-S., Thurston, G.D., Chen, L.C., "Characterization of Size-Fractionated World Trade Center Dust and Estimation of Relative Dust Contribution to Ambient Particulate Concentrations," Am. Chem. Soc. Symp. Ser. **919**, 114 (2006).

Mackey, E.A., Cronise, M.P., Fales, C.N., Greenberg, R.R., Leigh, S.D., Long, S.E., Marlow, A.F., Murphy, K.E., Oflaz, R., Sieber, J.R., Rearick, M.S., Wood, L.J., Yu, L.L., Wilson, S.A., Briggs, P.H., Brown, Z.A., Budahn, J., Kane, P.F., Hall Jr., W.L., "Development and Certification of the New SRM 695 Trace Elements in Multi-Nutrient Fertilizer," Anal. Bioanal. Chem., in press.

Macquart, R., Kim, S.-J., Gemmill, W.R., Stalick, J.K., Lee, Y., Vogt, T., zur Loye, H.-C., "Synthesis, Structure, and Magnetic Properties of Sr_2NiOsO_6 and Ca_2NiOsO_6: Two New Osmium-Containing Double Perovskites," Inorg. Chem. **44** (26), 9676 (2005).

Magbitang, T., Lee, V.Y., Miller, R.D., Toney, M.F., Lin, Z., Briber, R.M., Kim, H.C., Hedrick, J.L., "Templating Organosilicate Vitrification Using Unimolecular Self-Organizing Polymers: Evolution of Morphology and Nanoporosity Development With Network Formation," Adv. Mater. **17** (8), 1031 (2005).

Majkrzak, C.F., Berk, N.F., Krueger, S., Perez-Salas, U.A., "Structural Investigations of Membranes in Biology by Neutron Reflectometry," in *Neutron Scattering in Biology - Techniques and Applications*, edited by Fitter, J., Gutberlet, T., Katsaras, J., (Springer, Berlin), p. 225 (2006).

Majkrzak, C.F., O'Donovan, K.V., Berk, N.F., "Polarized Neutron Reflectometry," in *Neutron Scattering From Magnetic Materials*, edited by Chatterji, T., (Elsevier, Amsterdam), p. 397 (2006).

Malardier-Jugroot, C., van de Ven, T.G.M., Cosgrove, T., Richardson, R.M., Whitehead, M.A., "Novel Self-Assembly of Amphiphilic Copolymers into Nanotubes: Characterization by Small-Angle Neutron Scattering," Langmuir **21** (22), 10179 (2005).

Mamontov, E., "Observation of Fragile-to-Strong Liquid Transition in Surface Water in CeO_2," J. Chem. Phys. **123**, 171101 (2005).

Mamontov, E., Burnham, C.J., Chen, S.-H., Moravsky, A.P., Loong, C.-K., de Souza, N.R., Kolesnikov, A.I., "Dynamics of Water Confined in Single-and Double-Wall Carbon Nanotubes," J. Chem. Phys. **124**, 194703 (2006).

Mamontov, E., Kumzerov, Y.A., Yakhrushev, S.B., "Diffusion of Benzene Confined in the Oriented Nanochannels of Chrysotile Asbestos Fibers," Phys. Rev. E **72**, 051502 (2005).

Mamontov, E., Udovic, T.J., Rush, J.J., Isnard, O., "Dynamics of Hydrogen in $Pr_2Fe_{17}H_4$ and $Pr_2Fe_{17}H_5$," Mater. Res. Soc. Symp. Proc. **885**, A08-07 (2006).

Mamontov, E., Udovic, T.J., Rush, J.J., Isnard, O., "Dynamics of Hydrogen in $Pr_2Fe_{17}H_4$ and $Pr_2Fe_{17}H_5$ Studied by Quasielastic Neutron Scattering," J. Alloys Compd., in press.

Mansour, F., Dimeo, R.M., Peemoeller, H., "Anomalous Behavior of Confined-Supercooled Water Near the Bulk Water Hypothetical 2nd Critical Temperature," Mater. Res. Soc. Symp. Proc. **790**, P05-05 (2004).

Maple, M.B., Butch, N.P., Bauer, E.D., Zapf, V.S., Ho, P.-C., Wilson, S.D., Dai, P., Adroja, D.T., Lee, S.-H., Chung, J.-H., Lynn, J.W., "Non-Fermi Liquid Behavior and Quantum Criticality in $Sc_{1-x}U_xPd_3$ and $URu_{2-x}Re_xSi_2$," Physica B **378-380**, 911 (2006).

Maple, M.B., Butch, N.P., Frederick, N.A., Ho, P.-C., Jeffries, J.R., Sayles, T.A., Yanagisawa, T., Yuhasz, W.M., Chi, S., Kang, H.J., Lynn, J.W., Dai, P., McCall, S.K., McElfresh, M.W., Fluss, M.J., Henkie, Z., Pietraszko, A., "Field-Dependent Ordered Phases and Kondo Phenomena in the Filled Skutterudite Compound $PrOs_4As_{12}$," Proc. National Academy of Sciences **103**, 6783 (2006).

Mason, P.E., Neilson, G.W., Kline, S.R., Dempsey, C.E., Brady, J.W., "Nanometer-Scale Ion Aggregates in Aqueous Electrolyte Solutions: Guanidinium Carbonate," J. Phys. Chem. B **110** (27), 13477 (2006).

Mason, T.G., Graves, S.M., Wilking, J.N., Lin, M.-Y., "Effective Structure Factor of Osmotically Deformed Nanoemulsions," J. Phys. Chem. B, in press.

Masuda, T., Zheludev, A., Manaka, H., Regnault, L.-P., Chung, J.-H., Qiu, Y., "Dynamics of Composite Haldane Spin Chains in IPA-$CuCl_3$," Phys. Rev. Lett. **96**, 047210 (2006).

Masuda, T., Zheludev, A., Sales, B., Imai, S., Uchinokura, K., Park, S., "Magnetic Excitations in the Weakly Coupled Spin Dimers and Chains Material $Cu_2Fe_2Ge_4O_{13}$," Phys. Rev. B **72**, 094434 (2005).

Matan, K., Grohol, D., Nocera, D.G., Yildirim, T., Harris, A.B., Lee, S.H., Nagler, S.E., Lee, Y.S., "Spin Waves in the Frustrated Kagomé Lattice Antiferromagnet $KFe_3(OH)_6(SO_4)_2$," Phys. Rev. Lett. **96**, 247201 (2006).

Matos, M.A., White, L.R., Tilton, R.D., "Electroosmotically Enhanced Mass Transfer Through Polyacrylamide Gels," J. Colloids Inter. Sci. **300** (1), 429 (2006).

Matsuura, M., Hirota, K., Gehring, P.M., Chen, W., Ye, Z.-G., Shirane, G., "Composition Dependence of the Diffuse Scattering in the Relaxor $(1\text{-}x)Pb(Mg_{1/3}Nb_{2/3})O_3\text{-}xPbTiO_3$ (x = 0 and 0.10)," Physica B, in press.

McQueeney, R.J., Yethiraj, M., Montfrooij, W., Gardner, J.S., Metcalf, P., Honig, J.M., "Investigation of the Presence of Charge Order in Magnetite by Measurement of the Spin Wave Spectrum," Phys. Rev. B **73**, 174409 (2006).

McQueeney, R.J., Yethiraj, M., Montfrooij, W., Gardner, J.S., Metcalf, P., Honig, J.M., "Possible Large Spin-Phonon Coupling in Magnetite," Physica B, in press.

Mihailescu, M., Gawrisch, K., "The Structure of Polyunsaturated Lipid Bilayers Important for Rhodopsin Function: A Neutron Diffraction Study," Biophys. J. **90**, L04 (2006).

Mildner, D.F.R., Hammouda, B., Kline, S.R., "A Refractive Focusing Lens System for Small-Angle Neutron Scattering," J. Appl. Cryst. **38** (6), 979 (2005).

Motoyama, E.M., Mang, P.K., Petitgrand, D., Yu, G., Vajk, O.P., Vishik, I.M., Greven, M., "Magnetic Field Effect on the Superconducting Magnetic Gap of $Nd_{1.85}Ce_{0.15}CuO_4$," Phys. Rev. Lett. **96**, 137002 (2006).

Moyerman, S., Eckert, J.C., Borchers, J.A., Perdue, K.L., Doucet, M., Sparks, P.D., Carey, M.J., "Magnetic Structure Variations During Giant Magnetoresistance Training in Spin Valves With Picoscale Antiferromagnetic Layers," J. Appl. Phys. **99**, 08R505 (2006).

Moyerman, S.M., Gannett, W., Borchers, J.A., Doucet, M., Carey, M.J., Sparks, P.D., Eckert, J.C., "Ferromagnetic Relaxation in Spin Valves With Pico-Scale Antiferromagnetic Layers," IEEE Trans. Mag., in press.

Nakatsuji, S., Nambu, Y., Tonomura, H., Sakai, O., Jonas, S., Broholm, C., Tsunetsugu, H., Qiu, Y., Maeno, Y., "Spin Disorder on a Triangular Lattice," Science **309**, 1697 (2005).

Neff, H., Blomster, J.E., Glascock, M.D., Bishop, R.L., Blackman, M.J., Coe, M.D., Cowgill, G.L., Cyphers, A., Diehl, R.A., Houston, S., Joyce, A.A., Lipo, C.P., Winter, M., "Smokescreens in the Provenance Investigation of Early Formative Mesoamerican Ceramics," Latin. Am. Antiq. **17** (1), 104 (2006).

Neff, H., Blomster, J.E., Glascock, M.D., Bishop, R.L., Blackman, M.J., Coe, M.D., Cowgill, G.L., Diehl, R.A., Houston, S., Joyce, A.A., Lipo, C.P., Stark, B.L., Winter, M., "Methodological Issues in the Provenance Investigation of Early Formative Mesoamerican Ceramics," Latin Am. Antiq. **17** (1), 54 (2006).

Neumann, D.A., "Neutron Scattering and Hydrogenous Materials," Mater. Today **9** (1-2), 34 (2006).

Ni, S., Yin, W., Ferguson-McPherson, M.K., Satija, S.K., Morris, J.R., Esker, A.R., "Nanoscale Surface Patterns From 10_3 Single Molecule Helices of Biodegradable Poly(L-Lactic Acid)," Langmuir **22** (14), 5969 (2006).

Nico, J.S., Dewey, M.S., Gilliam, D.M., Wietfeldt, F.E., Fei, X., Snow, W.M., Greene, G.L., Pauwels, J., Eykens, R., Lamberty, A., Van Gestel, J., Scott, R.D., "Measurement of the Neutron Lifetime by Counting Trapped Protons in a Cold Neutron Beam," Phys. Rev. C **71**, 055502 (2005).

Nico, J.S., Snow, M.S., "Fundamental Neutron Physics," Annu. Rev. Nucl. Part. Sci. **55**, 27 (2005).

Nixon, B.T., Yennawar, H.P., Doucleff, M., Pelton, J.G., Wemmer, D.E., Krueger, S., Kondrashkina, E., "SAS Solution Structures of the Apo and $Mg^{2+}BeF_3$ — Bound Receiver Domain of DctD from *Sinorbizobium Meliloti*," Biochem. **44** (42), 13962 (2005).

Norman, A.I., Ho, D.L., Karim, A., Amis, E.J., "Phase Behavior of Block Co-Poly(ehylene Oxide-Butylene Oxide), $E_{18}B_9$ in Water, by Small Angle Neutron Scattering," J. Colloid Interface Sci. **288** (1), 155 (2005).

Norman, A.I., Ho, D.L., Lee, J.-H., Karim, A., "Spontaneous Formation of Vesicles of Diblock Copolymer EO_6BO_{11} in Water: A SANS Study," J. Phys. Chem. B **110** (1), 62 (2006).

Norman, A.I., Ivkov, R., Forbes, J.G., Greer, S.C., "The Polymerization of Actin: Structural Changes From Small-Angle Neutron Scattering," J. Chem. Phys. **123** (15), 154904 (2005).

Oates, K.M.N., Krause, W.E., Jones, R.L., Colby, R.H., "Rheopexy of Synovial Fluid and Protein Aggregation," J. Royal Soc. Inter. **3** (6), 167 (2006).

O'Brien, E.P., White, C.C., Vogt, B.D., "Correlating Interfacial Moisture Content and Adhesive Fracture Energy of Polymer Coatings on Different Surfaces," Adv. Eng. Mater. **8** (1-2), 114 (2006).

Ohn, H., Hussey, D., Jacobson, D., Arif, M., Nguyen, T., "The Capillary Pressure Properties of Gas Diffusion Materials Used in PEM Fuel Cells," ECS Trans. **1** (6), 481 (2006).

Oliveira, M.C., Baptista, A.J., Alves, J.L., Menezes, L.F., Green, D.E., Gnäupel-Herold, T., Iadicola, M.A., Foecke, T., Stoughton, T.B., "Two Stage Forming: Experimental and FE Analysis," in *Proceedings of the International Deep Drawing Research Group Conference* (Porto, Portugal), p. 279 (2006).

Ou-Yang, W.-C., Chang, C.-S., Chen, H.-L., Tsao, C.-S., Peng, K.-Y., Chen, S.-A., Han, C.C., "Micelle Like Aggregates in Solutions of Semirigid Hairy-Rod Polymers," Phys. Rev. E **72**, 031802 (2005).

Owejan, J., Trabold, T., Jacobson, D.L., Baker, D., Hussey, D.S., Arif, M., "*In Situ* Investigation of Water Transport in an Operating PEM Fuel Cell Using Neutron Radiography: Part 2 - Transient Water Accumulation in and Interdigitated Cathode Flow Field," Int. J. Heat Mass Transfer, in press.

Owen, T., Pynn, R., Martinez, J.S., Butler, A., "Micelle-to-Vesicle Transition of an Iron-Chelating Microbial Surfactant, Marinobactin E," Langmuir **21** (26), 12109 (2005).

Pal, D., DeBeer-Schmitt, L., Bera, T., Cubitt, R., Dewhurst, C.D., Jun, J., Zhigadlo, N.D., Karpinski, J., Kogan, V.G., Eskildsen, M.R., "Measuring the Penetration Depth Anisotropy in MgB_2 Using Small-Angle Neutron Scattering," Phys. Rev. B **73** (1), 012513 (2006).

Paul, R.L., "Cold Neutron Prompt Gamma-Ray Activation Analysis for Characterization of Hydrogen Storage Materials and Related Materials," Mater. Res. Soc. Symp. Proc. **927E**, EE03-05 (2006).

Paul, R.L., "Measurement of Hydrogen in Advanced Materials by Cold Neutron Prompt Activation Analysis," AIP Conf. Proc. **837** (1), 223 (2006).

Paul, R.L., "The Use of k_0 Factors in Cold Neutron Prompt Gamma-Ray Activation Analysis," Trans. Am. Nucl. Soc. **93**, 882 (2005).

Pencer, J., Krueger, S., Adams, C.P., Katsaras, J., "Method of Separated Form Factors for Polydisperse Vesicles," J. Appl. Cryst. **39**, 293 (2006).

Pencer, J., Mills, T., Anghel, V., Krueger, S., Epand, R.M., Katsaras, J., "Detection of Submicron-Sized Raft-Like Domains in Membranes by Small-Angle Neutron Scattering," Euro. Phys. J. E **18** (4), 447 (2005).

Pencer, J., Nieh, M.-P., Harroun, T.A., Krueger, S., Adams, C., Katsaras, J., "Bilayer Thickness and Thermal Response of Dimyristoylphosphatidycholine Unilameller Vesicles Containing Cholesterol, Ergosterol and Lanosterol: A Small-Angle Neutron Scattering Study," Biochim. Biophys. Acta **1720** (1-2), 84 (2005).

Peretich, M.E., Downing, R.G., "A Comparison of Charged Particle Detectors Using Neutron Depth Profiling," Trans. Am. Nucl. Soc. **93**, 866 (2005).

Peterson, V.K., Brown, C.M., Livingston, R.A., "Quasielastic and Inelastic Neutron Scattering Study of the Hydration of Monoclinic and Triclinic Tricalcium Silicate," Chem. Phys., in press.

Peterson, V.K., Garci Juenger, M.C., "Time Resolved Quasielastic Neutron Scattering Study of the Hydration of Tricalcium Silicate: Effects of $CaCl_2$ and Sucrose," Physica B, in press.

Peterson, V.K., Neumann, D.A., Livingston, R.A., "Effect of NaOH on the Kinetics of Tricalcium Silicate Hydration: A Quasielastic Neutron Scattering Study," Chem. Phys. Lett. **419**, 16 (2006).

Peterson, V.K., Neumann, D.A., Livingston, R.A., "Hydration of Cement: The Application of Quasielastic and Inelastic Neutron Scattering," Physica B, in press.

Peterson, V.K., Neumann, D.A., Livingston, R.A., "Inelastic Neutron Scattering Investigation of Hydrating Tricalcium and Dicalcium Silicate Mixture Pastes: $Ca(OH)_2$ Formation and Evolution of Strength," J. Mater. Res. **21** (7), 1836 (2006).

Phelan, D., Louca, D., Rosenkranz, S., Lee, S.-H., Qiu, Y., Chupas, P.J., Osborn, R., Zheng, H., Mitchell, J.F., Copley, J.R.D., Sarrao, J.L., Moritomo, Y., "Nanomagnetic Droplets and Implications to Orbital Ordering in $La_{1-x}Sr_xCoO_3$," Phys. Rev. Lett. **96**, 027201 (2006).

Pittler, J., Bu, W., Vaknin, D., Travesset, A., McGillivray, D.J., Lösche, M., "Charge Inversion at Minute Electrolyte Concentrations," Phys. Rev. Lett. **97**, 046102 (2006).

Pivovar, A.M., Curtis, J.E., Leao, J.B., Chesterfield, R.J., Frisbie, C.D., "Structural and Vibrational Characterization of the Organic Semiconductor Tetracene as a Function of Pressure and Temperature," Chem. Phys. **325**, 138 (2006).

Pozzo, D.C., Walker, L.M., "Small-Angle Neutron Scattering of Silica Nanoparticles Templated in PEO-PPO-PEO Cubic Crystals," Colloids and Surfaces A: Physicochem. Eng. Aspects, in press.

Pozzo, D.C., Walker, L.M., "Three-Dimensional Nanoparticle Arrays Templated by Self-Assembled Block-Copolymer Gels," Macromol. Symp. **227**, 203 (2005).

Prabhu, V.M., "Counterion Structure and Dynamics in Polyelectrolyte Solutions," Curr. Opin. Colloid Interface Sci. **10**, 2 (2005).

Prime, M.B., Gnäupel-Herold, T., Baumann, J.A., Lederich, R.J., Bowden, D.M., Sebring, R.J., "Residual Stress Measurements in a Thick, Dissimilar Aluminum Alloy Friction Stir Weld," Acta Mater., in press.

Prince, E., Toby, B.H., "A Comparison of Methods for Modeling the Effect of Axial Divergence in Powder Diffraction," J. Appl. Cryst. **38**, 804 (2005).

Pushin, D.A., Arif, M., Jacobson, D.L., Doe, C.K., Cory, D.G., "Reciprocal Space Neutron Imaging," Physica B, in press.

Rainville, S., Thompson, J.K., Myers, E.G., Brown, J.M., Dewey, M.S., Kessler Jr., E.G., Deslattes, R.D., Börner, H.G., Jentschel, M., Mutti, P., Pritchard, D.E., "A Direct Test of $E = mc^2$," Nature **438**, 1096 (2005).

Ramakrishnan, S., Gopalakrishnan, V., Zukoski, C.F., "Clustering and Mechanics in Dense Depletion and Thermal Gels," Langmuir **21** (1), 9917 (2005).

Ramazanoglu, M.K., Clegg, P.S., Wakimoto, S., Birgeneau, R.J., Noro, S., "Neutron Scattering and Magnetization Studies of $Ba_2Cu_{2.95}Co_{0.05}O_4Cl_2$: A Decorated Two-Dimensional Antiferromagnet," Phys. Rev. B **73**, 054418 (2006).

Rappl, T.J., Balsara, N.P., "Does Coarsening Begin During the Initial Stages of Spinodal Decomposition," J. Chem. Phys. **122**, 214903 (2005).

Ratcliff II, W., Kiryukhin, V., Kenzelmann, M., Lee, S.-H., Erwin, R., Schefer, J., Hur, N., Park, S., Cheong, S.-W., "Magnetic Phase Diagram of the Colossal Magnetoelectric $DyMn_2O_5$," Phys. Rev. B **72**, 060407(R) (2005).

Regan, K.A., Huang, Q., Lee, M., Ramirez, A.P., Cava, R.J., "Structure and Magnetism of $NaRu_2O_4$ and $Na_{2.7}Ru_4O_9$," J. Solid State Chem. **179**, 195 (2006).

Rodgers, L.E., Holden, P.J., Knott, R.B., Finnie, K.S., Bartlett, J.R.Foster, L.J.R., "Effect of Sol-Gel Encapsulation on Lipase Structure and Function: A Small Angle Neutron Scattering Study," J. Sol-Gel Sci. Technol. **33**, 65 (2005).

Rogado, N.S., Li, J., Sleight, A.W., Subramanian, M.A., "Magnetocapacitance and Magnetoresistance Near Room Temperature in a Ferromagnetic Semiconductor: La_2NiMnO_6," Adv. Mater. **17**, 2225 (2005).

Roh, J.H., Curtis, J.E., Azzam, S., Novikov, V.N., Peral, I., Chowdhuri, Z., Gregory, R.B., Sokolov, A.P., "Influence of Hydration on the Dynamics of Lysozyme," Biophys. J., in press.

Rowe, J.M., "Issues in the Design of a Cold Neutron Source," in Proceedings of the International Symposium on Research Reactor and Neutron Science (Daejon, Korea), p. 579 (2005).

Rubatat, L., Shi, Z., Diat, O., Holdcroft, S., Frisken, B.J., "Structural Study of Proton-Conducting Fluorous Block Copolymer Membranes," Macromol. **39** (2), 720 (2006).

Ruegg, M.L., Reynolds, B.J., Lin, M.Y., Lohse, D.J., Balsara, N.P., "Microphase and Macrophase Separation in Multicomponent A/B/A-C Polymer Blends with Attractive and Repulsive Interactions," Macromol. **39** (3), 1125 (2006).

Rule, K.C., Ruff, J.P.C., Gaulin, B.D., Dunsiger, S.R., Gardner, J.S., Clancy, J.P., Lewis, M.J., Dabkowska, H.A., Mirebeau, I., Manuel, P., Qiu, Y., Copley, J.R.D., "Field-Induced Order and Spin Waves in the Pyrochlore Antiferromagnet $Tb_2Ti_2O_7$," Phys. Rev. Lett. **96**, 177201 (2006).

Santonicola, G.M., Kaler, E.W., "Mixtures of *n*-Octyl-β-D-Glucoside and Triethylene Glycol Mon-*n*-Octyl Ether: Phase Behavior and Micellar Structure Near the Liquid-Liquid Phase Boundary," Langmuir **21** (22), 9955 (2005).

Schoen, K., Snow, W.M., Kaiser, H., Werner, S.A., "Virtual Excitation and Multiple Scattering Correction Terms to the Neutron Index of Refraction for Hydrogen," J. Res. Natl. Inst. Stand. Tech. **110** (3), 259 (2005).

Seo, P.-N., Bowman, J.D., Calarco, J.R., Chupp, T.E., Cianciolo, T.V., Desai, D., De Souza, R.T., O'Donnell, J.M., Frlež, E., Gentile, T., Greene, G.L., Grzywacz, R.K., Gudkov, V., Hersman, F.W., Jones, R.L., Mitchell, G.S., Penttilä, S.I., Počanić, D., Rykaczewski, K.P., Snow, W.M., Wilburn, W.S., Young, G.R., "A Precision Measurement of Neutron β-Decay Angular Correlations With Pulsed Cold Neutrons-The AbBA Experiment," AIP Conf. Proc. **769**, 704 (2005).

Seo, P.-N., Bowman, J.D., Carlini, R.D., Chupp, T.E., Covrig, S.D., Dabaghyan, M., Freedman, S.J., Gentile, T., Gericke, M.T., Gillis, R.C., Greene, G.L., Hersman, F.W., Ino, T., Jones, G.L., Kandes, G., Lauss, B., Leuschner, M.B., Lozowski, W.R., Mahurin, R., Mason, M., Masuda, Y., Mitchell, G.S., Muto, S., Nann, H., Page, S.A., Penttilä, S.I., Ramsay, W.D., Santra, S., Sharapov, E.I., Smith, T.B., Snow, W.M., Wilburn, W.S., Yuan, V., Zhu, H., "Measurement of Parity-Violating Gamma-Ray Asymmetry in Compound Nuclei With Cold Neutrons," AIP Conf. Proc. **819**, 81 (2006).

Seo, P.-N., Bowman, J.D., Carlini, R.D., Chupp, T.E., Coulter, K.P., Dabaghyan, M., Dawkins, M., Desai, D., Freedman, S.J., Gentile, T., Gericke, M.T., Gillis, R.C., Greene, G.L., Ino, T., Ishimoto, S., Jones, G.L., Lauss, B., Leuschner, M.B., Lozowski, B., Mahurin, R., Masuda, Y., Mitchell, G.S., Muto, S., Nann, H., Page, S.A., Penttilä, S.I., Ramsay, W.D., Santra, S., Sharapov, E.I., Smith, T.B., Snow, W.M., Wilburn, W.S., Yuan, V., Zhu, H., "The 2004 NPDGamma Commissioning Run-Measurement of Parity-Violating Gamma-Ray Asymmetries in Neutron Capture on Al, Cu, Cl, In, and B," AIP Conf. Proc. **769**, 696 (2005).

Seo, Y.-S., Satija, S.K., "No Intrinsic Depletion Layer on a Polystyrene Thin Film at a Water Interface," Langmuir, in press.

Shang, T., Smith, K.A, Hatton, T.A., "Self-Assembly of a Nonionic Photoresponsive Surfactant Under Varying Irradiation Conditions: A Small-Angle Neutron Scattering and Cyro-TEM Study," Langmuir **22** (4), 1436 (2006).

Shapiro, S.M., Xu, G., Gu, G., Gardner, J., Fonda, R.W., "Lattice Dynamics of the High-Temperature Shape-Memory Alloy Nb-Ru," Phys. Rev. B **73**, 214114 (2006).

Shaw, W.J., Ferris, K.F., Krueger, S., Perez-Salas, U., Silin, V., McGillivray, D.J., Campbell, A.A., Paine, M.L., Snead, M.L., "The Orientation of an Amelogenin on Hydroxyapatite Determined Using Neutron Scattering, Solid-State NMR and Computational Methods," in *Proceedings of the 8th International Conference on the Chemistry and Biology of Mineralized Tissues*, (Banff, Alberta, Canada), p. 150 (2005).

Shirane, G., Xu, G., Gehring, P.M., "Dynamics and Structure of PMN and PZN," Ferroelectrics **321**, 7 (2005).

Silverstein, M.S., Bauer, B.J., Hedden, R.C., Lee, H.-J., Landes, B.G., "SANS and XRR Porosimetry of a Polyphenylene Low-*k* Dielectric," Macromol. **39** (8), 2998 (2006).

Simons, D., Kim, K., Benbalagh, R., Bennett, J., Chew, A., Gehre, D., Hasegawa, T., Hitzman, C., Ko, J., Lindstrom, R., MacDonald, B., Magee, C., Montgomery, N., Peres, P., Ronsheim, P., Yoshikawa, S., Schuhmacher, M., Stockwell, W., Sykes, D., Tomita, M., Toujou, F., Won, J., "Round-Robin Study of Arsenic Implant Dose Measurement in Silicon by SIMS," Appl. Surf. Sci., in press.

Sirota, E.B., "Physical Structure of Asphaltenes," Energy & Fuels **19** (5), 1290 (2005).

Skripov, A.V., Soloninin, A.V., Buzlukov, A.L., Voyevodina, L.S., Cook, J.C., Udovic, T.J., Hempelmann, R., "Hydrogen Motion in C14-type $HfCr_2H_x$: Quasielastic Neutron Scattering and NMR Studies," J. Phys.: Condens. Matter **17** (33), 5011 (2005).

Smith, G.S., Kuhl, T.L., Hamilton, W.A., Mulder, D.J., Satija, S., "Structure of Confined Polymer Thin Films Subject to Shear," Physica B, in press.

Smith, K.A., Hatton, T.A., Shang, T., Cicciarelli, B., "A New Class of Nonionic Photosensitive Surfactants: Some Insights Concerning Conformations," 4th SMA Programme on Molecular Engineering of Biological and Chemical Systems, http://hdl.handle.net/1721.1/7486 (2005).

Sokolov, A.P., Gregory, R.B., "Internal Dynamics of Proteins and DNA: Analogy to Glass-Forming Systems," in *Neutron Scattering in Biology - Techniques and Applications*, edited by Fitter, J., Gutberlet, T., Katsaras, J., (Springer, Berlin), p. 485 (2006).

Soles, C.L., Tsai, A.M., Cicerone, M.T., "Glass Dynamics and the Preservation of Proteins," in *Misbehaving Proteins: Protein (Mis)Folding, Aggregation, and Stability*, edited by Murphy, R.M., Tsai, A.M., (Springer, New York), p. 193 (2006).

Stalick, J.K., Waterstrat, R.M., "The Zirconium-Platinum Phase Diagram," J. Alloys Compd., in press.

Stanley, C.B., Hong, H., Strey, H.H., "DNA Cholesteric Pitch as a Function of Density and Ionic Strength," Biophys. J. **89**, 2552 (2005).

Stanley, C.B., Rau, D.C., "Preferential Hydration of DNA: The Magnitude and Distance Dependence of Alcohol and Polyol Interactions," Biophys. J., in press.

Stefanescu, E.A., Dundigalla, A., Ferreiro, V., Loizou, E., Porcar, L., Negulescu, I., Garno, J., Schmidt, G., "Supramolecular Structures in Nanocomposite Multilayered Films," Phys. Chem. Chem. Phys. **8**, 1739 (2006).

Stock, C., Buyers, W.J.L., Yamani, Z., Broholm, C.L., Chung, J.-H., Tun, Z., Liang, R., Bonn, D., Hardy, W.N., Birgeneau, R.J., "Central Mode and Spin Confinement Near the Boundary of the Superconducting Phase in $YBa_2Cu_3O_{6.353}$ (T_c = 18 K)," Phys. Rev. B **73**, 100504(R) (2006).

Stoltz, C., Ramesha, K., Piccoli, P., Toby, B.H., Eichhorn, B.W., "$A_{0.3}ZrNF_{1.3}$ Phases (A = Na, K) With Layered ZrNCl-Type Structures Prepared by Anion Metathesis," Chem. Mater. **17** (21), 5291 (2005).

Stone, M.B., Broholm, C., Reich, D.H., Tchernyshyov, O., Vorderwisch, P., Harrison, N., "Quantum Criticality in an Organic Magnet," Phys. Rev. Lett. **96**, 257203 (2006).

Stone, M.B., Lumsden, M.D., Jin, R., Sales, B.C., Mandrus, D., Nagler, S.E., Qiu, Y., "Temperature-Dependent Bilayer Ferromagnetism in $Sr_3Ru_2O_7$," Phys. Rev. B **73**, 174426 (2006).

Stone, M.B., Tian, W., Granroth, G.E., Lumsden, M.D., Chung, J.-H., Mandrus, D.G., Nagler, S.E., "Spin-Dynamics of the Low-Dimensional Magnet $(CH_3)_2NH_2CuCl_3$," Physica B, in press.

Stone, M.B., Zaliznyak, I.A., Hong, T., Broholm, C.L., Reich, D.H., "Quasiparticle Breakdown in a Quantum Spin Liquid," Nature **440** (7081), 187 (2006).

Stover, T., Lamaze, G., "Compton Suppression for Neutron Activation Analysis Applications at the National Institute of Standards and Technology (NIST)," Nucl. Instrum. Meth. Phys. Res. B **241**, 223 (2005).

Sturgeon, R.E., Willie, S.N., Yang, L., Greenberg, R., Spatz, R.O., Chen, Z., Scriver, C., Clancy, V., Lam, J.W., Thorrold, S., "Certification of a Fish Otolith Reference Material in Support of Quality Assurance for Trace Element Analysis," J. Anal. At. Spectrom. **20** (10), 1067 (2005).

Sun, Y.P., Huang, Q.Z., Wu, L., He, M., Chen, X.L., "A Neutron Powder Investigation of the Structure of $KCaCO_3F$ at Various Temperatures," J. Alloys Compd. **417** (1-2), 13 (2006).

Swallen, S.F., Mapes, M.K., Kim, Y.S., McMahon, R.J., Ediger, M.D., Satija, S.K., "Neutron Reflectivity Measurements of the Transitional Motion of Tris (Naphthylbenzene) at the Glass Transition Temperature," J. Chem. Phys. **124**, 184501 (2006).

Thomas III, S.W., Long, T.M., Pate, B.D., Kline, S.R., Thomas, E.L., Swager, T.M., "Perpendicular Organization of Macromolecules: Synthesis and Alignment Studies of a Soluble Poly(iptycene)," J. Am. Chem. Soc. **127** (51), 17976 (2005).

Thundathil, M.A., Jones, C.Y., Snyder, G.J., Haile, S.M., "Nonstoichiometry, Structure, and Electrical Properties of '$SrPrO_3$'," Chem. Mater. **17** (20), 5146 (2005).

Toby, B.H., "CMPR- A Powder Diffraction Toolkit," J. Appl. Cryst. **38**, 1040 (2005).

Trabold, T., Owejan, J., Jacobson, D.L., Arif, M., Huffman, P., "*In Situ* Investigation of Water Transport in an Operating PEM Fuel Cell Using Neutron Radiography: Part 1- Experimental Method and Serpentine Flow Field Results," Int. J. Heat Mass Transfer, in press.

Tremsin, A.S., Feller, W.B., Downing, R.G., Mildner, D.F.R., "The Efficiency of Thermal Neutron Detection and Collimation With Microchannel Plates of Square and Circular Geometry," IEEE Trans. Nucl. Sci. **52** (5), 1739 (2005).

Triolo, R., Lo Celso, F., Benfante, V., Gorgoni, C., Barker, J., Butler, P.D., Ruffo, I., "Fingerprinting White Marbles of Archaeometric Interest by Means of Combined SANS and USANS," Nuovo Cimento, in press.

Tsianou, M., Alexandridis, P., "Molecular Recognition Between Cyclodextrine and Hydrophobic Domains for Control of Associating Polymer Networks," Polym. Prepr. **46** (2), 1123 (2005).

Tung, S.-H., Huang, Y.-E., Raghavan, S.R., "A New Reverse Wormlike Micellar System: Mixtures of Bile Salt and Lecithin in Organic Liquids," J. Am. Chem. Soc. **128** (7), 5751 (2006).

Tuteja, A., Mackay, M.E., Hawker, C.J., Van Horn, B., Ho, D.L., "Molecular Architecture and Rheological Characterization of Novel Intramolecularly Crosslinked Polystyrene Nanoparticles," J. Polym. Sci., Part B: Polym. Phys. **44**, 1930 (2006).

Valincius, G., McGillivray, D.J., Febo-Ayala, W., Vanderah, D.J., Kasianowicz, J.J., Lösche, M., "Enzyme Activity to Augment the Characterization of Tethered Bilayer Membranes," J. Phys. Chem. B **110** (21), 10213 (2006).

Vajk, O.P., Kenzelmann, M., Lynn, J.W., Kim, S.B., Cheong, S.-W., "Neutron-Scattering Studies of Magnetism in Multiferroic $HoMnO_3$," J. Appl. Phys. **99**, 08E301 (2006).

Viciu, L., Bos, J.W.G., Zandbergen, H.W., Huang, Q., Foo, M.L., Ishiwata, S., Ramirez, A.P., Lee, M., Ong, N.P., Cava, R.J., "Crystal Structure and Elementary Properties of Na_xCoO_2 (x = 0.32, 0.51, 0.6, 0.75, and 0.92) in the Three-Layer $NaCoO_2$ Family," Phys. Rev. B **73**, 174104 (2006).

Viciu, L., Huang, Q., Cava, R.J., "Stoichiometric Oxygen Content in Na_xCoO_2," Phys. Rev. B **73**, 212107 (2006).

Vogt, B.D., Kang, S., Prabhu, V.M., Rao, A., Lin, E.K., Satija, S.K., Turnquest, K., Wu, W.-L., "The Deprotection Reaction Front Profile in Model 193 nm Methacrylate-Based Chemically Amplified Photoresists," Proc. SPIE **6153**, 615316 (2006).

Vogt, B.D., Lee, H.-J, Wu, W.-L, Liu, Y., "Specular X-Ray Reflectivity and Small Angle Neutron Scattering for Structure Determination of Ordered Mesoporous Dielectric Films," J. Phys. Chem. B **109** (39), 18445 (2005).

Volkovitsky, P., Gilliam, D.M., "Possible PET Isotope Production Using Linear Deuteron Accelerators," Nucl. Instrum. Meth. Phys. Res. A **548**, 571 (2005).

Wakimoto, S., Samara, G.A., Grubbs, R.K., Venturini, E.L., Boatner, L.A., Xu, G., Shirane, G., Lee, S.-H., "Dielectric Properties and Lattice Dynamics of Ca-Doped $K_{0.95}Li_{0.05}TaO_3$," Phys. Rev. B, in press.

Wang, H., "SANS Study of the Early Stages of Crystallization in Polyethylene Solutions," Polymer **47** (14), 4897 (2006).

Wang, H., "Small Angle Neutron Scattering Study of Polyethylene Crystallization From Solution," in *Lecture Notes in Physics: Progress in Understanding of Polymer Crystallization*, edited by Reiter, G., Strobl, G., (Springer, Berlin), p. 179 (2006).

Wang, H., Christopherson, G.T., Xu, Z.Y., Porcar, L., Ho, D.L., Fry, D., Hobbie, E.K., "Shear-SANS Study of Single-Walled Carbon Nanotube Suspensions," Chem. Phys. Lett. **416**, 182 (2005).

Wang, H., Xu, Z., Eres, G., "Order in Vertically Aligned Carbon Nanotube Arrays," Appl. Phys. Lett. **88**, 213111 (2006).

Wietfeldt, F.E., Dewey, M.S., Gilliam, D.M., Nico, J.S., Fei, X., Snow, W.M., Greene, G.L., Pauwels, J., Eykens, R., Lamberty, A., Van Gestel, J., "Measurement of the Neutron Lifetime by Counting Trapped Protons," J. Res. Natl. Inst. Stand. Technol. **110** (4), 327 (2005).

Wietfeldt, F.E., Huber, M., Black, T.C., Kaiser, H., Arif, M., Jacobson, D.L., Werner, S.A., "Measuring the Neutron's Mean Square Charge Radius Using Neutron Interferometry," Physica B, in press.

Wilburn, W.S., Bowman, J.D., Mitchell, G.S., O'Donnell, J.M., Penttilä, S.I., Seo, P.-N., Calarco, J.R., Hersmann, F.W., Chupp, T.E., Cianciolo, T.V., Rykaczewski, K.P., Young, G.R., De Souza, R.T., Snow, W.M., Desai, D., Greene, G.L., Grzywacz, R.K., Frlež, E., Počanić, D., Gentile, T.R., Gudkov, V., Jones, G.L., "Measurement of Neutron Decay Parameters-The abBA Experiment," J. Res. Natl. Inst. Stand. Technol. **110** (4), 389 (2005).

Wilking, J.N., Graves, S.M., Chang, C.B., Meleson, K., Lin, M.Y., Mason, T.G., "Dense Cluster Formation During Aggregation Gelation of Attractive Slippery Nanoemulsion Droplets," Phys. Rev. Lett. **96** (1), 015501 (2006).

Wilson, K.S., Allen, A.J., Washburn, N.R., Antonucci, J.M., "Interphase Effects in Dental Nanocomposites Investigated by Small-Angle Neutron Scattering," J. Biomed. Mater. Res., in press.

Wilson, S.D., Dai, P., Li, S., Chi, S., Kang, H.J., Lynn, J.W., "Resonance in the Electron-Doped High-Transition-Temperature Superconductor $Pr_{0.88}LaCe_{0.12}CuO_{4-\delta}$," Nature **442**, 59 (2006).

Wong-Ng, W., Yang, Z., Cook, L.P., Huang, Q., Kaduk, J.A., Frank, J., "Chemical Interaction Between $Ba_2YCu_3O_{6+x}$ and CeO_2 at p_{O2} = 100 Pa," Solid State Sci. **7** (11), 1333 (2005).

Wu, H., Zhou, W., Udovic, T.J., Rush, J.J., Yildirim, T., "Structure and Vibrational Spectra of Calcium Hydride and Deuteride," J. Alloys Compd., in press.

Wu, L., Lodge, T.P., Bates, F.S., "SANS Determination of Chain Conformation in Perpendicular-Aligned Undecablock Copolymer Lamellae," Macromol. **39** (1), 294 (2006).

Wyslouzil, B.E., Wilemski, G., Strey, R., Heath, C.H., Dieregsweiler, U., "Experimental Evidence for Internal Structure in Aqueous-Organic Nanodroplets," Phys. Chem. Chem. Phys. **8** (1), 54 (2006).

Xavier, J.H., Sharma, S., Seo, Y.S., Isseroff, R., Koga, T., White, H., Ulman, A., Shin, K., Satija, S.K., Sokolov, J., Rafailovich, M.H., "Effect of Nanoscopic Fillers on Dewetting Dynamics," Macromol. **39** (8), 2972 (2006).

Xia, Z.C., Shi, M.F., Gnäupel-Herold, T., Miller, C.E., Konieczny, A., Chen, X.M., Lou, M., "A Benchmark Test for Springback: Experimental Procedures and Results of a Slit-Ring Test," SAE Trans.: J. Mater. Manufacturing **114**, 19 (2006).

Xiao, Y.G., Huang, Q., Ouyang, Z.W., Lynn, J.W., Liang, J.K., Rao, G.H., "Crystal and Magnetic Structures of Laves Phase Compound $NdCo_2$ in the Temperature Range Between 9 and 300 K," J. Alloys Compd., in press.

Xiao, Y.G., Huang, Q., Ouyang, Z.W., Wang, F.W., Lynn, J.W., Liang, J.K., Rao, G.H., "Canted Magnetic Structure Arising From Rare-Earth Mixing in the Laves-Phase Compound $(Nd_{0.5}Tb_{0.5})Co_2$," Phys. Rev. B **73**, 064413 (2006).

Xu, G., Gehring, P.M., Shirane, G., "Persistence and Memory of Polar Nanoregions in a Ferroelectric Relaxor Under an Electric Field," Phys. Rev. B **72**, 214106 (2005).

Xu, G., Gehring, P.M., Stock, C., Conlon, K., "The Anomalous Skin Effect in Single Crystal Relaxor Ferroelectric PZN-*x*PT and PMN-*x*PT," Phase Transitions **79** (1-2), 135 (2006).

Xu, T., Zvelindovsky, A.V., Sevink, G.J.A., Lyakhova, K.S., Jinnai, H., Russell, T.P., "Electric Field Alignment of Asymmetric Diblock Copolymer Thin Films," Macromol. **38** (26), 10788 (2005).

Yamaura, K., Huang, Q., Moldovan, M., Young, D.P., Wang, X.L., Takayama-Muromachi, E., "Metallic Conductivity and a Ca Substitution Study of $NaRh_2O_4$ Comprising a Double Chain System," Physica B **378-380**, 1134 (2006).

Yamaura, K., Huang, Q., Zhang, L., Takada, K., Baba, Y., Nagai, T., Matsui, Y., Kosuda, K., Takayama-Muromachi, E., "Spinel-to-$CaFe_2O_4$-Type Structural Transformation in $LiMn_2O_4$ Under High Pressure," J. Am. Chem. Soc. **128** (29), 9448 (2006).

Yang, C.C., Lee, S.F., Yao, Y.D., Li, W.-H., Lii, K.H., Lynn, J.W., "Magnetic Structures of $[Co_3(pyz)(HPO_4)_2F_2]$, a Fluorinated Cobalt Phosphate With a Pillared Layer Structure," Physica B **378-380**, 1140 (2006).

Yardimci, H., Chung, B., Harden, J.L., Leheny, R.L., "Phase Behavior and Local Dynamics of Concentrated Triblock Copolymer Micelles," J. Chem. Phys. **123**, 244908 (2005).

Ye, F., Dai, P., Fernandez-Baca, J.A., Sha, H., Lynn, J.W., Kawano-Furukawa, H., Tomioka, Y., Tokura, Y., Zhang, J., "Evolution of Spin-Wave Excitations in Ferromagnetic Metallic Manganites," Phys. Rev. Lett. **96**, 047204 (2006).

Ye, F., Fernandez-Baca, J.A., Dai, P., Lynn, J.W., Kawano-Furukawa, H., Yoshizawa, H., Tomioka, Y., Tokura, Y., "Electronically Smecticlike Liquid-Crystal Phase in a Nearly Half-Doped Manganite," Phys. Rev. B **72**, 212404(R) (2005).

Ye, F., Ren, Y., Huang, Q., Fernandez-Baca, J.A., Dai, P., Lynn, J.W., Kimura, T., "Spontaneous Spin-Lattice Coupling in the Geometrically Frustrated Triangular Lattice Antiferromagnet $CuFeO_2$," Phys. Rev. B **73**, 220404 (R)(2006).

Yethiraj, M., Christen, D.K., Gapud, A.A., Paul, D.McK., Crowe, S.J., Dewhurst, C.D., Cubitt, R., Porcar, L., Gurevich, A., "Temperature and Field Dependence of the Flux-Line-Lattice Symmetry in V_3Si," Phys. Rev. B **72**, 060504(R) (2005).

Yildirim, T., Harris, A.B., "Magnetic Structure and Spin Waves in the Kagomé Jarosite Compound $KFe_3(SO_4)_2(OH)_6$," Phys. Rev. B **73**, 214446 (2006).

Yildirim, T., Hartman, M.R., "Direct Observation of Hydrogen Adsorption Sites and Nanocage Formation in Metal-Organic Frameworks," Phys. Rev. Lett. **95**, 215504 (2005).

Yildirim, T., Íñiguez, J., Ciraci, S., "Molecular and Dissociative Adsorption of Multiple Hydrogen Molecules on Transition Metal Decorated C_{60}," Phys. Rev. B **72**, 153403 (2005).

Yim, H., Kent, M.S., Mendez, S., Lopez, G.P., Satija, S.K., Seo, Y., "Effects of Grafting Density and Molecular Weight on the Temperature-Dependent Conformational Change of Poly(*N*-Isopropylacrylamide) Grafted Chains in Water," Macromol. **39** (9), 3420 (2006).

Yim, H., Kent, M.S., Sasaki, D.Y., Polizzotti, B.D., Kiick, K.L., Majewski, J., Satija, S., "Rearrangement of Lipid Ordered Phases Upon Protein Adsorption Due to Multiple Site Binding," Phys. Rev. Lett. **96**, 198101 (2006).

Yim, H., Kent, M.S., Satija, S.K., Mendez, S., Balamurugan, S.S., Balamurugan, S., Lopez, G.P., "Evidence for Vertical Phase Separation in Densely Grafted, High-Molecular-Weight Poly(*N*-Isopropylacrylamide) Brushes in Water," Phys. Rev. E **72**, 051801 (2005).

Yun, S.I., Briber, R.M., Kee, R.A., Gauthier, M., "Dilute-Solution Structure of Charged Arborescent Graft Polymer," Polymer **47** (8), 2750 (2006).

Yun, S.I., Terao, K., Hong, K., Melnichenko, Y.B., Wignall, G.D., Britt, P.F., Mays, J.W., "Solution Properties of 1,3-Cyclohexadiene Polymers by Laser Light Scattering and Small-Angle Neutron Scattering," Macromol. **39** (2), 897 (2006).

Zambrano, E., Kotlarchyk, M., Langner, A., Faraone, A., "Isomeric and Concentration Effects of C4-Cosurfactants on Four-Component Microemulsions Investigated by Neutron Spin-Echo and Small Angle Scattering," J. Phys.: Condens. Matter., in press.

Zank, J., Reynolds, P.A., Jackson, A.J., Baranyai, K.J., Perriman, A.W., Barker, J.G., Kim, M.-H., White, J.W., "Aggregation in a High Internal Phase Emulsion Observed by SANS and USANS," Physica B, in press.

Zeisler, R., Mackey, E.A., Lamaze, G.P., Stover, T.E., Spatz, R.O., Greenberg, R.R., "NAA Methods for Determination of Nanogram Amounts of Arsenic in Biological Samples," J. Radioanal. Nucl. Chem. **269** (2), 291 (2006).

Zeisler, R., Murphy, K.E., Becker, D.A., Davis, W.C., Kelly, W.R., Long, S.E., Sieber, J.R., "Standard Reference Materials (SRMs) for Inorganic Containments," Anal. Bioanal. Chem., in press.

Zhang, Q., Rao, G.H., Huang, Q., Feng, X.M., Ouyang, Z.W., Liu, G.Y., Toby, B.H., Liang, J.K., "Selective Substitution of Vanadium for Molybdenum in $Sr_2(Fe_{1-x}V_x)MoO_6$ Double Perovskites," J. Solid State Chem., in press.

Zhang, Z., Louca, D., Visinoiu, A., Lee, S.-H., Thompson, J.D., Proffen, T., Llobet, A., Qiu, Y., Park, S., Ueda, Y., "Local Order and Frustration in the Geometrically Frustrated Spinels $Cd_{1-x}Zn_xV_2O_4$," Phys. Rev. B **74**, 014108 (2006).

Zhao, P., Cullen, J., Wuttig, M., Kang, H.J., Lynn, J.W., Lograsso, T.A., Moze, O., "Lattice and Spin Dynamics in bcc Fe, 10 at. % Be," J. Appl. Phys. **99**, 08R101 (2006).

Zhou, J., Deyhim, A., Krueger, S., Gregurick, S.K., "LORES: Low Resolution Shape Program for the Calculation of Small Angle Scattering Profiles for Biological Macromolecules in Solution," Comp. Phys. Comm. **170**, 186 (2005).

Zhou, J., Gregurick, S.K., Krueger, S., Schwarz, F.P., "Conformational Changes in Single-Strand DNA as a Function of Temperature by SANS," Biophys. J. **90** (2), 544 (2006).

Zhou, J., Krueger, S., Gregurick, S.K., "A Coarse Graining Approach to Determine Nucleic Acid Structures From Small Angle Neutron Scattering Profiles in Solution," Nucl. Acids. Res. **33** (19), 6361 (2005).

Zhou, N., Lodge, T.P., Bates, F.S., "Influence of Conformational Asymmetry on the Phase Behavior of Ternary Homopolymer/Block Copolymer Blends Around the Bicontinuous Microemulsion Channel," J. Phys. Chem. B **110** (9), 3979 (2006).

Zhu, Z., González, Y.I., Xu, H., Kaler, E.W., Liu, S., "Polymerization of Anionic Wormlike Micelles," Langmuir **22** (3), 949 (2006).

Instruments and Contacts

High resolution powder diffractometer (BT-1):

J.K. Stalick,	(301) 975-6223	judith.stalick@nist.gov
Q.Z. Huang	(301) 975-6164	qing@nist.gov

Residual stress and texture diffractometer (BT-8):

T. Gnaeupel-Herold	(301) 975-5380	tg-h@nist.gov

30-m SANS instrument (NG-7):

L. Porcar	(301) 975-5049	lionel.porcar@nist.gov
P.D. Butler	(301) 975-2028	butler@nist.gov
J. Krzywon	(301) 975-6650	jeffery.krzywon@nist.gov
J.G. Barker	(301) 975-6732	john.barker@nist.gov

30-m SANS instrument (NG-3) (CHRNS):

B. Hammouda	(301) 975-3961	hammouda@nist.gov
S.R. Kline	(301) 975-6243	steven.kline@nist.gov
B. Greenwald	(301) 975-5797	bryan.greenwald@nist.gov
J.G. Barker	(301) 975-6732	john.barker@nist.gov

USANS, Perfect Crystal SANS (BT-5) (CHRNS):

A. Jackson	(301) 975-3146	Andrew.jackson@nist.gov
M.-H. Kim	(301) 975-6469	man-ho.kim@nist.gov
P.D. Butler	(301) 975-2028	butler@nist.gov
J.G. Barker	(301) 975-6732	john.barker@nist.gov

Cold neutron reflectometer-vertical sample-polarized beam option (NG-1):

C.F. Majkrzak	(301) 975-5251	cmajkrzak@nist.gov
J.A. Dura	(301) 975-6251	jdura@nist.gov

Advanced neutron diffractometer/reflectometer (NG-1):

C. Majkrzak	(301) 975-5251	charles.majkrzak@nist.gov
J.A. Dura	(301) 975-6251	jdura@nist.gov

Cold neutron reflectometer-horizontal sample (NG-7):

S.K. Satija	(301) 975-5250	satija@nist.gov

Double-focusing triple-axis spectrometer (BT-7):

Y. Chen	(301) 975-6442	ying.chen@nist.gov
J.W. Lynn	(301) 975-6246	jeff.lynn@nist.gov

Triple-axis spectrometer (BT-9):

W. Ratcliff	(301) 975-4316	william.ratcliff@nist.gov
R.W. Erwin	(301) 975-6245	rerwin@nist.gov
J.W. Lynn	(301) 975-6246	jeff.lynn@nist.gov

SPINS, Spin-polarized triple-axis spectrometer (NG-5) (CHRNS):

J.-H. Chung	(301) 975-8369	jae-ho.chung @nist.gov
H.-J. Kang	(301) 975-4863	hye.kang@nist.gov

FANS, Filter-analyzer neutron spectrometer (BT-4):

T.J. Udovic	(301) 975-6241	udovic@nist.gov
J. Leao	(301) 975-8867	juscelino.leao@nist.gov

DCS, Disk-chopper time-of-flight spectrometer (NG-4) (CHRNS):

J.R.D. Copley	(301) 975-5133	jcopley@nist.gov
Y. Qiu	(301) 975-3274	yiming.qiu@nist.gov
C.M. Brown	(301) 975-5134	craig.brown@nist.gov

HFBS, High-flux backscattering spectrometer (NG-2) (CHRNS):

V. Garcia Sakai	(301) 975-4404	vicky@nist.gov
G. Gašparović	(301) 975-8396	goran.gasparovic@nist.gov

NSE, Neutron spin echo spectrometer (NG-5) (CHRNS):

A. Faraone	(301) 975-5254	antonio.faraone@nist.gov
J.S. Gardner	(301) 975-8396	jason.gardner@nist.gov
M. Nagao	(301) 975-5505	michihiro.nagao@nist.gov

Prompt-gamma neutron activation analysis (NG-7):

R.M. Lindstrom	(301) 975-6281	dick.lindstrom@nist.gov
R.L. Paul	(301) 975-6287	rpaul@nist.gov

Thermal neutron prompt-gamma activation analysis (VT-5):

E.A. Mackey	(301) 975-5149	liz.mackey@nist.gov

Other activation analysis facilities:

R.R. Greenberg	(301) 975-6285	rgreenberg@nist.gov

Cold neutron depth profiling (NG-1):

G. Downing	(301) 975-3782	gregory.downing@nist.gov

Neutron interferometer (NG-7):

D. Jacobson	(301) 975-6207	jacobson@nist.gov
D. Hussey	(301) 975-6465	daniel.hussey@nist.gov
M. Arif	(301) 975-6303	muhammad.arif@nist.gov

Neutron Imaging Facility (BT-2):

M. Arif	(301) 975-6303	muhammad.arif@nist.gov
D. Jacobson	(301) 975-6207	jacobson@nist.gov
D. Hussey	(301) 975-6465	daniel.hussey@nist.gov

Fundamental neutron physics station (NG-6):

NG-6M: M.S. Dewey	(301) 975-4843	mdewey@nist.gov
NG-6U: H.P. Mumm	(301) 975-8355	pieter.mumm@nist.gov
NG-6: J. Nico	(301) 975-4663	nico@nist.gov

Theory and modeling:

T. Yildirim	(301) 975-6228	taner@nist.gov
N.F. Berk	(301) 975-6224	nfb@nist.gov

Sample environment:

J. Leao	(301) 975-8867	juscelino.leao@nist.gov
D.C. Dender	(301) 975-6225,	dender@nist.gov

NIST CENTER FOR NEUTRON RESEARCH

For copies of or information on this report, contact:

Ronald L. Cappelletti
(301) 975-6221
ronald.cappelletti@nist.gov

For additional information on the Facility, contact:

Patrick D. Gallagher
(301) 975-6210
patrick.gallagher@nist.gov

Dan Neumann
(301) 975-5252
dan.neumann@nist.gov

To obtain guidelines for preparing proposals to conduct research at the facility, contact:

William A. Kamitakahara
(301) 975-6878
william.kamitakahara@nist.gov

Location of all contacts:

NIST Center for Neutron Research
National Institute of Standards and Technology
100 Bureau Drive, Mail Stop 8560
Gaithersburg, MD 20899-8560

Copies of this report and other information are available electronically. Please visit our website.
www.ncnr.nist.gov

NIST CENTER FOR NEUTRON RESEARCH
National Institute of Standards and Technology
100 Bureau Drive, MS 8562
Gaithersburg, MD 20899-8562

www.ncnr.nist.gov

NIST
National Institute of Standards and Technology
Technology Administration, U.S. Department of Commerce